Università degli Studi di Messina

Department of Chemical, Biological, Pharmaceutical and Environmental Sciences

Ph.D. Course in Applied Biology and Experimental Medicine
Curriculum: Pharmacological Sciences
XXXVI CYCLE
S.S.D. CHIM/08

In Silico Methods for Inhibitor Binding Analysis on Human Carbonic Anhydrase Isoforms And Tyrosinase Enzyme Aimed To The Development of New Therapeutics

Ph.D. Thesis of:

Federico Ricci

Supervisor:

Prof.ssa Laura De Luca

Coordinator of Ph.D. course:

Prof.ssa Nunzia Carla Spanò

2022/2023

Dedicated to my dad, who always supported my interest for science and valued my rational thinking.

Index

Forewords

The rising of computational methods applied to life science, as well as the increase of computer performance determined a considerable growth in the speed and accuracy of drug discovery accompanied by a reduction in cost when compared to the traditional high throughput screening approach.

Metalloenzymes represents one of the widest classes of enzymes present in nature. Indeed, they cover several classes of enzymes playing a crucial role in the survival of living organisms. Conversely, as for other enzymes, their overexpression leads to various disorders, spanning from metabolic disorder to cancer and infection. Thus, a plethora of metalloenzymes are nowadays attractive drug targets, being subject of study since decades.

It is not possible to provide an in depth and comprehensive review on all the present metalloenzymes due to their number. Therefore, in this work the attention is focused on two metalloenzyme families: human Carbonic anhydrases (hCAs), involved in several kinds of diseases according to the isoform examined, and Tyrsosinases, which catalyze the rate-limiting steps in melanin production.

Indeed, the PhD thesis presented here is articulated in two parts. **Part I** deals with two subsets of hCAs, specifically, hCAs V (**Chapter 1**), with a major attention on hCA VA which configures as anti – obesity target, and hCA IX and XII (**Chapter 2**) which are established anti – cancer targets, especially in the context of hypoxic tumors. **Part II** concerns Tyrosinase inhibition, focusing on the inhibition of two isoenzymes: mushroom Tyrosinase (AbTYR, **Chapter 4**) and human Tyrosinase (hTYR, **Chapter 5**). For each of the three topics discussed the state of art is given (**Section 1.1.** and **1.2** of Chapter 1, **Section 2.1.** and **2.2** of Chapter 2, respectively for hCA VA, and hCA IX/XII and **Chapter 3** for Tyrosinases), providing an overview on the structure, the catalysis and the general features required for the inhibition of the five enzymes examined. This is done in order to provide a proper understanding of our contribution to the three topics (**Section 1.3**; **2.3**; **Chapter 4** and **Chapter 5**) concerning the inhibitor design, made through in – silico techniques that span from homology modelling to docking, pharmacophore Virtual screening (VS) and Molecular dynamics (MD) simulations. As result, the computational workflows described in the four sections led to i) the discovery of 30 hCA VA inhibitors (**VAME 1 – 30**), out of which 20 were showing ki values below 100 nM and one of them (**VAME 28**) selectively inhibited hCA VA; ii) the identification of hot

– spot residues responsible for ligand selectivity towards hCA XII, starting from the retrospective analysis on hCA XII, IX – mimic and II of two in - house selective hCA XII inhibitors; iii) the identification and binding – mode depiction of potent AbTYR inhibitors (compounds **19p**, **19s** and **19t**); iv) the discovery of a potent dual AbTYR/hTYR inhibitor (**Compound 7**) by means of comparative docking studies of two inhibitors showing potent inhibition of the single isoenzymes. Several collaborators were involved the three projects which are listed in Acknowledgements.

Introduction to metalloenzymes and the therapeutic application of their inhibitors

Metalloenzymes encompass a wide range of protein families that employ metal ions as essential cofactors for their catalytic activity, directly bound to the protein or included in prosthetic groups through coordination complexes.

There is no accountable percentage of the existing metalloproteins in living organisms with respect to other superfamilies. Nonetheless, up to Lothian et al., due to technical limitations, the number of the currently identified metalloproteins is just one third of the proteins predicted to bind metals. Not only, human metalloproteome results way larger in comparison to the one of procaryotes, often used as protein expression systems. [1]

Metalloenzyme families can follow two different classifications. The former, as for metalloproteins, depends on the coordination sphere present in the enzyme active site, either referred to the metal ion or to the chelating species. Therefore, the classes listed below and the examples reported, belong to this type of classification:

1. **Heme Metalloenzymes:** Heme metalloenzymes contain a heme prosthetic group, which contains an iron ion coordinated within a porphyrin ring. Well know examples include Cytochrome P450 enzymes, involved in detoxification and metabolism of various compounds and Catalase which prevents Oxygen reactive species (ROS) formation by decomposing hydrogen peroxide to water and oxygen.

2. **Non-Heme Iron proteins:** which contain Iron as well as co-factor, but differently from the previous class, it is not complexed by heme prosthetic group, as Ribonucleotide reductase, essential for DNA synthesis by converting ribonucleotides to deoxyribonucleotides.

3. **Iron-Sulfur Cluster Proteins:** Iron-sulfur cluster proteins present Iron coordinated with a tetrahedral geometry by cysteinyl thiolate groups. Their main role regards electron transfer and redox reactions. Aconitase, which catalyzes the isomerization of citrate to isocitrate in the citric acid cycle, represents one of the most famous examples.

4. **Zinc-Containing Metalloenzymes:** Zinc is a common metal ion in metalloenzymes and is crucial for structural stability and catalysis, acting mainly as electrophilic species and coordinated by histidine, glutamic acid and cysteine residues. [2] Carbonic anhydrases,

which catalyze the interconversion of carbon dioxide and bicarbonate ions, represent one of the famous family of zinc-containing metalloenzymes.

5. **Manganese-Containing Metalloenzymes:** Manganese metalloenzymes utilize manganese ions in their active sites. An example is the mitochondrial superoxide dismutase (Mn-SOD), involved in antioxidant defense by neutralizing superoxide radicals. [3]

6. **Magnesium-Containing Metalloenzymes:** Magnesium serves as a cofactor in various enzymatic reactions. Ribonucleases, essential for living organisms since it cleaves precursor transcripts to produce the mature 5'-end of tRNAs, require magnesium for proper substrate binding and catalysis.[4]

7. **Cuproproteins:** Copper is often essential for electron transfer and redox reactions in these enzymes. Cuproproteins can be further divided into the three following categories according to the nature of the metal center (geometry, ligands and EPR spectrum):

   o Type I copper proteins (T1Cu) present a single copper ion coordinated by two histidine residues and a cysteine residue in a trigonal planar structure, and a variable axial chelator (often methionine sulfur). A common subset of type I Copper proteins is the one of the so-called Blue Copper proteins for their intense color.

   o Type II copper centers (T2Cu) show a square planar coordination by N or N/O chelators, frequently three histidine and a water molecule or a hydroxide ion.

   o Type III copper centres (T3Cu) contain a binuclear copper center, each coordinated by three histidine residues and a bridging ligand. Differently from the other two types, these proteins exhibit no EPR signal due to strong antiferromagnetic coupling (i.e. spin pairing) between the two $S = 1/2$ metal ions due to their covalent overlap with a bridging ligand.

   Several known enzymes as Nitrite oxidase (type I Blue copper enzyme), present in bacteria, Dopamine beta – hydroxylase (type II cuproenzyme) and Tyrosinase (type III copper enzyme), which will be discussed more in detail in the next chapters, are counted among these classes.

8. **Molybdenum-Containing Enzymes:** Molybdenum enzymes have molybdenum ions as cofactors, many times participating in oxygen transfer reactions. Nitrate reductase, involved

in the reduction of nitrate to nitrite in plants, represent a common example of molybdoenzyme.[5]

9. **Nickel-Containing Enzymes:** Nickel enzymes utilize nickel ions for catalysis and play roles in diverse metabolic processes. Examples include Urease which catalyzes the hydrolysis of urea into ammonia and carbon dioxide and Nickel – Superoxide dismutase (Ni-SOD) present in some bacteria.[6]

10. The latter classification instead, as all the other enzymes, belongs to the type of reaction catalysed, therefore we can distinguish among oxidoreductases, hydrolases, transferases, lyases, isomerases, ligases and translocases. These seven classes can be further divided into more specific categories, such as kinases which belong to transferases.

As just seen, metalloenzymes cover diverse crucial biological functions, thus, as for other enzymes, alteration in their expression or function may lead to several diseases. Indeed, a plethora of metalloenzymes are nowadays consolidated trends in medicinal chemistry. One of the most famous cases is human Carbonic anhydrase (hCAs) superfamily, whose inhibitors have been employed for the treatment of oedema from decades. Nevertheless, the research is still ongoing because various hCA isoforms are expressed in fewer tissues and involved in many pathologic processes, such as epilepsy, obesity and cancer.

Some metalloenzymes configures as attractive as anti-viral targets too. In this context HIV-Integrase binders, designated to inhibit the integration of viral DNA into the host genome, constitute one of the most novel treatments for HIV infections.

Not only, metalloenzymes ligands find application also in cosmetic and for the treatment of skin related diseases. Tyrosinase inhibitors, for example, covers fields from skin hyperpigmentation disorders, such as melasma and melanomas to fruit browning in food industry.

Increasing awareness of the role metalloenzymes play in disease and their importance as a class of targets has amplified interest in the development of new strategies to develop inhibitors and ultimately useful drugs.[7]
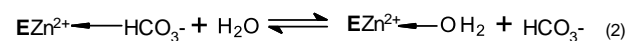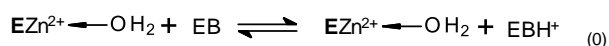
The use of computational study for metalloproteins have presented more challenging that other proteins, that derives from the complex nature of the metal coordination bond.

Fortunately, nowadays, many computational methods have been successfully applied to discovery new metalloenzymes ligands.

PART 1

Overview on human Carbonic Anhydrases (hCAs)

Carbonic anhydrases (CAs, EC 4.2.1.1) play a pivotal role in most organisms/tissues, being involved in a multitude of physiologic and pathologic functions. They catalyse the reversible hydration of carbon dioxide or dehydration of carbonic acid, generating bicarbonate and protons in the first case, or CO_2 and water in the second one. The hydration mechanism, schematized below, involves firstly the deprotonation of a water molecule which generally coordinate Zn ion (although other metal ions, such as Cd, Fe or Co were also identified) together with three chelating residues in a tetrahedral geometry (0).[8] Then, once deprotonated, the hydroxide ion acts a nucleophile on CO_2 molecule forming bicarbonate ion still bound to the metal ion (1). Finally, a water molecule replaces the bicarbonate ion and a proton shuttle network deprotonate the water molecule restoring the active form of the enzyme (2); (0).

$$\mathbf{E}Zn^{2+}\text{---}OH_2 + EB \rightleftharpoons \mathbf{E}Zn^{2+}\text{---}OH_2 + EBH^+ \quad (0)$$

$$\mathbf{E}Zn^{2+}\text{---}OH^- + CO_2 \rightleftharpoons \mathbf{E}Zn^{2+}\text{---}HCO_3^- \quad (1)$$

$$\mathbf{E}Zn^{2+}\text{---}HCO_3^- + H_2O \rightleftharpoons \mathbf{E}Zn^{2+}\text{---}OH_2 + HCO_3^- \quad (2)$$

Up to date we can enumerate up to six different CA subfamilies, specifically α , β , γ , δ , ζ and η. In vertebrates it is know the expression of just α subfamily, while regarding the other ones, they are expressed mainly in bacteria, fungi, plants and some Archea organisms (β and γ), as well as algae (δ and ζ) and protozoa (η). In the work here reported the attention is focused just on α carbonic anhydrases, specifically the human isoforms (hCAs).[9] In this context, up to fifteen hCA isoforms were characterized: eleven of them show catalytic activity (I - VII, IX and XII – XIV), while three of them are acatalytic (VIII, X and XI).

Table 1. Table showing CO_2 hydration activity, subcellular location and distribution of known hCA isoforms. Data taken from ref.[10]

hCA isoform	Catalytic activity (CO_2 hydration)	Subcellular location	Organ/Tissue distribution
hCA I	Low	Cytosol	Erythrocytes, gastrointestinal tract, and eye
hCA II	High	Cytosol	Erythrocytes, eye, gastrointestinal tract, bone osteoclasts, kidney, lung, testis, and brain
hCA III	Very Low	Cytosol	Skeletal muscle and adipocytes
hCA IV	Medium	Transmembrane – extracellular active site	Kidney, lung, pancreas, brain capillaries, colon, heart muscle, and eye
hCA VA	Low	Mitochondrial	Liver
hCA VB	High	Mitochondrial	Heart and skeletal muscle, pancreas, kidney, spinal cord, and gastrointestinal tract
hCA VI	Low	Saliva and milk secretion	Salivary and mammary gland
hCA VII	High	Cytosol	Central nervous system (CNS)
hCA VIII	Acatalytic	Cytosol	CNS
hCA IX	High	Transmembrane – extracellular active site	Tumors and gastrointestinal mucosa
hCA X	Acatalytic	Cytosol	CNS
hCA XI	Acatalytic	Cytosol	CNS
hCA XII	Low	Transmembrane – extracellular active site	kidney, intestine, reproductive epithelia, eye, tumors, and CNS
hCA XIII	Low	Cytosol	Kidney, brain, lung, gut, and reproductive tract
hCA XIV	Low	Transmembrane – extracellular active site	Kidney, brain, liver, and eye

The different tissue expression and the subcellular location of each isoform strongly influence their role in both physiological processes as well as in pathological ones. Indeed, starting from hCA I and II already approved for the treatment of oedema and glaucoma, hCAs configures as promising drug targets involved other diseases such as epilepsy, obesity or cancer. Nevertheless, due to the wide distribution of hCA I and II which leads to off - target effects, selective inhibition of specific isoenzymes over the aforementioned ones is a constant challenge in the design of new hCAs inhibitors that may be candidates for clinical trials. The main issue in achieving selectivity is principally due to the common structural features shared by the whole subset.
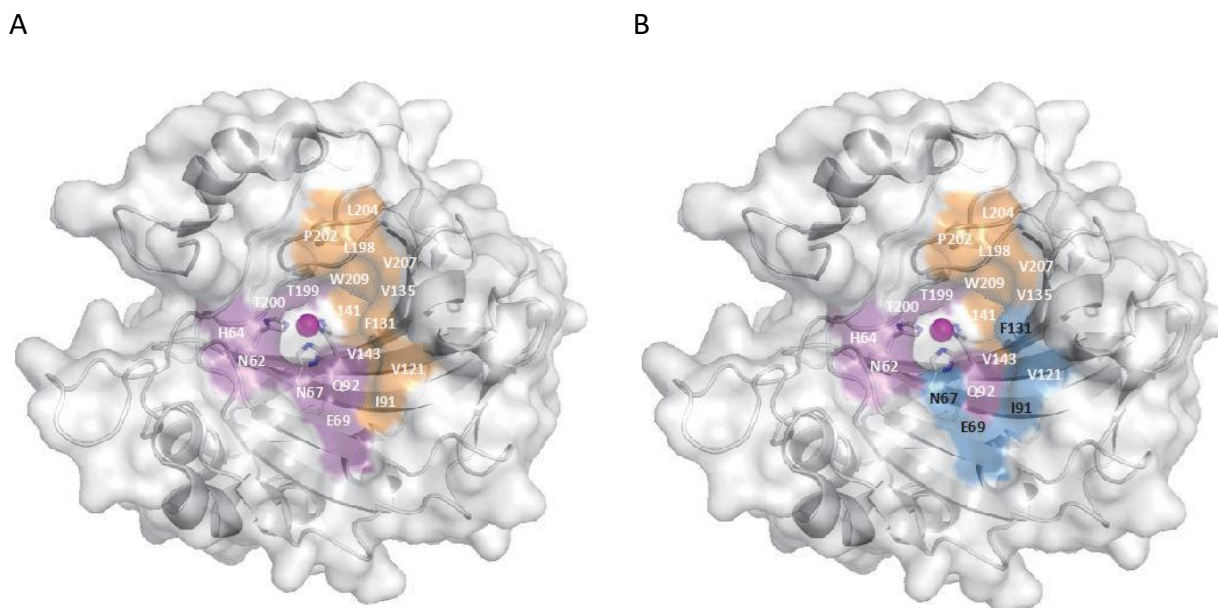
Figure 1. Pockets in α CAs (hCA II taken as reference). Zinc ion is represented as a magenta sphere while coordinating histidines as sticks. (A) Hydrophilic and hydrophobic regions of the active site have been coloured purple and orange, respectively. (B) Isoform unique residues that constitute the selective pocket are shown in blue. Images taken from ref. [11].

Firstly, all hCA are characterized by two main surfaces: a hydrophobic one, assumed to be involved in CO2 recognition, and a hydrophilic one designated to stabilize conserved water molecules (including the catalytic one) during proton shuttling process. (Figure 1A) Then, Zn ion as well as zinc – coordinating histidines (H94, H96 and H119, taking hCA II as numbering reference) are conserved too in all the catalytic isoforms.
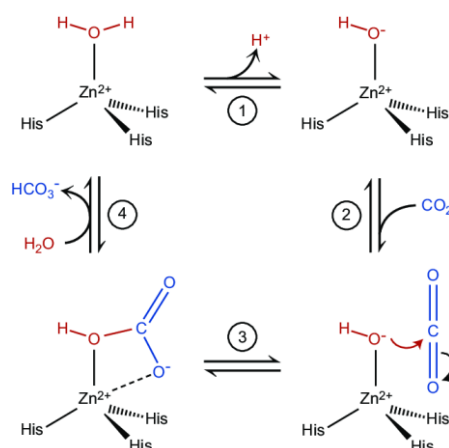

Figure 2. The active site chemistry of carbonic anhydrase mediated reversible catalysis of carbon dioxide (CO_2) hydration and bicarbonate (HCO_3^-) dehydration. A divalent zinc ion is activated by coordination to three histidine (His) molecules in a tetrahedral arrangement that permits binding of water, its hydrolysis to a zinc-hydroxide (reaction 1), nucleophilic attack on the carbonyl bond of carbon dioxide (reaction 2) to produce bicarbonate in the active site (reaction 3), and release of bicarbonate and regeneration of zinc-bound water (reaction 4). Reaction 1 is facilitated by rapid shuttling of the proton produced in reaction 1 to bulk water by hydrogen ion-titratable amino acid side chains leading out of the active site. Zn^{2+} = divalent positively charged zinc ion. Figure supplied by David Silverman, Ph.D., University of Florida, Gainesville, Florida.

Finally, despite the overall sequence identity among all the hCA isoforms results moderate, the active site itself is well conserved. Starting from the deeper side of the enzyme were Zinc ion placed and going towards the entrance, several residues involved in substrates or inhibitors binding, such as T199, T200, Q92, V143 and the proton shuttling H64 are highly conserved. Even so, thanks to crystallography, mutagenesis and NMR studies, some amino acids (mainly at the outer rim of the active site) for which ligand selectivity may be addressed as the case of position 131, were highlighted. (Figure 1B and 2). Thus, besides the plethora of hCA II co – crystal structures available with respect to the ones of the other isoenzymes, taking into account point mutation, especially at the entrance of the binding site, may be suggested for designing new selective binders for specific isoforms. (Figure 3) [11]
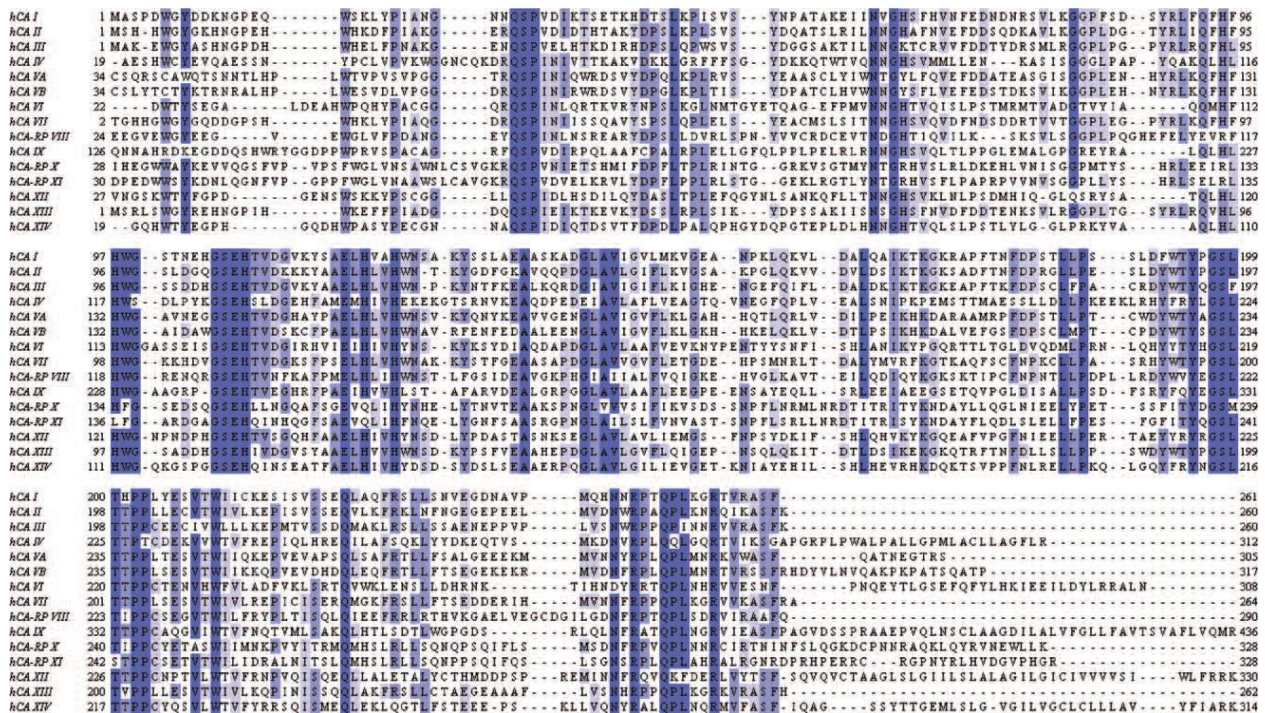

Figure 3. Multiple sequence alignment of the hCA isoforms. Gradients of blue represent sequence conservation from most (dark blue) to least conserved (light blue). Image taken from ref.[12]

Concerning the inhibitors, several classes with different trends in potency and selectivity and unique inhibition mechanisms were identified. They can be briefly classified as follows:

- Zinc binders, which are characterized by a chelating group able to displace the catalytic water molecule and to hydrogen – bond T199. Sulfonamides and their isosters represent the main example of this class;

- Water anchoring ligands, which present a group that hydrogen – bond the catalytic water and T199. Phenols and polyamine display this inhibition mechanism;

12

- Inhibitors occluding the active site entrance. As coumarins, this class contain a so called "sticky group" which exploit the esterase activity of α – CAs to form a metabolite able to bind residue a the outer rim of CA, blocking the access to the pocket;
- Proton shuttle inhibitors which bind CA out the active site and stabilize H64 out conformation, e.g. the one in which the residue cannot accept the proton from the active water. 2 - (benzylsulfonyl) - benzoic acid is one the few hCA showing this inhibition mechanism;
- Inhibitors with an unknown mechanism.

The first three classes often present a tail binding either the entrance or the outer part of the cavity.[9]

In the following chapters four hCA isoforms are taken into consideration: hCA VA and VB in order to return potential anti - obesity agents, while hCA IX and XII to provide new chemotherapics. In terms of the chemical space analysed, the attention is focused on zinc – binder inhibitors, with a major interest in sulfonamide – like compounds.

Chapter 1: Human Carbonic Anhydrases (hCAs) V for the Treatment of Obesity

1.1. Obesity and Its Current Treatment

According to a WHO (World Health Organization) report of 2016, more than 650 million people present obesity. In principle the definition of obesity is referred to a condition in which the body mass index (BMI) is ≥ 30. Nevertheless, the pathogenesis which lead to the unbalance between the calories acquired versus their expenditure, is not exclusively related to the food consumption. Indeed, despite behavioral and psychological factors are involved, several metabolic components, as well as age, play key roles in obesity etiology and co - morbidities. Anatomically speaking, adipose tissue, gastrointestinal muscles and nervous system (central and peripheral) are the main characters controlling body weight and appetite. Chemically speaking instead, insulin, leptin, cholecystokinin (CCK), glucagon-like peptide-1 (GLP-1), peptide YY (PYY), and ghrelin act at the hypothalamic level, which communicate with the reward center influencing the aforementioned sensation.

- Insulin is a pancreatic hormone well known for its function in glucose blood levels balance and tissue absorption. Nonetheless, insulin receptors are present as well in the hypothalamus and determine a decrease in food intake.

- Leptin, an anorexigenic hormone, is produced by adipose tissue and regulates lipid metabolism. It crosses the blood-brain barrier through a transport system, informing the hypothalamus of energy status. This down-regulates appetite stimulators and up-regulates anorexigenic alpha-melanocyte-stimulating hormone, reducing food intake. Leptin is anti-obesity, but obesity leads to resistance in its satiety effects. Leptin activates the sympathetic nerve system, affects renal hemodynamics, blood vessel tone, and blood pressure modulation.

- Ghrelin is a gut peptide growth hormone which possesses orexigenic properties. It impacts hypothalamic receptors, hindering insulin secretion and controlling gluconeogenesis and glycogenolysis. As a rapid initiator of feeding, its levels rise before food intake. Ghrelin's signaling reduces thermogenesis, regulates energy expenditure, and promotes adiposity.

Beyond this, it influences various systems, impacting areas like cardioprotection, muscle atrophy, bone metabolism and cancer.

- Cholecystokinin, a gut peptide hormone and brain neuropeptide, plays a role in stimulating digestion, slowing gastric emptying, boosting intestinal motility, increasing pancreatic digestive enzymes and bile release from the gallbladder, thus regulating appetite.

- Glucagon-like peptide-1 (GLP-1) is a postprandial gut hormone and its receptor (GLP-1R) are distributed in multiple organs. Its key roles include stimulating insulin secretion, promoting β-cell growth and survival, inhibiting glucagon release, and curbing appetite. Moreover, stimulation enhances calcium levels, adenylate cyclase activity, and signaling pathways. GLP-1 acts as a cardiovascular protector by thwarting thrombosis, averting atherogenesis, and guarding against vascular inflammation and oxidative stress.

- Peptide YY, co-released with GLP-1, reacts to meals and operates via the anorexinergic pathway in the hypothalamus. This pathway reduces intestinal motility, slows gallbladder and gastric emptying, leading to appetite reduction and heightened satiety.

Due to their importance in the physical and nervous regulation of food intake, alteration in the aforementioned chemical production and in their receptor expression/functionality are both cause and consequence of obesity condition.[13, 14] Furthermore, components of the resident gut bacteria, such as the LPS of the *phylum Bacteriodetes , contribute to obesity disease.*

Obesity involves an inflammation state characterized by an increased adipose tissue and reduced adiponectin levels. Adipose tissue is divided into white (WAT) and brown (BAT), however the WAT has a major implication in adiposity and in its complications. Although adiponectin is produced in the adipose tissue, it contrasts the inflammatory response inhibiting TNF-α expression and its expression is conversely inhibited by TNF-α and IL − 6. Not only, reduced adiponectin levels are appreciated in conditions of hypoxia and oxidative stress. [13, 15]In summary, three main effects are determined by the increment of the adipose tissue: infiltration of immune cells in the adipose tissue and release of pro-inflammatory cytokines and product of fatty acids oxidation which leads to ROS formation and infiltration of inflammatory cells in other tissues such as the pancreatic one; increment of circulating LPS from gut bacteria due to the enhanced intestinal permeability which stimulate toll-like receptors 4 (TLR − 4) inflammatory response; formation of perivascular adipose tissue which determine local inflammation, endothelial disfunction and vessel hardening and constriction.
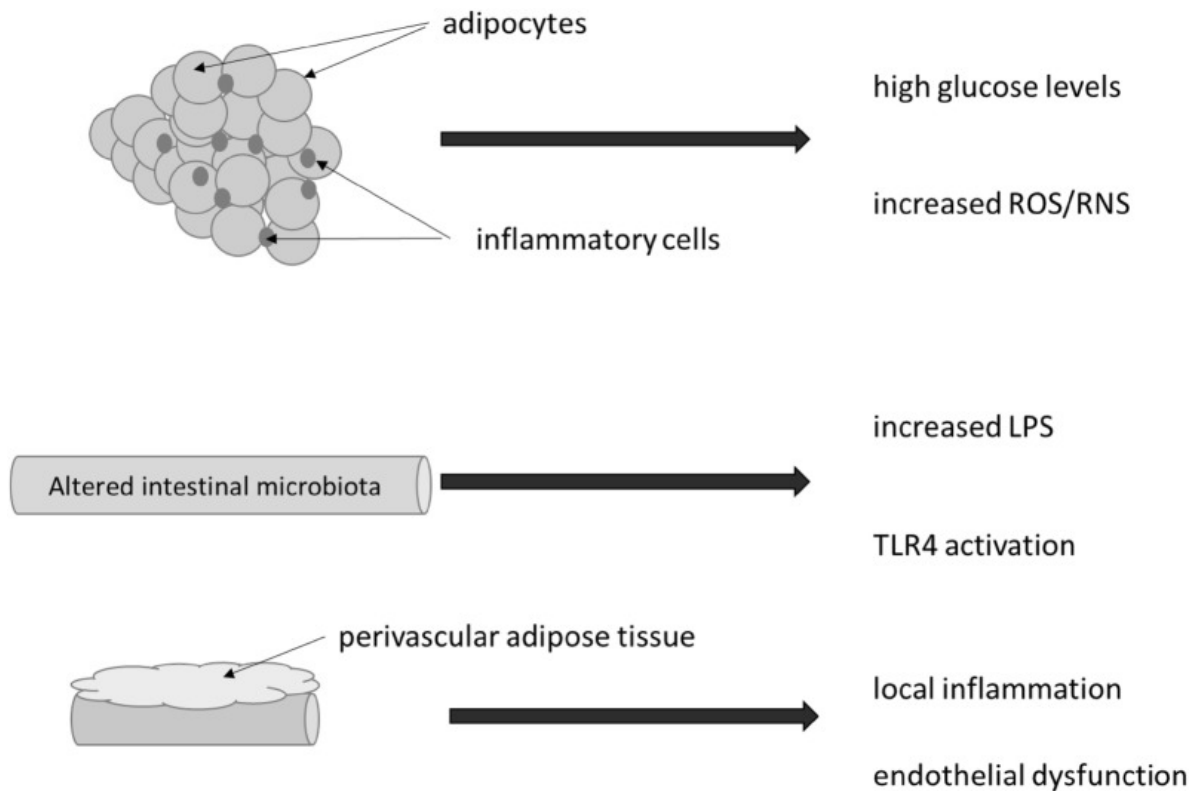
Figure 4. Process of inflammation in obesity. Circulating biomarkers observed in obese patients confirm the infiltration of inflammatory cells in adipose tissue. In addition, an increased in the amount of reactive oxygen species (ROS) and reactive nitrogen species (RNS) is also appreciated. In parallel, alteration of the microbiota is related to increased lipopolysaccharide (LPS) release in the bloodstream which activates toll like receptor 4 (TLR4). Finally, increased perivascular adipose tissue enhance local vessel inflammation and impairment of endothelium function. Image taken from ref.[13]

Hence, the most predictable outcomes are hypertension, atherosclerosis, eventually followed by plaque rupture due also to the lower adiponectin levels, and insulin resistance (Type 2 Diabetes). (Figure 4)

Currently, apart from changes in the food intake habits, such as meal replacement, calories restriction and several diets, two types of approaches are common for severe obesity treatment: surgery and pharmacotherapy.

The most famous intervention for obese patients is Bariatric surgery for which four different types can be distinguished according to the gastro - intestinal modification performed: adjustable gastric banding (LAGB); Roux – en – Y gastric bypass (RYGB); Sleeve gastrectomy (SG); Bilio-pancreatic diversion with duodenal switch (BPD-DS). Additionally, a common alternative for individuals who cannot undergo Bariatric surgery is the intragastric balloon (IGB).

Despite the efficacy in weight loss and co-morbidities reduction (eg. hypertension, diabetes, dyslipidemia), several serious side – effects due to the intolerance of the adjustments, especially with LABG and SG, lead to the device removal. These include: dumping syndrome, nutritional

deficiencies, as well as psychological disorders such as anorexia and bulimia nervosa.[16] Regarding the pharmacological treatment, from 2019 to now several changes in the anti-obesity drug market occurred. Several drugs employed for decades for overweight disorders have been recently withdrawn by FDA or EMA for their life-threatening side effects. This is the case of some proopiomelanocortin (POMC) receptors agonists whose pharmacological effect is the appetite reduction, which are often peripheral 5-hydroxytryptamine 2B (5-HT2b) receptor agonists. Among them we can enumerate fenfluramine and dexfenfluramine determining valvulopathy and the well – known Lorcaserin (Belviq®) revealing high risk of breast cancer.

Still, present approved anti-obesity act mainly at two levels: on the central nervous system, determining satiety by contacting dopaminergic neurons of ventral tegmental area (VTA), the nucleus accumbens, gabaergic neurons, POMC and neuropeptide Y receptors of the arcuate nucleus (ARC); on the peripheral one, influencing gastric and intestinal motility, absorption and hormone realease by stimulating GLP-1 receptors or altering fat absorption inhibiting lipase. The mechanism just mentioned are resumed in Figure 5.
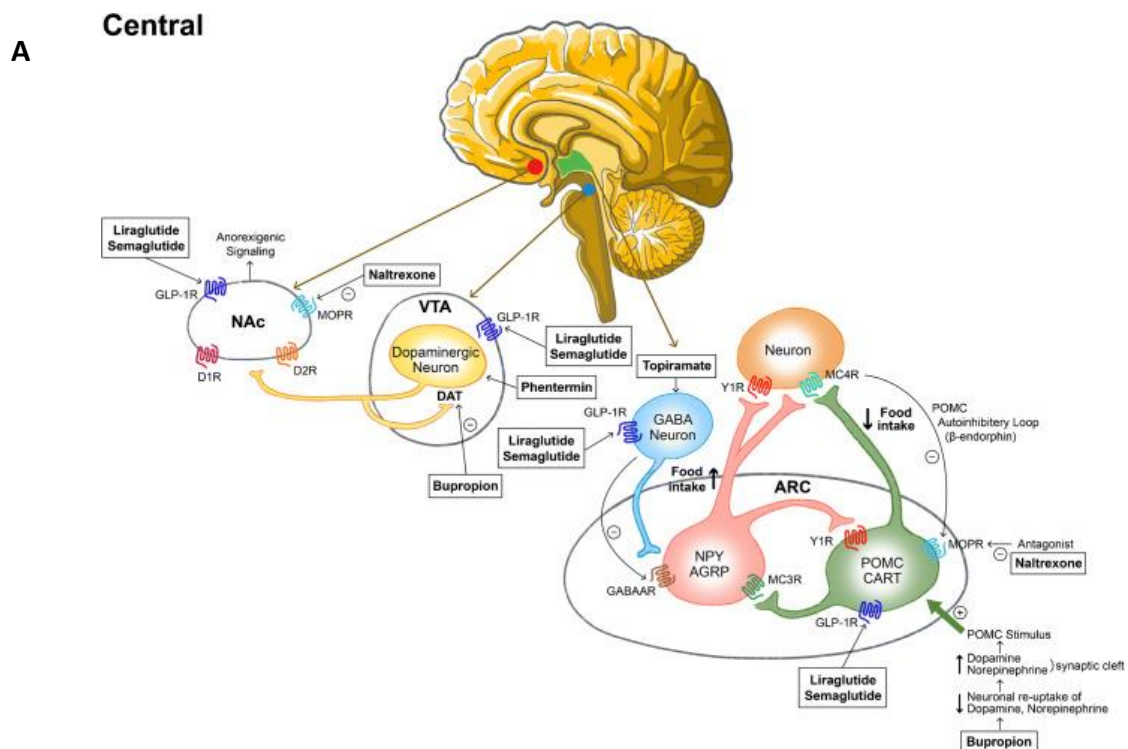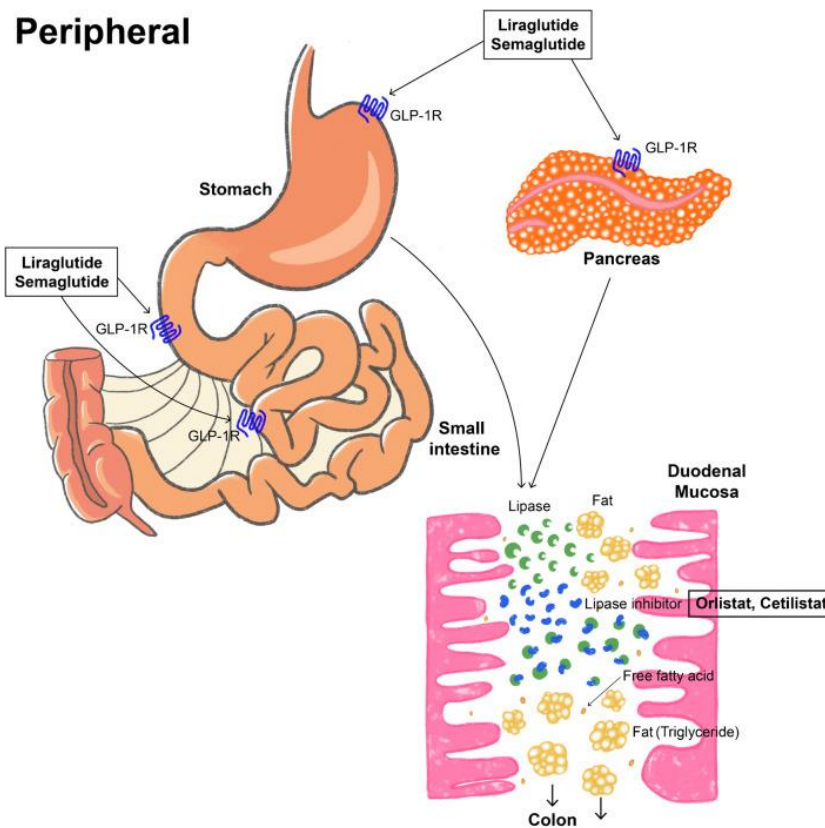
Figure 5. (A) Mechanisms of anti-obesity drugs acting on central nervous system. Notes: AGRP, agouti-related peptide; ARC, arcuate nucleus; CART, cocaine- and amphetamine-regulated transcript; DAT, dopamine active transporter; D1R, dopamine 1-class receptor; D2R, dopamine 2-class receptor; GABA, gamma-aminobutyric acid; GABAAR, γ-aminobutyric acid type A receptor; GLP-1R, glucagon-like peptide-1 receptor; MC3R, melanocortin-3 receptor; MC4R, melanocortin-4 receptor; MOPR, μ-opioid receptor; NAc, nucleus accumbens; NPY, neuropeptide Y; POMC, proopiomelanocortin; VTA, ventral tegmental area; Y1R, neuropeptide Y receptor type 1. (B) Mechanisms of anti-obesity drugs hitting peripheral nervous system. Notes: GLP-1R, glucagon-like peptide-1 receptor. Images taken from ref.[17]

Below are summarized some of the current p.a. or association approved by FDA and EMA, their mechanism of action and their main side-effects:

- Naltrexone/bupropion (Contrave®) associate two μ - opioid antagonist acting on NAc (naltrexone) and inhibiting β-endorphin auto-loop stop signal on POMC/CART neurons (naltrexone and bupropion), also used for nicotine and alcohol addiction treatment. Several uncomfortable side effects such nausea, constipation, dizziness and headache determine continuous adjustment of the dosage. Not only, monitoring is mandatory in patient with suicidal tendencies.

- Orlistat (Xenical®) is a lipase inhibitor which blocks the absorption of at least one-third of the fatty acid consumed. Despite it shows modest efficacy in comparison to other anti - obesity drugs, its side-effects, apart from the ones due to non-absorbed fats such as steatorrhea, are well tolerated.

- Liraglutide (Victoza®) is a GLP-1 agonist acting on different levels due to the expression of GLP-1 receptors: on one side it reduces appetite at the hypothalamus and at the cortex, on the other side reduce glucagone secretion and glucose blood concentration, enhance satiety slowing gastric – emptying. Similarly to naltrexone/bupropion association, severe side – effects are demonstrated by Liraglutide vomiting, diarrhoea , but also high risk of pancreatitis and neoplasm. Therefore, in depth post – marketing surveillance is advised for this drug.

- Phentermine/topiramate extended-release (ER) (Qysmia®), combine an indirect sympathomimetic (phentermine) which enhances dopamine, noradrenaline and serotonin release and antagonize neuropeptide Y, with a multi – target kainate/AMPA antagonist (topiramate) used for decades for epilepsy treatment. Their mechanism is not properly elucidated yet, but they reduce the appetite through the biochemical pathways just mentioned, a weight loss seems to be produced via carbonic anhydrase inhibition and will be further discussed in the next paragraph. Nonetheless, the association just reported is approved by FDA and not by EMA due to the potential cardiovascular risk, drug addiction, as well as language and memory impairment produced by phentermine.

Finally, diverse drug under development can be enumerated. Some of them have the same mechanism of action of the aforementioned but with different pharmacokinetic properties, such as Semiglutide, long – acting GLP-1R agonist. On the other hand, several dual ligands are taken into account for novel treatment. These includes dual GLP-1R/GCGR Agonists as SAR425899 (Sanifi) and MEDI0382 (Cotadutide; AstraZeneca) and triple Monoamine reuptake (dopamine, norepinephrine and serotonin) inhibitors as Tesofensine. Furthermore, newer anti – obesity targets were explored and are now on Phase2 trials too as the case of dual Amylin/Calcitonin agonists and Sodium-Glucose Co-Transporter-2 inhibitors.

Nevertheless, all the attempts done still need consistent improvements, considering the following factor: a low potency/efficacy, as well as a poor pharmacokinetic lead to higher drug dosages which in the aforementioned cases bring to unacceptable side effects. In the following paragraph, considering the background and challenge just highlighted, the attention is focused on the proposal of selective Carbonic anhydrase V (A and B) inhibitors as new anti-obesity drugs.

1.2. Characterization of hCA V Isoforms and Their Importance as Anti – Obesity Targets

In the previous paragraph several anti-obesity drugs were enumerated. Among them, topiramate, that is a medicine used to treat epilepsy, shows its anti - obesity activity apparently on GABA receptors inhibiting the appetite, however it may not be the only reason behind the severe weight – loss induced during epilepsy treatment with this drug.[18] Epileptic patient treated with Zonisamide[19] experienced as well the same anorexigenic effect and both chemicals show low nanomolar inhibition of some carbonic anhydrases, specifically hCA II and VA.

Together, the relationship between carbonic anhydrases and fatty acid metabolism was elucidated. Specifically, hCA VA and VB, despite having a different tissue distribution, they are both localized in mitochondria. Here, furnishing carbon units as bicarbonate ions to pyruvate carboxylase(PC), methylcrotonyl – CoA carboxylase (MCC) and propionyl – CoA carboxylase, they influence several biosynthetic pathways spanning from lipogenesis to gluconeogenesis and ureagenesis.[20]

The effect on lipogenesis is mainly caused by the increased concentration of Oxalacetate (OAA) produced by pyruvate carboxylase which use the HCO_3^- generated by hCA VA in mitochondrial matrix, prior action of hCA II that converts HCO_3^- into CO_2 enabling its passage through the mitochondrial membrane. This leads to an indirect overproduction of citrate which leaves the Krebs cycle, cross the mitochondria and, once converted in acetyl – CoA, enters in the fatty acid biosynthetic pathway. (Figure 6) The hypothesis just discussed was then supported by in vitro studies on adipocites, where the concentration of C^{14} – labelled Krebs cycle intermediates as well as citrate and malate were reduced in presence of the hCA inhibitor 6-ethoxyzolamide (ETZ) without a strong impact on ATP production.[21]
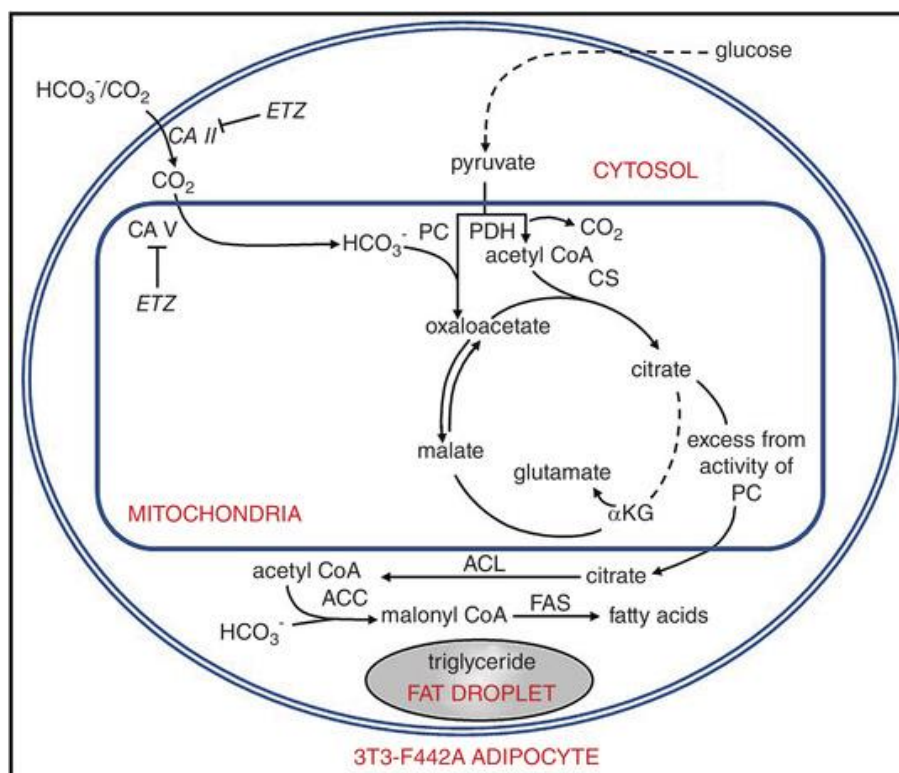
Figure 6. Proposed physiological role of carbonic anhydrase VA in adipocytes for de novo lipogenesis. Abbreviations: ACC, acetyl-CoA carboxylase; ACL, ATP citrate lyase; αKG, α-ketoglutarate; CS, citrate synthase; ETZ, 6-ethoxyzolamide; FAS, fatty acid synthetase; PC, pyruvate carboxylase; and PDH, pyruvate dehydrogenase. Image taken from ref.[21]

Getting deeper in the structure and topology of the two isoenzyme, they are solved in the mitochondrial matrix and present a length of 305 and 317 a.a. respectively, whose section from a.a. 37 to 297 belongs to the active domain as for the other hCA.[Holmes RS. JDMGP 2020]

hCA VA and VB are present in several mammals, sharing almost most of the sequence (up to 89% of identity between hCA VB and murine one) as shown in table 2.

Table 2. Percentage of identity for mammalian CA5A and CA5B and other vertebrate CA5 amino acid sequences. Data taken from ref. [Holmes RS. JDMGP 2020]

	hCA VA	Murine CA VA	Opossum CA VA	hCA VB	Murine CA VB	Opossum CA VB	Chicken CA V	Zebra fish CA V
hCA VA	100	72	67	59	59	61	64	50
Murine CA VA	72	100	63	57	57	57	63	50
Opossum CA VA	67	63	100	63	62	67	66	54
hCA VB	59	59	63	100	89	80	69	54
Murine CA VB	59	57	62	89	100	79	69	53
Opossum CA VB	61	57	67	80	79	100	74	57
Chicken CA V	64	57	66	69	69	74	100	58
Zebra fish CA V	50	50	54	54	53	57	58	100

More in detail, considering that so far, no 3D structures of hCA VA or VB are available, mouse CA VA (mCA V) was exploited to retrieve structural insights related both to catalysis and ligand binding by means of X-Ray diffraction and site directed mutagenesis.
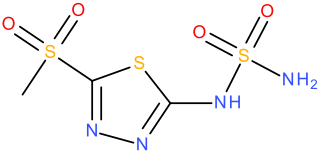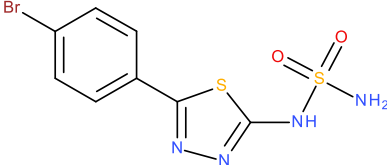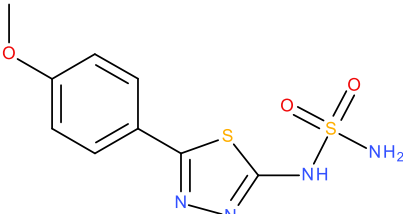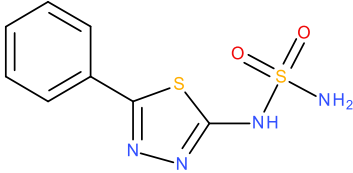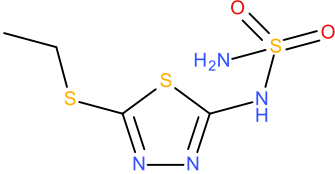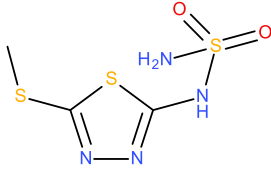
The initial obtainment of the apo structure (PDB code: 1DMX) and the acetazolamide (AZM) co – crystal (PDB code: 1DMY) of mCA V, opened the discussion towards the identification of the possible residues involved in the proton shuttling, as the single mutants Y64→H and Y64→A were showing comparable activity to the wild – type enzyme. This effect might be due to the bulky P65, which preserve Y64 from solvent exposure. In addition, the distance of Y131 to the Zinc – bound water suggested its role of proton shuttling residue.[22] Later, a double mutant Y64→H and P65→A(PDB code: 1URT) demonstrated a significant enhancement of the proton transfer activity, therefore supporting again the involvement of H64 in hCA VA catalysis.[23]
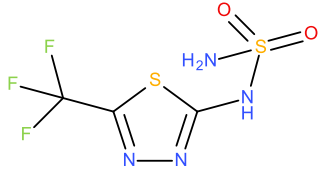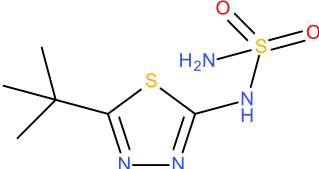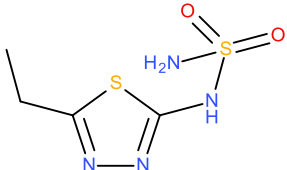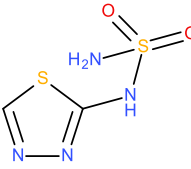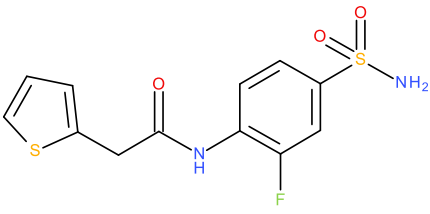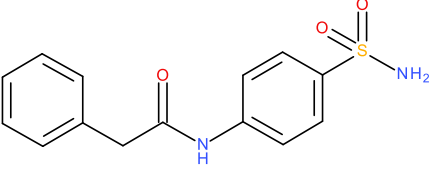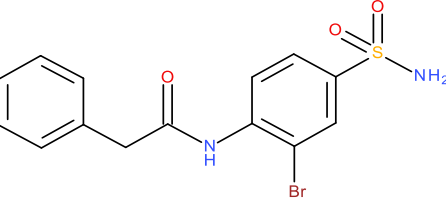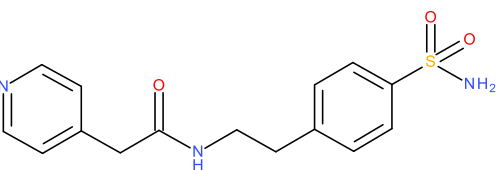
Finally in 2002, Jude et al. elucidated the importance of Y131 in proton shuttling process comparing the hCA II wild type (PDB code: 2CBA), γ – CA from Methanosarcina thermophila (PDB code: 1QRG) the previous double mutant hCA VA activity and structure with a newer expressed one where P65 and Y131 were replaced by Ala and Cys – methylimidazole respectively (PDB code: 1KEQ). Here it seems that the bulky P65 does not significantly impair proton shuttling process with respect to the Y64H/P65A mutant. Moreover, the comparison the hCA II and *M. thermophila* γ – CA water molecules trajectories suggest a different mechanism and highlight Y131 role. Taken together these three findings provide hints for plausible residues that may be targeted for the selective inhibition of hCA VA.[24]

Dealing with zinc binder inhibitors, along with other type of hCA inhibitors, results difficult, considering that the only available co – crystal is the one with AZM. Nevertheless, X – Ray data keep confirming the possibility to hydrogen bond Y131 in order to selectively inhibit hCA VA, in view of the difference in AZM tail conformation and interactions between hCA VA and hCA II. [22]

Other information on the SAR can be traced only through inhibition data from stopped – flow hydration assays. In the following table are reported some of the most selective inhibitors against hCA VA collected from literature.

Table 3. Some hCA VA inhibitors reported in literature. The compound series analysed have been grouped in four sections (A to D) according to their affinity against hCA VA and selectivity over hCA II. Ki against hCA VB and hCA I are also shown. (A) Compounds with high affinity against hCA VA and high selectivity over CA II. (B) Compounds with high affinity against hCA VA and intermediate selectivity over CA II. (C) Compounds with intermediate affinity against hCA VA and high selectivity over CA II. (D) Compounds with intermediate affinity against hCA VA and intermediate selectivity over CA II.

(A) Compound High affinity (ki<50nM) – High selectivity over CA II (selectivity ratio>10)	Ki VA	Ki VB	Ki II	Ki I	Selectivity ratio II/VA-II/VB	Ref.
2j	8.7 nM	2.7 nM	0.94 µM	0.103 µM	108.05 - 348.15	[25]
2i	4.2 nM	4.5 nM	0.82 µM	5.85 µM	195.24 - 182.2	[25]
2h	8.0 nM	1.3 nM	0.54 µM	0.102 µM	67.5 - 415.385	[25]
2g	9.2 nM	7.5 nM	0.87 µM	1.66 µM	94.565 – 116	[25]
2f	9.3 nM	23.1 nM	1.13 µM	1.89 µM	121.505 - 48.92	[25]
2e	32 nM	2.9 nM	0.92 µM	2.4 µM	28.75 – 317.24	[25]

Compound						
2d	7.3 nM	3.9 nM	1.08 µM	6.86 µM	147.945 – 276.92	[25]
2c	10.4 nM	2.8 nM	0.90 µM	5.54 µM	86.54 – 321.43	[25]
2b	18.7 nM	63 nM	0.95 µM	7.01 µM	50.8 – 15.08	[25]
2a	28.3 nM	74 nM	0.97 µM	7.42 µM	34.275 - 13.11	[25]
5b	6.9 nM	7.9 nM	390 nM	161 nM	56.52 – 49.37	[26]
7a	6.7 nM	7.9 nM	107 nM	108 nM	15.97 – 13.54	[26]
7f	7.1 nM	5.9 nM	395 nM	263 nM	55.63 – 66.95	[26]
7i	7.6 nM	9.3 nM	97 nM	73 nM	12.76 – 10.4	[26]

Compound						
7h	7.3 nM	9.0 nM	74 nM	71 nM	10.14 – 8.2	[26]
7g	6.8 nM	6.8 nM	69 nM	75 nM	10.14 – 10.14	[26]
19	21 nM mCA	-	240 nM	1200 nM	11.428	[27]
16	5.9 nM	7.8 nM	5246 nM	1773 nM	889.15 – 672.56	[28]
17	21 nM	7.3 nM	398 nM	4382 nM	18.95 – 54.52	[28]
8	17.1 nM	26.4 nM	1207 nM	1241 nM	70.58 – 45.72	[28]
10	16.6 nM	40.3 nM	1563 nM	920 nM	94.16 – 38.78	[28]
11	27.5 nM	67.3 nM	2459 nM	1042 nM	89.42 – 36.54	[28]
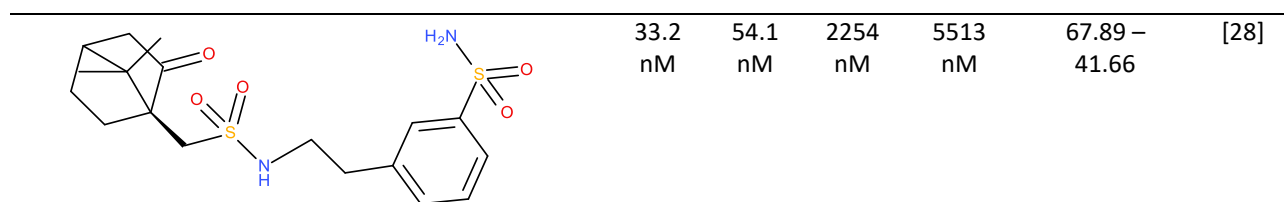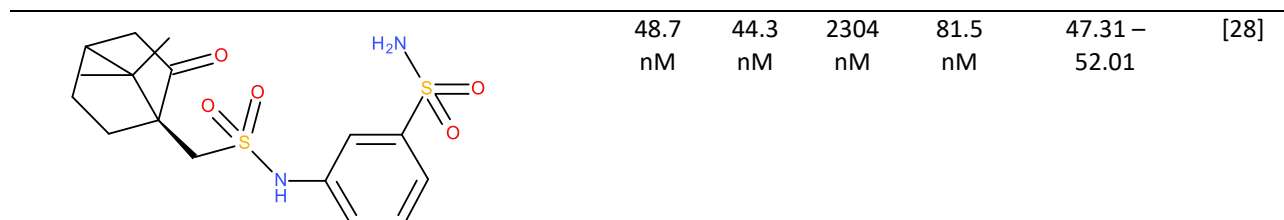
	Ki VA	Ki VB	Ki II	Ki I	Selectivity ratio II/VA-II/VB	Ref.
13	33.2 nM	54.1 nM	2254 nM	5513 nM	67.89 – 41.66	[28]
15	48.7 nM	44.3 nM	2304 nM	81.5 nM	47.31 – 52.01	[28]
(B) Compound High affinity (ki<50nM) – Intermediate selectivity over CA II (1< Selectivity ratio< 10)	**Ki VA**	**Ki VB**	**Ki II**	**Ki I**	**Selectivity ratio II/VA-II/VB**	**Ref.**
5a	7.2 nM	7.0 nM	50 nM	61 nM	6.94 – 7.14	[26]
5c	7.7 nM	8.6 nM	50 nM	77 nM	6.49 – 5.81	[26]
5d	7.5 nM	8.7 nM	52 nM	84 nM	6.93 – 5.98	[26]
5e	9.1 nM	7.2 nM	52 nM	60 nM	5.71 – 7.22	[26]
5f	10.2 nM	8.0 nM	53 nM	68 nM	5.20 – 6.625	[26]
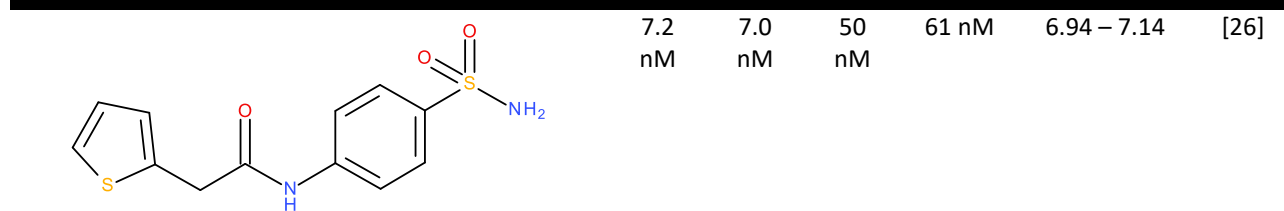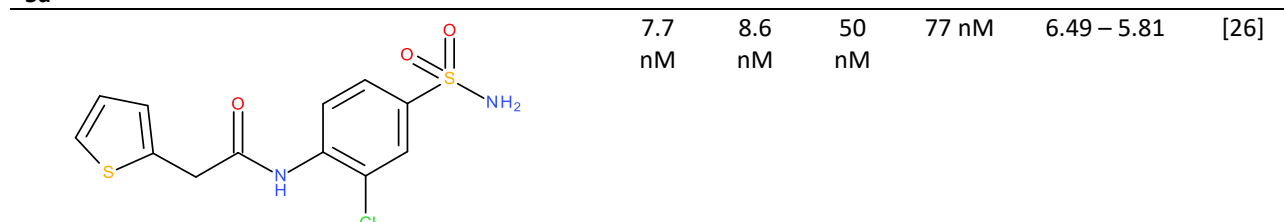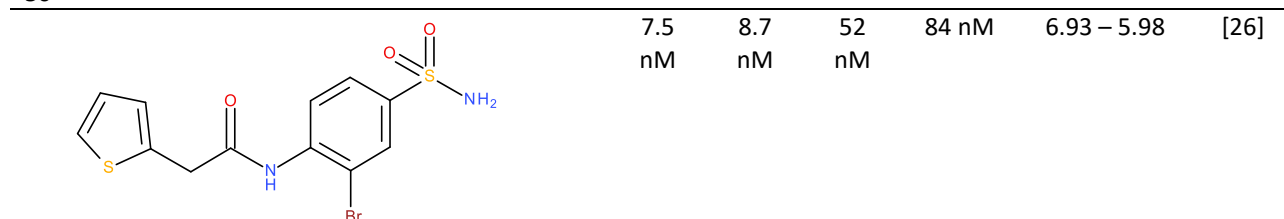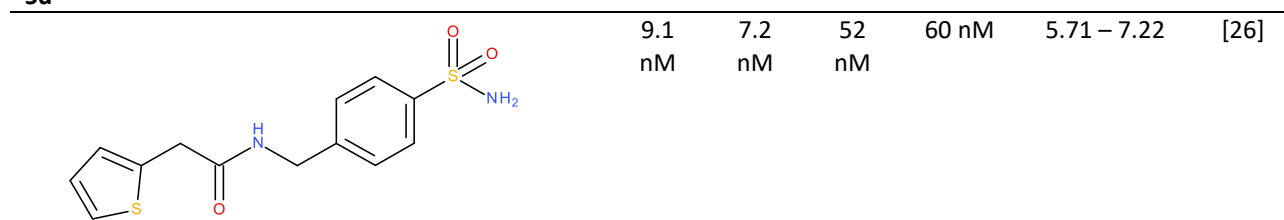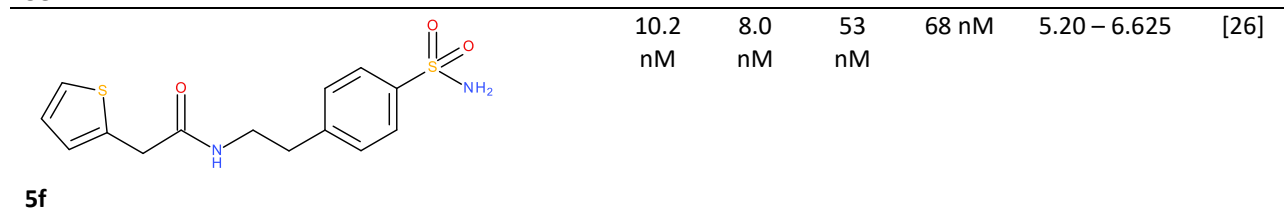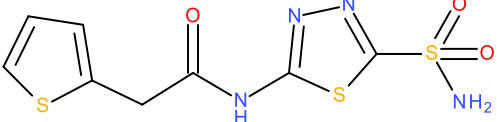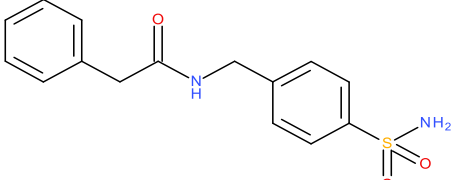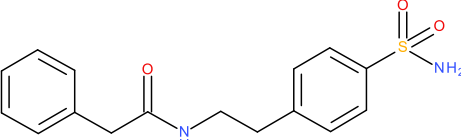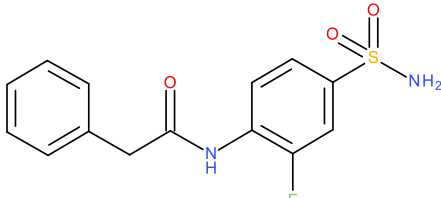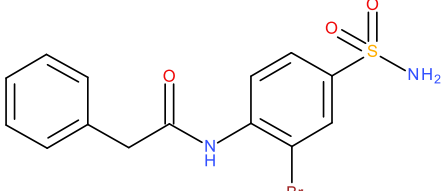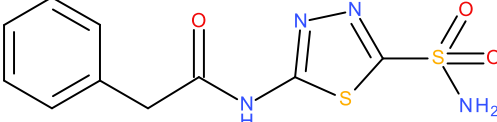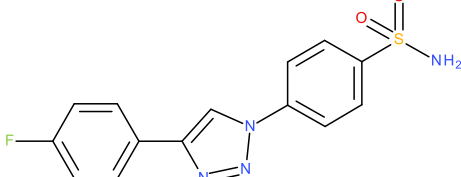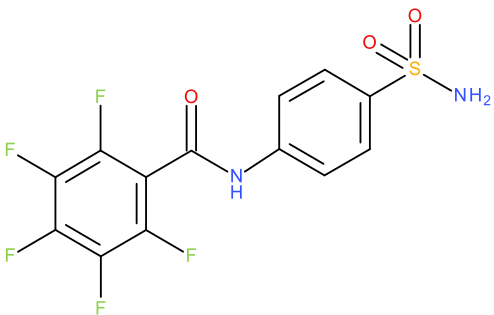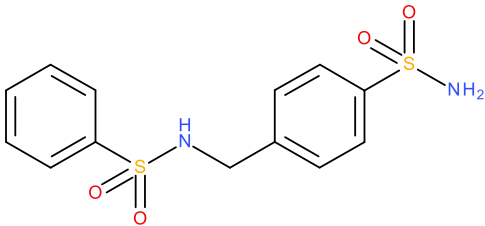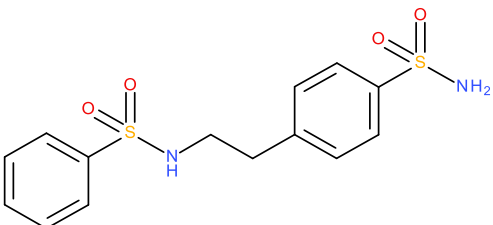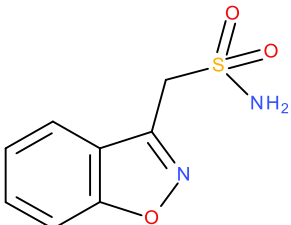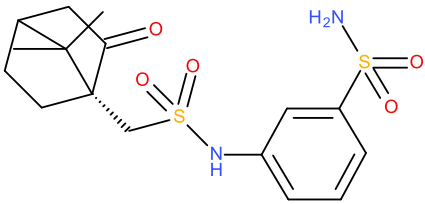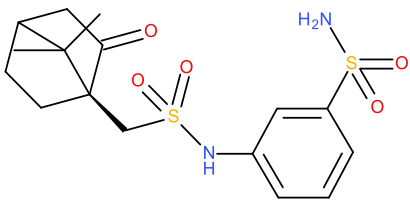
Structure						
6	7.6 nM	7.4 nM	51 nM	72 nM	6.71 – 6.89	[26]
7b	8.6 nM	8.3 nM	54 nM	75 nM	6.28 – 6.51	[26]
7c	8.1 nM	8.2 nM	67 nM	60 nM	8.27 – 8.17	[26]
7d	8.3 nM	8.1 nM	61 nM	67 nM	7.35 – 7.53	[26]
7e	8.2 nM	8.1 nM	58 nM	61 nM	7.07 – 7.16	[26]
8	8.4 nM	6.1 nM	51 nM	63 nM	6.07 – 8.36	[26]
18	14.2 nM	11.2 nM	40.3 nM	4600 nM	2.84 – 3.60	[29]

Structure						
14	19.6 nM	54.2 nM	33.8 nM	4000 nM	1.72 – 0.62	[29]
13	12.8 nM	10.6 nM	18.6 nM	2100 nM	1.45 – 1.75	[29]
20	21 nM mCA	-	105 nM	800 nM	5.25	[27]
16	13 nM mCA	-	66 nM	1400 nM	5.076	[27]
21	15 nM mCA	-	75 nM	430 nM	5.00	[27]
15	18 nM mCA	-	63 nM	14200 nM	3.50	[27]
17	17 nM mCA	-	37 nM	3300 nM	2.18	[27]

Compound	Ki VA	Ki VB	Ki II	Ki I	Selectivity ratio II/VA-II/VB	Ref.
18	10 nM mCA	-	17 nM	950 nM	1.70	[27]
24	24 nM mCA	-	40 nM	81 nM	1.67	[27]
25	26 nM mCA	-	28 nM	69 nM	1.08	[27]
4	20 nM	6033 nM	35 nM	56 nM	1.75	[26]
14	35.3 nM	38.4 nM	78.9 nM	9711 nM	2.235 – 2.05	[28]
(C) Compound Intermediate affinity (50nM< ki<150nM) – High selectivity over CA II (Selectivity ratio> 10)	**Ki VA**	**Ki VB**	**Ki II**	**Ki I**	**Selectivity ratio II/VA-II/VB**	**Ref.**
9	68.6 nM	30 nM	1165 nM	3130 nM	16.98 – 38.83	[28]
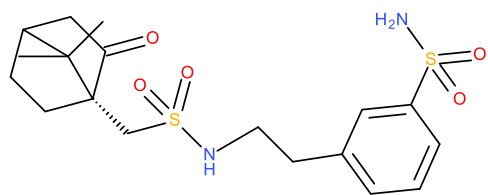
	Ki VA	Ki VB	Ki II	Ki I	Selectivity ratio	Ref.
12	64.5 nM	36.2 nM	963 nM	4964 nM	14.93 – 26.60	[28]

Compound	Ki VA	Ki VB	Ki II	Ki I	Selectivity ratio II/VA-II/VB	Ref.
13	85 nM mCA	-	214 nM	17650 nM	2.52	[27]
9	74 nM mCA	-	133 nM	14600 nM	1.80	[27]
5	128 nM	-	348 nM	952 nM	2.72	[30]
8	160 nM	-	565 nM	1095 nM	3.53	[30]
13	129 nM	-	670 nM	96 nM	5.19	[30]
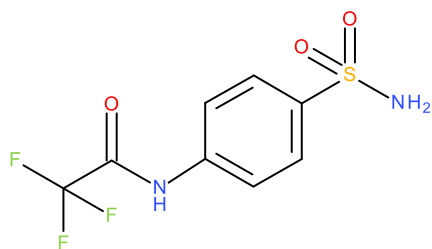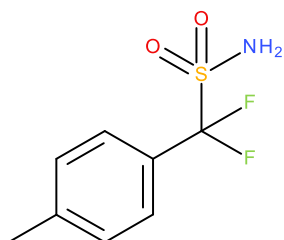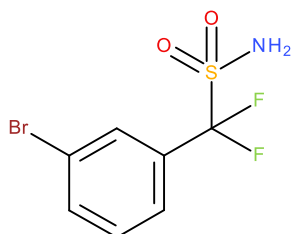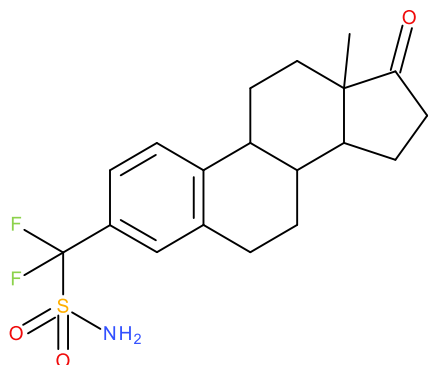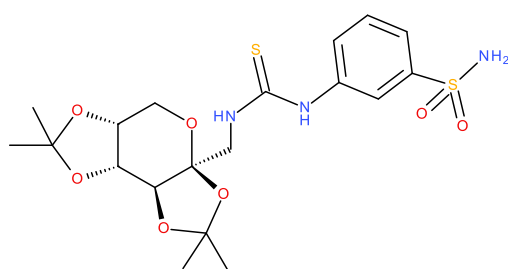
| | 122 nM | - | 750 nM | 10200 nM | 6.15 | [31] |

5

Rough 2D comparison of the compounds reported outlines a very flat SAR characterized by a ZBG linked to an aromatic or lipophile spacer (mainly benzene or thiadiazol) then attached to a hydrophobic tail, often containing an hydrogen - bond acceptor coherently with AZM binding – mode in hCA VA. Sulfamide ZBG seems to provide an enhancement in the selectivity of sulfonamide – like inhibitors, as demonstrated by the series of Smaine et al.. Although its role was not elucidated by any X-Ray NMR or Modelling studies.

Hence, a more in - depth 3D analysis, either ligand or structure – based might be advised whether the aim is the development of hCA inhibitors exploitable as anti – obesity drugs with reduced side effects.

1.3. Structure-Guided Identification of a Selective Sulfonamide-Based Inhibitor Targeting the Human Carbonic Anhydrase VA Isoform

Keeping in mind the issues highlighted in the previous paragraph, in few words the lack of both structural and ligand SAR information, we decided to exploit both ligand and structure based approaches to develop a virtual screening(VS) workflow articulated in four main steps: 1) creation and validation of a ligand – based(LB) pharmacophore starting from some of the compounds reported in the literature (Table 3 and Figure 8); 2) screening of 209,000 compounds from Specs through the ligand based model generated; 3) filtering of the results using a structure – based(SB) pharmacophore from AZM in complex with mCA VA; 4) development of a hCA VA homology model and evaluation of the hit binding modes through docking simulations. (Figure 7) Thus, each section of the Result and Discussion sub - paragraph will give a detailed description of the four procedures and the results obtained at each step of the protocol just resumed.

Finally, a comparison with hCA II binding – mode of two potent hCA VA inhibitors retrieved through this VS workflow, has been provided to shed light on their different selectivity over this isoform.
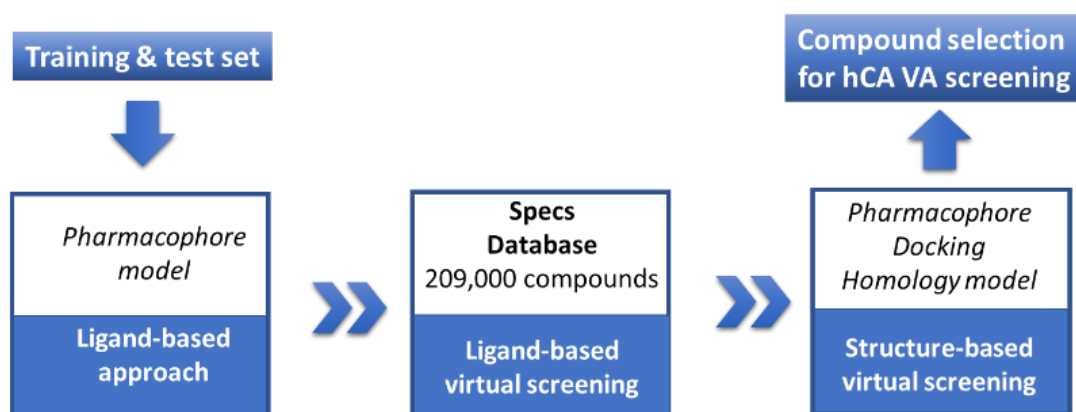
Figure 7. Overview of the applied computational strategy to select human carbonic anhydrase (hCA) VA sulfonamide‐based inhibitors. Taken from ref.[32]

1.3.1. Results and Discussion

Ligand based Pharmacophore creation

To carry out the first step of the VS workflow, we started selecting according to their structural diversity 16 inhibitors from Table 3 which showed Ki on CA V≤ 150 nM and a selectivity ratio ≥ 1, and used them to search for the three - dimensional spatial arrangements of the most relevant features crucial for CA V inhibitory effects on LB pharmacophore. Although the molecules chosen present various type of scaffolds they are all characterized by an $ArSO_2NH_2$ or $ArNHSO_2NH_2$ group as zinc - binding moiety essential for hCA inhibition.

The initial subset of compounds was divided into a (i) training and a (ii) test set by means of clustering procedure. Specifically, the clustering has been performed either by changing the similarity measurement (Pharmacophore Alignment score or Pharmacophore RDF - code similarity) or adjusting the cluster distance within the range of 0.4 (default value) to 0.5 in each clustering run. The other clustering parameters were left as default. At each clustering run the biggest cluster was used as training set while the remaining ones were used as test for generating several pharmacophore hypotesis.
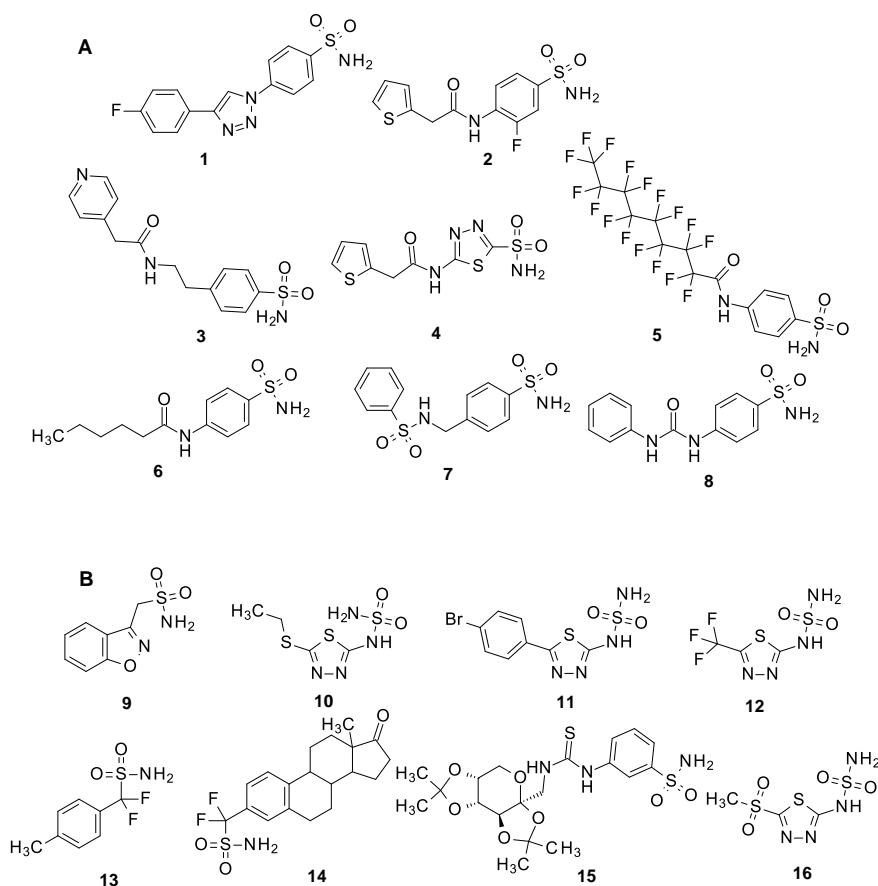
Figure 8. Chemical structures of 16 well-known human carbonic anhydrase (hCA) V inhibitors employed as the training set (a) and test set (b) taken from literature, reported in Table 3.

In detail, from each combination of training and test set of the initial 16 arylsulfonamides a LB pharmacophore was generated selecting the one with best score among the ones proposed by LigandScout software.

Through this procedure 10 different pharmacophores were selected for an initial validation using receiver operating characteristic (ROC) curve. Specifically, to evaluate the efficiency of each model in discriminating between active and inactive compounds we took up 1707 molecules, of which 47 were sulphonamides - based inhibitors of hCA VA (the majority was the remaining compounds from Table 3) with a ki ≤ 10000 nM and 1660 decoys generated through DUD – E web tool giving the set of active compounds as input(http://dude.docking.org/). The validation here reported, which took into account the Enrichment Factor (EF) and the Area under the curve (AUC) of the ROC curve to determine the efficiency of the LBVS procedure (pharmacophore and settings), led us to choose for further refinement a pharmacophore composed of nine pharmacophoric features: three hydrogen bond acceptors (in red), two hydrogen bond donors (in green), three hydrophobic features (in yellow) and one aromatic ring feature (in blue). The refinement of the selected model

consisted in marking as optional three lipophilic features and one H – bond donor, yielding better results during the second validation step which considered the same efficiency parameter of the previous one. As shown in Figure 9, the final pharmacophore created presented at 100% of the screening process an AUC of 0.82 and an EF of 27.2, thus able to retrieve more likely active molecules and being suitable for our screening purposes.
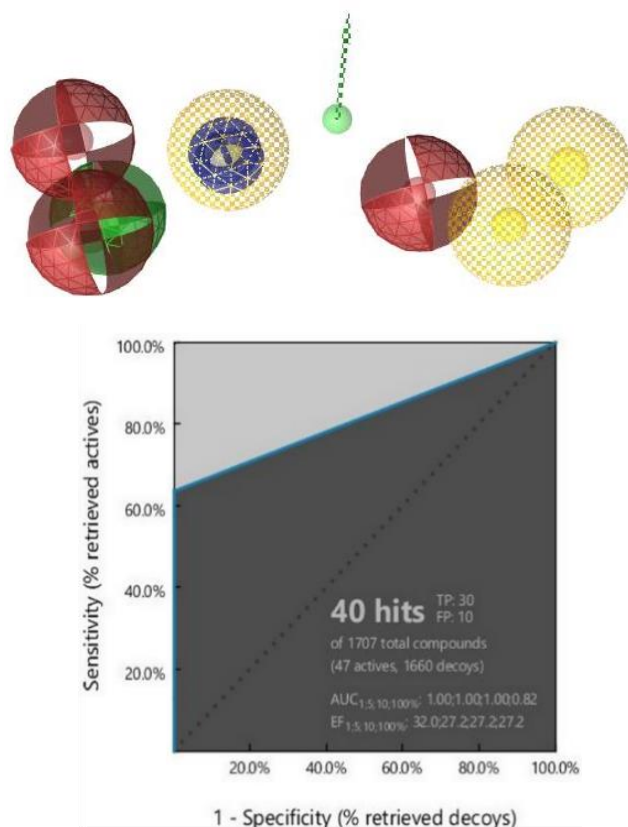
Figure 9. The LB pharmacophore model: three hydrogen bond acceptors (red); two hydrogen bond donors (green arrow); hydrophobic features (yellow) and one aromatic feature (blue circle). All optional features are not fully coloured. Receiver operating characteristic validation curve for the pharmacophore model. Taken from ref.[32]

Ligand – based Virtual screening

Following the obtainment of the LB pharmacophore model, we proceeded to perform virtual screening on the "Specs Compound Library" containing 209,000 compounds, accessible through the Specs database (https://www.specs.net). This screening was conducted using LigandScout software[33] with the aim of identifying new potential inhibitors for CA V. Through the in-silico screening of the entire database, we identified a total of 1,738 molecules. Among these, our selection criteria included sulfonamide-based compounds meeting the following prerequisites: (i) a fit score exceeding 80 and (ii) distinct chemical structures. Consequently, from this refined database, the second phase of our LB VS campaign yielded a reduced set of 81 sulfonamides out of

the initial 1,738 compounds, all of which had previously matched the pharmacophore features. The comprehensive list of these 81 potential hits is available in the Supporting Information: Table S1.

Structure based pharmacophore virtual screening

In the subsequent phase of our research, we aimed to further narrow down the selection of the 81 sulfonamide-based compounds retrieved from LBVS to submit to biochemical evaluation of their inhibitory activity on hCA VA. To achieve this, we created an additional SB pharmacophore model using LigandScout software.[33] We exploited the crystal complex of murine mitochondrial CA V and AZM (PDB code 1DMY) as it is the only PDB powerful to provide structural information about CA VA ligand binding.[22] As illustrated in Figure 10, the SB pharmacophore model was composed of five hydrogen bond acceptor features, contacting three crucial residues: T199, T200, and Y131.
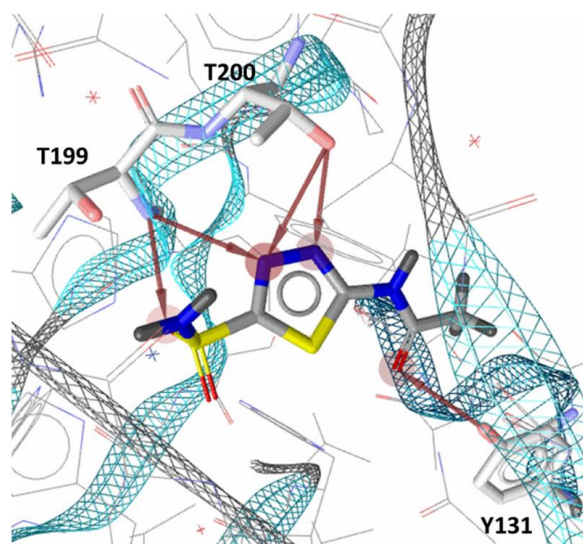
Figure 10. SB pharmacophore model generated from the X-ray crystal structure of acetazolamide (AZM) in complex with murine CA V (PDB code: 1DMY).[22] The red arrows represent H-bond acceptor features. Image taken from ref.[32]

In our quest to identify additional potential interactions within the CA V binding pocket, we refined the model with features derived from the apo-structure of murine CA V (as shown in Figure 11A) via the "Create Apo Site Grids" tool, integrated into LigandScout 4.4.[33] This analysis led to the discovery of supplementary plausible features, resulting in an enriched pharmacophore model, which finally encompassed six hydrophobic spheres, two positive ionizable regions, two aromatic rings, five hydrogen bond acceptors, and five hydrogen bond donor functionalities (as depicted in Figure 11B. Following the Apo Site analysis, the SB-based pharmacophore search allowed us to single out 38 molecules with a fit score value exceeding 70. The entire list of these 38 selected compounds is present as well in Supporting Information: Table S1
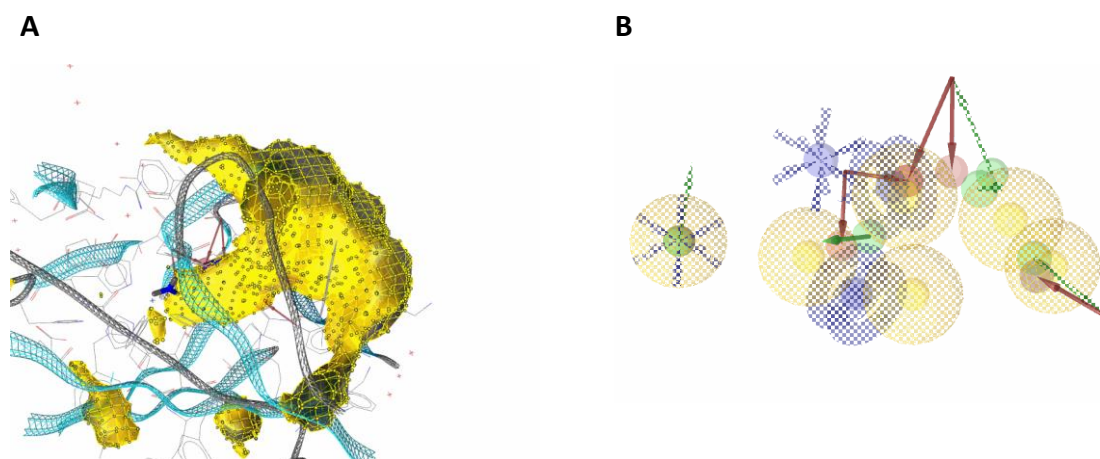
Figure 11. (a) Apo Site Grid generated starting from the X-ray crystal structure of acetazolamide (AZM) in complex with CA V (PDB code: 1DMY). (b) The merged pharmacophore model: six hydrophobic spheres (light yellow spheres); two positive ionizable (blue star); two aromatic rings (blue circle); five H-bond acceptors (red arrows); five H-bond donors (green arrows). Optional features are not fully colored.

Homology modelling of hCA VA and Docking simulation

To assess the capability of the 38 chosen molecules to interact with the active site of hCA VA, docking simulations were performed. Given the absence of X-ray data for hCA VA in the literature, we fine - tuned an homology model for hCA VA using the TopModel server.[34] The model's quality was evaluated using TopScore, a metaModel Quality Assessment Program (meta-MQAP) which predict protein errors combining 15 different evaluation metrics through deep neural networks. The validation yielded a value close to 0.1, indicating the highest quality value, particularly within the active site region. Additionally, Ramachandran plots, constructed using Procheck Tool, showed that 92.6% of the psi-phi angles fell within favoured regions, while 7.4% were within allowed or generously allowed regions (refer to Supporting Information: Figures S1 and S2). The model was subjected to minimization with Prime and served as receptor for our docking investigations run on Gold suite 5.0.1, using the CHEMPLP scoring function. As a result of this process, we identified 30 molecules, as shown in Figures 12 and 13, whose corresponding docking score values are reported in Supporting Information: Table S2.

These 30 selected ligands, named VAME-01 to VAME-30, shared a common (hetero)arylsulfonamide component linked to distinct hydrophobic tails via a suitable linking moiety containing amine, amide, imine, or thiourea chemical functionality.
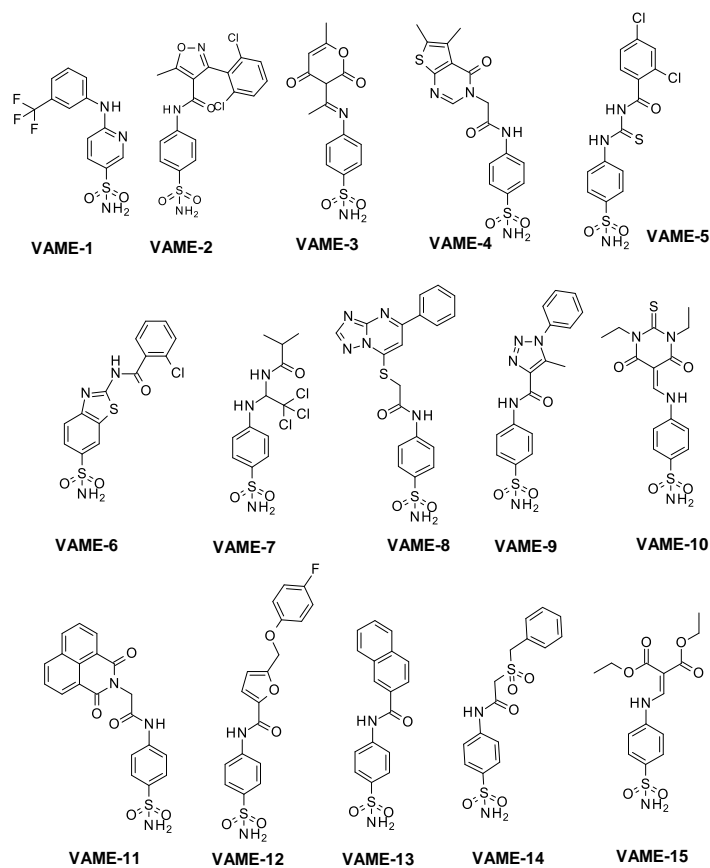
Figure 12. Chemical structures of selected compounds **VAME 01-15**
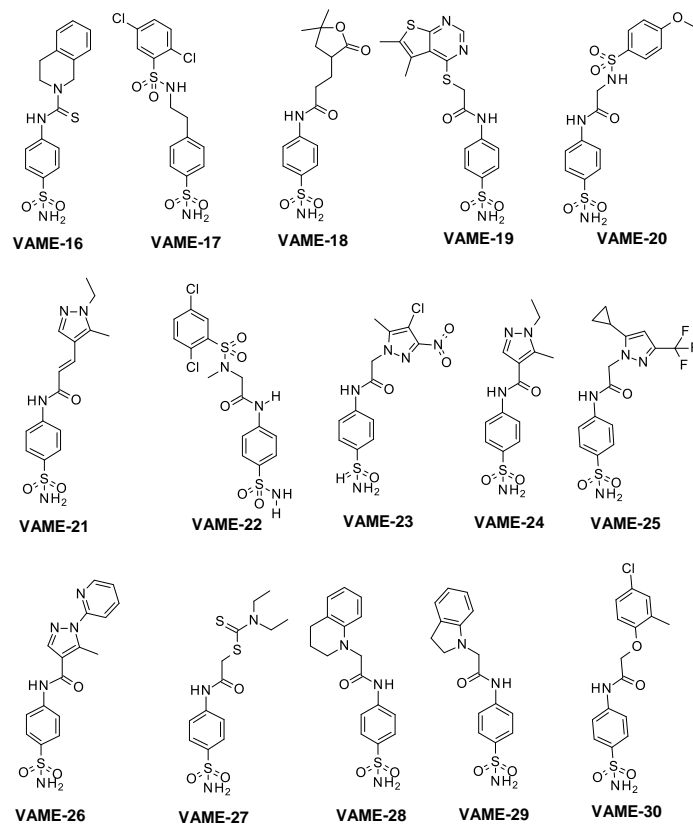
Figure 13. Chemical structures of selected compounds **VAME-16 - VAME-30**
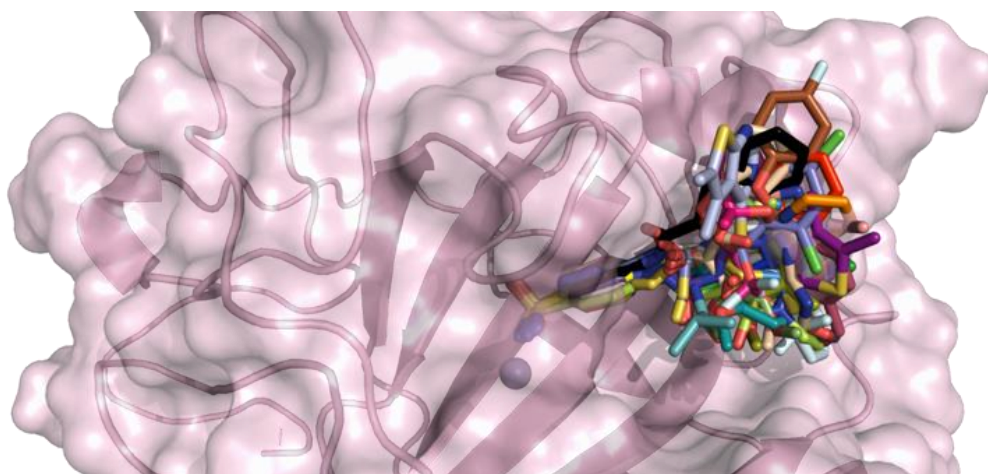
Figure 14. Putative binding poses of the 30 compounds, VAME-01–30, with the modelled human carbonic anhydrase (hCA) VA. The inhibitors are represented as coloured sticks and the protein as a pink surface. Zinc ion is depicted as a gray sphere. Figure made by Pymol (https://pymol.org).

Figure 14 illustrates the superimposed poses selected from docking of the thirty molecules, all of which were capable of occupying the catalytic site of the modelled hCA VA.

As expected, each compound anchored itself to the zinc-containing catalytic site through the sulphonamide moiety while positioning the remaining molecular fragment between the two surfaces of the cavity. Finally, none of the selected sulfonamides raised PAINS alerts, as confirmed by the SwissADME platform (www.swissadme.ch)[35] Based on this favourable predicted recognition in hCA VA, the 30 potential hits were purchased from the Specs supplier to evaluate their inhibitory effects on hCAs. Prior purchasing them, a literature search was conducted using Data Warrior software together with CHEMBL database, in order to check whether they were tested already on some hCA isoforms and as results none of them was previously tested on hCA VA.

In Silico analysis of hCA selectivity

The 30 small molecules fetched through our virtual screening workflow were submitted to stopped – flow CO_2 hydration assay to evaluate their inhibitory activity towards various hCA isoforms. The resulting inhibition data are collected in Table 4 in comparison with reference compounds AZM, TPM and ZNS.

Table 4. Inhibition data of tested sulfonamides and sulfamides **VAME-1 - VAME30** and reference compounds **AZM, ZNS** and **TPM** and their selectivity ratios for the inhibition of hCA VA over the hCA I/ hCA II isozymes

Cmps	K_i (nM)*			selectivity ratio	
	hCA I	hCA II	hCA VA	hCA I/hCA VA	hCA II/hCA VA
VAME-01	15.9	8.4	33.4	0.48	0.25
VAME-02	28.7	20	73.8	0.39	0.27
VAME-03	730.8	83.6	85.3	8.57	0.98
VAME-04	34.6	8.2	78.2	0.44	0.10
VAME-05	23.9	3.7	82.3	0.29	0.04
VAME-06	39.4	6	93.6	0.42	0.06
VAME-07	45.3	26.2	511.8	0.09	0.05
VAME-08	73.1	14.3	84.1	0.87	0.17
VAME-09	279.3	23.3	73.4	3.81	0.32
VAME-10	435.7	46.8	96.0	4.54	0.49
VAME-11	9.1	28.2	96.5	0.09	0.29
VAME-12	92.4	24.2	89.7	1.03	0.27
VAME-13	954	309.8	551.9	1.73	0.56
VAME-14	72	28.2	170.5	0.42	0.17
VAME-15	18.2	5.1	182.5	0.10	0.03
VAME-16	411.2	658.2	162.7	2.53	4.05
VAME-17	4.6	3.8	299.2	0.02	0.01
VAME-18	15.6	1.6	242.9	0.06	0.01
VAME-19	927.3	311.2	794.4	1.17	0.39
VAME-20	47.9	7.4	431.0	0.11	0.02
VAME-21	53.4	18.2	83.3	0.64	0.22
VAME-22	67.9	20.9	418.6	0.16	0.05
VAME-23	77.9	22.4	93.9	0.83	0.24
VAME-24	27.1	5.6	77.9	0.35	0.07
VAME-25	57.4	9.2	207.9	0.28	0.04
VAME-26	86.3	13.6	528.5	0.16	0.03
VAME-27	52.5	18.9	93.5	0.56	0.20
VAME-28	927.4	379.1	54.8	16.92	6.92
VAME-29	76.9	26.3	93	0.83	0.28
VAME-30	60.1	21.7	742.6	0.08	0.03
AZM	250	12.1	63.0	3.97	0.19
ZNS**	56	35	20.0	2.80	1.75
TPM**	250	10	63.0	3.97	0.16

* Mean from 3 different assays. by a stopped flow technique (errors were in the range of ± 5-10 % of the reported values). **Data taken from literature[36]

As result, all the 30 molecules demonstrated inhibition of hCA VA showing Ki values in the range of 33.4 to 794.4 nM. Moreover, the majority of chemicals, precisely 19, had Ki in the low nanomolar range (≤ 100 nM). Then 7 compounds presented a selectivity ratio ≥ 1 over hCA I. Among them, one molecule (VAME – 28) resulted highly selective over hCA II too (sel. Ratio: 6.92).

Interestingly, it shared almost the whole scaffold with another molecule of the series (VAME – 29) having no selectivity over the aforementioned isoform. Thus, we performed comparative docking studies of the two derivatives on hCA II, in order to investigate how the simple expansion of a five membered aliphatic ring to six membered one leads to a 25 – fold enhancement of the ligand selectivity.
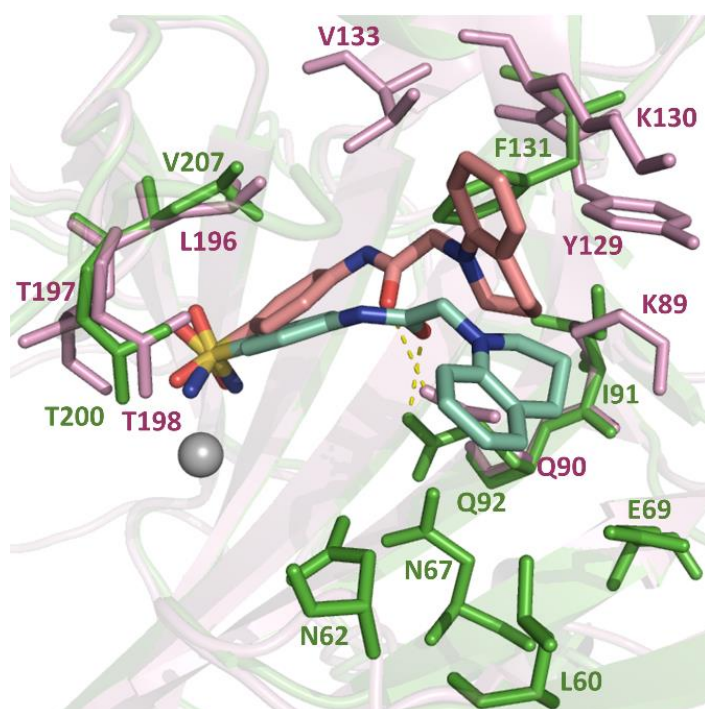
Figure 15. Superimposed binding modes of VAME-28 bound to human carbonic anhydrase (hCA) VA (ligand as salmon stick and protein as a pink cartoon) and to hCA II (ligand as green-cyan stick and protein as a green cartoon). Interacting residues of hCA VA and hCA II are shown in pink and green, respectively. Hydrogen bonds are represented as yellow dashes. Zinc ion is depicted as a gray sphere. Figure made by Pymol. (https://pymol.org)

Figure 15 illustrates the hypothetical interaction pattern of VAME-28 in complex with the modeled hCA VA superimposed to its binding mode in hCA II (PDB code 6XXT)[37]. In this comparison, it can be noticed that VAME-28 adopts two distinct binding poses in hCA II and hCA VA respectively. While the 4-aminobenzenesulfonamide group occupies a similar position near the zinc center in both proteins, the orientation of the quinolinyl-tail differs significantly. This difference likely arises from the broader hydrophobic surface of hCA VA with respect to hCA II, as evidenced by the

dissimilar orientation of the crucial residue F131 in hCA II (see Figure 15), corresponding to Y129 in hCA VA. Thus, it may be speculated that F131 conformation could potentially push VAME-28 away from the hydrophobic wall of hCA II active site. Conversely, the docked pose of VAME-28 in hCA VA suggests enhanced stabilization through interactions with the hydrophobic area characterized by V133, Y129, and K130. These interactions may help explain the approximately seven-fold improved affinity of VAME-28 for hCA VA (Ki value of 54.8 nM) compared to hCA II (Ki value of 379.1 nM).
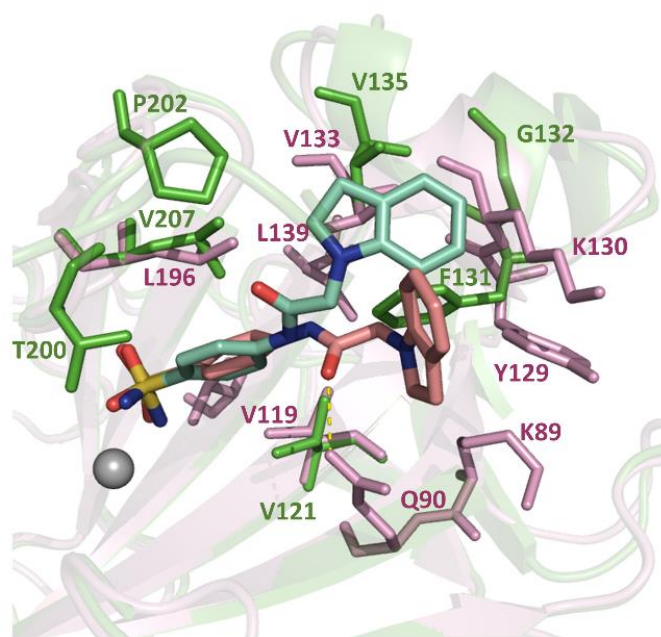
Figure 16. Superimposed binding modes of VAME-29 bound to human carbonic anhydrase (hCA) VA (ligand as salmon stick and protein as a pink cartoon) and to hCA II (ligand as green-cyan stick and protein as a green cartoon). Interacting residues of hCA VA and hCA II are shown in pink and green, respectively. Hydrogen bonds are represented as yellow dashes. Zinc ion is depicted as a gray sphere. Figure made by Pymol. (https://pymol.org)

Figure 16 shows instead the hypothesized binding poses of VAME-29 when docked into hCA II and hCA VA. The docking simulations reveal that this inhibitor can accommodate the indolyl-tail in the hydrophobic regions of both hCA II and hCA VA, potentially establishing favorable interactions with F131 and V135 in hCA II, as well as with Y129 and V133 in hCA VA. These findings align with the ability of compound VAME-29 to exhibit inhibitory effects on both hCA II and hCA VA.

Collectively, these in silico insights suggest that the replacement of a five-membered ring with a six-membered one in the VAME-28 inhibitor introduces significant steric hindrance, resulting in distinct binding orientations at active site entrance and leading to different affinities of the ligands.

1.3.2. Materials and methods

Ligand – based Virtual screening parameters

LigandScout V4.4.8[33] was employed for both LB pharmacophore generation and virtual screening (VS) procedures. The selected molecules, (training and test sets) were sketched using Vega 3.2.2.[38] The pharmacophore model was created using the "merged features" option, and the icon best mode was chosen as the conformer generation method, while other parameters were kept at their default settings. This LB pharmacophore model served as a reference for querying the SPECS database in search of potential inhibitors. The library, downloaded as sdf was processed using Icon fast default settings. All the structures having unspecified chiral centers were discarded from the VS. All VS operations were conducted with the "Get best matching conformation" option selected as the retrieval mode, and the resulting hits from the screening were ranked based on their pharmacophore fit scores.

Structure - based pharmacophore virtual screening parameters

The crystal complex of murine mitochondrial CA V and AZM (PDB code 1DMY) was downloaded for RCSB and a SB pharmacophore has been constructed by means of LigandScout Suite[33]. In order to explore additional potential chemical features derived from the protein's apo-structure, we generated an "apo-site" pharmacophore model, focusing solely on the buriedness surface. We set the option to "Append to existing pharmacophore." The ApoSites generation parameters applied are the following: (i) Surface Grid = 0.25; (ii) Buriedness = 0.40; (iii) HBA Max = 7; (iv) HBD Max = 7; (v) Positive Ionizable Max = 7; (vi) Negative Ionizable Max = 7; (vii) Aromatic Max = 7; (viii) Hydrophobic Max = 7. Subsequently, the model was refined, marking all the features except those related to the AZM zinc-chelator atoms marked as optional.

This resulting pharmacophore then served as the basis for further screening of the hits retrieved by LB model, filtering out molecules displaying a pharmacophore fit-score value below 70.

Homology modelling

The hCA VA structure was generated using TopModel [34], starting from two distinct murine alpha-carbonic anhydrase V structures used as primary templates (PDB IDs: 1KEQ[24] and 1URT [23]), along with the structure of the complex between murine mitochondrial CA V and the transition state analog AZM (PDB ID: 1DMY)[22]. To assess the model's quality, we measured the Topscore, which measure the LDDT (local distance difference test) error, indicating the degree of uncertainty

in the interatomic distances calculated for a specific model. Low Topscore values signify higher model quality. Hydrogen atoms were added to the model using the H++ server (http://biophysics.cs.vt.edu/). Subsequently, the homology model we constructed was submitted to energy minimization via Prime software, applying OPLS3e forcefields and restraining to both the Zn atom and the histidines involved in zinc chelation (H94, H96, and H119).

Docking analysis

The hCA VA structure we modelled was employed for conducting docking studies of the 38 selected molecules. 3D coordinates of the ligands were generated using Vega 3.2.2[38], deprotonating primary and secondary sulfonamide groups, then calculating charges through the Gasteiger method and using SP4 forcefield and finally minimizing them using AMMP with the Conjugate Gradient method (1000 steps). Then they were subsequently docked into the hCA V by means of Gold Suite 5.0.1[39]. In the case of hCA V, the region of interest defined as receptor encompassed residues within a 15 Å radius from the original position of AZM in the X-ray structure of murine alpha-carbonic anhydrase V. The fitness function CHEMPLP was selected, and standard default settings were applied throughout the calculations. Each ligand underwent 100 genetic algorithm runs, without enabling the "early termination" option. Results were clustered together when the difference in ligand-all atom RMSD was less than 0.75 Å. The highest GOLD fitness score among the runs was chosen for subsequent analysis and visualization. Side chains of specific residues, including L65, Q92, V121, Y131, K132, V135, L141, L198, T199, and T200, were allowed to rotate based on internal rotamer libraries in GOLD Suite 5.0.1.

For the docking of VAME-28 and VAME-29 on hCA II, we utilized the 3D structure of 4-(4-aroylpiperazine-1-carbonyl) benzenesulfonamide derivative in complex with hCA II (PDB code 6XXT).[37] In this process, we removed the ligand complexed with hCA II, aligned the PDB structure 1DMY to it, excluded the murine CA VA structure, and saved the complex hCAII-AZM to extract the AZM coordinates for subsequent docking. We employed the Sequence and Structural alignment method on MOE and added hydrogens using the Protonate 3D option and OPLS-AA forcefields, while leaving other settings as default.

The same docking settings that were used for CA VA were also applied to GOLD for docking the two derivatives onto hCA II, using as well AZM centroid to define the dockable region and sampling AZM coordinates as described earlier. The two docking protocols outlined here differ exclusively on the flexibility of side chains: in the first docking protocol, some were set as flexible, whereas in the

latter case, they were held rigid. Molecular models of the docked ligands were visualized using Pymol software. (https://pymol.org)

Chapter 2: Dual Inhibition of Human Carbonic Anhydrases IX and XII for Cancer Treatment

2.1 Characterization and Role of hCA IX and hCA XII in Cancer Proliferation and Survival

Cancers represent one the most widespread life - threatening diseases, concerning both well developed nations as well as the third world.

Apart from tumour invasion, progression and resistance, one of the main issues in cancer treatment regards the side effects of both chemo and radio therapies.

In this context, herein is borne out the idea that selectively targeting hCA IX and XII might be a safe and efficient way to treat various cancer diseases, preferably in combination with other chemoterapeutical meds. High levels of the two isoforms were appreciated in various malignant tumors like carcinoma of the cervix, breast, head and neck, lung, colon, esophagus, vulva, ovary, pleural mesothelium, and tumors of the brain, supporting their importance in cancer growth, proliferation and survival. [10, 40]

The first lead behind this assumption is the tissue hypoxia, which is a frequent condition produced by the lack of oxygen derived from the growing cancer cells that replace vessels, resulting in a reduced blood supply. As consequence, glucose catabolism is shifted towards anaerobic glycolysis increasing lactate production and lowering the pH of tumour microenviroment.[10] Physiological hCAs are the main actor in pH balance suggesting their involvement in cancer homeostasis. As a matter of fact, both hCA IX and XII are established biomarkers of different hypoxic tumours. Hypoxia inducible factor 1α (HIF − 1α) directly up-regulate the expression of hCA IX due to the missing proteasome degradation of HIF - 1α mediated by FIH -1(asparaginyl hydroxylase factor), PHDs (prolyl hydroxylase domain proteins) and Von Hippel Lindau tumor suppressor protein(pVHL), occurring in normoxia condition (Figure 17). The decrease of oxygen prevents HIF − 1α inactivation and leads to its dimerization with HIF − 1β finally promoting the transcription of CA IX genes. Nonetheless, overexpression of hCA IX was encountered also in other non-hypoxic tumors such renal clear cell carcinoma (RCC).
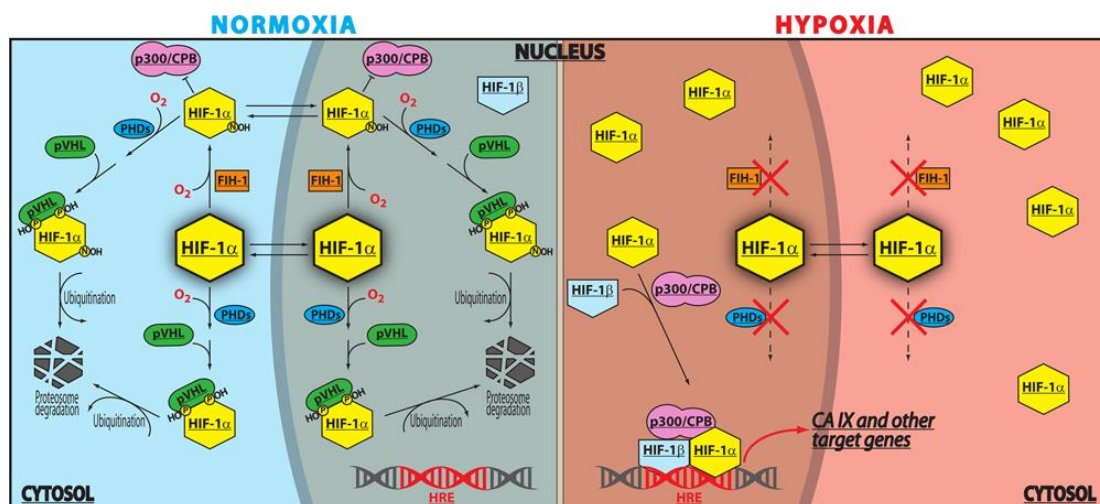
Figure 17. Schematic representation of CA IX expression mediated by hypoxia inducible factor vs normoxia – related proteins. Notes: HIF-1α (Hypoxia Inducible Factor 1 subunit α); HIF-1β (Hypoxia Inducible Factor 1 subunit β); PHDs (ProlylHydroxylase Domain proteins); FIH-1 (asparaginyl hydroxylase Factor Inhibiting HIF-1); pVHL (von Hippel Lindau tumor suppressor protein); CBP (CREB binding protein); HRE (Hypoxia Response Element). Image taken from ref.[40]

hCA IX function in tumor survival was properly elucidated too, since a straight correlation between lactate overproduction, already mentioned, and the induction of apoptosis by the intracellular pH drop can be done. Together with efflux pumps and channels, like the Na^+/HCO_3^- cotransporter (NBC) or the HCO_3^-/Cl^- anion exchanger(AE), its activity seize the protons belonging to lactate production from the cancer cell cytoplasm as schematized in Figure 18.[40]
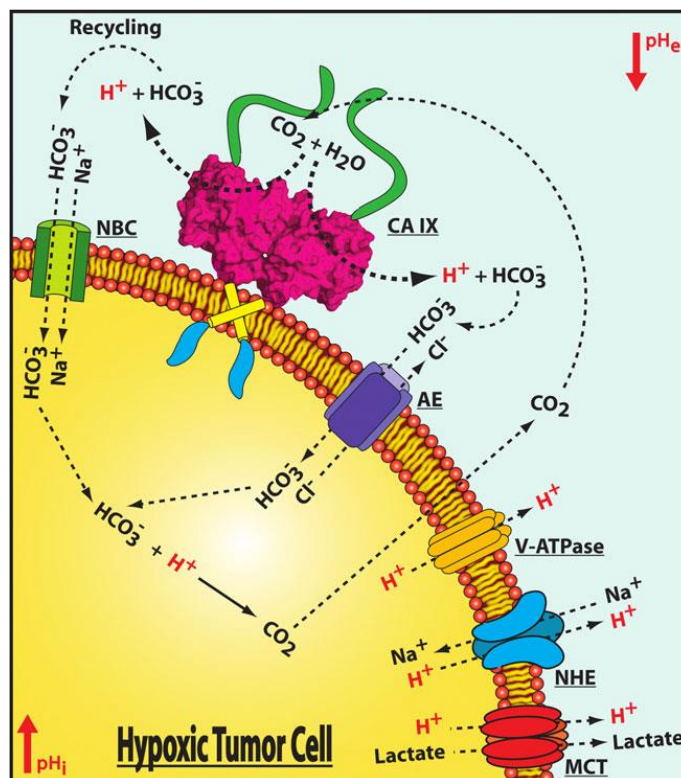
Figure 18. pH regulation process within the tumor cells under hypoxic conditions. Notes: Proteins involved in the process are schematically reported: monocarboxylate transporter (MCT), V-type H^+ATPase (V-ATPase), Na+/H+ exchanger (NHE), bicarbonate co-transport (NBC), anion exchanger (AE), and carbonic anhydrase IX (CA IX). Representation from ref. [40]

46

This effect on one side protects neoplasm cells from apoptosis activation, maintaining a neutral intracellular pH, and on the other side promote tumor invasiveness and metastasis dropping extracellular pH (pHe). Mutagenesis studies on hCA IX further confirmed its role in pHe regulation. Finally, a very complex interactome of hCA IX was highlighted encompassing: i) protein involved in cell adhesion as β – catenin; ii) mediator of nucleo-cytoplasmic transport machinery like XPO1 exportin and TNPO1 importin, which bind C- terminus of hCA IX (a.a. 418 – 459); iii) protein related to gene transcription as the case of CAND1, that form complexes with hCA IX still through interaction mediated by hCA IX residues 418 – 459, and iv) matrix metalloproteinase 14 (MMP – 14), promoting metastasis.[40]

Regarding hCA XII, less details about its real function are available in the literature in comparison to hCA IX. Nevertheless, several evidence related to its expression are reported. Firstly, as for hCA IX, it is influenced by HIF - 1α and hypoxia, as well as to pVHL. Apart from the protagonists of hypoxia response, evidence of the association of hCA XII expression and positive ER – α were also reported. Not only, a study of 2010 conducted on MDA-MB-231 human breast cancer cell lines, lined a very complex relationship between hCA XII and different moderators of cell invasion. These included MMP – 2, MMP – 9 and u – PA whose activity was impaired in hCA XII knockdown cells. Simultaneously, the expression of two endogenous inhibitors of MMP – 2 and u – PA, TIMP and PAI, was increased. Interestingly, also p38 – MAPK pathway was impaired in knockdown hCA XII transfected cells, driving to a reduced cell migration and invasion potential.[41] Taken together, all these hints strongly suggest that also hCA XII should be targeted to fight cancer.

Figure 19. Schematic domain organization of hCA IX. The signal peptide (SP), the PG domain, the CA domain, the TM segment, and the IC tail are reported. The numbers of the first and last amino acid of each domain are shown. Taken from ref. [40]

Getting deeper in their architecture, hCA IX and XII share in terms of subcellular location, topology and sequence, several common features. They are both dimeric membranes bound proteins of 459 and 354 a.a. respectively, presenting an extracellular catalytic domain, well conserved also in other hCA. The two include at the N – terminus a signal peptide, and glycosylation sites in their extracellular domain corresponding to T115 and N346 in hCA IX, and N28, N80 and N162 in hCA XII.(Figure 19 and 20) Aside from proteoglycan – like(PG) domain, which is a unique part of the

extracellular portion of hCA IX and strongly affects its catalytic activity,[40] the rest of the topology of the two isoenzymes is pretty similar, characterized by the extracellular CA catalytic domain (a.a. 137 – 391 and 29 – 289 respectively for hCA IX and XII) and , then by a transmembrane region (a.a 415 – 433 in hCA IX and 302 – 322 in hCA XII) and a final cytosolic region.
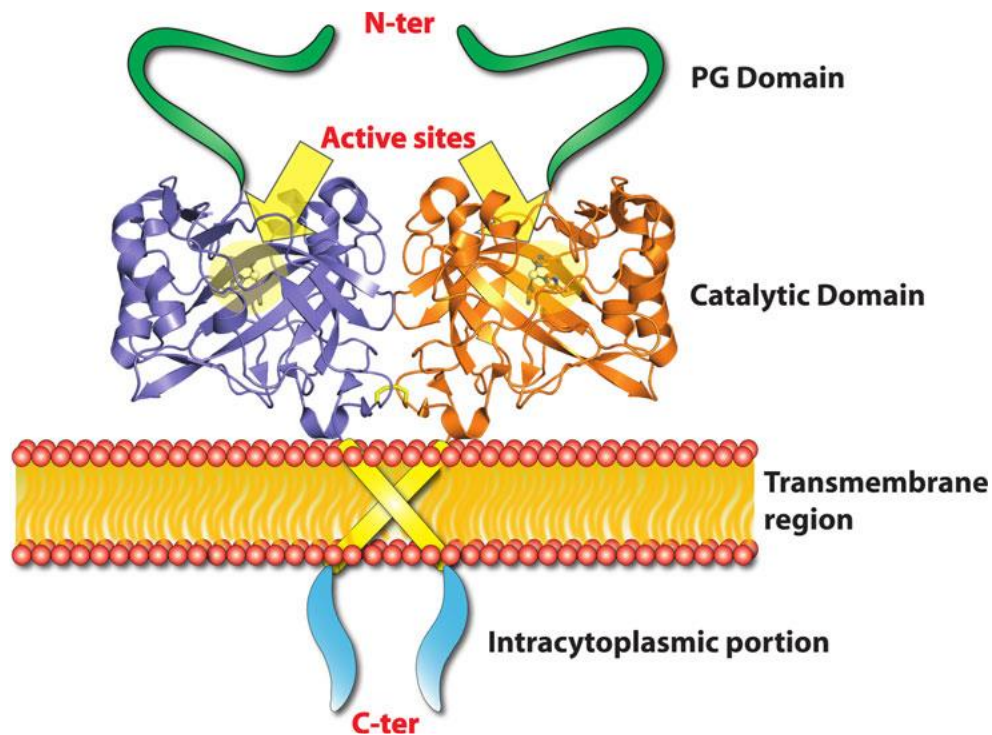
Figure 20. Model showing the structural arrangement of the full-length CA IX dimer on the cell membrane. In yellow is reported the disulfide bond between C174 of the two monomers. Taken from ref. [40]

Other characteristic features of these two enzymes regards residue involved in the protein dimerization, in the case of hCA IX is the disulfide bond between C174, while for hCA XII are two transmembrane GXXXG and GXXXS motifs whose depletion lead to complete loss of hCA XII quaternary structure.(Figure 21)[40, 42] Furthermore, phosphorylation sites at the intracellular C – terminus, were also identified, resulting crucial in hCA IX catalytic activity and in hCA XII metabolic signaling and kinases recruiting.[40, 42]
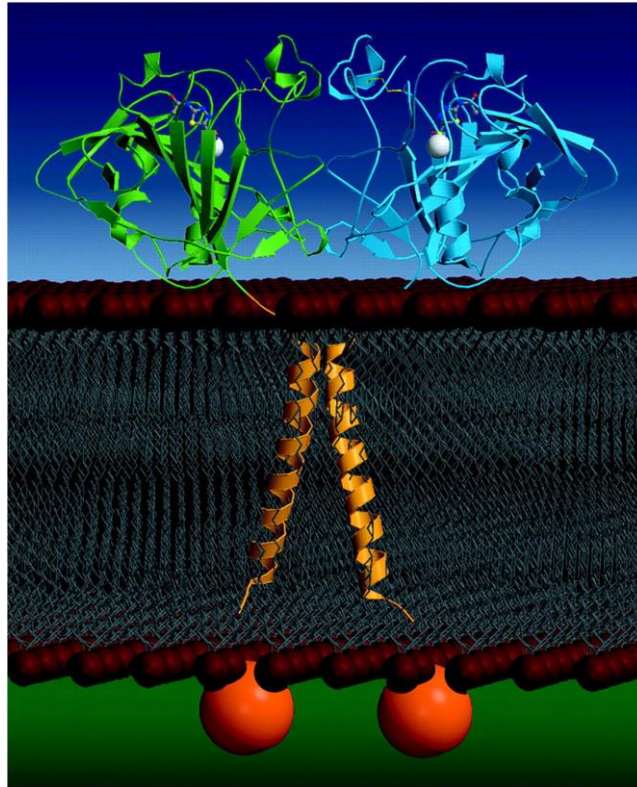
Figure 21. Crystal structure of CAXII. (PDB code: 1JCZ) Human carbonic anhydrase XII was crystallized at pH 7.5. Taken from ref. [42]

Finally, for what concerns the enzymes active sites, the conic shape of α – hCAs is retained as well as the Zinc – coordinating histidines (H94, H96 and H119), the one commonly involved in the proton shuttling(H64) and the residues N62, L198, T199 and T200, often involved in ZBG inhibitors binding are conserved as for the widely expressed. Even so, different residues, mainly at section 257 – 268 (referring to hCA IX sequence numbering) present several differences with respect to other hCAs, thus being an interesting druggable region to target.[40]

Crystallography made an important effort in providing diffraction data of the two isoforms, also in complex with some inhibitors, although several mutations with respect to wild – type were performed to obtain the dimer of hCA IX, and just recently in 2020 the native wild type CA domain was obtained. Nevertheless, decades of X-Ray experiments performed on a mutated hCA II (65A/S, 67N/Q, 69E/T, 91I/L, 131F/V, 132G/D, 135V/L, 169K/E, 203L/A, and 205C/G; taking as reference one of the most recent PDB: 6VKG and using hCA II residue numbering), so called hCA IX – mimic,[43] permitted the retrieval of several information about ligand binding, similarly to hCA XII for which various co – crystals are available on the RCSB PDB, thanks to its easy production, good validation metrics and binding site identity with the wild – type hCA IX.

In point of fact a plethora of selective hCA IX/XII inhibitor are now reported in literature.[44] The main example is SLC – 0111 that is already on Phase 2 clinical trials. The next section will give indeed an overview on the most potent and selective hCA IX/XII inhibitors for which structural information about their binding – mode are available, with a major focus on sulfonamide – like inhibitors and the newest approaches for the design of selective ones.

2.2. Application of Multiple Tail Approach on Sulfonamide – like Inhibitors for the Selective Inhibition of hCA IX and XII

All the speculation done in previous paragraph regarding the inhibition of hCA IX and XII as possible cancer treatment found an evidence if we have a look on the various binders investigated, both for therapy and diagnostic purposes, and that already passed different clinical trials. Below are reported some substances interacting with hCA IX/XII, that span from small molecules to monoclonal antibodies.

Table 5. Agents targeting hCA IX/XII in clinical trials. Data taken from ref. [10]

Clinical trial	Class	CTID	Treatment	Status
SLC-0111	Small molecule	NCT02215850	Advanced solid tumors	Phase I (Completed)
E7070	Small molecule	NCT00003891	Solid tumors	Phase I (Completed)
		NCT00080197	Metastatic breast cancer	Phase II (Completed)
		NCT01692197	Relapsed AML and High – Risk Myelodysplastic Syndrome	Phase II (Completed)
Girentuximab(cG250)	Monoclonal antibody	NCT00087022	Patients undergoing non – metastatic kidney cancer	Phase III (Completed)
BAY 79-4620	Antibody-Drug Conjugate	NCT01028755	Advance stage tumor	Phase I (Completed)
^{124}I-cG250	PET tracer	NCT00003102	Kidney Cancer	Phase I (Completed)
Zr^{89}-gerentuximab	Image agent	NCT02883153	Renal cell Carcinoma	Phase III (Completed)
In^{111}-DOTA-gerentuximab-IRDye800CW	Image agent	NCT02497599	Renal cell Carcinoma	Recruiting
^{124}I-cG250	Image agent	NCT00606632	Renal cell Carcinoma	Phase III (Completed)

Note: Information acquired from clinical Trials.gov.
Abbreviation: hCA, human carbonic anhydrase.

Thus, these molecules constitute an attractive alternative to cancer treatment, especially to circumvent cancer resistance mechanism to the current chemicals in use.[10] Even so, the research

on the topic is still open and diverse selective hCA IX/XII ligands with various mechanism of action are under evaluation. Moreover, in several works is taken in exam the development of dual inhibitors targeting also other anti – cancer targets. For example, recent works released inhibitors of hCA IX/XII showing dual activity on Vascular Endothelial Growth Factor (VEGFR – 2)[44, 45] on monoamine oxidases (MAOs)[46] and thioredoxin reductase[47] thus hitting tumor pH regulation and either angiogenesis or oxidative stress.

Nonetheless, selective inhibition of hCA IX and XII remains a tricky task due to the high conservation of hCAs. Concerning sulphonamide – like compounds, a common trend in their inhibition data is the high potency (in nanomolar range) not always flanked by a high selectivity. However, a fine - tuning of the early described "tail approach" brought to the identification of very selective sulphonamides or bio – isosteres.[48] Before describing the concept, it needs to be highlighted how greatly vary the conservation of the hCA active site among the isoform, going from bottom to the entrance.
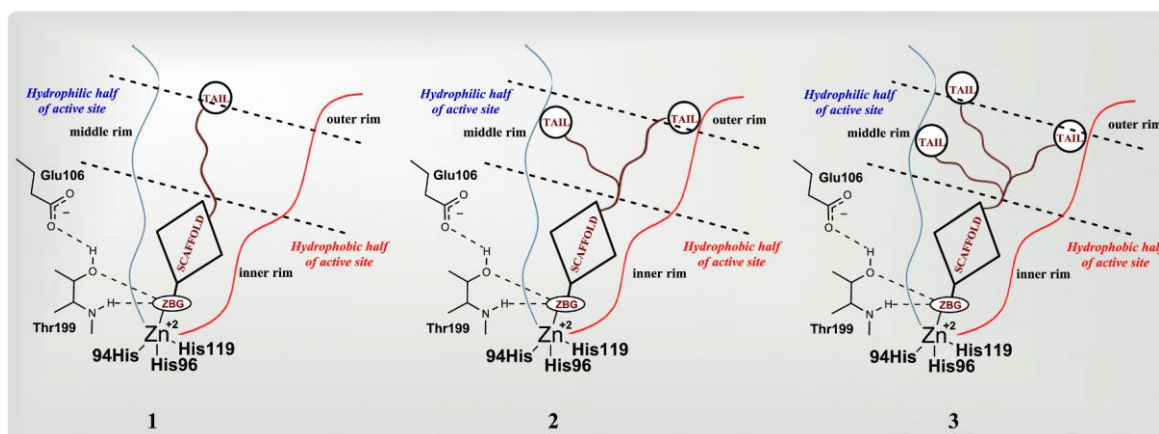
Figure 22. Schematic representation of the (1) "single tail", (2) "dual-tail" and (3) "three-tails" approach for the design of selective zinc-binding CAIs. Scheme taken from ref.[44]

Briefly, walking aside the two surfaces (hydrophobic and hydrophilic), starting from where the ZBG anchors the Zinc ion, three different rims can be distinguished: an inner one, a middle and an outer one. The more we go towards outer rim the more the residues are less conserved. Thus, the strategy consists in enriching the ZBG scaffold, often benzene - or aryl – sulphonamide, with one or more tails aimed to contact the middle or the outer rim of the catalytic site. Compound selectivity is presumably addressed to differences in size or in hydrophilicity/hydrophobicity ratio of each pocket side at these two levels. (Figure 22) [44]

Currently, hCA IX/XII selective inhibitors with up to three tails were designed using this approach. Various linkers connecting the ZBG scaffold with the tails, whose compounds showed nice

selectivity profile during stopped – flow assay, can be mentioned. Among them we can include azines, specifically pyridines, pyridones, pyrimidines and triazines. (Figure 23)
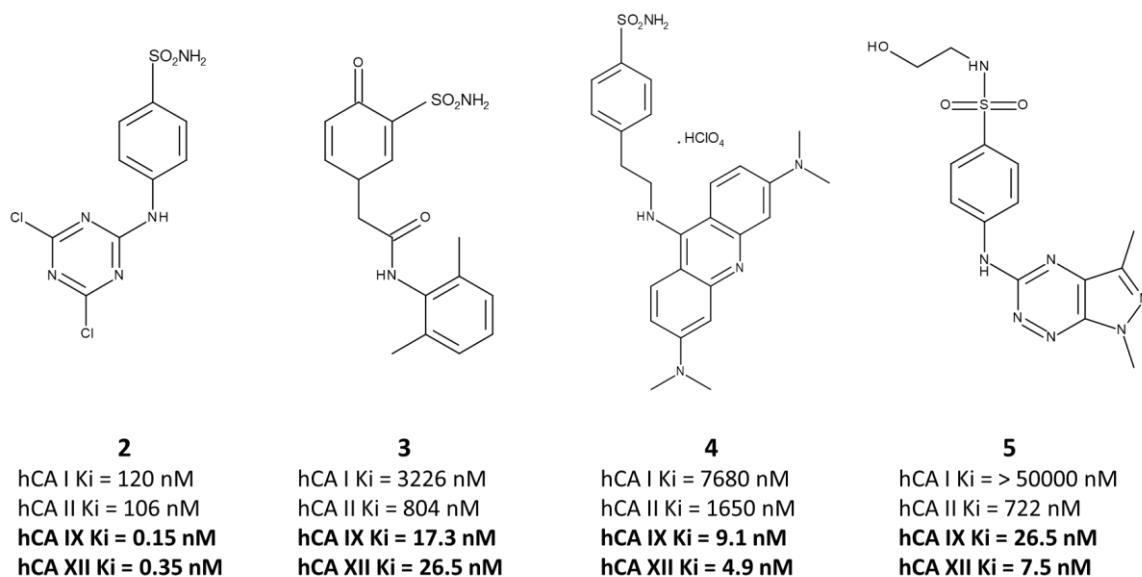
Figure 23. Selective and potent hCA IX and hCA XII inhibitors based on Azine or fused Azine moiety. Compounds taken from ref. [44]

A particular mention should be done for compounds **2-5**, not only for their promising potency and selectivity, as for compound 2 and 4, but also for their novelty in the context of hCA IX/XII inhibitor scaffolds. Indeed compound 3 presents salt – like characteristics, thus being an interesting candidate for targeting extracellular CAs, while compound **5** is Sildenafil analogue containing a secondary sulfonamide, not common in classical ZBG sulfonamides.[44]

Several azoles, encompassing a plethora of scaffolds, which encodes pyrazoles, triazoles, oxadiazole and conjugated or fused rings is also present in literature.[44]

6
hCA I Ki = 19081 nM
hCA II Ki = 117 nM
hCA IX Ki = 15 nM

7
hCA I Ki = 1197 nM
hCA II Ki = 490 nM
hCA IX Ki = 19 nM

8
hCA I Ki = > 50000 nM
hCA II Ki = 4736 nM
hCA IX Ki = 111 nM
hCA XII Ki = 20.3 nM
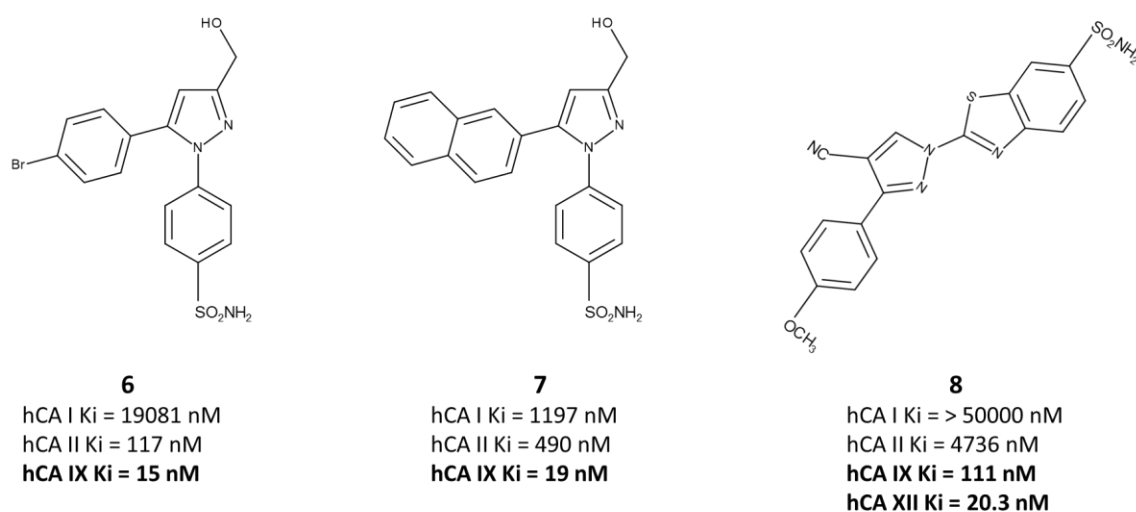
Figure 24. Some hCA IX/XII selective pyrazoles. Compounds taken from ref. [44]

Here, the multiple tail scheme is completely fulfilled and led to very interesting selectivity data (compound **8**). Additionally, some 1,5-diaryl pyrazole derivatives (compound 6 and 7) confirmed their antiproliferative activity, due to their hCA IX inhibition in synergy with other anti − cancer drugs, as they demonstrated a restoring of doxorubicin cytotoxicity on breast cancer MDA-MB-231 cells.(Figure 24) Furthermore, some oxadiazoles, as Epacadostat previously identified as inhibitor of another anti − cancer target (IDO − 1), resulted to be a highly selective inhibitor on IX/XII too, configuring as one of the most suitable candidate for in vitro and in vivo evaluation.[44]

9 (Epacadostat)
hCA I Ki = 8262 nM
hCA II Ki = 917.4 nM
hCA IX Ki = 3.0 nM
hCA XII Ki = 6.2 nM

10
hCA I Ki = 1790 nM
hCA II Ki = 4165 nM
hCA IX Ki = 33.1 nM
hCA XII Ki = 18.8 nM

11
hCA I Ki = 883 nM
hCA II Ki = 11 nM
hCA IX Ki = 6.4 nM
hCA XII Ki = 2.8 nM
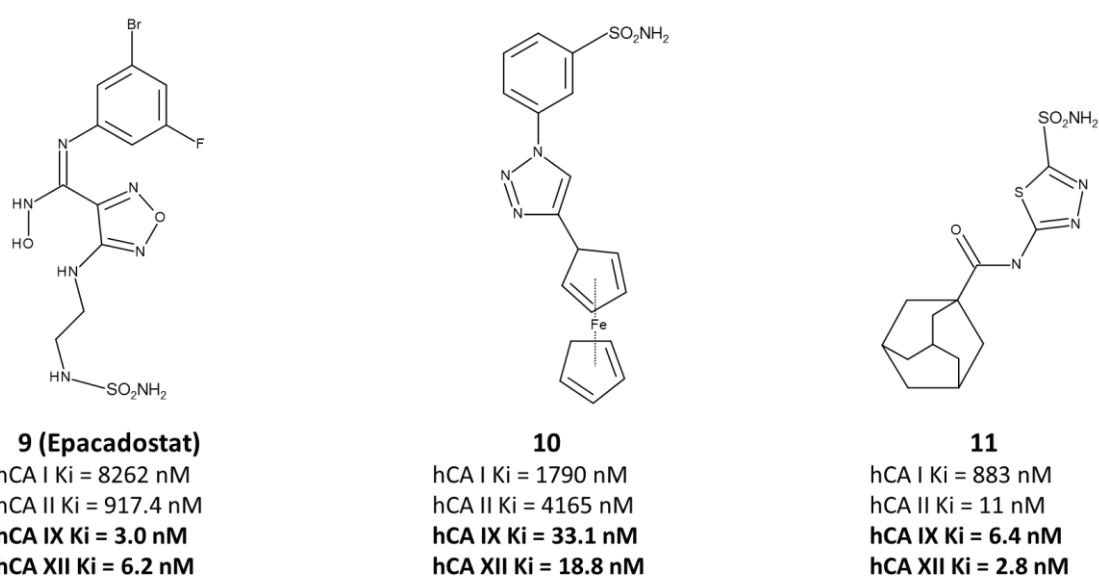
Figure 25. Some selective hCA IX/XII azole derivatives. Compounds taken from ref.[44]

Considering also the chemical space covered by this class of sulfonamides, compound 10 stand out for its triazol - ferrocene tail that conferred interesting selectivity for the tumor isoforms. On the other hand, also some hindered AZM derivatives, presenting a thiadiazol scaffold as the most classical hCA inhibitor, but engineered with a bulkier tail (as rimantadine), resulted more selective than the standard.(Figure 25)

Bringing back the dual inhibition theme, some derivatives bearing an isatine moiety, a very powerful scaffold already endowed in some tyrosine – kinase inhibitors such as Nintedanib and Sunitinib, were taken in exam for hCA IX/XII inhibition. 23 isatine – pyrazole benzenesulphonamides, showing potent inhibition of the tumor isoforms with a preference for hCA IX, were synthesized exploiting this clue and two molecules, compounds 12 and 13, showed impressive selectivity over the cytosolic isoenzymes I and II.[49]

12
hCA I Ki = 510 nM
hCA II Ki = 565 nM
hCA IX Ki = 1.1 nM
hCA XII Ki = 3.3 nM

13
hCA I Ki = 414 nM
hCA II Ki = 454 nM
hCA IX Ki = 1.0 nM
hCA XII Ki = 18.5 nM

14
hCA I Ki = 406.9 nM
hCA II Ki = 823.8 nM
hCA IX Ki = 5.2 nM
hCA XII Ki = 6.3 nM
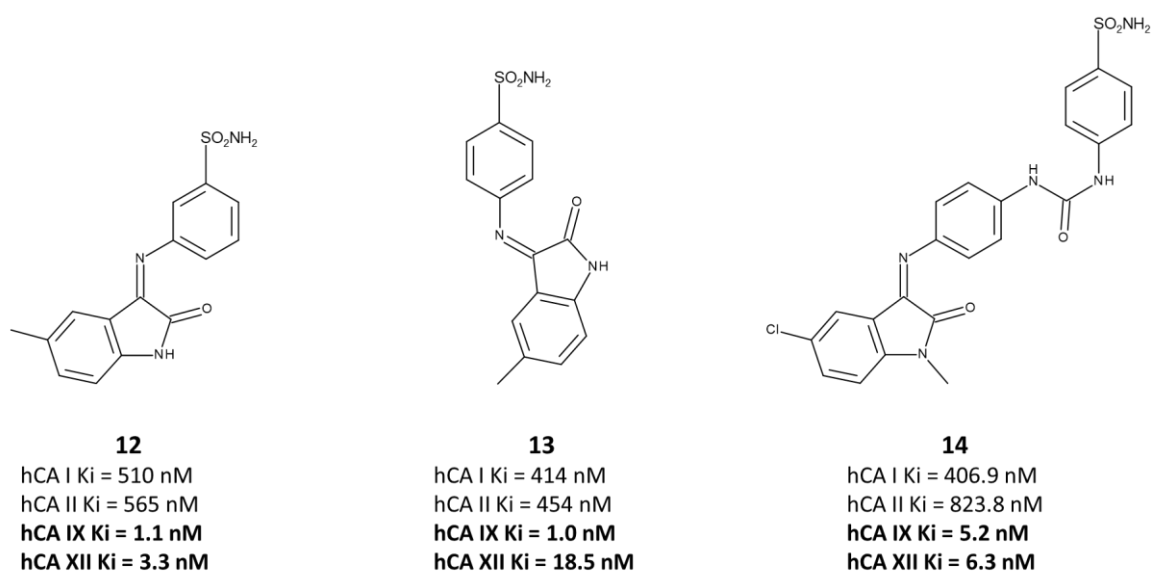
Figure 26. Some isatine based benzenesulphonamide selectively targeting hCA IX/XII. Compounds taken from ref.[44]

Then, based on a QSAR and structure – based analysis another series of 1H-indole-2,3-dione 3-(N - phenyl-thiosemicarbazones) incorporating the same moiety was obtained.[50, 51] Among them, compound **14** demonstrated not just selective inhibition of hCA IX/XII, but also anti – proliferative activity towards breast cancer MDA – MB – 231 and MCF – 7 cell lines and potent inhibition of VEGFR – 2 receptor, further confirming the usefulness of isatine ring embodiment in anti – cancer drug design. (Figure 26)

Finally, another trend in selective sulfonamide design is presented is recent studies, which reside in taking inspiration from either sweeteners or carbohydrate to decorate zinc binder's tail or to bear

the ZBG. From here, two new attractive classes of selective hCA IX/XII sulphonamide - like inhibitors were developed: Saccarin(SAC) and Acesulfame K (Ace K) (compounds **15** and **17**) based inhibitors and carbohydrate – based ones.
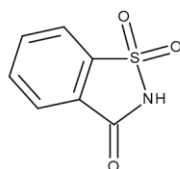
15 Saccarin (SAC)
hCA I Ki = 18540 nM
hCA II Ki = 5950 nM
hCA IX Ki = 103 nM
hCA XII Ki = 633 nM
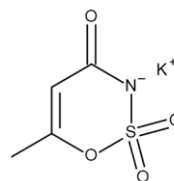
16 Acesulfame K (Ace K)
hCA I Ki = > 20000 nM
hCA II Ki = > 20000 nM
hCA IX Ki = 2400 nM
hCA XII Ki = > 20000 nM

Figure 27. Chemical structure of Saccarin (15) and Acesulfame K(16)

The first two classes present two very inspiring scaffolds for selective design, as on one side they configure as selective lead compounds for hCA IX (SAC also for hCA XII) inhibition, but on the other side show safe ADMET profiles as being already approved by FDA as food additive. (Figure 27) Indeed, lead optimized derivatives of SAC and Ace K very promising selectivity profiles reaching Ki values for hCA I and II > 50000 nM.[44] Interestingly, some of them were tertiary(compounds 19 and 20) sulphonamides/sulphamates whose mechanism of action is not elucidated yet. (Figure 28)
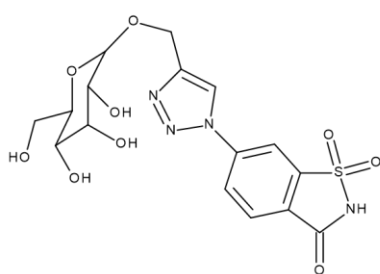
17
hCA I Ki = >50000 nM
hCA II Ki = >50000 nM
hCA IX Ki = 49.5 nM
hCA XII Ki = 572 nM
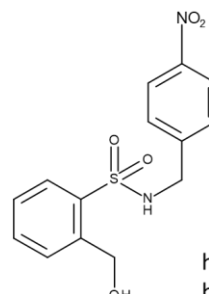
18
hCA I Ki = >10000 nM
hCA II Ki = >10000 nM
hCA IX Ki = 20 nM
hCA XII Ki = 54 nM
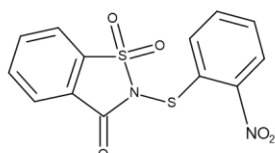
19
hCA I Ki = >10000 nM
hCA II Ki = >10000 nM
hCA IX Ki = 18 nM
hCA XII Ki = 4.0 nM
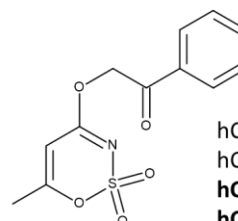
20
hCA I Ki = >10000 nM
hCA II Ki = >10000 nM
hCA IX Ki = 15.3 nM
hCA XII Ki = 126 nM

Figure 28. Some SAC/Ace K based hCA IX/XII inhibitors with, secondary (**17** and **18**) and tertiary (**19** and **20**) sulphonamide/sulfamate groups. Compounds taken from ref. [44]

Carbohydrates based inhibitors instead were designed using a strategy initially introduced by Winum et al. called "sugar approach", which before raised selectivity also in other hCAs as demonstrated by Topiramate endowing this type of moiety ([doi.org/10.1002/med.20141](doi.org/10.1002/med.20141))(10.1016/j.bioorg.2022.105920). Also in this case, a variety of linkers that connect the sugar to ZBG, encompassing secondary or tertiary sulfonamide included in pyrrolidine or piperidine cycles, as well as ureidic ones, provided inhibitors with outstanding potency and/or selectivity. (Figure 29)

21
hCA I Ki = 4260 nM
hCA II Ki = 271 nM
hCA IX Ki = 2.1 nM
hCA XII Ki = 9.8 nM

22
hCA I Ki = 9500 nM
hCA II Ki = 725 nM
hCA IX Ki = 2 nM
hCA XII Ki = 1 nM

23
hCA I Ki = > 20000 nM
hCA II Ki = > 20000 nM
hCA IX Ki = 11 nM
hCA XII Ki = 85 nM
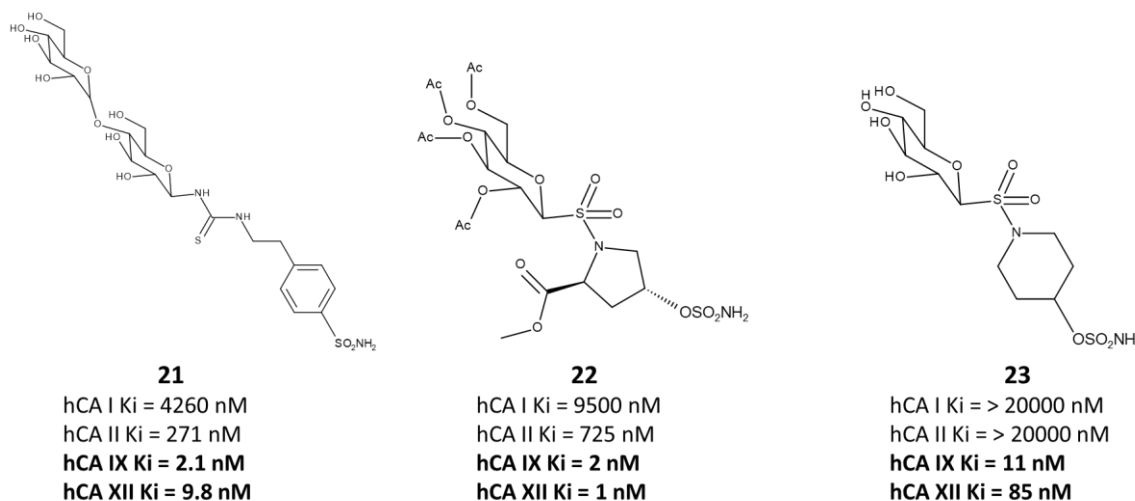
Figure 29. Some sugar - based sulphonamides/sulfamates displaying selective inhibition of hCA IX and XII. Compounds taken from ref. [44]

A massive contribution in selective inhibition design was given by crystallography which enabled the investigation of key interaction between selective binders and the two isoenzymes subject of this study. In particular, co – crystals of some selective hCA IX inhibitors in complex with hCA IX – mimic were deposited in RCSB PDB. These included the lead compound SLC – 0111 (Ki of 45 nM and 4.4 nM respectively on hCA IX and XII) [30] (PDB code: 5JN3), Epacadostat (PDB code: 6VKG), Saccarin (PDB code: 4RIV) and Acesulfame K (PDB code: 5WGP). Giving a brief resume, the main reasons behind their selectivity, as predictable, resides in the shape and interaction patterns at the entrance of hCA binding site. More in detail, analyzing Epacadostat binding mode in hCA IX – mimic with its respective one in hCA II, a meaningful difference in the shape of hCA IX and II is represented by the mutation at position 131 (Phe to Val) which enables several lipophilic interactions in hCA IX with respect to hCA II in which just a simple phi – phi T shaped interaction is formed by the phenil tail of Epacadostat. Hydrogen bond networks, encountered in selective ureido benzenesulfonamides too and involving not only Q92 (conserved in hCA II) but also N67, seem to play an important role in hCA IX ligand selectivity. [43, 52]

Concerning hCA XII, up to 30 X – Ray structure are available on RCSB PDB, of which 28 are in adduct with ZBG inhibitors. Despite the co – crystalized inhibitors were tested by thermal shift

assay (TSA), thus providing not comparable data with the inhibitors previously reported, also in this case some hints about specific hCA XII binding can be found. The main one regards S132, hydrogen bonded by ligands showing interesting selectivity accounted comparing their Kd values between hCA XII and II (See PDB code: 5LL9).

Taken together, all the crystallographic and activity data, as well as the hypothesis provided by molecular modelling studies on hCA IX and XII can provide valuable tools for selecting new candidates that may even reach clinical trials. [53]

2.3. From Retrospective to Perspective Studies on 1,2,3,4-Tetrahydroisoquinolin-2-ylsulfonamides as hCA IX/XII Inhibitors using a fast and accurate ensemble docking protocol

Although several promising binders of hCA IX/XII were identified so far, still some flaws in tracing a proper SAR able to highlight the chemical patterns involved in ligand selectivity are present. As confirmation, some of the compound series reported in the previous paragraph, although containing very potent and selective hCA IX/XII inhibitors, had as well several inactive or non – selective compounds [44, 54, 55]

Herein a similar case is reported, where a series of 1,2,3,4-tetrahydroisoquinolin-2-ylsulfonamides, showing initially low nanomolar inhibition hCA II (compound **4** taken as reference), loosed their affinity during a second screening once hindered with an aryl moiety at C-1 of the isoquinoline ring (compounds **1**, **2** and **3**), despite bearing a primary sulfonamide group which often ensures potency for hCAs. Surprised by these results, during my PhD research activities we have also investigated their ability to inhibit hCA XII. Differently from any expectation, they exhibit low nanomolar inhibition of hCA XII, configuring as selective hCA XII. (Figure 30) With the aim to explain the different affinity of compounds **1**-**3** among the three isoforms, we performed a retrospective study, combining both a computational workflow on hCA IX and XII and crystallographic binding – mode depiction on hCA II. Briefly the modelling pipeline is composed of four main steps: i) development of an ensemble docking protocol on hCA IX – mimic and hCA XII to identify a reliable pose prediction of the compounds on the two isoforms; ii) binding - energy calculation of the compounds on the three isoforms (hCA II, XI – mimic and XII); iii) binding mode comparison between the three isoforms using docking complexes of compounds in hCA IX – mimic and XII, and co – crystals of the three compounds with hCA II ; iv) Molecular Dynamic (MD)

simulations of both docking complexes and hCA II co-crystal structures. A detailed description of these four steps will be then given in the sub-sections of the next Result and Discussion part.

A

B

Code name	R	K_i (nM) [a]			
		hCA I	hCA II	hCA IX	hCA XII
EM_2 (1)	C_6H_5	8980 [b]	15700 [b]	8440 [b]	6.5
EM_4 (2)	4-F-C_6H_4	4430 [b]	14980 [b]	5590 [b]	6.5
EM_6 (3)	4-$NH_2C_6H_4$	8070 [b]	11300 [b]	6780 [b]	5.5
DT_9 (4)	CH_3	2800 [c]	87.3 [c]	9.4 [c]	n. d.
SLC-0111		5080 [d]	960 [d]	45 [d]	4.5 [d]
AZM		250 [d]	12.5 [d]	25.8 [d]	5.7 [d]

[a] Errors in the range of ±5-10 % of the reported values, from 3 different assays.
[b] data taken from reference[56]
[c] data taken from reference [57]
[d] data taken from reference[37]
n. d. = not determined

Figure 30. Main scaffold (A) and table reporting the R groups, the activity data of each compound object of this study, including the standard compounds (AZM and SLC − 0111)

2.3.1 Result and Discussion

Considering that compounds **2** and **3** showed both a very similar structure and activity values on the different hCA isoforms, we decided to focus our attention on compound **2** and its unsubstituted analogue **1**. As our aim was to identify the key interactions behind the different affinity of our compounds **1** and **2**, the first goal in this study was the identification of a reliable docking pose of the two in the different hCA isoforms. A primary importance was given to the prediction of their binding mode on the tumor-expressed isoforms hCA IX and hCA XII.

Development of an ensemble docking protocol on hCA IX – mimic and hCA XII

Due the presence on RCSB PDB of a large collection of three-dimensional structures of hCA XI-mimic and hCA XII in complex with various inhibitors, we developed an appropriate ensemble docking method able to consider the protein flexibility without any loss in the docking performance speed. Material and methods section (vide infra) detailed the above-mentioned protocol that included the following steps: a) selection and protein preparation; b) clustering of the PDB structures; c) validation of the docking settings.

Thus, we started collecting several PDB structures containing both apo proteins or co − crystal adducts with substrate or inhibitors of hCA IX − mimic and XII. Then, a selection according to the sequence identity or to nature of the co − crystallized ligands was made, as described more in detail in the Material and methods section. Finally, an in − depth validation of the docking procedure, using the representative conformations of the two proteins obtained via RMSD

hierarchical clustering, was performed to exploit it for the modelling studies of our in – house compounds.

A
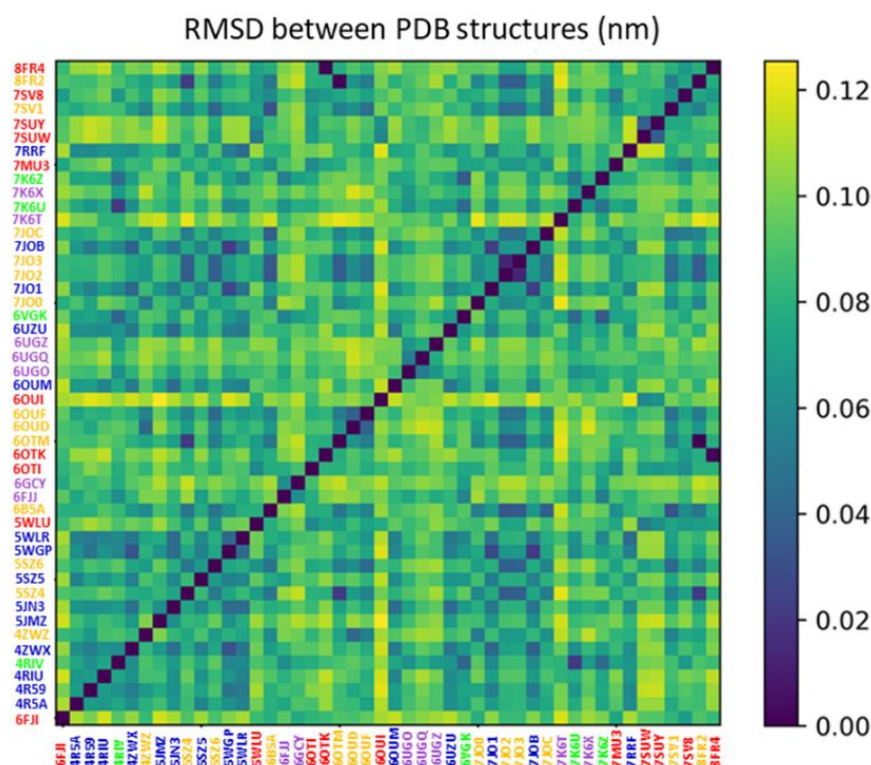
B
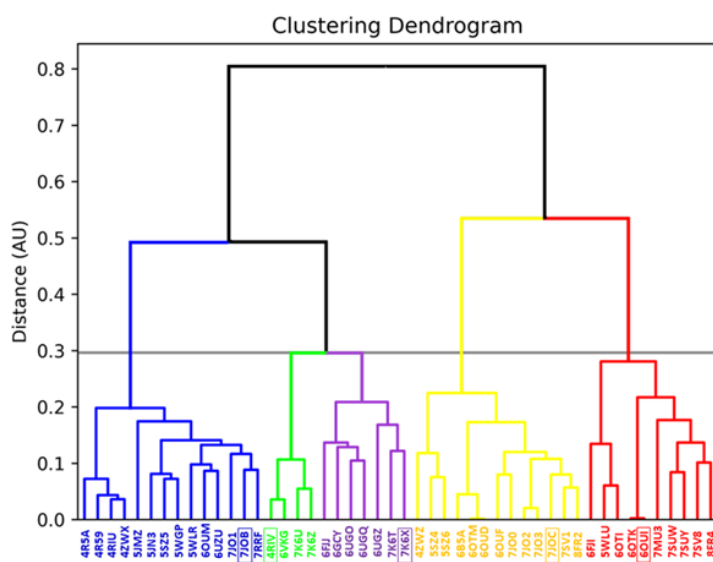
C
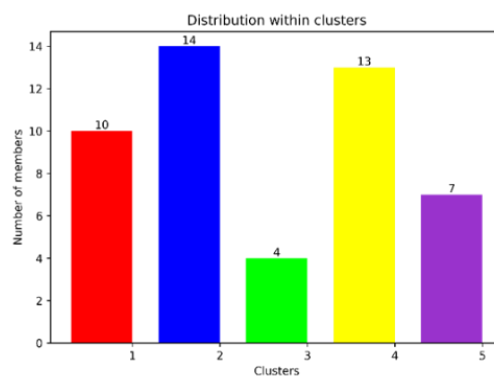
Figure 31. Hierarchical clustering of hCA IX – mimic PDB structures. Distance matrix plotted as heatmap by TTClust. Each square represents an RMSD value (expressed in nm) between two PDB structures, according to the key on the right side of the image. PDB structures were labelled using a colour code that represents the cluster they belong to: Cluster 1 (red); Cluster 2 (blue); Cluster 3 (green); Cluster 4 (yellow); Cluster 5 (violet). (B) Dendrogram generated by the Matplotlib package included in TTClust, reporting the ward linkage matrix of the clustering run. On the x axis are reported the PDB structures used, labelled using the same colour-coding of Figure A, on the y axis is reported the distance at which distinct members are merged in the same cluster. The grey horizontal line represents the distance cutoff chosen by the auto - clustering algorithm to define the final number of clusters generated. On the x axis representative frames are highlighted by the coloured squares. (C) Histogram plotting the population of each cluster.
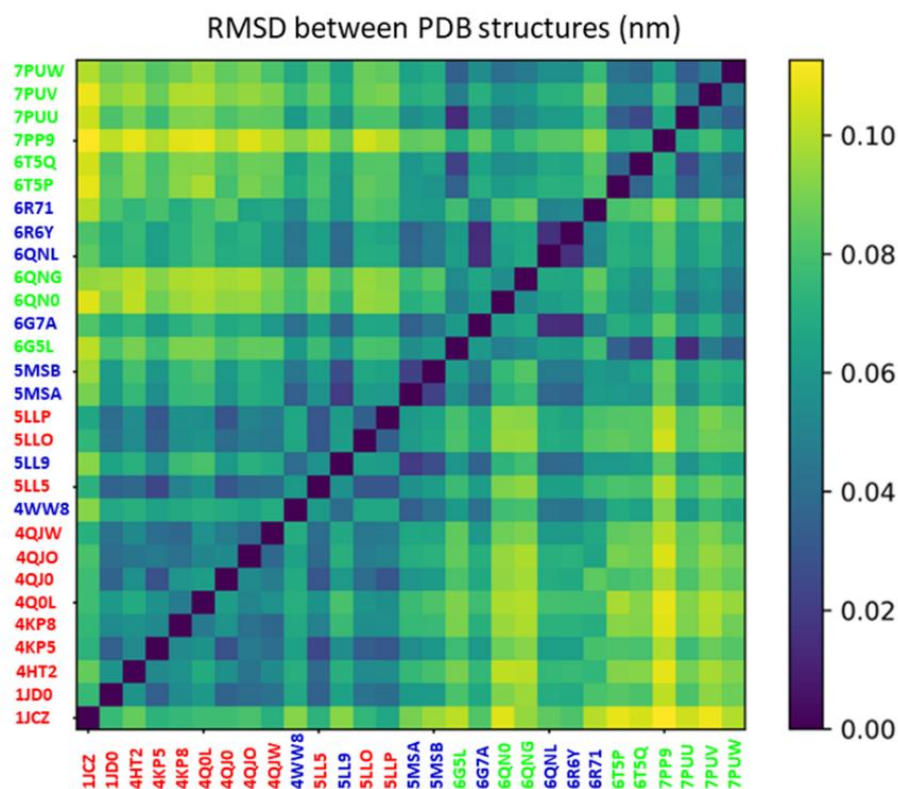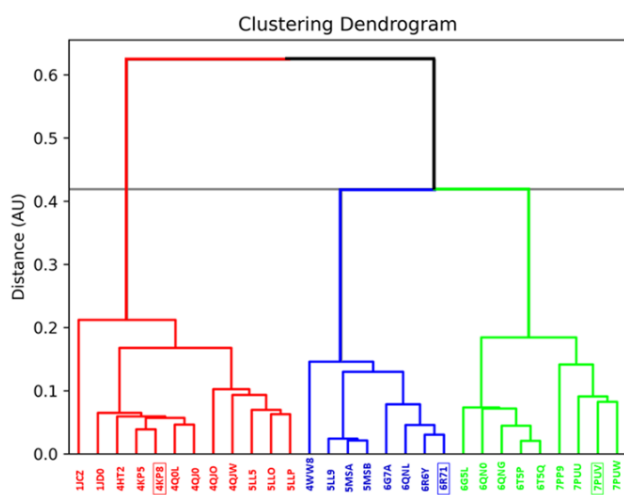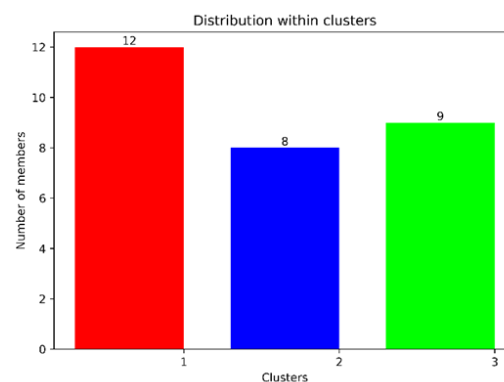
Figure 32. Hierarchical clustering of hCA XII PDB structures. Distance matrix plotted as heatmap by TTClust. Each square represents an RMSD value (expressed in nm) between two PDB structures, according to the key on the right side of the image. PDB structures were labeled using a colour code that represents the cluster they belong to: Cluster 1 (red); Cluster 2 (blue); Cluster 3 (green); Cluster 4 (yellow); Cluster 5 (violet). (B) Dendrogram generated by the Matplotlib package included in TTClust, reporting the ward linkage matrix of the clustering run. On the x axis are reported the PDB structures used, labeled using the same colour-coding of Figure A, on the y axis is reported the distance at which distinct members are merged in the same cluster. The grey horizontal line represents the distance cutoff chosen by the autoclustering algorithm to define the final number of clusters generated. On the x axis representative frames are highlighted by the coloured squares. (C) Histogram plotting the population of each cluster.

Agglomerative hierarchical clustering, performed using TTClust, produced five and three representative conformations of hCA IX – mimic and hCA XII, that were employed for our docking

studies[58] (See paragraph " Ensemble docking settings" of Materials and methods section and Figure 31 and 32).

The ensemble docking method schematized before was able to reproduce the native conformation of 24/46 (52.17%) and 24/28 (85.17%) ligands co-crystallized respectively on hCA IX-mimic and hCA XII during re-docking and cross-docking experiments, with an RMSD value ≤ 2.6 Å. Additionally, the 33.3% (8/24) and the 45.83% (11/24) of the successful results for hCA IX-mimic and hCA XII respectively, are obtained by docking the ligand in the representative structure of the cluster that includes the native protein, thus supporting the usage of protein clustering procedure prior ensemble docking. (See Table 6 A and B).

Therefore, the same ensemble docking protocol was employed to decipher the pose of compound **1** and **2** inside hCA IX – mimic and hCA XII binding site. Considering that both of compounds were assayed as racemic mixture, we carried out the docking simulations for each pair of enantiomers and investigated the binding – mode of both structures to give insights about possible hCA XII eutomer labeling.

Table 6. Validation report of the ensemble docking protocol. Each PDB structure was coloured according to the same scheme of Figure 31 and 32. Column "Ligand" reports the molecule ID of the respective co-crystallized ligand. RMSD values were calculated using two different methods, one considering the displayed heavy – atoms (v. atoms), the other one considering the maximum common structure (MCS). "RMS success" indicates docking poses with a RMSD value lower than 2.6 Å than the X-Ray conformation. "Best receptor" column reports ensemble receptor associated to the docking pose selected, which correspond to the representative structure of the respective cluster. "Ensemble success" indicates whether the ligand is docked into the representative structure of the cluster including its native protein. Validation report for (A) hCA IX - mimic co-crystallized ligands and (B) hCA XII co-crystallized ligands. Tables were generated using Microsoft Office Excel (2016).

A

PDB	Ligand	RMSD(v.atoms)	RMSD(MCS)	RMS Success	Best receptor	Ensemble success
4R5A	3J4	3.1017	3.1017	N	2	Y
4R59	3J3	3.6445	3.6445	N	3	N
4RIU	3QR	4.9948	4.9948	N	3	N
4RIV	LSA	0.5355	0.5355	Y	3	Y
4ZWX	5KZ	5.8004	5.8004	N	1	N
4ZWZ	510	5.7604	5.7604	N	3	N
5JMZ	AYX	1.737	1.3454	Y	4	N
5JN3	WWZ	2.3865	2.3865	Y	1	N
5SZ4	72D	1.2903	1.2903	Y	1	N
5SZ5	72E	0.8895	0.8895	Y	5	N
5SZ6	72G	2.8122	2.8122	N	3	N
5WGP	AUD	2.7312	2.7312	N	5	N
5WLR	86B	2.2755	2.2755	Y	2	Y
5WLU	42G	8.7954	8.7954	N	1	Y
6B5A	CQS	6.6935	6.6935	N	3	N
6GCY	3QR	1.6848	1.6848	Y	2	N
6OTI	N84	1.1975	1.1975	Y	1	Y
6OTK	N7S	1.227	1.227	Y	2	N
6OTM	N8A	5.2245	5.2245	N	3	N
6OUD	N7M	2.5763	2.5763	Y	4	Y
6OUF	N7A	3.4537	3.4537	N	3	N
6OUI	N7D	1.682	1.682	Y	1	Y
6OUM	N7J	2.0029	2.5887	Y	1	N
6UGO	Q77	0.6489	0.6489	Y	1	N
6UGQ	Q7A	0.5921	0.5921	Y	3	N
6UGZ	Q71	0.5379	0.5379	Y	1	N
6UZU	6LU	0.4462	0.4462	Y	2	Y
6VKG	BBJ	4.4966	4.4966	N	2	N
7JO0	VFG	1.1861	1.1861	Y	4	Y
7JO1	VFJ	0.7875	0.7875	Y	1	N
7JO2	VFM	1.2345	1.2345	Y	1	N
7JO3	VGS	1.4046	1.4046	Y	1	N
7JOB	VGV	0.9935	0.9935	Y	1	N
7JOC	ARZ	1.3635	1.4069	Y	1	N
7K6T	VYV	6.8116	6.8116	N	2	N
7K6U	VYY	1.8855	1.8855	Y	3	Y
7K6X	VZ1	5.4748	5.4748	N	2	N
7K6Z	VZD	7.4252	7.4252	N	2	N
7MU3	ZOA	7.7721	7.7721	N	2	N
7RRF	6IV	8.7299	5.9885	N	2	Y
7SUW	U77	10.8145	10.8145	N	2	N
7SUY	C97	5.2357	5.2357	N	3	N
7SV1	U6V	5.9846	5.9846	N	1	N
7SV8	U7J	6.8455	6.9133	N	2	N
8FR2	NBA	5.2245	5.2245	N	3	N
8FR4	N7S	1.2286	1.2286	Y	2	N

B

PDB	Ligand	RMSD (v. atoms)	RMSD (MCS)	RMS Success	Best Receptor	Ensemble success
1JD0	AZM	1.7663	1.4845	Y	3	N
4HT2	V50	3.2523	2.3647	Y	3	N
4KP5	E1F	1.3429	1.1299	Y	3	N
4KP8	E1G	2.6207	2.3699	Y	3	N
4Q0L	V14	2.1967	2.0946	Y	1	Y
4QJ0	WWX	6.2328	6.2181	N	3	N
4QJO	V1F	2.3241	2.1240	Y	1	Y
4QJW	WWO	1.3826	1.3826	Y	1	Y
4WW8	VD9	1.7984	1.5341	Y	2	Y
5LL5	6YH	2.2718	2.2718	Y	2	N
5LL9	6YQ	2.7461	2.7461	N	3	N
5LLO	5EF	1.6284	1.4957	Y	1	Y
5LLP	6Z9	5.6776	5.6631	N	3	N
5MSA	3TV	1.4824	1.2310	Y	2	Y
5MSB	V13	1.0366	0.6775	Y	2	Y
6G5L	EM5	1.4295	1.4295	Y	3	Y
6G7A	EOQ	1.8460	1.8460	Y	2	Y
6QN0	J8Q	2.4455	2.3392	Y	3	Y
6QNG	J95	1.8615	1.7572	Y	2	N
6QNL	J92	4.0770	3.9768	N	3	N
6R6Y	EA3	1.6793	1.1828	Y	3	N
6R71	JTW	1.5965	1.5965	Y	3	N
6T5P	VD8	1.8624	1.0794	Y	2	N
6T5Q	MKQ	0.6322	0.6322	Y	1	N
7PP9	7VZ	1.8672	1.7006	Y	3	Y
7PUU	840	1.4766	1.1614	Y	2	N
7PUV	84Z	1.6793	1.5647	Y	2	N
7PUW	84I	1.3682	1.3682	Y	1	N

Cluster 1 = ▬
Cluster 2 = ▬
Cluster 3 = ▬
Cluster 4 = ▬
Cluster 5 = ▬

RMSD (v. atoms) = RMSD considering the displayed heavy – atoms (value in Å)

RMSD (MCS) = RMSD considering the maximum common structure (value in Å)

Ensemble docking on hCA XII of in-house derivatives.

Considering the promising selectivity of derivatives **1** and **2**–towards hCA XII, we started our computational analysis on this isoform.

The (S) – enantiomers of compounds **1** and **2** were the first ones examined through our docking simulations. Despite the two selected compounds demonstrated the overlapped K_i values of 6.5 nM toward the hCA XII isoform, they possessed different binding modes as depicted in Figure 33.

Figure 33. Superposition of the (S) enantiomer binding mode of compounds **1** (green sticks) and **2** (purple sticks) inside hCA XII binding site (cyan). Interacting residues are represented as thin sticks and zinc ion as a grey sphere. Crucial hydrogen bonds are highlighted by yellow dashes while lipophilic interactions by surfaces.

The two inhibitors **1-2** were canonically bound to catalytic site through the sulfonamide ZBG group. Intriguingly, the remaining 1-arylisoquinoline scaffold of the **1-2** are oriented toward two distinct areas. The C-1 aryl substituent of compound 1 (green sticks) occupied the lipophilic cavity defined by V121, L198, L141 near to the entrance of the active site whereas the dimethoxysubstituted-benzene ring engaged two hydrogen-bond interaction with not conserved K67 with the two methoxy group. The wide cavity of hCA XII allows a different positioning for inhibitor **2** (purple sticks), for which the dimethoxysubstituted-benzene ring interacted with the side chain of polar residue S135; additionally, the fluorine atom was hydrogen bound with N62. The two above mentioned polar interactions could explain the different orientation of 1-arylisoquinoline ring to respect parent compound **1**. Subsequently, we decided to explore the hypothetical binding mode of the (R)-**1** and (R)-**2** on hCA XII.
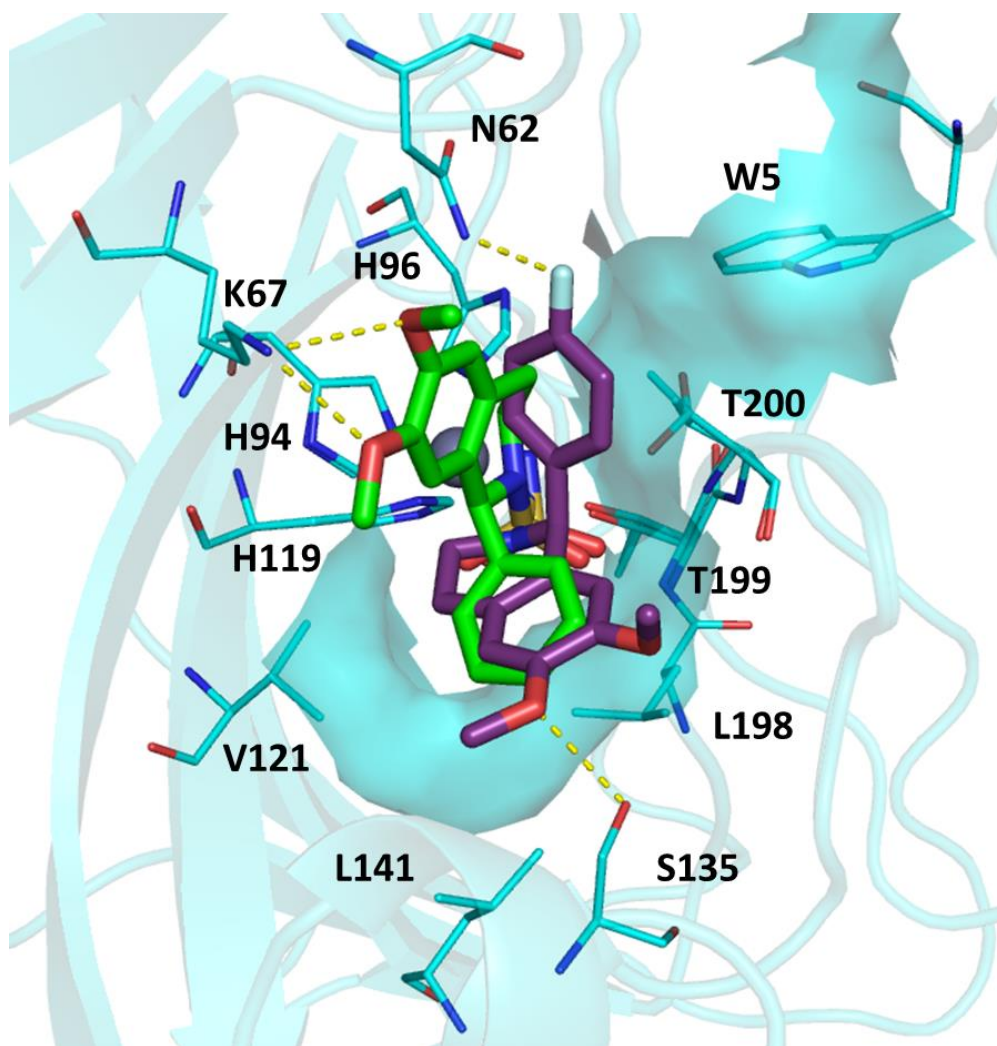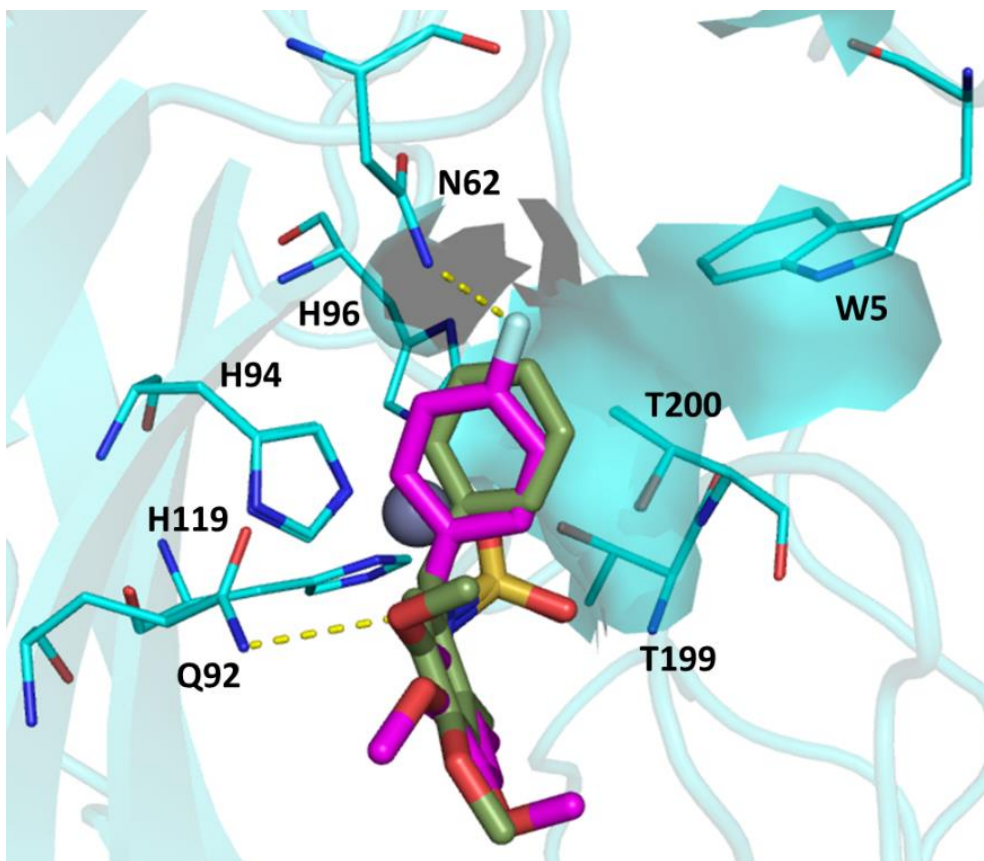
Figure 34. Superposition of the (R) enantiomer binding mode of compounds **1** (smudge sticks) and **2** (magenta sticks) inside hCA XII binding site (cyan). Interacting residues are represented as thin sticks and zinc ion as a grey sphere. Crucial hydrogen bonds are highlighted by yellow dashes while lipophilic interactions by surfaces.

Each single (*R*)-enantiomer for the two compounds displayed a very similar orientation that is a hybrid binding mode between the ones discussed before for compounds (*S*)-1 and (*S*)-2. In detail, the C–1 substituent of inhibitors (*R*)-**1** and (*R*)-**2** was located in the same region of hCA XII cavity as found for enantiomer (*S*)-**2**, forming hydrophobic interactions with T200, while the dimethoxyphenyl ring contacts the hydrophilic surface hydrogen– bonding Q92, similarly to compound (S)-1 (Figure 34). Therefore, we can conclude that in hCA XII it seems that no eutomer can be distinguished and that the two enantiomers could both contribute to the high activity.

Ensemble docking on hCA IX – mimic of in-house derivatives.

With the purpose to explain the low activity of compound **1** and **2** on hCA IX, (K_i values of 8440,00 and 5590,00 nM, respectively) we performed the ensemble docking protocol described before using representative structures of hCA IX - mimic. In this case we chose to compare their binding mode with previously reported parent compound **4** that was previously discovered as a potent hCA IX inhibitors at low nanomolar concentration (K_i of 9.4 nM), so that compound **4** proved to be about 1000-fold more potent hCA IX inhibitor when compared to analog compounds **1-2**.

Also in this case we started analyzing the (S) – enantiomers. For all studied compounds the sulfonamide retained the key binding interactions at the bottom of the cavity. Concerning the tails of the molecules, the dimethoxyisoquinoline ring of inhibitors **1-2** were overlapped, whereas the smaller hydrophobic C-1 substituent allows that compound **4** assumed a divergent orientation for which the dimethoxyisoquinoline ring approach the opposite surface of the hCA IX - mimic cavity (Figure 35), generating a more favorable orientation of compound **4** in terms of shape complementarity with the pocket.

Figure 35. Superposition of the (S) enantiomer binding mode of compounds **1** (green sticks), **2** (purple sticks) and **4** (orange sticks) inside hCA IX-mimic binding site (yellow). Interacting residues are represented as thin sticks and zinc ion as a grey sphere. Crucial hydrogen bonds are highlighted by yellow dashes while lipophilic interactions by surfaces.

In detail, compound **4** established several lipophilic interactions at the entrance of the binding-site, mainly between the methyl group and L141, V143, V207, W209 side chains. On the contrary, the presence of the C-1 aryl substituent on compound **1** and **2** induced a different positioning thus causing loss of these interactions, facing just the hydrophilic surface (Figure 35). For inhibitor **2** it was found just a weak contact between fluorine atom and N62.

Considering instead the docked *R*-enantiomers of the three compounds inside hCA IX-mimic and, while compound (*R*)-**4** showed a similar orientation and pattern of lipophilic interaction at the entrance of hCA IX with respect to (*S*)-**4** enantiomer, two exceptions occurred for enantiomer (R) **1** and **2** docked in hCA IX: (a) (R)-1 showed an unusual pose, where no zinc coordination by the sulfonamide group was present, further supporting its weak activity towards hCA IX; (b) compound (R)-**2** assumed the same orientation of compound (R)-**4** but due to the bulk of the C - 1 substituent it did not get deep in the lipophilic cavity (lined by V121, L141, V143, L198, V207 and W209) with the whole tetrahydroisoquinoline scaffold as compound **4** (R/S) did. (Figure 36)
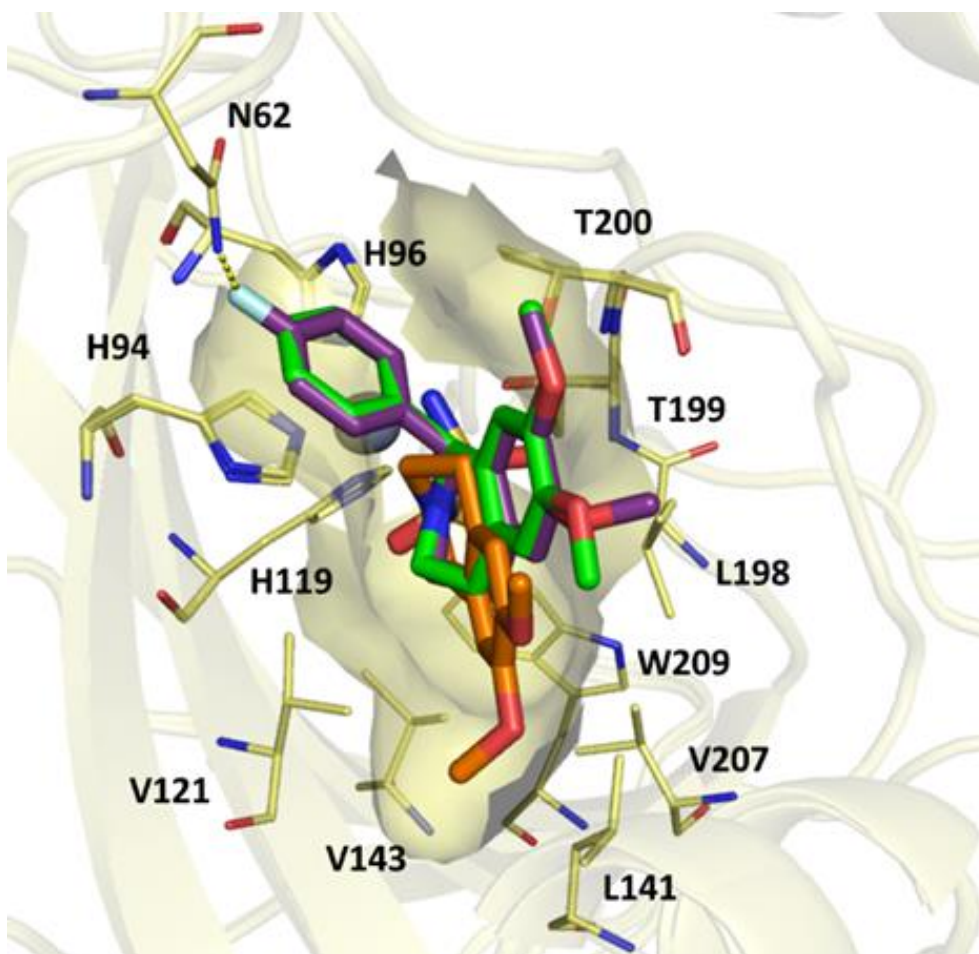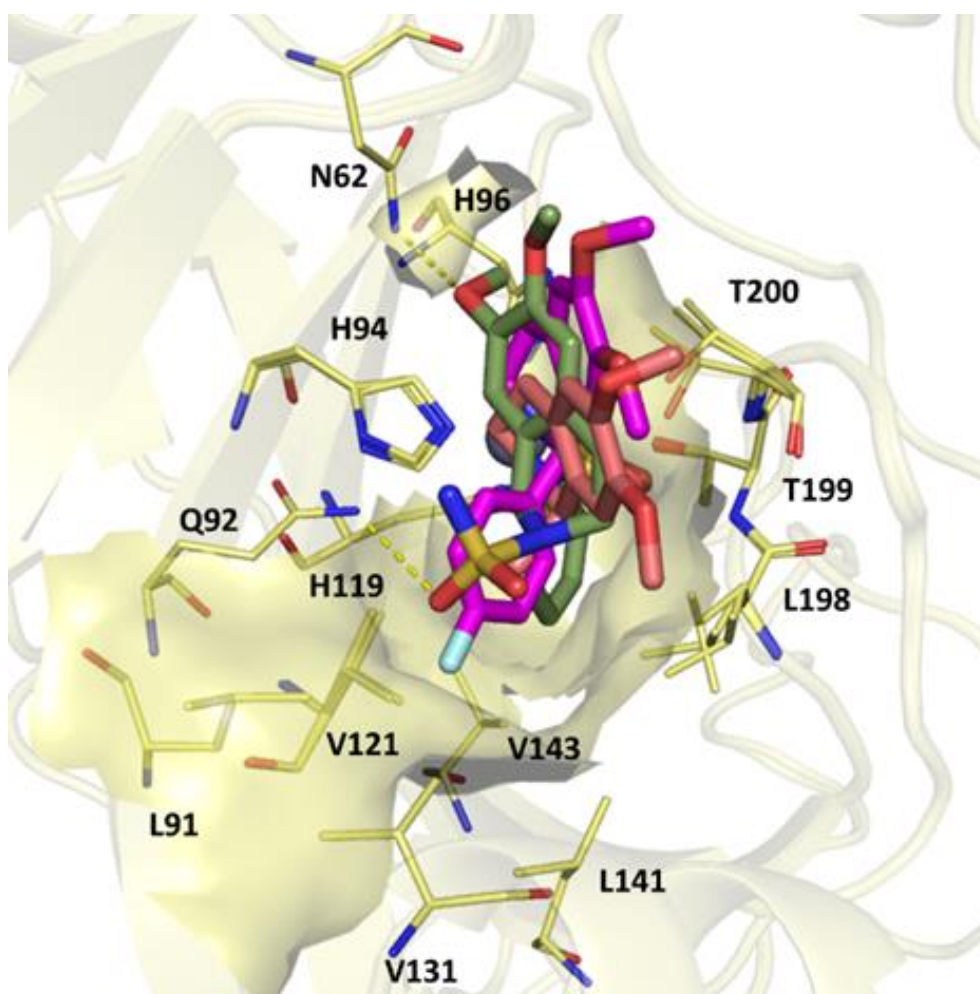

Figure 36. Superposition of the (R) enantiomer binding mode of compounds **1** (smudge sticks), **2** (magenta sticks) and **4** (salmon sticks) inside hCA IX-mimic binding site (yellow). Interacting residues are represented as thin sticks and zinc ion as a grey sphere. Crucial hydrogen bonds are highlighted by yellow dashes while lipophilic interactions by surfaces.

X-ray analysis of hCA II in complex with compounds 1 and 2 and comparison with their hCA XII docking poses

To confirm that compounds **1** and **2** can bind the CA active site through the sulfonamide moiety as classical ZBG, their co-crystal complex with hCA II have been solved by the Institute of

Biostructures and Bioimaging (IBB) of the Italian National Research Council of Naples. For both compounds the S-enantiomers have been solved inside of the cavity. The structural information of the complexes will be deposit into Protein Data Bank.

The docked poses of the two compounds (both R and S enantiomers **1** and **2**) in hCA XII were compared with their respective crystalized S enantiomers in hCA II, trying to understand the missing points in hCA II that led to this different affinity against hCA XII and hCA II.

Figure 37. Superposition of the binding modes of both (R) (hot pink sticks) and (S) (purple sticks) enantiomers of compound **2** and (S) – **2** one (magenta sticks) respectively inside hCA XII binding site (cyan) and hCA II (pink). Interacting residues are represented as thin sticks and zinc ion as a grey sphere. Crucial hydrogen bonds are highlighted by yellow dashes while lipophilic interactions by surfaces.

In the same manner, the X – Ray structures of the S – enantiomers of compounds **1** and **2** on hCA II were superimposed to the one of compound **4** earlier deposited on RCSB Protein Data Bank (PDB code: 3PO6) with the opposite purpose. From the former comparison, at first sight, compound (S) – **2** and its R enantiomer in hCA XII presented an almost overlapped binding mode with the one of

68

the S enantiomers in hCA II. Nevertheless, a key difference stands out: while in hCA II the two methoxy groups seemed meaningless for a proper recognition in this isoenzyme, in hCA XII they were either orientated towards the hydrophilic side of the active site or to S135, forming profitable hydrogen bonds. (Figure 37). Then, making the same analysis on compound **1**, apart from the S – enantiomer in hCA XII which showed a unique binding mode, still forming a rich pattern of H – bonds through the two methoxy groups and hydrophobic interactions through the phenyl ring, respectively with the hydrophilic and lipophilic surface of the enzyme, the same previous assumption can be done. In one case (hCA II) apart from hydrophobic/π – π interaction with H94 and A65, no other interactions were formed by the rest of the scaffold. In hCA XII, as previously described, both lipophilic contacts and hydrogen bonds were involved in the binding of both enantiomers of compound **1**. (Figure 38)
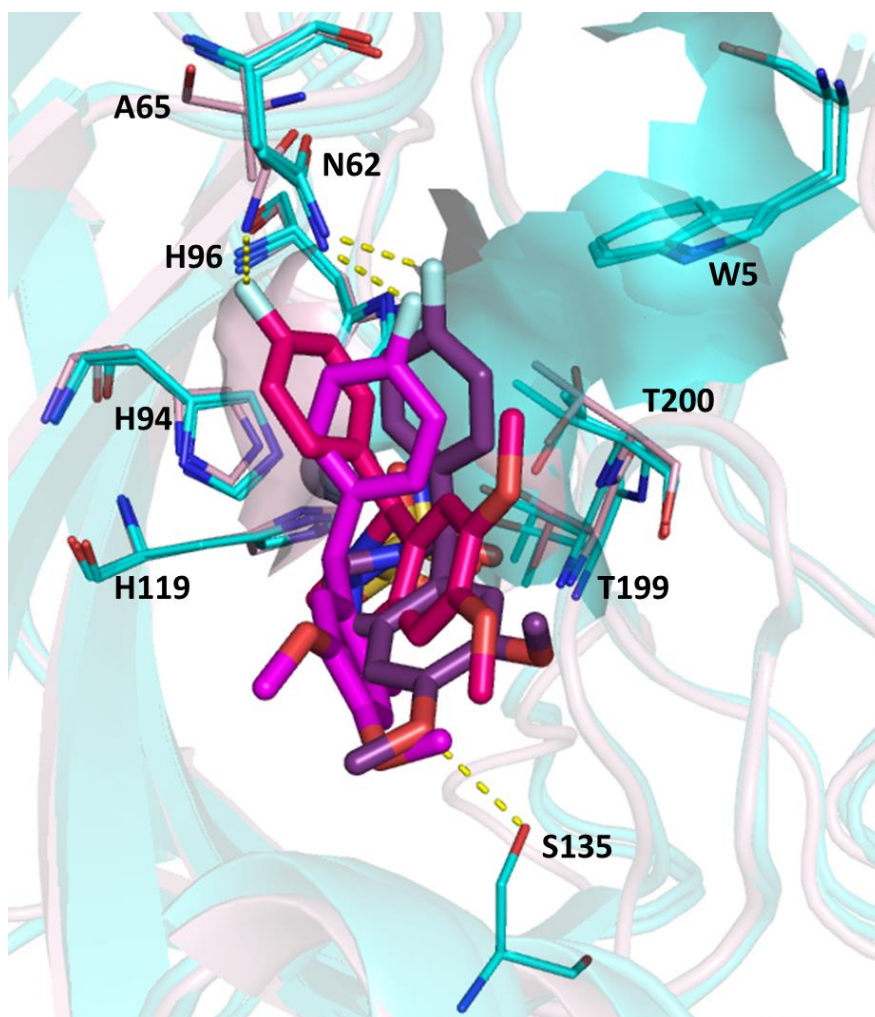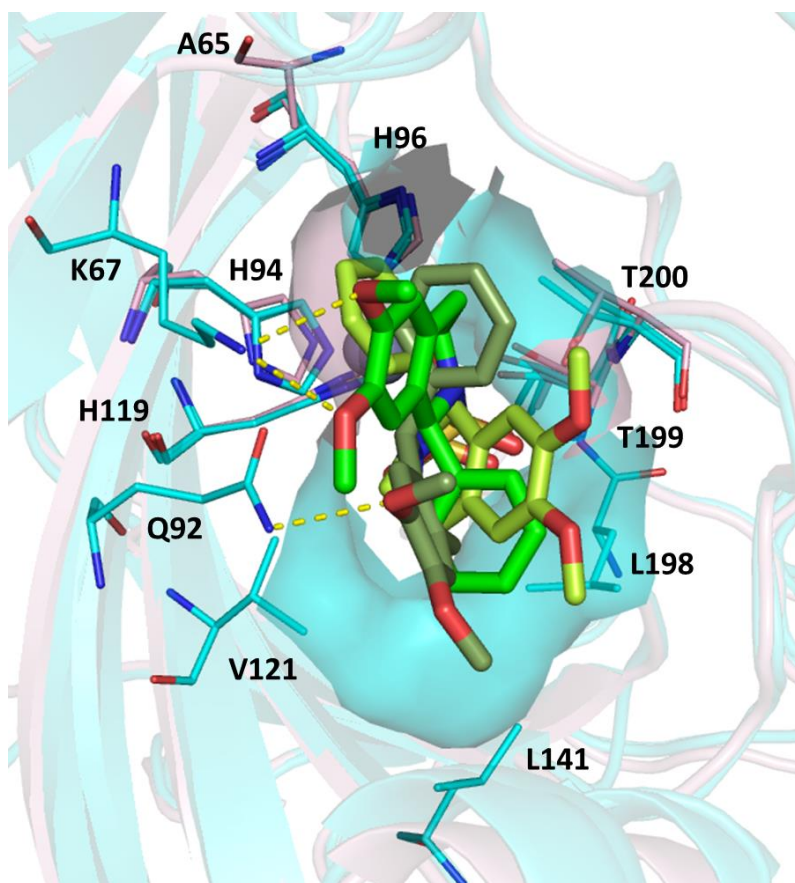

Figure 38. Superposition of the binding modes of both (R) (smudge sticks) and (S) (green sticks) enantiomers of compound **1** and (S) – **1** one (lime sticks) respectively inside hCA XII binding site (cyan) and hCA II (X- Ray)(pink). Interacting residues are represented as thin sticks and zinc ion as a grey sphere. Crucial hydrogen bonds are highlighted by yellow dashes while lipophilic interactions by surfaces.

Taking into account instead the crystallographic pose of compound (S) - **4** in hCA II and superimposing it with the ones of the other two hCA XII inhibitors, a reversed condition is shown. Here, its methyl group forms several lipophilic interactions with the hydrophobic sub – pocket of hCA II (lined by V121, F131, L141 and V143) which orientate the 3,4 dimethoxyphenyl moiety towards the hydrophilic side of the binding site, which hydrogen bond N92 and N67. Conversely, the X-Ray conformations of compound (S) – 1 and (S) – 2 in hCA II showed an overlapped orientation, where just one and lipophilic interaction, described before justifying their weak/non – existent activity on hCA II. (Figure 39)
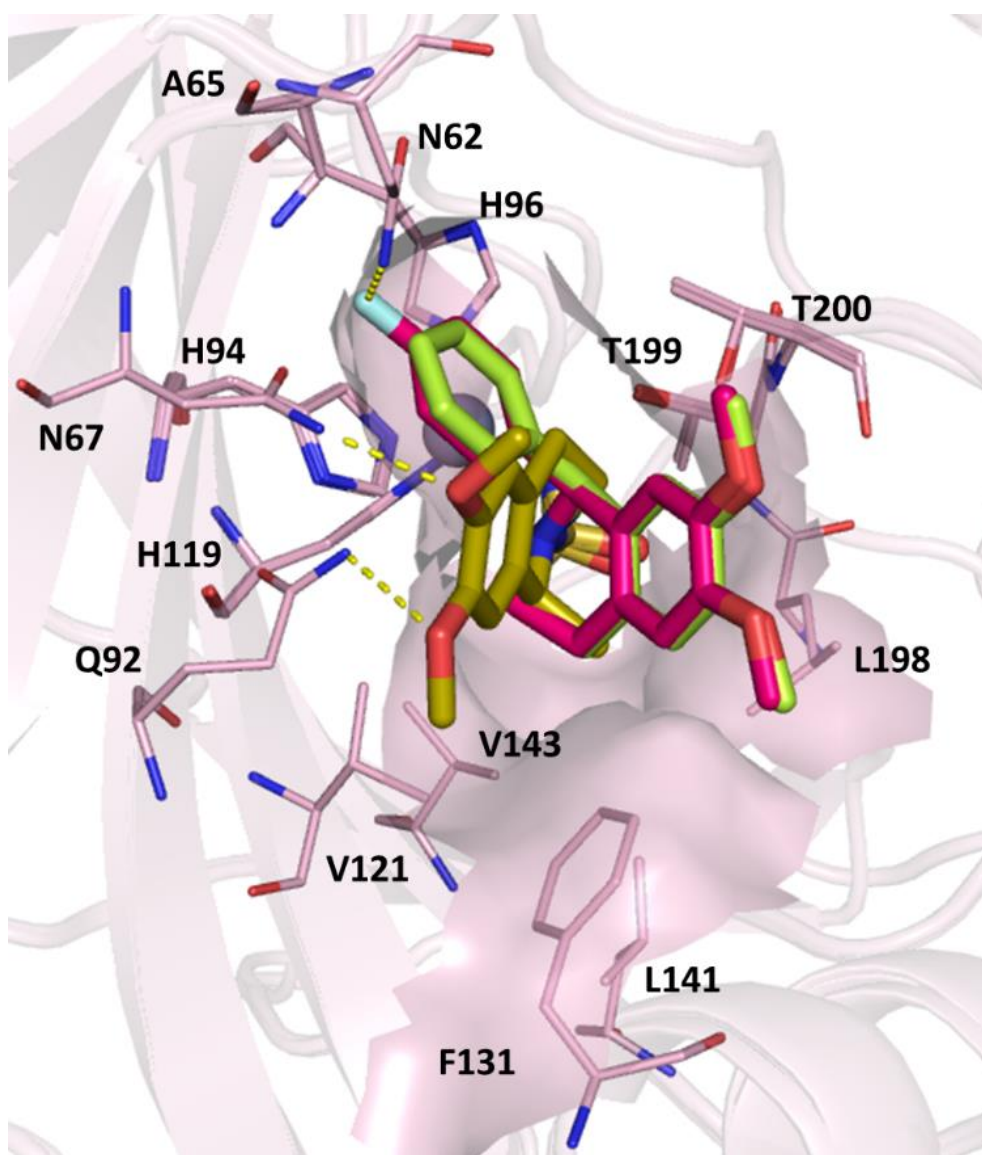
Figure 39. Superposition of hCA II X-Ray structures (pink) in complex with the (S) enantiomers of **1** (lime), **2** (hot pink) and **4** (olive). Interacting residues are represented as thin sticks and zinc ion as a grey sphere. Crucial hydrogen bonds are highlighted by yellow dashes while lipophilic interactions by surfaces.

Binding energy calculation

Binding energy values obtained from MM – GBSA calculation, reflected the inhibitor activity too, further supporting the hypothesis made by the analysis of the minimized docking poses and crystal structures described above. As shown in Table 7, more negative values were appreciated by compound **1** and **2** on hCA XII with respect to the ones encountered on hCA II X - Ray structures and hCA IX – mimic docking complexes.

Table 7. Binding energy values obtained from MM-GBSA calculations of compounds **1** and **2** (both R and S enantiomers) on the three hCA isoforms. Binding energy values on hCA II crystals (column hCA II X-Ray) are available just for the co-crystallized (S) enantiomers Notes: n.a = data not available.

	MM – GBSA ΔG binding energy		
Ligand	hCA II X-Ray	hCA IX - mimic docking	hCA XII docking
1(R)	n.a.	-19.84	-22.68
1(S)	-5.74	-15.46	-20.5
2(R)	n.a.	-11.64	-31.92
2(S)	-8.62	-24.15	-24.28

MD simulation of compound 1 and 2 on hCA XII, IX and II.

Lastly, to further reinforce the speculation on the selectivity of inhibitors **1** and **2** for hCA XII, we performed robust 200 ns Molecular dynamics (MD) simulations on their docking complexes with IX – mimic and XII and on their X – Ray co – crystals with hCA II. This was done in order to evaluate possible differences of the stability, expressed in terms of ligand RMSD values or interaction occurrence along the simulation, of two molecules among the three isoforms.

Figure 40. Desmond Simulation interaction diagram (SID) of compound (S) – **1** of 200 ns MD simulation on hCA XII (A and B) and IX – mimic (C and D) docking complexes and on hCA II X- Ray co – crystal structures (E and F). Protein – ligand contact barplot (left), reporting on the x axis the interacting residue while on y axis is reported the interaction frequency expressed as fraction. The type of interaction established by each residue are characterized according to the colour scheme on top. Values with a fraction exceeding 0.1(100%) occur when multiple type of contacts are formed by the same residue with a ligand or co-factor (e.g. metals), or when the same interaction involves multiple ligand atoms. Plots of the RMSD values along the MD simulations (right), reporting the protein Cα and ligand RMSD values (Å) along the simulation, calculated upon the alignment schematized by the colour coding on top.
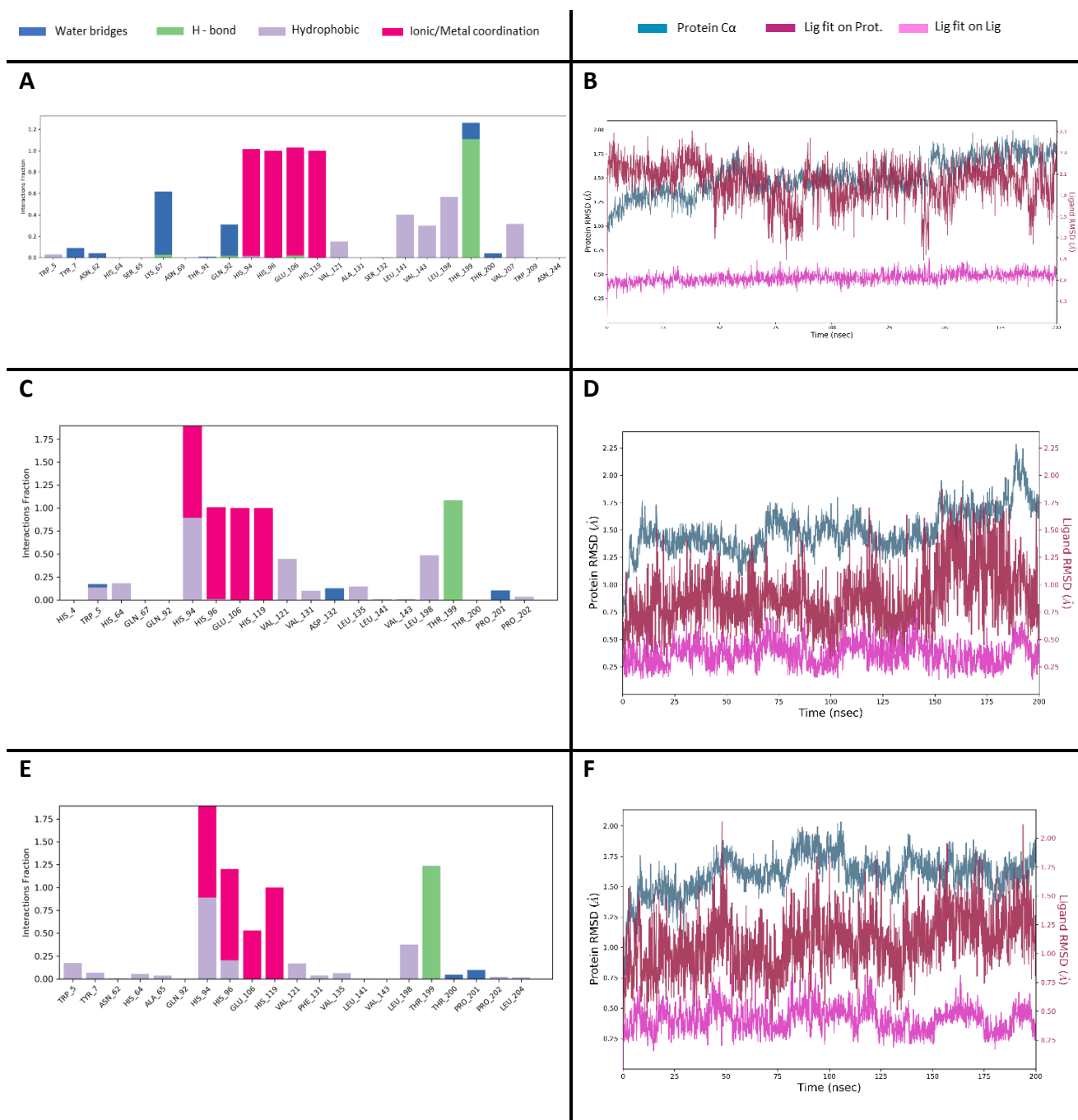
Figure 41. Desmond Simulation interaction diagram (SID) of compound (S) – **2** 200 ns MD simulation on hCA XII (A and B) and IX – mimic (C and D) docking complexes and hCA II X- Ray co – crystal structures (E and F). Protein – ligand contact barplot (left), reporting on the x axis the interacting residue while on y axis is reported the interaction frequency expressed as fraction. The type of interaction established by each residue are characterized according to the color scheme on top. Values with a fraction exceeding 0.1(100%) occur when multiple type of contacts are formed by the same residue with a ligand or co-factor (e.g. metals), or when the same interaction involves multiple ligand atoms. Plots of the RMSD values along the MD simulations (right), reporting the protein Cα and ligand RMSD values (Å) along the simulation, calculated upon the alignment schematized by the colour coding on top.

As result, all the (S)-enantiomers of the two inhibitors stably chelated Zn ion and hydrogen bonded T199 along the whole simulation in all the isoenzymes, apparently displaying no differences among the three isoforms. (Figure 40 and 41 A, C and E)

Nevertheless, both (S) enantiomers retain the hydrogen bond networks (mainly mediated by water bridges) and the lipophilic interactions at the entrance of the binding site of hCA XII already detected in the minimized docked poses. (Figure 40A and 41A)

On the contrary, in the other two isoforms (hCA IX and II) the only consistent interactions were lipophilic, mainly involving H94, and no hydrogen bonds stabilized the docked poses of the two compounds or justified the position of the aryl moiety towards the hydrophilic surface of the enzyme.(Figure 40 and 41 B and C) This is reflected by the ligand RMSD, which despite showing comparable values to the ones of two compounds into hCA XII, show a very irregular slope trend which reflects changes in the position and conformation of the ligands (See Lig fit on Prot and Lig fit on Lig of figure 40 D and F and 41 F).
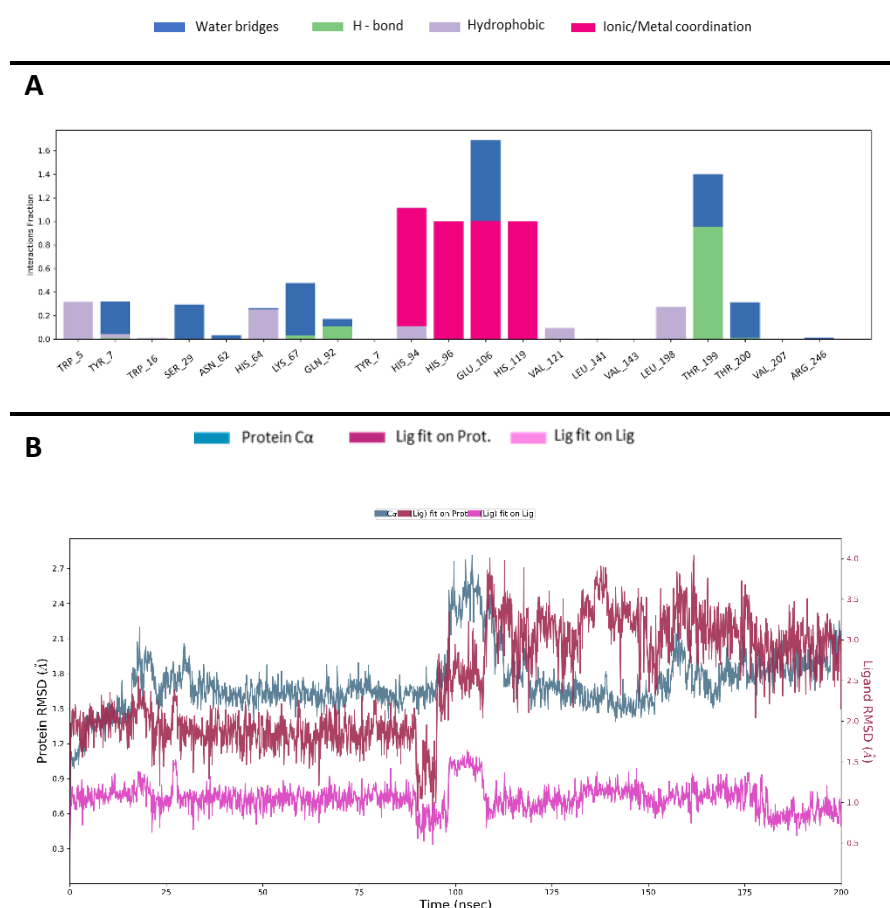
Figure 42. Desmond Simulation interaction diagram (SID) of compound (R) – **1** 200 ns MD simulation on hCA XII. Protein – ligand contact barplot (A), reporting on the x axis the interacting residue while on y axis is reported the interaction frequency expressed as fraction. The type of interaction established by each residue are characterized according to the color scheme on top. Values with a fraction exceeding 0.1(100%) occur when multiple type of contacts are formed by the same residue with a ligand or co-factor (e.g. metals), or when the same interaction involves multiple ligand atoms. Plots of the RMSD values along the MD simulations (B), reporting the protein Cα and ligand RMSD values (Å) along the simulation, calculated upon the alignment schematized by the colour coding on top
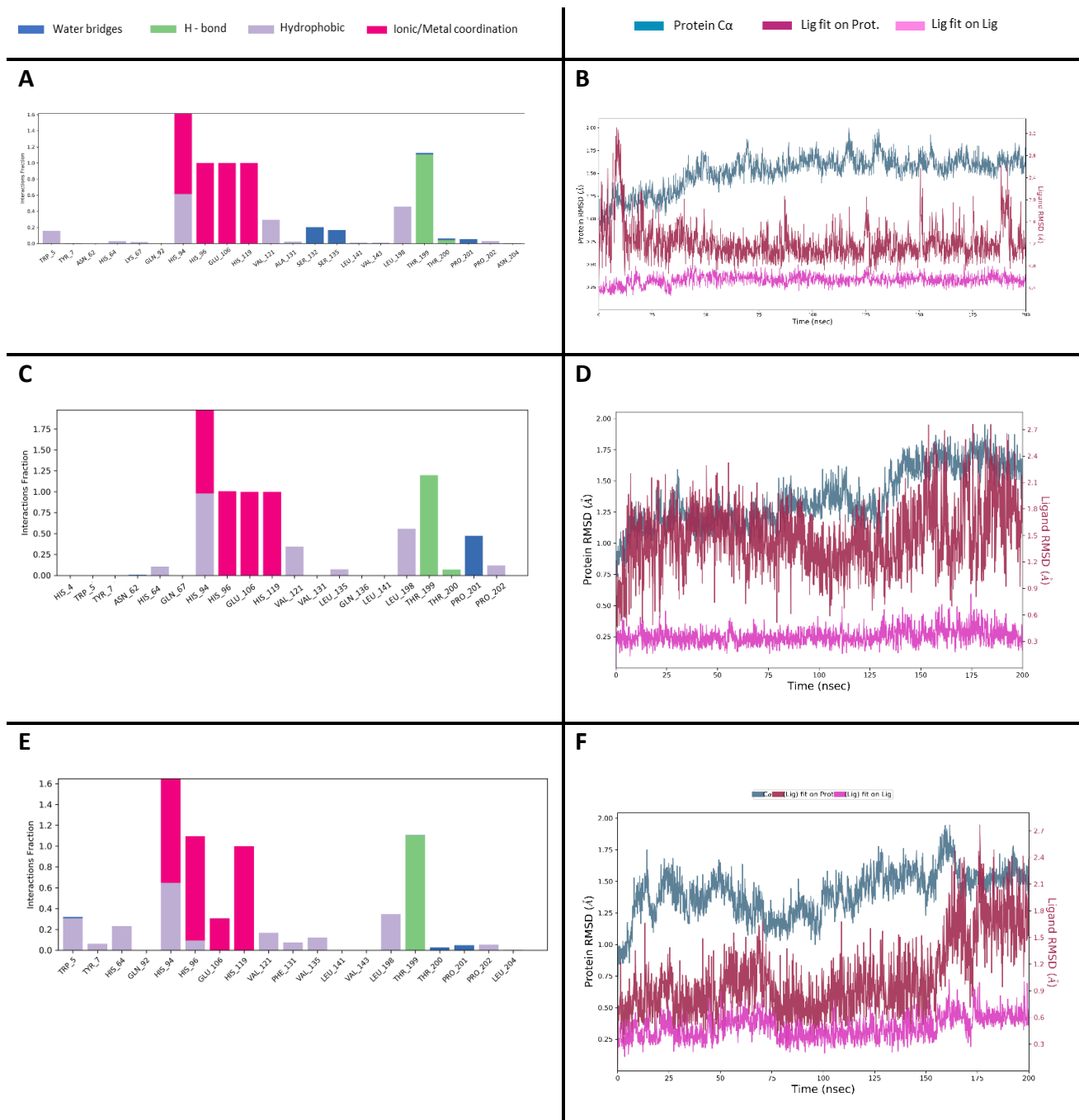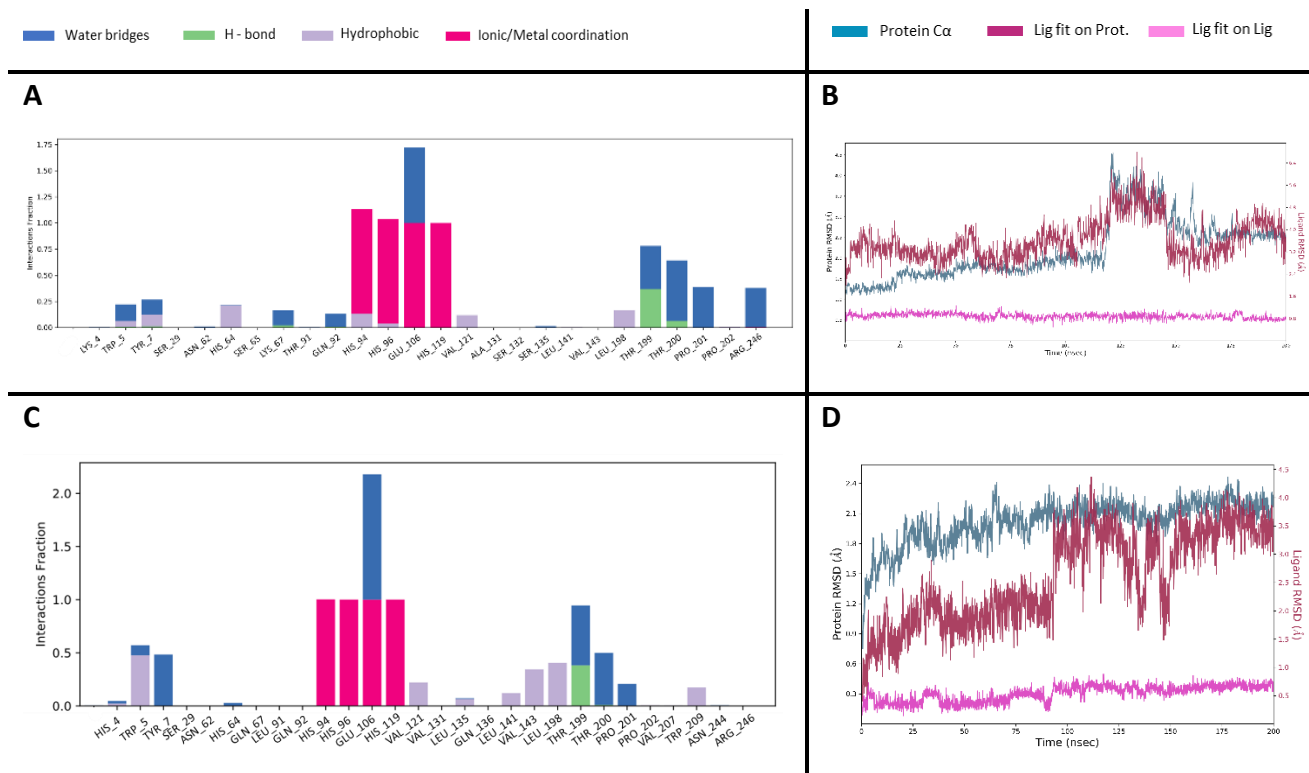
Figure 43. Desmond Simulation interaction diagram (SID) of compound (R) – **2** 200 ns MD simulation on hCA XII (A and B) and IX – mimic (C and D) docking complexes. Protein – ligand contact barplot (left), reporting on the x axis the interacting residue while on y axis is reported the interaction frequency expressed as fraction. The type of interaction established by each residue are characterized according to the color scheme on top. Values with a fraction exceeding 0.1(100%) occur when multiple type of contacts are formed by the same residue with a ligand or co-factor (e.g. metals), or when the same interaction involves multiple ligand atoms. Plots of the RMSD values along the MD simulations (right), reporting the protein Cα and ligand RMSD values (Å) along the simulation, calculated upon the alignment schematized by the colour coding on top.

The MD trajectory analysis was done as well for the simulations of the (R) enantiomers of the two compounds. (Figure 42 and 43) However, it was done just for hCA IX – mimic and XII docking complexes, as no co -crystals formed with these enantiomers so far confirming that they do not bind hCA II. In the same way, no simulation on hCA IX – mimic in complex with compound (R) - **1** were needed, as its docked pose predicted a binding mode where no zinc coordination was found, already not interpretating it as a hCA IX binder. (Figure 42)

Examining the R enantiomers behaviors during the simulations in hCA IX – mimic and XII, interesting results, with regards to the hydrogen bonds formed by the methoxy group, were appreciated.

Compound (R) – **1**, differently from the static pose on hCA XII formed more hydrogen bonds with the hydrophilic surface of the enzyme, mainly contacting K67 as its S enantiomer did. Additionally, due to the interactions of the di - methoxy moiety just mentioned, it pushed the phenyl ring

towards the upper bottom part of the enzyme forming lipophilic interactions with W5 and the proton shuttling histidine (H64), additional to the one with H94. (Figure 42A)

Compound (R) – **2** showed in hCA XII the same pattern of interaction of inhibitor (R) – **1**, despite with a lower frequency along the simulation. (Figure 43A) Concerning its trajectory on hCA IX – mimic, the lipophilic interactions present in docking pose are noticed, although the number of contacts with the hydrophilic side of the active site, seen in its simulation in hCA XII, were missing. (Figure 43A and 43C)

Conclusion

In conclusion, taking together the results from the docking studies, the MM – GBSA binding energy calculations and the MD simulations, we can speculate that both enantiomers should be active on hCA XII, while for hCA II and IX just the S enantiomers should be able to bind them. Nevertheless, even the S enantiomers cannot provide a pattern of interaction in hCA II and IX as rich as the ones they have on hCA XII, since the hindrance brought by the introduction of the aryl moiety lead to a re – orientation of the methoxy groups that lose any profitable h – bond/ water bridge with key residues at entrance of the active site. The same bulk in hCA XII permits instead multiple ligand conformations where non – conserved residues, including K67 and the section A131-S135, are always targeted.

As a future perspective these structural hints might be taken into account to develop a pharmacophore able to merge the multiple binding – modes reported here, involved in hCA XII selectivity, in a unique model, coherently with the well-established tail approach.

2.3.2. Materials and methods

Ensemble docking protocol for hCA IX-mimic and hCA XII

Selection and preparation of protein complexes

From RCSB Protein Data Bank we collected three-dimensional structures of hCA IX-mimic and hCA XII isoforms of hCA. The selection criterion was the collection of the apo-structures or complexes

containing sulfonamides, sulfamides and sulfamates, thus restricting the ensemble to 60 PDBs for hCA IX and the ensemble of 41 PDBs for hCA XII. Then, we discarded 12 PDB of hCA IX-mimic that contained several mutations (< 6) in the catalytic site to respect to the wild-type hCA IX. Moreover, 12 hCA XII structures were discarded as displaying a chimeric sequence so that we reduced this set to 29 structures.

Subsequently, we selected the chain A of each complex; then, we aligned the sequences by multiple sequence alignment using the Multiple sequence viewer in Maestro and the superimposition of the backbones was performed using as reference the apo hCA IX - mimic (PDB 6FJI) and the hCA XII in complex with acetate (PDB 1JCZ). Taking as reference the PDB with the shortest sequence, the N and C termini were truncated.

For hCA IX – mimic the following mutations were carried out thus obtaining structures that possesses the same residues present in the wild-type enzyme active site

Gly132(hCA IX-mimic/hCA II)→Asp (hCA IX wild-type)

Val135(hCA IX-mimic/hCA II)→Leu (hCA IX wild-type)

Cys206(hCA IX-mimic/hCA II)→Gly (hCA IX wild-type)

For the PDB 6VKG and 7MU3 structures, the above-mentioned mutations were present; nonetheless the protein 7MU3 assumed an alternative conformation for Leu134 and Asp131 sidechains. Therefore, we modelled the sidechain of these two residues in the remaining 46 PDBs through the rotation of the sidechain dihedrals, taking the orientation of the PDB 6VKG as reference conformation. In order to avoid clashes and overlaps on the modeled structures, a minimization of these two sidechains has been performed during the final step of the protein preparation. For PDB 7MU3 structures, we maintained both the sidechain conformation with the highest occupancy in one case (Leu134) and alternative occurrence possessing the same conformation present in the PDB 6VKG (Asp132), based on the consideration that both conformations possessed an occupancy value of 0.5.

Next, each complex was processed by using the Protein preparation workflow tool implemented in Maestro[59] as detailed below. In "review and modify" panel, we removed alternates with the lowest occupancy for each residue and detected co-crystalized ligand and co-factors. The "preprocess" step was carried out to achieve the following tasks: (a) assign bond order by using the CCD database; (b) add/replace hydrogens; (c) create zero-order bonds to metals; (d) convert

selenomethionine to methionine residue; (e) fill in missing loops (using Prime); (f) generate het states (with Epik) setting a pH range of 7.4 +/- 2.0; (g) fill in missing side chains (with Prime); (h) cap termini. The "diagnose and analyze" step allowed us to check issues as overlaps, missing atoms, wrong valences and to check the protonation states assigned by Epik in the previous step to the ligands and to the histidine residues; in the case of detection of multiple states for the ligand, we kept the first one for which the sulfonamide group displayed the nitrogen atom in deprotonated form able to coordinate the zinc ion; histidine protonation states were also adjusted in some cases to have the same protonation state in all the protein generating the same topology in each structure; no adjustment was needed in all the hCA XII complexes, while for hCA IX-mimic His protonation states were set as follows: His 4 = HID; His 10 = HID; His 15 = HID; His 17 = HID; His 36 = HID; His 64 = HID; His 94 = HID; His 96 = HID; His 107 = HID; His 119 = HIE; His 122 = HID.

Finally, the side chains of the above-mentioned mutated residues (Asp132 and Leu135 of hCA IX-mimic) were minimized using the 3D builder with OPLS_2005 force fields and the ligands were extracted from the complexes.

PDB clustering

After the extraction of the ligands from the corresponding complexes of both hCA IX-mimic and hCA XII, we sampled a unique centroid from the superimposed ligand heavy-atoms using Discovery Studio. Then, by means of VEGA ZZ software, we renumbered the residues of each protein structure to generate structures possessing the same topology; in detail, we started from 4 for hCA IX-mimic and from 3 for hCA XII; then, we identified the residues at 10Å from the centroid coordinates present in the PDB used as reference for the initial superimposition (PDB 6FJI for hCA IX-mimic and PDB 1JCZ for hCA XII; the selected residues are listed below:

hCA IX-mimic: Trp6; Tyr8; Leu61; Asn63; His65; Ser66; Gln68; Thr70; Leu92; Gln93; Phe94; His95; His97; His120; Leu121; Val122; His123; Trp124; Val131; Asp132; Ala134; Leu135; Leu141; Val143; Ser197; Leu198; Thr199; Thr200; Pro201; Pro202; Leu203; Ala204; Gly206; Val207; Trp209;

hCA XII: Trp5; Tyr7; Asn65; His67; Ser68; Lys70; Leu71; Thr89; Gln90; Leu91; His92; Leu93; His94; Glu105; His118; Ile119; Val121; His122; Tyr123; Ala131; Ser132; Ser135; Leu141; Ala142; Val143; Ser197; Leu198; Thr199; Thr200; Pro201; Pro202; Cys203; Asn204; Thr206; Val207; Trp209;

Finally, we merged all the PDB structures in VMD[60] software as a unique trajectory, saved as dcd file, and we performed RMSD clustering analysis using TTClust tool.[58] The RMSD matrix was created considering backbone and sidechain atoms of the residues just listed above. Auto-clustering was employed for the calculation and ward was set as clustering method (default). Frame was set as unit for the timed barplot. The representative frame of each cluster was then selected for our docking studies (See Figure 31 and 32).

Ensemble docking setting

As ascertained the conformations of the binding site for hCA IX-mimic and hCA XII through the clustering methodology, we employed selected PDB structures for our ensemble docking studies; these proteins corresponded to the representative frame for each cluster.

PDB codes of hCA IX – mimic representative structures	
Cluster 1	6OUI
Cluster 2	7JOB
Cluster 3	4RIV
Cluster 4	7JOC
Cluster 5	7K6X

PDB codes of hCA XII structures	
Cluster 1	4KP8
Cluster 2	6R71
Cluster 3	7PUV

By using the default settings of the Glide Receptor grid generation tool, we generated a grid based on the co-crystallized ligand for each of the above-listed PDB structures.

All the ligands were initially sketched as mol files with ChemDraw, the structures were merged into one sdf file, and then minimized 3D coordinates were created using LigPrep; the chiralities were retained when specified; otherwise, we created a maximum of 32 stereoisomers, generating possible states (with Epik) at a target pH of 7.0 +/- 2.0 and adding metal coordination states. For each ligand the states with lowest metal state penalty and the sulfonamide nitrogen deprotonated

were selected for our docking studies. Then, the following were applied for ensemble docking using the Glide Virtual Screening workflow (Vsw)[61]:

- Dock using Glide SP
- Dock flexibly
- Generate a maximum of 20 poses per ligand
- Post-minimize docking poses
- After docking, keep 100% of the docked ligands
- Retain all good scoring states

In the case of docking into multiple receptor grids using only the SP protocol, the Glide Vsw returns by default the pose with the best (the most negative) Glide SP score and the ensemble receptor associated with the selected pose.

The fine-tuned settings reported above belongs to a validation based on re-docking and experiments conducted evaluating the ability to reproduce the native conformation of the ligands co-crystallized on the 48 and 29 protein structures clustered; the procedure employed the representative conformations, that have been obtained by the clustering procedure. From the validation set of hCA IX - mimic, we excluded the PDB 6FJI since it contained the apo – protein and PDB 6FJJ, as it presents the same ligand with the same conformation of PDB 4RIV. We retained the ligand co-crystallized on PDB 6GCY, in view to the fact that regardless it presents the same ligand of PDB 4RIU, a different conformation/binding mode in the two structures is show. For hCA XII we discarded just the PDB 1JCZ, as it represents as well the apo-protein.

We considered the method successful if more than the 50 % of the selected docking poses reproduce the X-Ray conformation with an RMSD value ≤ 2.6 Å. (See validation report in Table 6A and 6B of Result and discussion).

MM – GBSA binding energy calculation

Docking complexes obtain from the Vsw protocol were firstly refined using the Prime refine complexes panel, performing a local optimization of the residues at 5 Å from the ligand centroid and employing an implicit VSFG water model and OPLS4 forcefield on Schrödinger Suite. Apart from the residues flexibility, which were kept fix, the same water model and forcefield were set during binding energy calculation. Apart from collecting the ΔG bind values, the results were saved

as well as PDB and employed for interaction analysis and binding mode comparison using LigandScout and Pymol software respectively.

MD simulation on hCA XII, IX – mimic and XII

The refined complexes obtained from the MM – GBSA binding energy calculation and the hCA II X – Ray structures of compound **1** and **2** (R/S) were again submitted to the "Protein Preparation workflow" as described in the "*Selection and preparation of protein complexes*" , additionally refining the polar hydrogen orientation through the "Optimize hydrogen – bonds" panel, although keeping fix the protomers and tautomers of H64(proton – shuttling histidine) and H94, H96 and H119 (Zinc coordinating – histidines).

MD simulation were performed on Desmond software (2021). An explicit 10 x 10 x 10 orthorombic TIP4PEW water box was generated for each complex submitted to the MD simulation. Na^+ and Cl^- counterion were added after charge calculation, as well as an additional 0.15 M salt buffer of the same ions. Also in this case OPLS4 forcefield were employed.

A 200 ns MD production phase using NPT ensemble with Martyna – Tobias – Klein barostat and Nose -Hoover chain thermostat was performed on the systems just prepared. The default Desmond protocol was used for equilibration and relaxation of the systems. Atom coordinates during production step were collected each 100 ps obtaining ≈ 2000 frames per simulation.

PART II

Chapter 3: Targeting Human Tyrosinase for Melanogenesis Disorders: From Hyperpigmentation to Parkinson's disease

3.1 Melanine Biosynthesis and Associated Disorders

Melanogenesis represent the various biochemical pathways determining melanin pigment production. Multiple biosynthetic schemes of melanin were depicted, as up to two type of melanin polymers can be distinguished in human.(Figure 44) [62] These include:

- Eumelanin is an insoluble black/dark brown pigment which is composed of 5,6 – dihydroxy - indole or 5,6 – dihydroxy-indole -2- carboxilic acid units.

- Pheomelanin instead is a soluble orange/yellow pigment formed by benzothiazine or benzothiazole monomers

Eumelanine
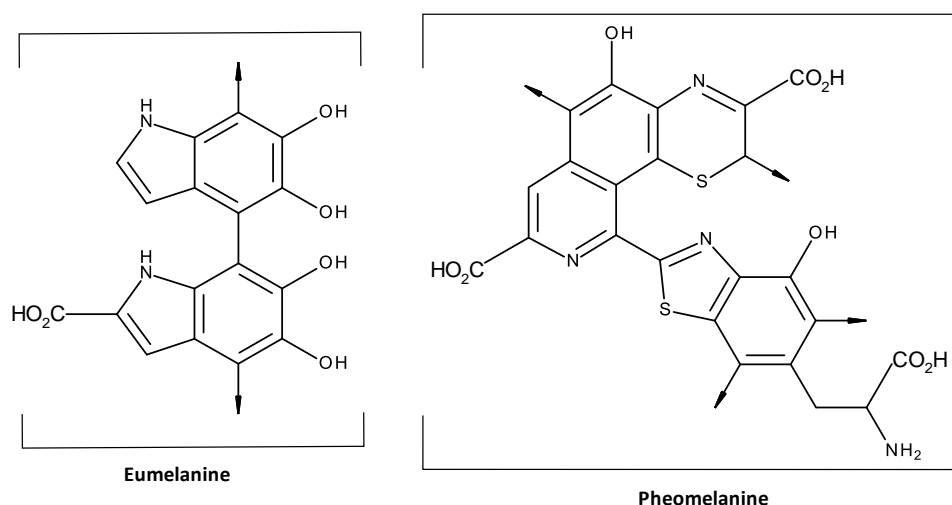
Pheomelanine

Figure 44. Examples of core units of Eumelanine (left) and Pheomelanin (right) polymers. Arrows indicate possible attachments to the rest of the polymer.

Both are majorly distributed in skin, hair and eye, determining their colour. In detail, two main types of cells differentiated from the neural crest multipotent ones, melanocytes and keratinocytes, are characterized by the presence of the two pigments. Specifically, keratinocytes respond to UV radiation(UVR) damage activating a complex signalling process involving i) the release of α -MSH which bind its extracellular receptor in the melanocytes and ii) stimulate cAMP/CREB intracellular pathway which promote the transcription of several enzyme and

regulators of melanin production in the melanocytes through the microphtalmia – associated transcription factor (MIFT), which after maturation is given back to the keratinocytes, preventing the tissue damage from UVR. (Figure 45) [63, 64]

Figure 45. Role of MITF in melanogenesis cascade in human skin. It is represented by the interaction between a melanocyte and several associated keratinocytes, so called epidermal melanin unit. MITF plays a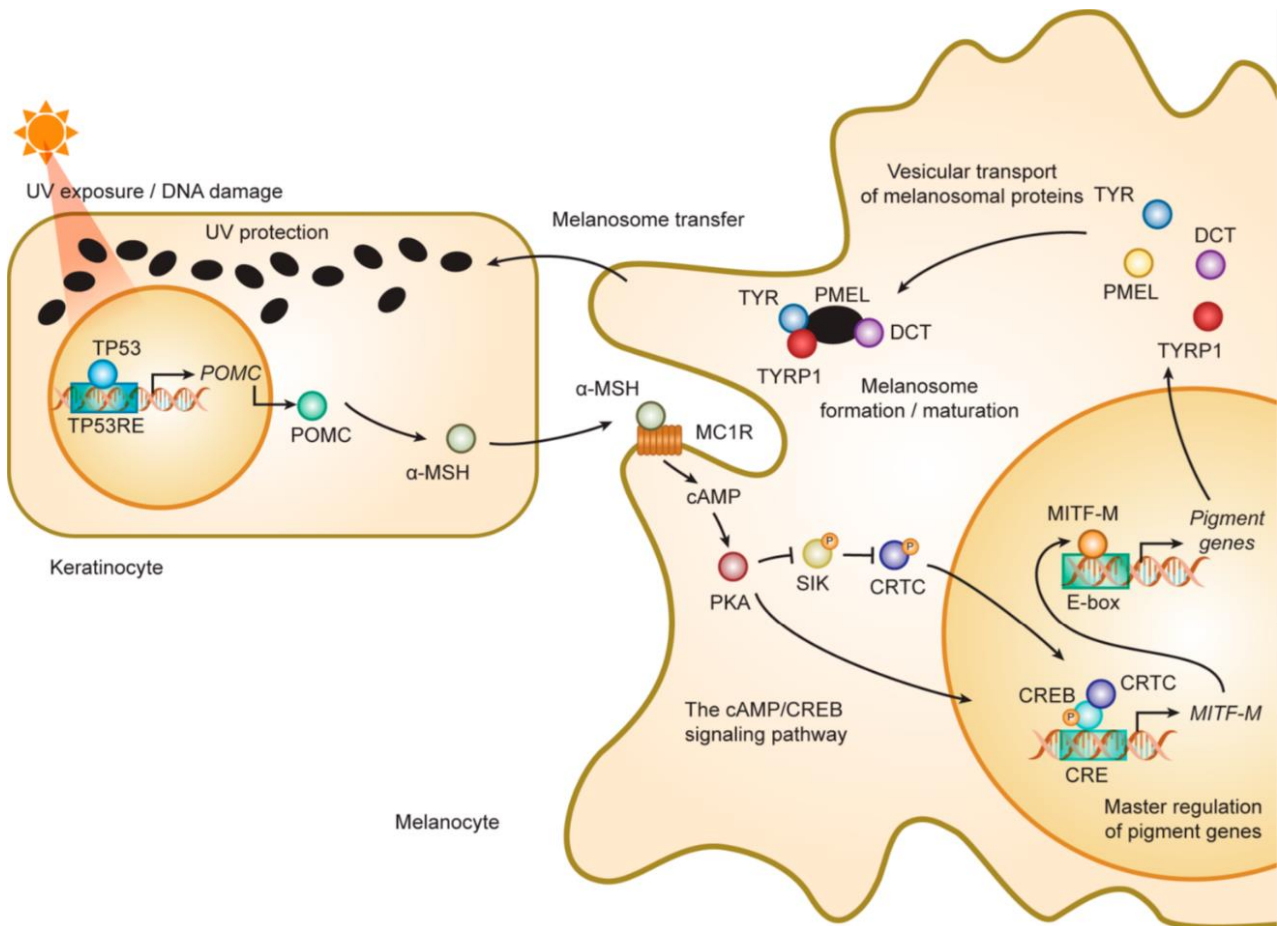 master role in the cascade process for the activation/differentiation of the melanocyte followed by the induction of melanogenesis cascade such as during UV-induced tanning reaction. UV damages DNA in keratinocytes. DNA damage activates TP53 that initiates the transcription of POMC. POMC is cleaved into peptides including α-MSH. α -MSH secreted from keratinocytes binds MC1R and increases cAMP in melanocytes. PKA activated by cAMP activates CREB transcriptional activity in two ways: (i) Phosphorylate CREB; (ii) inhibiting SIK, a negative regulator of CREB co-activator CRTCs, by phosphorylating SIK. CREB activates the transcription of MITF-M. MITF-M activates the transcription of pigment genes including TYR, TYRP1, DCT, and PMEL. Image take from ref. [63]

A specific organelle, the melanosome, is designated for the synthesis and storage of melanin, and according to its maturation and the type of melanin produced presents differences in shape and colour along its maturation process. At the end of the maturation the eumelanosome is ellipsoidal and black, presenting a lactice – like internal substructure, while the pheomelanosome is round and red with granular inside. Although, both present the enzymes involved in melanin synthesis anchored to their membrane. (Figure 46) [63]
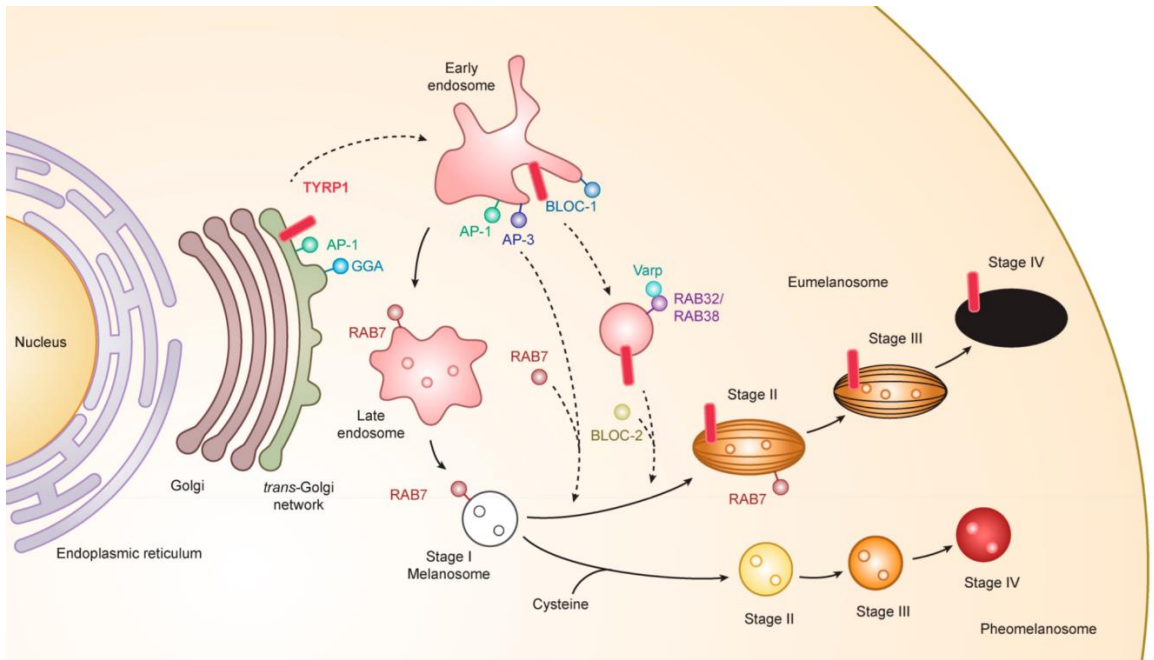
Figure 46. Melanogenesis and intracellular tracking for melanosome biosynthesis. MITF activate melanogenesis by inducing the transcription of pigment genes such as TYR, TYRP1, DCT, and PMEL, leading to their transport from the trans-Golgi network to the early endosome and then to the late one to form the melanosomes. Melanosomes have four maturation stages that differ in shape and amounts of melanin pigments. TYRP1, AP-1 and GGA play key roles in the sorting process of export from trans-Golgi network via early/late endosomes to stage I melanosomes by two other mechanisms: (i) BLOC-1/RAB32/RAB38/Varp/BLOC-2; (ii) AP-1 or AP-3. RAB7 is required for the stage I melanosome formation and the TYRP1 sorting from early/late endosomes to stage I melanosomes. Abbreviations: AP, adaptor protein; BLOC, biogenesis of lysosome-related organelles complex; GGA, Golgi-localized γ-ear-containing ADP-ribosylation factor-binding protein. Image taken from [63]

Figure 47 shows the various biosynthetic steps bringing to the formation of the two pigments. As visible, L – Tyrosine, the initial precursor of melanin can take several routes and lead several products. Some of these were properly confirmed experimentally, while others where just hypothesized and require further validation.
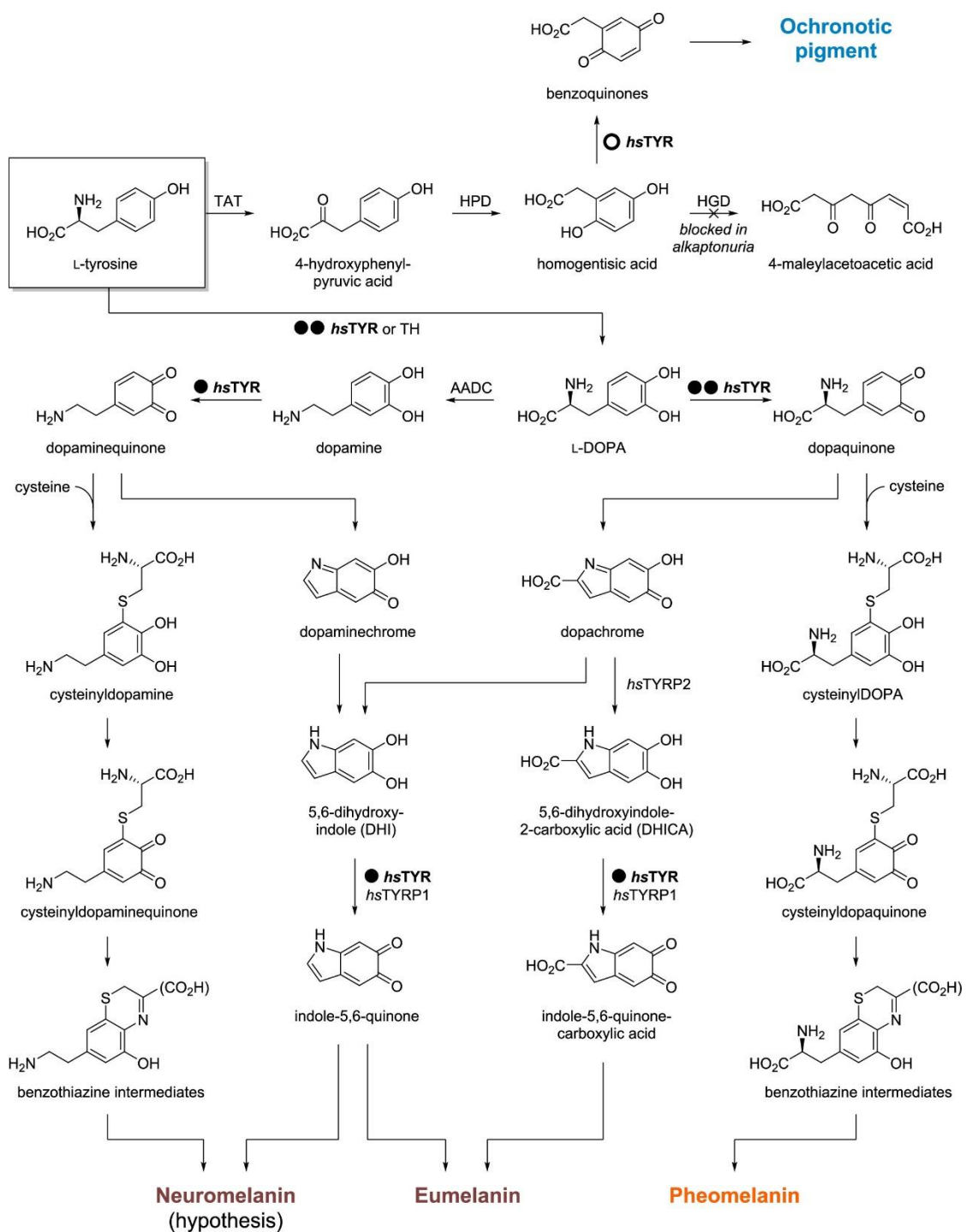
Figure 47. Different L – tyrosine pathways related to melanogenesis. Reaction catalyzed by tyrosinase(hTYR) were marked according to the number of experimental evidences: (●●) demonstrated; (●) suspected; (○) hypothesized. Image taken from [62]

Nevertheless, two steps are the rate limiting ones in both eu- and pheo- melanin biosynthesis: the oxidation of L – Tyrosine in L – DOPA (tyrosine hydroxylase or monophenolase) and the subsequent one in L – dopachrome (DOPA oxidase or diphenolase). The two are catalysed by the same enzyme, Tyrosinase (commonly known as hTYR or hsTYR), thus its inhibition lead to complete disruption of the pigment production.

In view of this, several diseases related to pigmentation disorders are related to Tyrosinase activity. They can be classified into three main classes of disorders: hypopigmentation diseases, hyperpigmentation ones and pathologies with mixed hypo and hyper pigmentation, then subdivided into congenital or acquired. A most famous example of hypopigmentation is Albinism or oculocutaneous Albinism, in which suppression of gene OA1 or OCA1 lead in one case to lack of melanosome maturation or to hTYR monophenolase activity loss. (10.3390/ijms2117612) [62]

Regarding hyperpigmentation, hTYR results one of the main attractive target, as being involved in several disorders such as solar lentigo, melasma, congenital melanocytic naevi, erythromelanosis follicularis faciei et colli, erythema dyschromicum perstans, or postinflammatory hyperpigmentation. These diseases, despite not very frequent or life threatening, can determine a very stressful condition in patients due to the disfigurements, as they may experience several psychological problems related to self – acceptance and aesthetic.

Considering more dangerous conditions, relationships between hTYR activity and melanoma were found. Although melanin physiological role is to protect as well the DNA from UVR damage, a different behaviour in melanoma cells regarding melanin storage has been documented: while in the case of melanocytes melanin accumulation is prevented by its transport to keratinocytes, in the case of melanoma cells they keep retaining melanin, then worsening the patitent survival. Additionally, targeting melanin production in melanomas make the neoplastic cells more susceptible to either radio and chemotherapy. As confirm, melanoma cells depigmented by the hTYR inhibitor phenylthiourea resulted more sensitive both to radiotherapy and to cyclophosphamide. [62]

Despite being more present in the tissues/organs previously mentioned, melanogenesis occurs as well in other less predictable tissues. Indeed a third type of melanin, Neuromelanin, differing from the previous for its tissue distribution, was also identified, specifically in the Sustatia nigra region in the CNS, configuring hTYR as intersting target for Parkinson's disease (PD) treatment. A discussion is still open regarding the involvement of hTYR in neomelanin production, since few mRNA encoding hTYR genes was found in the CNS and a major role is given to Tyrosine hydroxylase(HT). Nevertheless, different experimental data suggest that. Firstly overexpression of hTYR in rats led to the accumulation of neuromelanin and subsequent age dependent PD development. Then, correlations were found between cutaneous melanoma and PD, as this type of cancer has a major

incidence with respect to other type of tumors in people affected by PD, thus supporting that the ectopic production of melanine has detrimental effects on CNS. [62]

An additional pathway of L - Tyrosine is shown in Figure 47, where L -Tyrosine is converted in 4 – maleylacetoacetic acid, passing through the formation homogentisic acid (HGA) intermidiate. People presenting a mutation of the homogentisic acid dehydrogenase (HGD) accumulate homogentisic acid intermediate which is then oxidated into benzoquinone that forms the ochronotic pigment. Its formation leads to a blue pigment deposition in skin, tendons, cartilages, eyes, ears and finally tissue destruction. Hypothesis regarding the possible catalysis of HGA oxidation, being a suitable target for treatment of this rare pathology. [62]

As just described, Tyrosinase configure as fascinating target for the treatment of several disease, primarily involving cosmetics, then skin cancer field, neurodegeneration and finally rare disorders. Additionally, the employment of Tyrosinase inhibitors were also suggested for the treatment of fungal infections, and well – established agents in food industry for managing fruit/vegetables browning.[65, 66] In the following section a more detailed overview of Tyrosinase architecture belonging to humans but also other organisms are given. In the same manner, some potent inhibitors of hTYR and the differences in their assay data with respect to the one of other type of enzymes having Tyrosinase activity are also reported.

3.2. Characterization of Tyrosinase and Structural Differences Between Human Tyrosinase (hTYR) and Other Type 3 Polyphenol Oxidase (PPO3)

As anticipated in the previous paragraph, Tyrosinase catalyses the two rate limiting steps of melanin biosynthesis that consist in the oxidation of L – Tyrosine into L – DOPA and the subsequent oxidation of L – DOPA into L – dopaquinone, distinguishing a monophenolase activity and diphenolase activity. Precisely, the monophenolase activity represent the oxidation of monophenols (as L – Tyrosine) in ortho position, while the diphenolase activity oxidate o – diphenols into o – quinones. The two reactions may occur at the same time, as three states of the enzyme active site are characterized: a de -oxy form where no substrate is binded, an oxy form that binds both mono - and di - phenols and a met form that present the monophenolase oxidation transition state and bind as well diphenol substrates. [62]
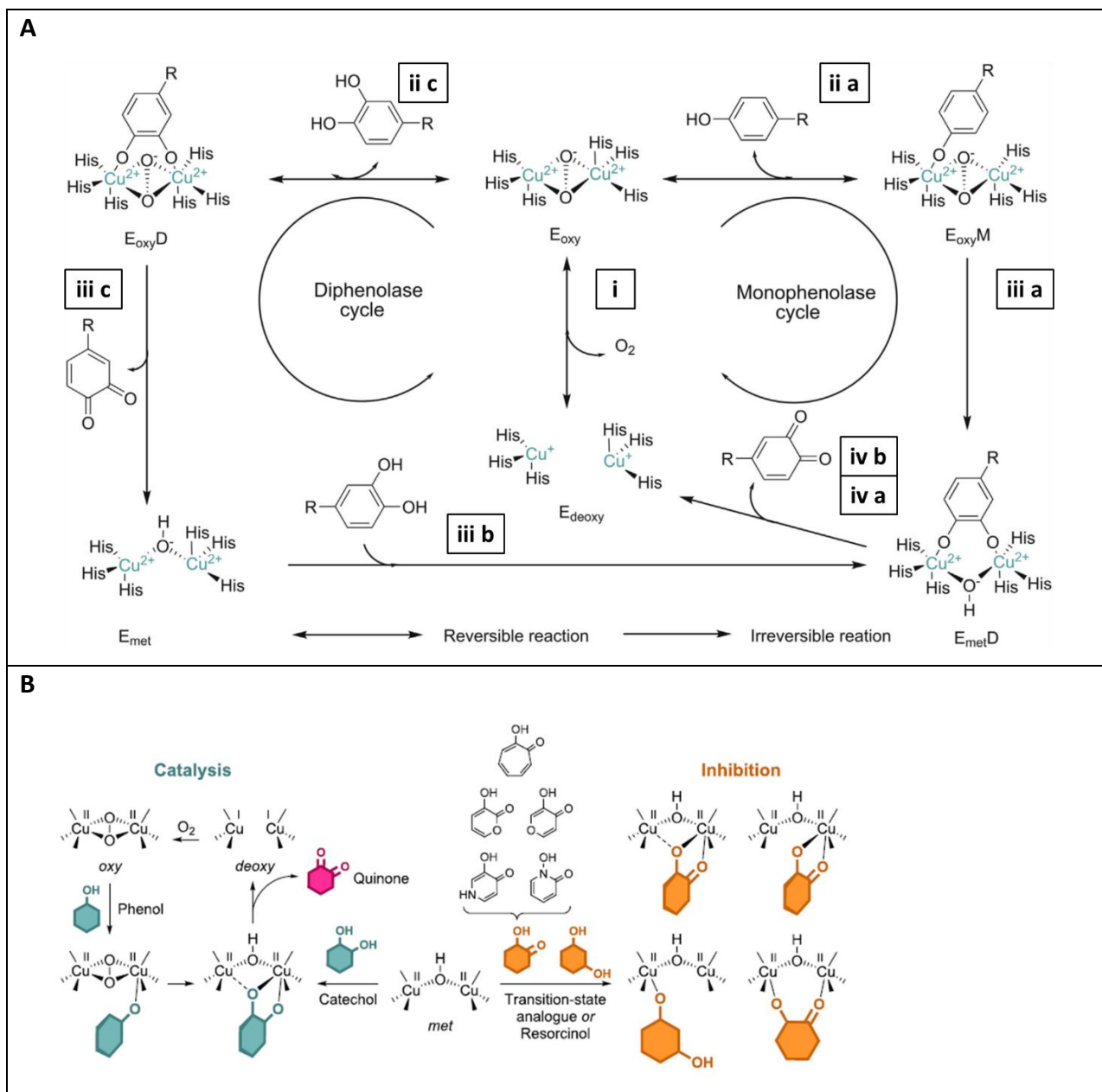
Figure 48. (A) Catalysis mechanism of Tyrosinase of mono and di – phenolase activity. Image taken from ref. [67] and modified with labels of our text (i-iv; a, b, c). (B) Schematic representation of catalysis vs reversible inhibition of Tyrosinase. Taken from ref. [62]

Resuming briefly, three ways can described (a, b or c), in which the substrates, enter chelating the copper ions, in the two catalytic cycles (monophenolase or diphenolase) : i) a reversible step were the de - oxy form binds O_2 and switch to the oxy – form; ii a) a reversible step were the oxy form binds the monophenol substrate; iii a) an irreversible oxidation of the monophenol to the diphenol intermediate leading to the met - form; iv a) an irreversible oxidation of the intermediate to quinone releasing the de – oxy form of the enzyme; or iii b) an irreversible binding of the met – form by a diphenol substrate which is, iv b) oxidated to quinone restoring the de- oxy form of the enzyme, or finally ii c) the diphenol substrate reversibly binds the oxy – form and is iii c) irreversibly oxidated to quinone releasing the met – form which bind another diphenol substrate following the

steps iii b) and iv b)(Figure 48A). [67] Reversible competitive inhibitors of human Tyrosinase, generally bind the met – form coordinating one or both copper – ions. (Figure 48B) [62]

To the structural point of view, Tyrosinase is a type – 3 copper enzyme, presenting two copper ions and three histine residues that chelate each metal ion together with the substrate oxygen in a tetrahedral geometry. [68] (Figure 49C)

Apart from humans, several organisms produce melanine, indeed several enzymes presenting tyrosinase activity belong to different organisms including bacteria, fungi and plants. Among the most famous we can enumerate the one from B. Megaterium (bacterium, PDB 3NM8), from A. Orzyae (fungi, PDB 4J3P), from I. Batatas (sweet potato, PDB 1BT3) and the one from A. bisporus (white button mushroom, PDB 2Y9X), whose structure was fully characterized, distinctly from hTYR for which the 3D structure is not available yet. They all present a N- terminal domain, a C – terminal domain and a central catalytic domain presenting four alpha- helixes where the di- copper center is inserted. This latter is well conserved also in hTYR. [68] Nevertheless, the whole architecture of human enzyme present, in terms of subcellular location, topology and sequence, several differences with the respect to the other tyrosinases.

Taking as an example the tyrosinase from A. bisporus (AbPPO3 or commonly known as AbTYR), which is currently the most used experimental model for screening purposes, due to its low cost in comparison with the human enzyme which is more difficult to express, AbTYR presents several dissimilarities. Firstly, the subcellular location and the topology of the two enzymes differ: AbTYR is a cytosolic tetramer, unlike hTYR which is a monomeric protein bound to the melanosome membrane.(Figure 49A and 49B) Moreover, they share a low sequence identity (23 %), which is also partially reflected in their binding site. One of the most relevant difference is the presence in AbTYR of a thioether bond between C83 and H85, absent in the human enzyme. (Figure 49C and 50B) [62]
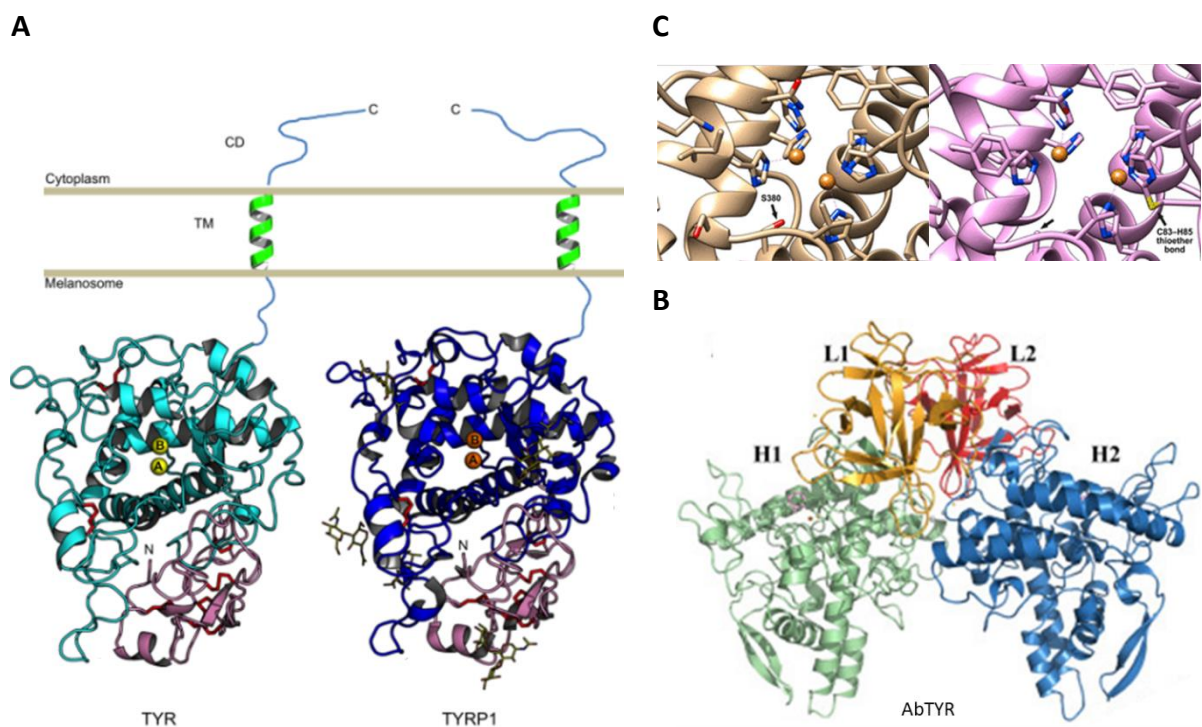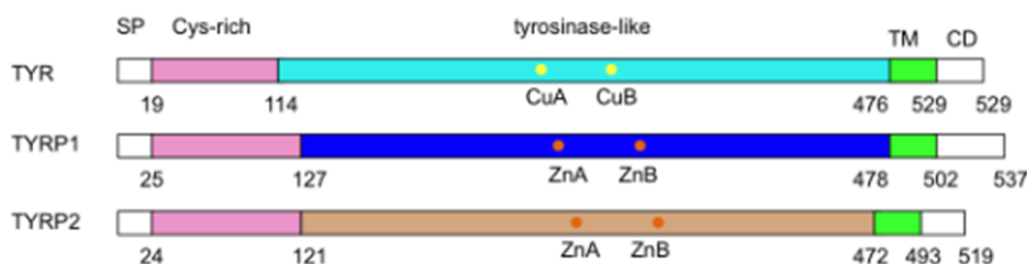
Figure 49. (A) Overall topology and quaternary structure representation of hTYR (left) and hTYRP1 (right). Image taken from ref. [69] (B) Overall topology and quaternary structure representation of AbTYR. Image taken from ref. [70]. (C) Comparison of hTYR and AbTYR active sites. Arrows indicates non – conserved crucial features. Image taken from ref. [62]

The elucidation of the X – Ray model of human tyrosinase related protein – 1 (hTYRP1) (PDB 5M8L) gave instead some 3D insights about hTYR, as they share a 40% of sequence identity and a 70% of sequence similarity. [69] Likewise, they share overall the same topology, being both composed of a signal peptide at the N -terminus (a.a. 1 – 19 in hTYR), a cystine rich N -terminus region (a. a. 19 – 114 in hTYR), a tyrosinase central domain (a.a.   114 – 476 in hTYR) a transmembrane section(position 476 – 497 in hTYR) and final C – terminal cytosolic domain (a.a. 498 – 529 in hTYR). Besides, the deposition of hTYRP1 crystal structure enabled to predict various di - sulfur bonds on hTYR. (Figure 50A)[69] Taken together, all these properties make hTYRP – 1 a suitable template for homology modelling of hTYR. However, using hTYRP- 1 for inhibitor screening purposes results tricky, as on one side it presents two Zinc ion in the catalytic site instead of copper ones, and on the other side, despite binding tyrosinase substrates, whether it has mono or diphenolase activity is still a question mark. [69]

Figure 50. (A) Sequence domains comparison between hTYR, hTYRP1 and hTYRP2. Notes: Cys – rich, cysteine rich domain; TM, transemebrane; SP, signal peptide; CD, cytosolic domain. Image taken from ref. [69]. (B) Multiple sequence alignment of hTYR (hsTYR), hTYRP1 (hsTYRP1), S. Castaneoglobisporus (scTYR) and AbTYR (AbPPO3 and AbPPO4). in yellow, histidine residues bound to CuA/ZnA; in orange, histidine residues bound to CuB/ZnB; in black, glycosylation positions; in green, cysteines responsible for the formation of a thioether bond at the active site; in blue, residues predicted to interact with hsTYR inhibitors through molecular modeling studies; in light gray, residues of hsTYR conserved in the other enzymes. Image taken from ref. [62].

Other information were obtained from endoglycosidase test, identifying asparagine glycosylation sites at position 86,111, 161,230, 290,337 and 371. [71] Finally, mutagenesis studies suggested V393, S380, whose mutation was also correlated to type 1 oculocutaneous albinism (OCA1), and V377, S375, M374 and the copper chelating hisitines H367 and H390 as crucial residues for the enzyme activity.[62, 72]

Switching to the inhibitor design topic, as previously mentioned, two main issues emerge: i) the difficulty, apart from the cost, of testing on purified hTYR containing all the functional features required for a proper assay (such as glycosylation, missing in E. Coli constructs); ii) the lack of 3D structure of the human enzyme.

A plethora of potent inhibitors tested on AbTYR are available, however very few of them are also potent inhibitors of hTYR. Not mentioning kojic acid, hydroquinone or arbutin which are reference

standards for assays, a representative case is Rucinol, displaying sub - micromolar activity on AbTYR ($IC_{50} = 0.6$ μM) and moderate activity on the human enzyme ($IC_{50} = 21$ μM). [62]

Nevertheless, a considerable effort has been made by computational chemists, as the development of various homology models of hTYR led to identification of some potent molecules.
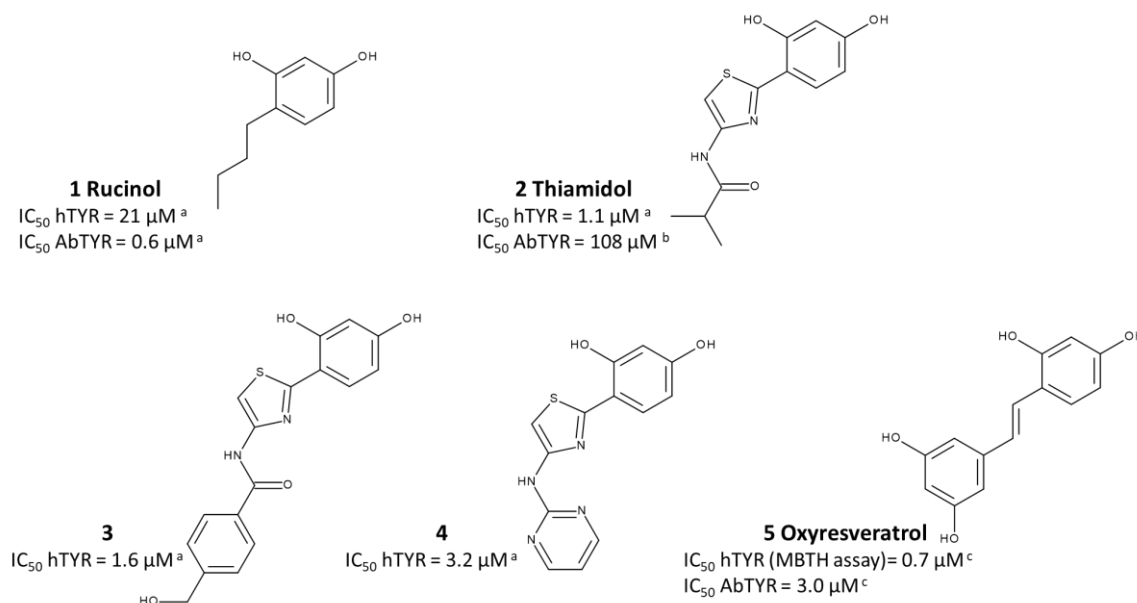
Figure 51. Some potent hTYR inihibitors bearing resorcinol moiety. Notes: MBTH, 3-methyl-2-benzothiazolinone hydrazone hydrochloride hydrate Tyrosinase assay; [a], Data taken from ref. [62]; [b], Data taken from ref. (10.1016/j.jid.2018.01.019); [c], Data taken from ref. (10.1016/j.molstruc.2022.134180);

The most relevant class are resorcinols (compounds **1 – 5**), for which Thiamidol[TM], specifically bearing a thiazole scaffold, is now the lead compound in the market of depigmenting agents. (Figure 51) [62] Interestingly, also stilbene motif resulted in dual inhibition of both AbTYR and hTYR, with a preference for hTYR. (10.1016/j.molstruc.2022.134180)
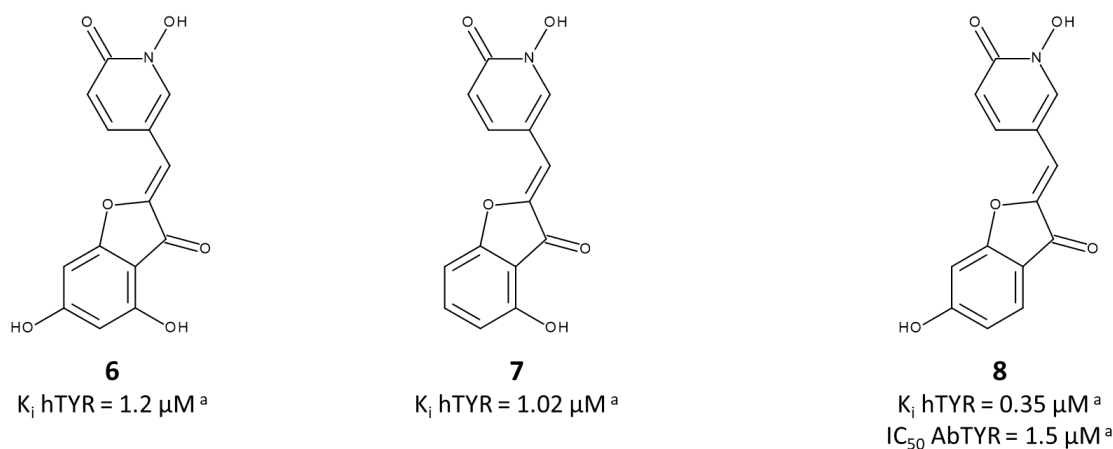
Figure 52. Some potent aurone derivatives inhibiting hTYR. Notes: [a], Data taken from ref.[73].

Another remarkable design strategy in hTYR inhibitors development was the fusion of an non-oxidizable 2-hydroxypyridine-N-oxide (HOPNO) ring, showing alone moderate activity on hTYR, with an aurone moiety, already known as flavonoid with anti – melanogenesis activity, which led to a very potent derivative (compound **8**). (Figure 52) [73]
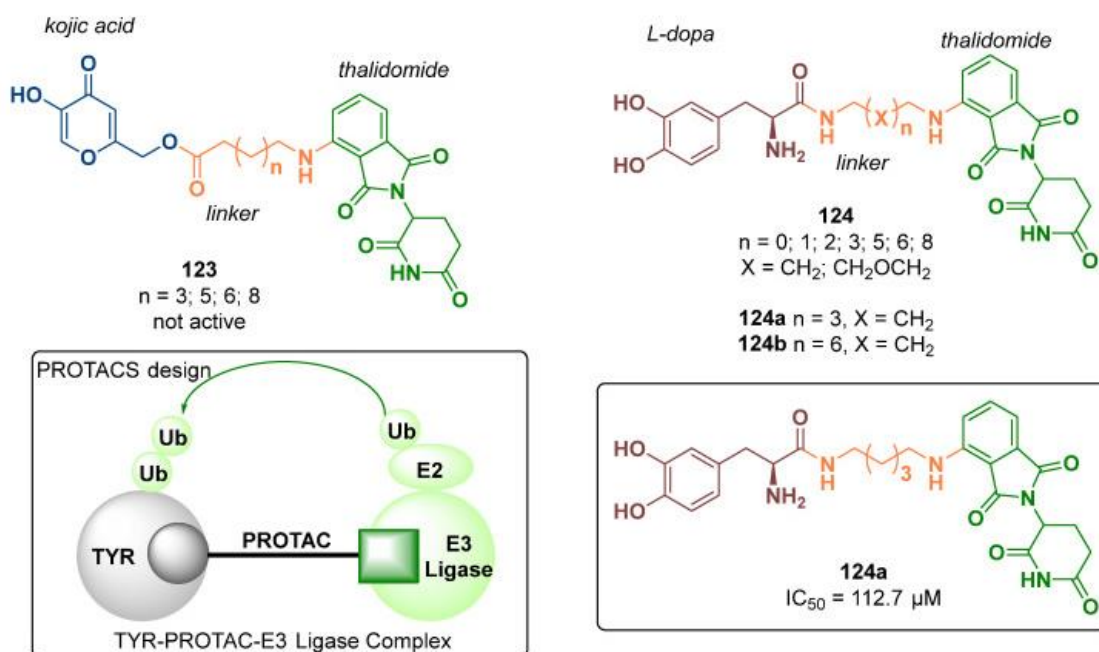
Figure 53. Some examples of designed PROTACs targeting hTYR (up). hTYR – E3 Ligase PROTAC mechanism (down left). Image taken from ref. [74]

Finally, some recent proteolysis-targeting chimeras (PROTACs), linking a hTYR specific binder (such as kojic acid or L – DOPA) with a E3 ubiquitin ligase binder (Thalidomide), were also synthesized with the aim of selectively ubiquitinating tyrosinase. In this context, the size and chemical nature of the linker connecting the E3 ligase binder to the hTYR one, plays an important role in their activity.(Figure 53)[74]

Despite along the years some very interesting advances in the design of hTYR inhibitors were made, still some limitations in tracing a proper SAR of hTYR ligands are present. AbTYR is still currently widely used for tests, as being very cheap in comparison to hTYR constructs, again resulting a useful tool for initial screening. Nevertheless, as highlighted previously, the structural differences between this latter enzyme and the human one determine glitches in the proper design of hTYR inhibitors that can be tested on it prior to the more expensive hTYR assays.

Thus, computational chemistry, until no crystals of hTYR will be deposited, may give a powerful aid for design new hTYR inhibitors, keeping in mind the differences between the proteins used for the biological assays.

In the next two chapters our contribution in this scenario is put forward, firstly giving some insights on the AbTYR inhibitor design (Chapter 4), then giving a deeper focus on the issue just reported, trying to shed light on the analogies and differences between hTYR and AbTYR that may be taken into account for designing new hTYR inhibitors (Chapter 5).

Chapter 4: Arylpiperazines as Novel Potent Inhibitors of Tyrosinase Activity and Melanin Synthesis

In the previous chapter, some of the most potent inhibitors of hTYR were reported. As seen, most compounds were characterized by a phenolic substructure presumably able to coordinate copper – ions. On AbTYR instead, due to its good availability, a large variety of both synthetic and natural compounds was explored for its inhibitory activity. As result, various studies reported active molecules in the low micromolar range including diverse moieties with respect to p – phenols or resorcinols, spanning from indoles, triazoles, benzimidazoles to ascorbic acid and coumarins. [74, 75]. Among the synthetic compounds binding AbTYR active site, p – fluorine phenyl moiety resulted powerful for reaching sub – micromolar activity.[76] Herein, the decoration of this privileged scaffold with an additional o – chlorine group and diverse types of tails is presented. (Figure 54) Specifically, two projects focused on the enrichment of this scaffold are considered in this chapter: the first deals with a potent series arylpiperazines embedding a cinnamic acid tail; the second one take in exam multiple scaffolds linked to the 3 – Chloro – 4 – fluorophenyl ring that will be discussed more in detailed in the text. An overview of their interesting biological activity, whereas a major attention will be given to their binding mode predicted by means of docking technique.
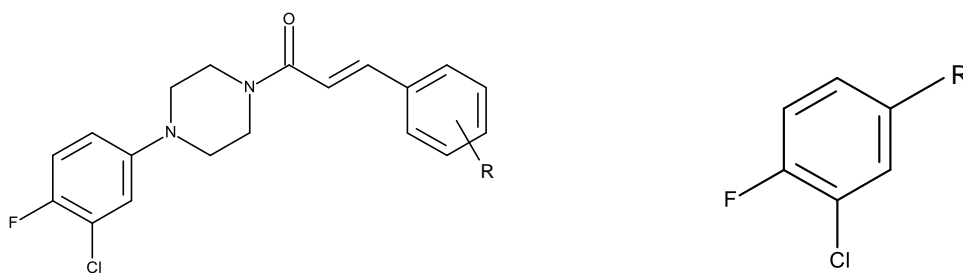
Figure 54. General scaffold of the series of compounds discussed in this chapter.

4.1 Results and discussion

Cinnamic acid derivatives linked to arylpiperazines as novel potent inhibitors of tyrosinase activity and melanin synthesis

Starting from previous studies that highlighted the potential of cinnamic acid derivatives such as ferulic acid, caffeic acid and p – coumaric acid as antimelanogenic agents,[77] and considering as well some synthetic compounds earlier discovered by Ielo et al.[76], which pointed out the high potency towards AbTYR brought by molecules having a 4 – fluorophenyl ring linked to a piperazine

moiety with a aroyl tail widely decorated, Romagnoli et al. decided to combine the two principles in a unique scaffolds having the structure reported below for which an entire series was synthesized.(Table 8)

Table 8. Inhibitory activity of cinnamides **19a-aa** object of this study compared to kojic acid as reference. Data taken from ref.[77]
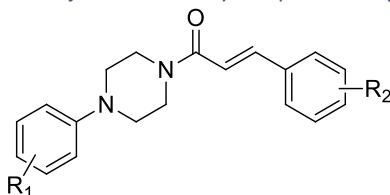
Compound	R_1	R_2	Diphenolase activity IC_{50}[a] μM
19a	4-F	4'-Cl	14.09±0.86
19b	4-F	4'-NO$_2$	N.I.
19c	4-F	3'-NO$_2$	23.32±1.40
19d	4-F	3'-OMe	9.96±2.16
19e	4-F	3',4'-OCH$_2$O-	N.I.
19f	4-F	3'-OBn	N.I.
19g	4-F	3'-NO$_2$, 4'-OMe	N.I.
19h	4-F	3'-NH$_2$, 4'-OMe	17.85±2.96
19i	4-F	2'-OMe, 5'-Cl	27.40±3.23
19j	3-F	3'-NO$_2$, 4'-OMe	N.I.
19k	3-F	3'-NH$_2$, 4'-OMe	>100
19l	3-Cl	3',4'-OCH$_2$O-	34.25±1.67
19m	2-Cl	2'-OMe, 5'-Cl	N.I.
19n	3-Cl, 4-F	4'-Cl	0.33±0.07
19°	3-Cl, 4-F	4'-NO$_2$	0.35±0.04
19p	3-Cl, 4-F	3'-NO$_2$	0.16±0.02
19q	3-Cl, 4-F	3'-OMe	0.25±0.03
19r	3-Cl, 4-F	3'-NO$_2$, 4'-OMe	0.51±0.10
19s	3-Cl, 4-F	3'-NH$_2$, 4'-OMe	0.53±0.08
19t	3-Cl, 4-F	2'-Cl, 3'-OMe	0.12±0.02
19u	3-Cl, 4-F	2'-OMe, 5'-Cl	0.46±0.15
19v	3,4-diF	3'-NO$_2$, 4'-OMe	15.47±3.33
19w	3,4-diF	3'-NH$_2$, 4'-OMe	6.84±1.18
19x	3,5-diF	3'-NO$_2$, 4'-OMe	N.I.
19y	2-F, 4-Cl	3'-NH$_2$, 4'-OMe	N.I.
19z	3-OMe	3'-OBn	N.I.
19aa			55.64±2.08
Kojic acid (1)			17.76±0.18

[a]IC_{50} values represent the concentration that caused 50% enzyme activity loss. All compounds were studied in a set of experiments performed in three replicates. N.I.: No Inhibition

The inhibitory activity of the compounds was evaluated on AbTYR and, as predictable, the derivatives bearing the p – fluoro substituent as R1 showed the lowest IC_{50} values. However, strikingly, the molecules also having a chlorine atom at position 3 presented the best biological data, as they came to display single digit micromolar concentrations in the enzyme inhibition.

Here is where our collaboration started, as we depicted their binding – mode in AbTYR to have more insight about the interaction making such potent inhibitors. Therefore, we performed a semi – flexible docking of the compounds on AbTYR(PDB code: 2Y9X), showing the binding mode of the best compounds **19p**, **19s** and **19t**, presenting different substitution patterns on the cinnamic moiety (respectively mono , 3,4 di substitution or 2,3 disubstitution of the phenyl ring), employing GOLD[39] software and analysing the molecule interactions on Discovery studio. The analysis of the top ranked poses (in terms of docking score) revealed results that match the activity profiles, underscoring the significance of the 1-(3-chloro-4-fluorophenyl) piperazine moiety. Indeed, this motif exhibited three crucial interactions frequently observed. Firstly, it engaged a halogen bond between the copper-chelating histidines, most commonly H61 and H263, and the fluorine atom. Then, the chlorine atom get nested in a pocket near the dicopper center, establishing hydrophobic interactions with H61, V283, and A286. Finally, a pi-pi stacking interaction occurred between the imidazole of the H263 side chain and the phenyl ring, contributing to stabilization.
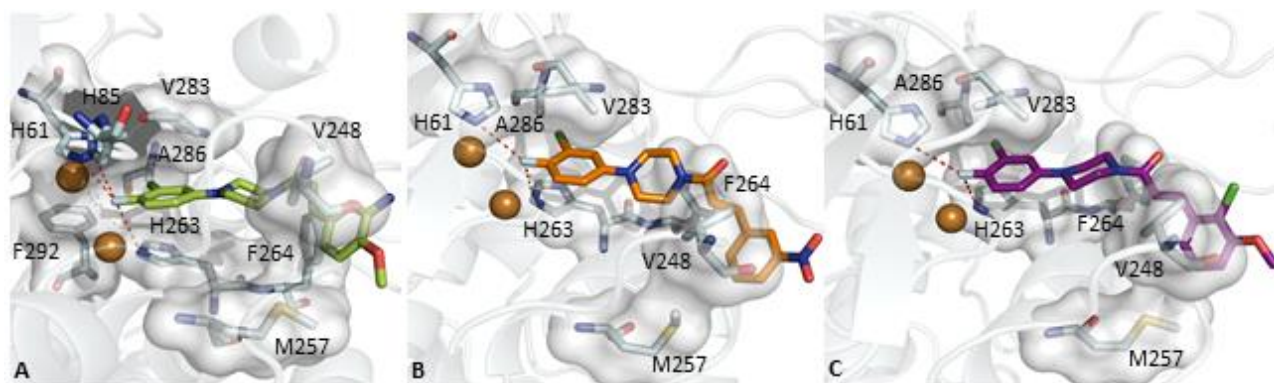
Figure 55. Best poses of the inhibitors **19s** (Panel A), **19p** (Panel B) and **19t** (Panel C) into the AbTYR binding site (PDB code 2Y9X) obtained from docking procedure. Compound **19s** is depicted as green sticks, while compounds **19p** and **19t** are displayed as orange and purple sticks, respectively. The amino acid residues of the binding site are represented by grey sticks. Halogen bonds are highlighted as red dashed lines. The image was created by using PyMOL software

Conversely, the piperazine ring did not appear to play a pivotal role in binding. However, it seemed to present the right balance between flexibility and rigidity, facilitating on one side the correct orientation of the 3-chloro-4-fluorophenyl ring in the active site, and on the other side, concerning the most active ligands **19s**, **19p**, and **19t**, it also formed hydrophobic contacts with F264. (Figure 55)

Regarding the cinnamoyl fragment, no ideal substitution pattern for the phenyl ring could be, as no specific interactions were detected concerning the substituents on the phenyl ring. Nevertheless, the double bond seemed to direct the phenyl ring towards a hydrophobic region characterized by V248 and M57 residues. This orientation allowed for lipophilic interactions between the two residues and the phenyl ring, as well as with its substituents when they were hydrophobic. Consequently, when assessing the binding modes of derivatives **19t** and **19s**, it was suggested that the p-methoxy group (in the case of compound **19t**) and the m-chlorine atom (for compound **19s**) could serve as effective substituents for establishing productive contacts with V248. Once the activity on AbTYR of the compounds was further confirmed by our computational study, the ability of the most potent compounds (**19n** – **19u**) to inhibit melanogenesis was evaluated in vitro and in vivo using A375 human melanoma cells and zebrafish model respectively. As result, one inhibitor (**19t**) was able to remarkably inhibit melanogenesis in zebrafish at 50 µM concentration, despite producing 100% mortality during Fish Embryo Acute Toxicity (FET) test. Nevertheless, another potent AbTYR inhibitor of the series (**19r**) successfully inhibited melanogenesis without any acute toxic effect, making it a suitable candidate for more in – depth trials.

Leveraging the 3-Chloro-4-fluorophenyl Motif to Identify Inhibitors of Tyrosinase from Agaricus bisporus.

Inspired by the results obtained together with Romagnoli, we engineered four different scaffolds previously identified by research group where this PhD was carried out with the 3 – Chloro – 4 – fluorophenyl moiety reported in this chapter. The reference compounds for the four chemical frames included: 1-(2,4-dichlorobenzoyl)-4-[(4-fluorophenyl)methyl]piperazine (**1a**); 2-(4-[(4-fluorophenyl)methyl]piperidin-1-yl)-1-[4-(4-hydroxyphenyl)piperazin-1-yl]ethan-1-one (**2a**); 3-([[(4-fluorophenyl)methyl]sulfanyl)-5-(pyridin-4-yl)-4H-1,2,4-triazol-4-amine (**3a**) and 1,1'-[methylenebis(sulfanediyl)]bis(4-fluorobenzene) (**4a**). (Figure 56)
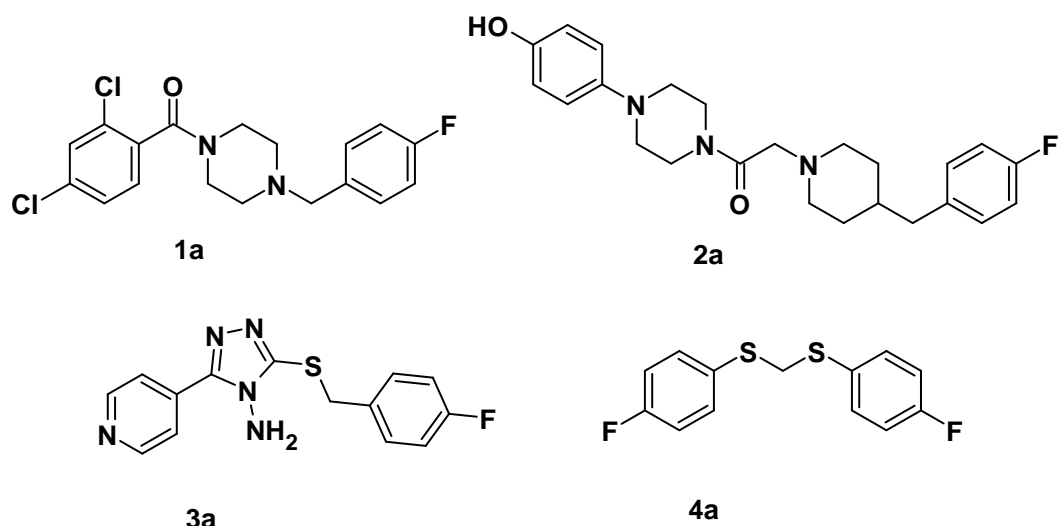
Figure 56. Reference compounds submitted to the structural modifications presented in this work. (CAM)

From this, the four different series schematized in Figure 57 were synthesized and evaluated for their inhibitory activity against AbTYR. (Table 9) Again, the structures bearing the $3 - Chloro - 4 -$ fluorophenyl fragment showed the best inhibitory activity among each series.

1a and 1d, RR^1= 2,4-Cl$_2$C$_6$H$_3$ **a,b,c**   R^2= H
1b and 1e, RR^1= 2CF$_3$-5FC$_6$H$_3$ **d,e,f**   R^2= Cl
1c and 1f, RR^1= benzothiophen-2-yl

2a, R^1 = R^2= H, R^3 = F, X= CH$_2$
2b R^1 = R^2= H, R^3 = F, X= N
2c, R^1 = H R^2= Cl, R^3 =F, X= N
2d, R^1 = Me R^2= Cl, R^3 =F, X= N

3a, R^1 = R^2= H, X= N
3b, R^1 = H R^2= Cl, X= N
3c, R^1 = Cl R^2= H, X= N
3d, R^1 = H R^2= Cl, X= CH

4a, R^1 = R^4 = F, R^2= R^3= H
4b, R^1 = R^2 = R^3= R^4= H
4c, R^1 = R^2 = R^3=H, R^4= F
4d, R^1 = R^2 = H, R^3=Cl, R^4= F
4e, R^1 = F, R^2 = H, R^3=Cl, R^4= F
4f, R^1 = R^4 = F, R^2= R^3= Cl

4g, R^1 = F, R^2 = H
4h, R^1 = H R^2= F
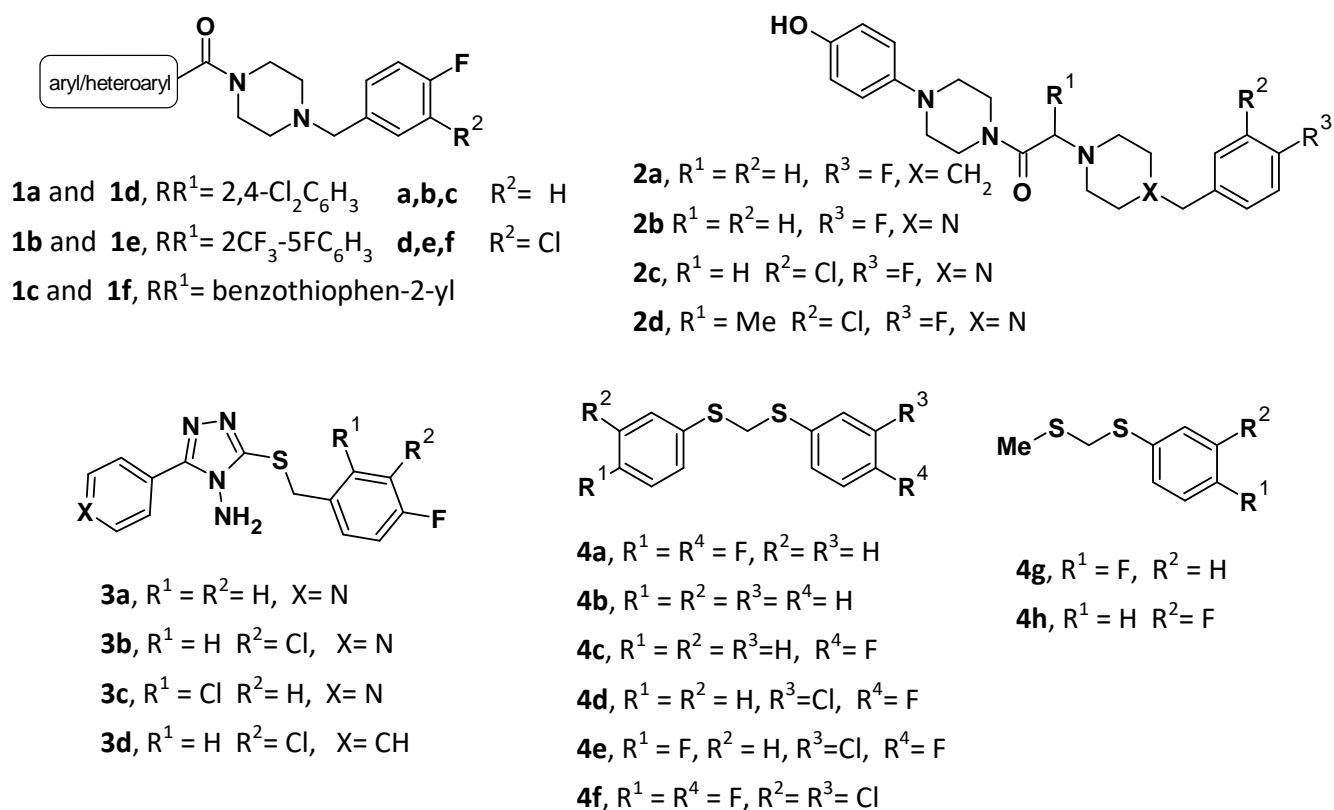
Figure 57. Compound series synthesized in this study, based on the scaffolds reported in Figure 56. (**1** d-f; **2** a-d; **3** a-d; **4** a-h)

Table 9. Inhibition data of the compounds tested on AbTYR diphenolase activity in this study and reference compound Kojic acid(KA)

Entry	IC$_{50}$ (μM) [a] ± SD [b]
1d	0.42 ± 0.03
1e	0.19 ± 0.07
1f	1.72 ± 0.11
2b	4.43 ± 0.54
2c	1.73 ± 0.28
2d	1.38 ± 0.15
3b	24.15 ± 1.02
3c	>350
3d	67.32 ± 6.67
4b	>350
4c	>350
4d	6.26 ± 0.37
4e	10.65 ± 1.51
4f	2.96 ± 0.34
4g	26.02 ± 2.63
4h	183.46 ± 6.12
Kojic Acid(KA)	17.76 ± 0.18

[a] All compounds were tested using a set of experiments performed in triplicate; IC$_{50}$ values correspond to the concentration causing 50% enzyme activity loss.
[b] SD represents the standard deviation.

Thus, to validate the crucial role of the 3-chloro-4-fluorophenyl component in its binding affinity within the AbTYR catalytic pocket, we employed a semi-flexible docking approach on four representative compounds (**1d**, **2c**, **3b**, and **4f**) using GOLD software [39]. Our molecular modelling analysis of the most potent inhibitors (**1d**, **2c**, **3b**, and **4f**) is presented in Figure 58. In all instances, the fluorine atom in the docked inhibitors established significant interactions within the AbTYR cavity, including:(i) participation in halogen bond interactions with the copper-coordinating histidine; (ii) role of metal acceptor toward the di-copper ions CuA and CuB, except for compound 3b, which interacted only with CuA (Figure 58C); (iii) formation of hydrophobic contacts with Phe292.
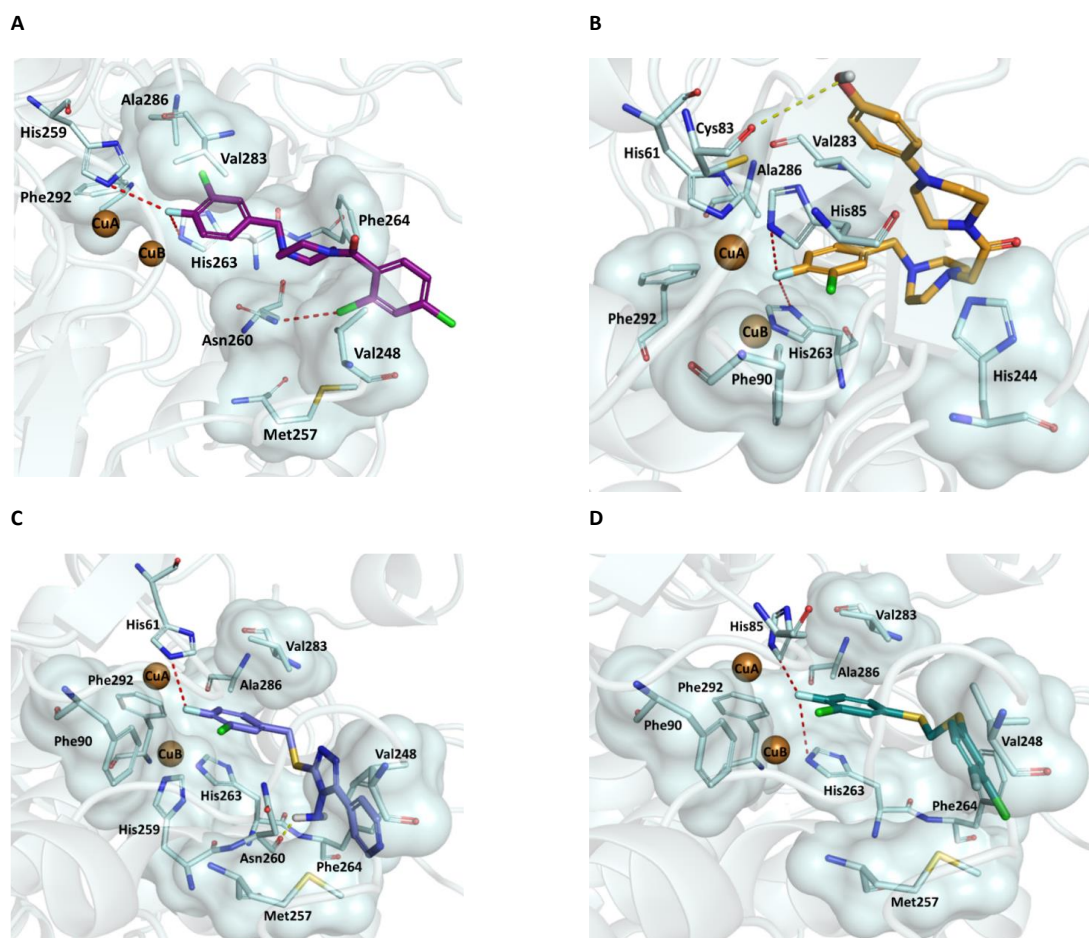
Figure 58. The top ranked poses of the compounds **1d** (purple sticks) (A), **2c** (orange sticks) (B), **3b** (slate sticks) (C), and **4f** (deep teal sticks) (D) docked in the catalytic cavity, whereas the di-copper ions are represented as brown spheres. The residues involved in the interactions are depicted as pale cyan sticks, adding the surface in the case of hydrophobic contacts. Halogen and hydrogen bonds are highlighted as red and yellow dashes, respectively. The AbTYR is depicted as a cartoon. Images generated using PyMOL software (www.pymol.org).

Additionally, we observed that the 4-fluorosubstituted phenyl ring contacted the side chain of His263 engaging pi-pi stacking interactions with it. Notably, in compounds **1d**, **3b**, and **4f**, the distinct fragments characterizing each chemotype exhibited a similar reconfiguration, establishing favourable contacts with the residues at the entrance of the catalytic site, such as Val248, Met257, Asn260, and Phe264.

On the contrary, compound 2c displayed a distinctive conformation, likely attributed to its higher length in comparison with the other compounds examined. Consequently, the 4-piperazinephenyl tail folded itself to facilitate its accommodation in the binding pocket. This binding mode was reinforced by hydrophobic interactions with the side chains of His244 and Val283, in addition to a

hydrogen bond formed between the phenolic OH group and Cys83. This observation suggests that the elongation of the chain should not compromise the overall binding affinity.

Finally, although a diverse placement of the 3-chloro-4-fluorophenyl ring was appreciated in the four compounds, the chlorine atom stabilized the binding to the catalytic cavity through van der Waals interactions in all the cases, specifically with Ala286 and Val283 in the case of ligand 1d and with Phe90 and Val283 in the one of inhibitors **2c**, **3b**, and **4f**.

Therefore, taking together activity data and modelling studies, we can conclude that also in this study the 3 – Chloro – 4 – fluorophenyl fragment, already proposed in the previous paragraph, plays a key role in enhancing the potency of AbTYR binders.

4.2. Materials and methods

For the two studies reported in the Result and discussion section, the same docking protocol on AbTYR (PB code: 2Y9X) using GOLD software[39] was employed. This was described more in depth previous publications from our research laboratory.[76, 78]

The top ranked poses from the docking procedure were then analysed using Discovery Studio together with LigandScout pharmacophores.(https://www.3ds.com/products-services/biovia/) [33]

Information regarding the compound synthesis and the biological assay procedures are described in detail in ref. [77] and [79].

Chapter 5: Learning on Human Tyrosinase: From Homology Modelling to New Inhibitors Selection

The thread introduced in Paragraph 3.2, regarding the difficulty of designing and testing hTYR inhibitors just from the structural and biological basis on AbTYR, is taken back here in this Chapter, as in first instance we also experienced this discrepancy in the activity data of some of our in-house potent AbTYR inhibitors. Indeed, this study started from a collaboration with the research group of professor Scheuermann from ETH Zurich University, who tested these derivatives against hTYR. [80] Among them, only the 3-(4-Benzyl-1-piperidyl)-1-[4-(4-hydroxyphenyl)piperazin-1-yl]propan-1-one (formerly known as compound **6b**, now named just compound **6**) showed inhibitory activity towards hTYR. Nevertheless, despite showing very promising activity against AbTYR (3.8 µM), it resulted a very poor inhibitor of the human enzyme displaying an IC$_{50}$ of 1.1 mM. The top player of hTYR inhibitors, Thiamidol, earlier mentioned in Paragraph 3.2, was again tested confirming its potency on hTYR (3.8 µM, experimental value) and conversely proving weak inhibition of AbTYR (108 µM, value taken from ref. [81]

Thus, our aim was to understand the structural analogies and differences of the two enzymes involved in ligand recognition, exploiting the computational analysis of the binding mode of these two inhibitors showing opposite activity on hTYR and AbTYR. The computational workflow developed during my second year of PhD at Freie Universität of Berlin together with the Molecular Design Lab of professor G. Wolber, aimed to achieve this purpose, included: i) an in -depth creation of an hTYR homology model; ii) comparative docking studies of the two inhibitors in the two enzymes; iii) binding energy calculation of the docking complexes through MM – GBSA method; iv) MD simulation of the docking complexes.
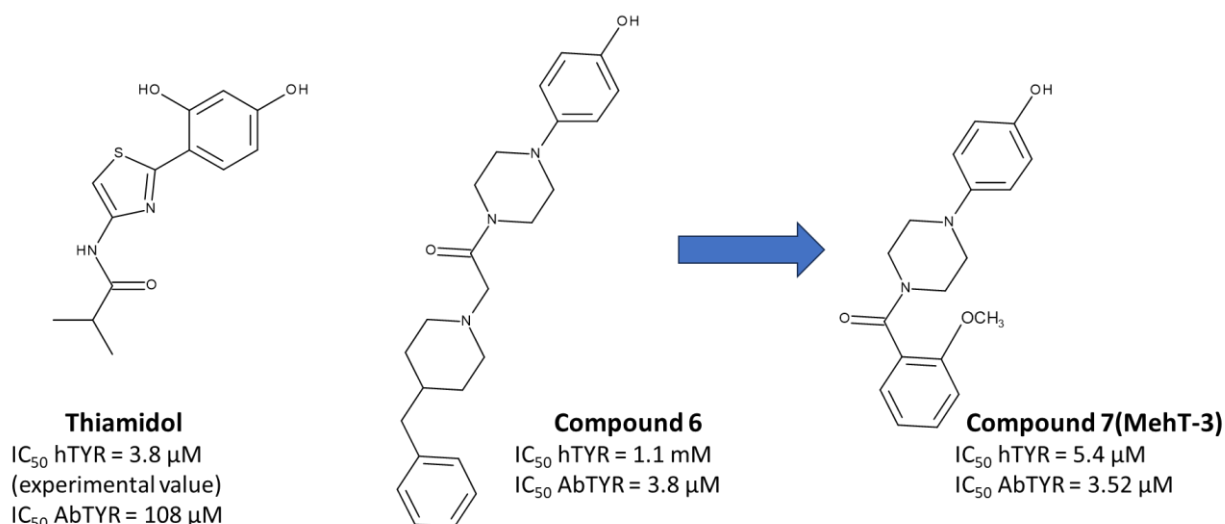
Figure 59. Compounds evaluated in this work

The final purpose of the study was the design of new inhibitors that can be tested firstly on the cheapest AbTYR and then confirmed by assays on the purified hTYR. This latter task has been achieved as we identified compound **7**, showing dual potent inhibition of AbTYR and hTYR(3.52 and 5.4 μM respectively). (Figure 59)

Therefore, the next Result and Discussion section will deal both with the individual results of each phase of the computational pipeline and with the description of the final outcome obtained.

5.1   Results and discussion

Building a homology model for hTYR by comparative modelling

In order to depict a proper binding mode of the inhibitors in a protein for which no 3D structures are available on the RCSB PDB, the obtainment of an homology model results a mandatory step. Therefore, an in depth generation, validation and selection protocol was applied to obtain the hTYR protein for our docking studies. This can be schematized as follows: i) creation and refinement of multiple models; ii) consensus evaluation of the protein geometry; iii) docking and subsequent MD simulations of ligands earlier co − crystallized on B. Megaterium Tyrosinase (BmTYR).

Thus, four software were employed, leading to six different models: AlphaFold V.2 [82], SwissModel [83], MODELLER through ModWeb server [84], and TopModel [34]. For MODELLER and SwissModel three different PDB templates: 5M8S, 5M8Q and 5M8L to map the 3D structure of the target. The templates were chosen either according to the highest sequence identity with the

target protein (5M8S and 5M8Q)[85] or the highest GMQE score (Global Model Quality Estimate score, a template evaluation metrics provided by Swiss Institute) [83] were chosen. AlphaFold and TopModel did not require template selection due to their algorithms [82, 86]. For refinement and validation processes, two models generated by AlphaFold were taken: the top-ranked solution generated by the program and a model retrieved from the AlphaFold repository (Figure 60A).

A

Generated models	Software	Template used (PDB code)	Template Identity(%)	GMQE score
Model 1	SwissModel	5M8L	43.32	0.69
Model 2	SwissModel	5M8Q	43.78	0.68
Model 3	AlphaFold v.2	Unbiased	NA	NA
Model 4	MODELLER	5M8S	44	NA
Model 5	TopModel	Unbiased	NA	NA
Models from repository				
Model 6	AlphaFold v.2	Unbiased	NA	NA

NA = Data not available

B

	1	3	5	4	6	2
1		1.49	0.70	0.74	1.49	0.74
3	1.49		1.54	1.60	0.20	1.44
5	0.70	1.54		0.87	1.55	0.88
4	0.74	1.60	0.87		1.60	0.77
6	1.49	0.20	1.55	1.60		1.44
2	0.74	1.44	0.88	0.77	1.44	

Figure 60. (A) List of the homology model created in this study and validation metrics for the template selection. (B) Correlation matrix reporting the backbone RMSD between the models evaluated (Model 1 – 6).

Of the six models above, we first analysed the orientation of the copper-chelating histidines: His180, His202, His211 and His363, His367, His90. All models correctly oriented the copper chelating histidine side chains in a tetrahedral geometry, and no substantial differences were observed. The models were then refined using the MOE Structure Preparation Wizard(Version 2020) [Molecular Operating Environment (MOE), 2022.02 Chemical Computing Group ULC, 1010 Sherbooke St. West, Suite #910, Montreal, QC, Canada, H3A 2R7, 2023] to obtain all-atom structures. The six models were then aligned and the root-mean-square deviations (RMSDs) of the common residues of all models were calculated and reported in a correlation matrix to determine if all the models generated, represent the same conformation or if there are significant differences. Also at this level, the models depict the same conformation, not surpassing 2Å (Figure 60B).

The models were further evaluated using the MOE Structure Preparation Wizard considering the following characteristics: (i) bond-length, (ii) Psi-Phi outliers (Figure S3A), (iii) atom clashes, (iv) presence of D-amino acids, and (v) presence of cis-peptides. The errors encountered at this step were partially fixed through local minimization of the residues side – chains, although the remaining ones were retained for consensus analysis using the SAVES online platform. SAVES

include several protein validation programs, including WHATCHECK [87], PROCHECK[88], ERRAT [89], VERIFY 3D [90], and PROVE [91]. WHATCHECK and PROCHECK analyze properties common to MOE and were therefore used for consensus prefiltering of the model. ERRAT quality factor, PROVE warnings, and VERIFY 3D score were considered only for eventual ranking of the models and not for filtering them. Figure 61 depicts the pre-filtering criteria considered. Model 1, Model 2, and Model 5 were filtered out after this analysis, as they contained either D-amino acids or clashes at the di – copper center.
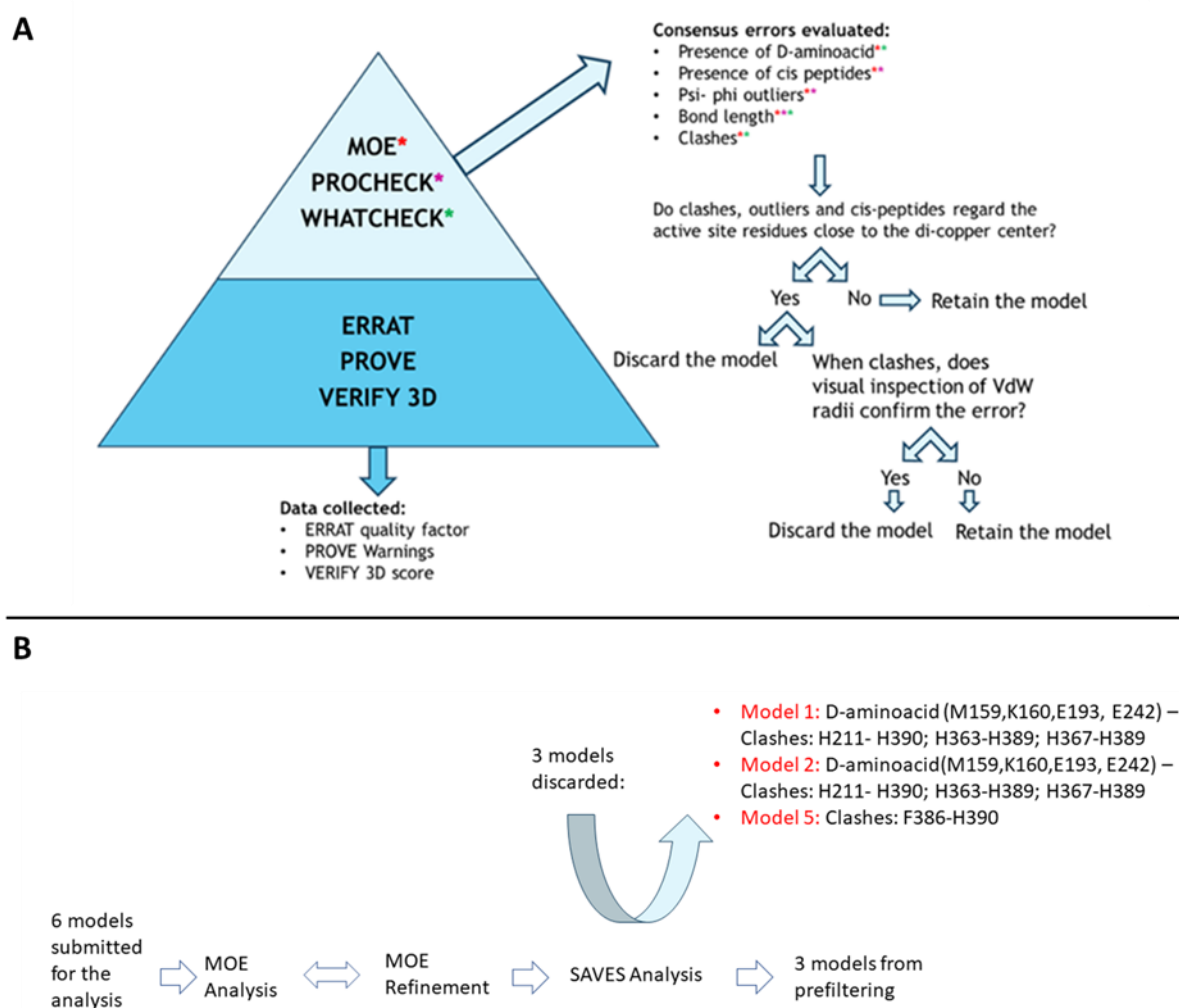
Figure 61. (A) Scheme of the criteria employed for prefiltering protein homology models. Common properties analysed via MOE, PROCHECK and WHATCHECK are flagged by the coloured asterisks. (B) Outcome of the homology modelling prefiltering procedure.

The three remaining models (Model 3, Model 4 and Model 6) were then filtered evaluating the binding modes of either enzyme substrates (L-tyrosine and L-DOPA) or with known inhibitors (such as hydroquinone and kojic-acid), previously co-crystallized on homologous proteins (BmTYR and TYRP1, PDB: 4P6R, 4P6S, 5I38, 5I3B, 5M8P, 5M8M) [92-94] with the hTYR model selected from pre

- filtering. The clusters obtained from docking were compared with the binding modes of X-Ray complexes, and the poses were selected accordingly to the highest superimposition with the co - crystalized ligand. These selected complexes were subjected to 50ns of MD simulation, and various properties, such as protein RMSD, ligand RMSD and ligand-protein interaction frequency were considered to choose the best homology structure. However, the validation of L-DOPA docking was excluded since none of the three models presented a binding mode consistent with crystallographic information.

Starting from the protein RMSDs, all models apart from Model 6, demonstrate a stable behavior with fluctuations ranging from 3 to 5 Å across all replicas of the submitted complexes. (Figure S4) In terms of ligand RMSDs, Model 3 and Model 4 display fluctuations ranging from 1 to 4.0 Å, while Model 6 shows less consistent results across the analysed replicas, particularly for the simulations conducted on hydroquinone complexes.

Major differences between Model 3 and Model 4 became visible when we looked deeper the interaction patterns during dynamics between the ligands (L-tyrosine, hydroquinone and kojic-acid) and the active site residues. The docked ligands binded CuA consistently throughout the simulation with the six histidines (His180, His202, His211, His363, His367, His369) coordinating with the two copper ions (CuA with His180, His202 and His211; CuB with His363, His367 and His369) in all frames of the simulations performed exclusively in the docking complexes derived from Model 4 (Figure S4). In addition, the authors of the PDB templates reported other interactions with conserved amino acids. We compared these interaction patterns with the ones found in our simulations and noticed that all the ligands submitted to MD simulation showed a phi – phi interaction with His367 (homologous to His208 of BmTYR and His381 of TYRP1) when docked in Model 4. Unlike, this interaction was missing for kojic-acid in complex with Model 3. All these observations taken together suggested us to select Model 4 for further investigation of the plausible binding modes of the hTYR ligands object of this study.

Comparative docking of Thiamidol and Compound 6 in hTYR and AbTYR

We rigidly docked the Thiamidol and Compound **6** in both hTYR and AbTYR crystal structure (PDB: 2Y9X) and then, after docking complex minimization, a binding mode comparison of the two in the two enzymes was made.

Starting from Thiamidol in hTYR, bearing a Resorcinol moiety recurring in hTYR binders, it coordinates one copper ion in the active site (CuA) through the para – hydroxyl group of the above – mentioned part. The same, forms an additional hydrogen bond with S380, crucial residue for the enzyme activity. Other hydrogen bonds involving the ortho hydroxyl group of resorcinol and N364 sidechain carbonyl were also encountered. Then, this moiety is also involved in lipophilic contact and π – π stacking interactions respectively with V377 and H367. Several lipophilic interactions at the entrance of the binding site, hitting I368, F347 and A357 are formed by both thiazole ring and isopropyl amido group. Finally, the amide linking group forms an H – bond with the sidechain hydroxyl group of S360. (Figure 62A)

Figure 62. Minimized complexes of Thiamidol (sticks with colored heteroatoms) in hTYR homology model (purple) and AbTYR X-ray structure (PDB code: 2Y9X) (cyan) obtained after MM-GBSA binding energy calculation. Copper-ions (CuA and CuB) are represented as spheres, while the copper-chelating histidines and the interacting residues are highlighted by thin sticks. The yellow dashes represent hydrogen-bonds, and the surfaces defines lipophilic contacts. (A) Interactions found for Thiamidol in hTYR. (B) Interactions found for Thiamidol in AbTYR. (C) Superimposition of Thiamidol complexes showed in (A) and (B) including the homologous residues of the interacting ones.

Regarding Thiamidol binding mode in AbTYR, the same coordination of CuA by the p – hydroxyl group seen in hTYR was encountered too, involving as well h – bonds with the copper chelating histidines. In contrast, the orientation of the o – hydroxyl group results different with the one seen in hTYR, forming instead an h – bond with M280. Similarly, the amide group hydrogen – bond G281. (Figure 62B) Nevertheless, with respect to the residues engaged in h – bonds with these two ligand moieties in hTYR (N364 and S360), no correlation between the two hydrogen bonds formed in the two isoenzymes could be done, as the amino acids involved were in completely different regions of the active site. Lipophilic interactions, at the bottom and at middle part of the active site, are retained instead, contacting A286 and V283 with the resorcinol ring and F264 with the thiazole one. Surprisingly, no interactions were found for the isopropyl group, presumably due to a possible clash with F264. Additionally, having a look on the superposition of Thiamidol binding modes in the two enzymes, it may be speculated that hydrophobic interactions of the isopropyl group found in hTYR were stabilized by the h – bond between the amide group and S360. (Figure 62C) The comparison overall was in good agreement with the biological data, since Thiamidol displayed high potency towards the human enzyme and showed instead inhibition of AbTYR at 108 μM concentration.

Likewise, the binding mode of Compound **6**, which showed an inverted behaviour in hTYR and AbTYR with respect to Thiamidol, was elucidated in the two isoforms applying the same procedure used for Thiamidol.

Concerning its binding mode on hTYR, it was noticed that the interactions involving the phenolic moiety were, apart from the ones of the missing ortho – hydroxyl group, almost the same of the ones showed by Thiamidol resorcinol ring. It chelated CuA ion, hydrogen – bonded S380 and H367, and forms hydrophobic contacts with V377 and $\pi - \pi$ stack H367. Nonetheless, despite a lipophilic interaction between the piperazine ring and I368 is suggested by LigPlus and by LigandScout receptor binding surfaces, no any other interaction were formed by Compound 6 tail. (Figure 63A) This strongly reinforce the activity data showed by this inhibitor, displaying an IC_{50} towards hTYR in the micromolar range.
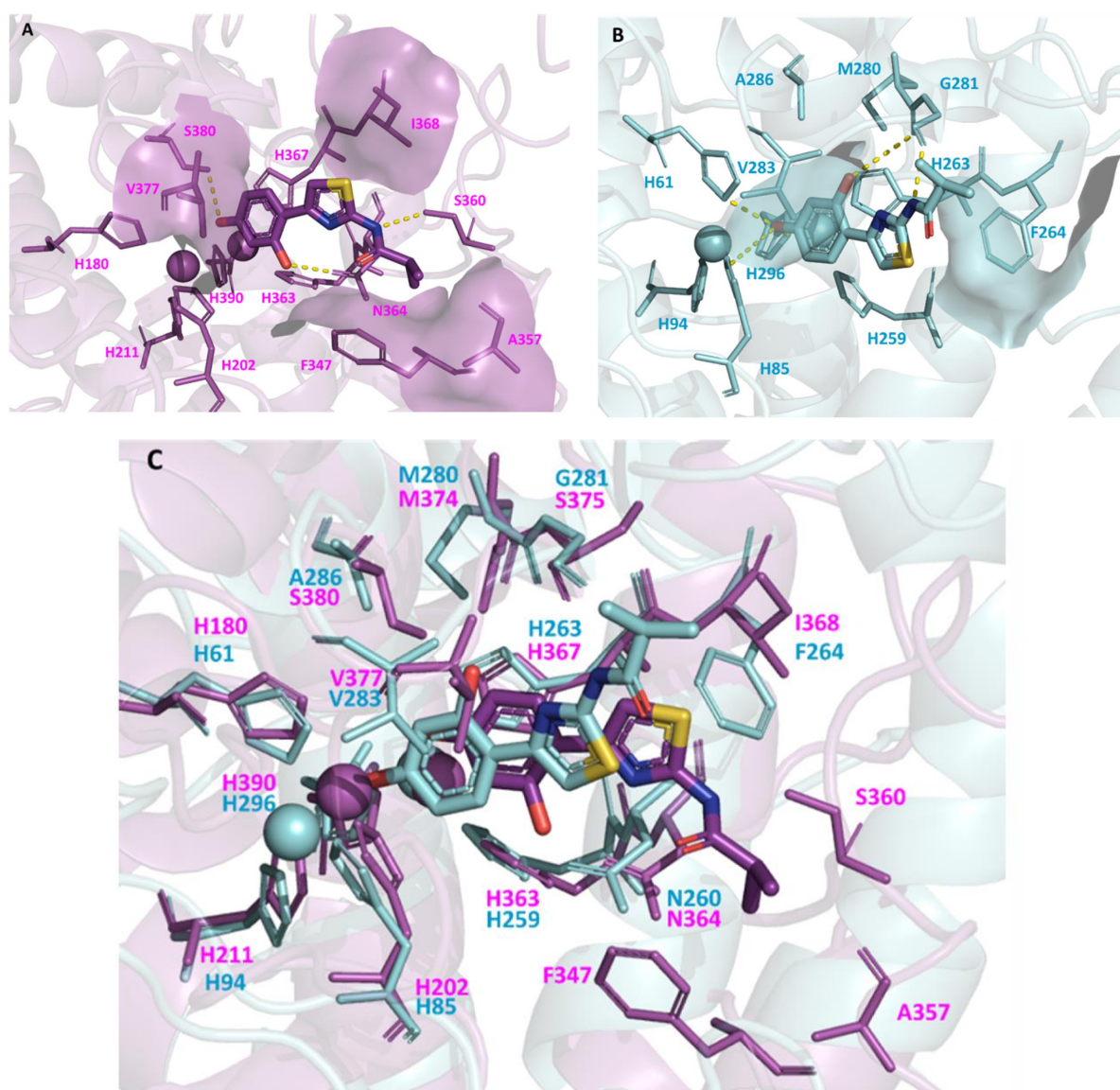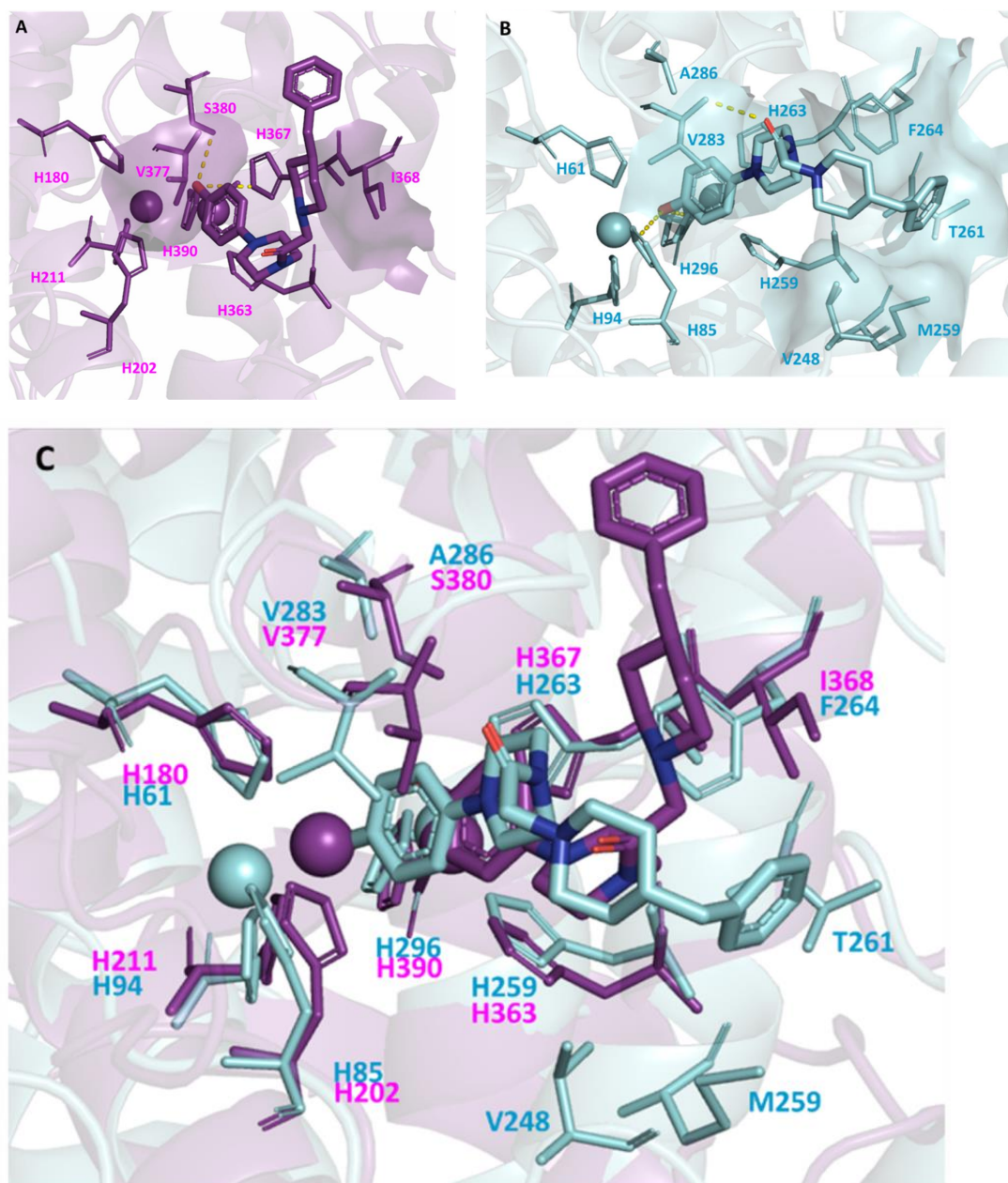
Figure 63. Minimized complexes of compound 6 (sticks with colored heteroatoms) in hTYR homology model (purple) and AbTYR X-ray structure (PDB code: 2Y9X) (cyan) obtained after MM-GBSA binding energy calculation. Copper-ions (CuA and CuB) are represented as spheres, while the copper-chelating histidines and the interacting residues are highlighted by thin sticks. The yellow dashes represent hydrogen-bonds, and the surfaces define lipophilic contacts. (A) Interactions found for 6 in hTYR. (B) Interactions found for 6 in AbTYR. (C) Superimposition of compound 6 complexes shown in (A) and (B) including the homologous residues of the interacting ones.

On the contrary its pose on AbTYR, apart from displaying the canonical interactions at bottom of the binding site, involving CuA coordination, H-bonds with copper chelating histidines and lipophilic interactions with A286, V283 and H263 (formed also by Thiamidol), it presented an extended pattern of lipophilic interactions made by tail. Specifically, the piperazine tail contacted F264 and inserted the benzyl piperidine moiety in a hydrophobic surface lined by M259, T261 and V248, additionally forming a π-π T-shaped between the phenyl ring and F264 sidechain. An

additional h – bond with V283(conserved in hTYR) backbone amino group was also formed. (Figure 63B)

Comparing the orientation of this moiety just described with the one depicted for hTYR, it also visible that in the latter case it occupy an hydrophilic and solvent exposed region of hTYR binding pocket, where this moiety, to SAR point of view, results useless, thus displaying also in this case the reversed activity of this inhibitor against the two enzymes. (Figure 63C)

Again superimposing Compound **6** binding mode on AbTYR with the one of Thiamidol on hTYR they seemed to target the same region of the two enzymes. However, while in the former case (AbTYR) this region is presented an organised α-helix characterized by an hydrophobic surface, in the latter case it was characterized by an extended loop with an unpredictable conformation, suggesting that the hydrophobic interaction at the hTYR active site entrance may be restricted to I368, V377 and F347. (Figure 64)
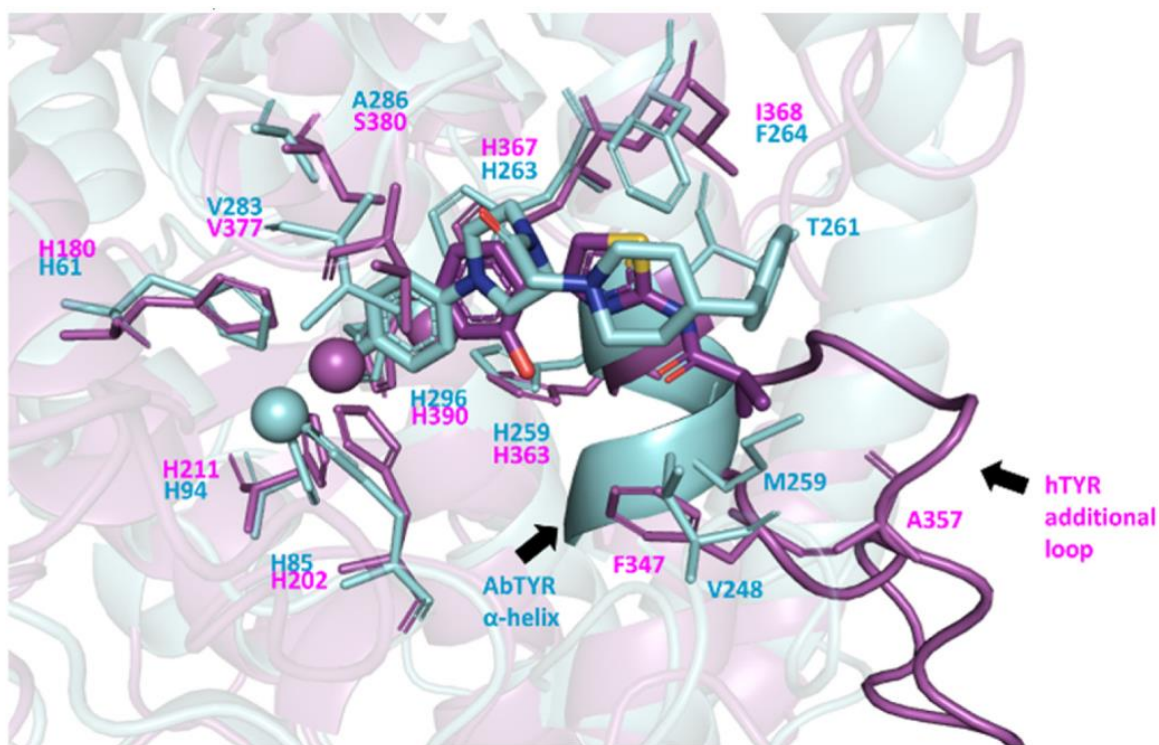
Figure 64. Superimposition of Thiamidol binding mode in hTYR (purple) with the one of compound 6 in AbTYR (cyan). Ligands are represented by sticks with colored hetero-atoms while residues giving key interaction are highlighted by thin sticks. The cartoon representation highlights the variable region at the entrance of the active site between hTYR and AbTYR.

Finally, binding energy values predicted using the molecular mechanics generalized Born surface area (MMGBSA) calculation method, further supported the hypothesis regarding the different activity and binding mode of the two inhibitors in hTYR and AbTYR, as more a negative value is

shown by Thiamidol in hTYR with respect to its pose in AbTYR and the opposite situation is shown by the complexes of Compound **6** in the two enzymes (See Table 10)

Table 60. MM-GBSA calculation of the difference in binding energy of the enzyme inhibitor complex indicates stronger binding affinity of Thiamidol for hTYR and of compound 6 for AbTYR.

Compound	MMGBSA ΔG Bind (kcal/mol)	
	hTYR	**AbTYR**
Compound **6**	0	-4.54
Thiamidol	-14.81	3.34

Identification and binding mode prediction on hTYR and AbTYR of Compound 7

Taken together the hints of the previous paragraph, which overall suggested that, with respect to the hydrogen bond network, the length of the scaffold together with the shape of the ligand and the lipophilic interactions at the entrance of TYR binding site, had a major implication in determining the potency towards both isoenzymes, we selected among a newly synthesized series of in – house compounds, a derivative presenting a shortened scaffold and retaining a high potency towards AbTYR initially named MehT – 3, now referred as compound **7**. [95]

Before performing in vitro testing of the AbTYR inhibitor on hTYR, we firstly evaluated its binding mode in both hTYR and AbTYR using the protocol employed for the other two compounds.

The docked pose predicted on hTYR Model 4 showed that compound **7** forms, as well as the other two molecules examined, the typical interactions at the bottom of the active site involving the CuA ion, the S380, the copper – chelating histines and V377. However surprisingly, it had almost all the hydrophobic interaction formed by Thiamidol tail, specifically involving I368 and F347. (Figure 65A) Moreover, superimposing its minimized docking complex on hTYR with the one Thiamidol, it showed an almost identical shape in hTYR active site, further configuring as a promising candidate for hTYR screening. (Figure 65B)
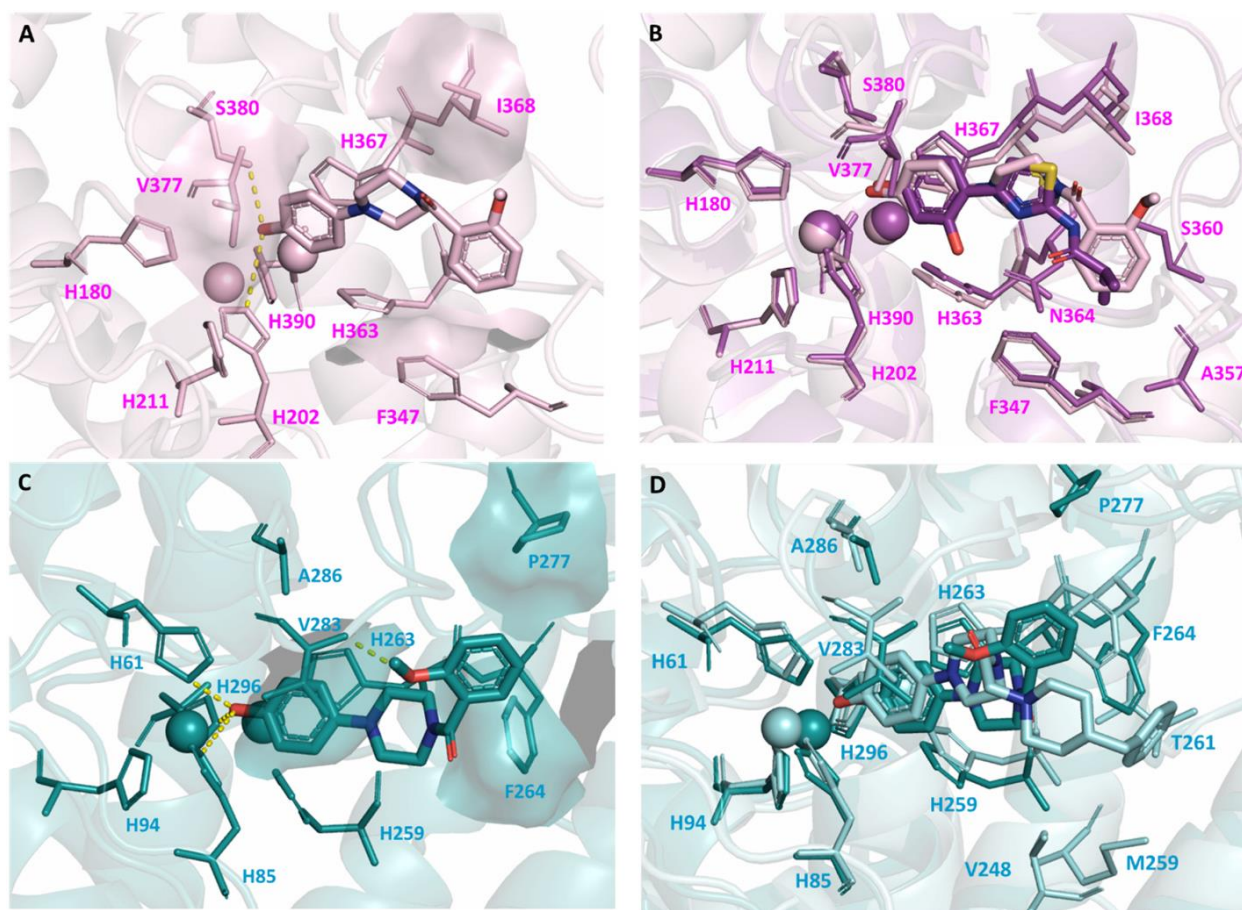
Figure 65. A) Minimized complexes of **7** (MehT-3) in hTYR homology model (pink) and B) its superimposition with Thiamidol on hTYR (purple); C) Minimized complexes of 7 (MehT-3) in AbTYR X-ray structure (PDB code: 2Y9X) (teal) and D) its superimposition with 6 on AbTYR (cyan). Copper-ions (CuA and CuB) are represented as spheres, while the copper-chelating histidines and the interacting residues are highlighted by thin sticks. The yellow dashes represent hydrogen-bonds, and the surfaces defines lipophilic contacts.

We also considered its pose on AbTYR and apart from the classic interactions formed by the other two compounds, an hybrid conformation was shown by its ((2) – methoxy – benzoyl) – piperazine tail which, despite losing some lipophilic interaction (e.g the ones with V248, M259 T261 formed by Compound 6), it was still able to form some with F264 and P277. Additionally, the h – bond with V283 previously seen on Compound **6**, was also encountered.(Figure 65C and 65D) This latter interaction was not seen for any on the three molecules on hTYR, possibly due to the different conformation of the residue and its flanking amino acid in the two isoforms.

MM – GBSA binding energy calculation showed results coherent with the docking hypothesis on hTYR homology model and AbTYR X – Ray structure, as well as with activity data on mushroom tyrsosinase, showing negative values (-36.15 kcal/mol and -10.42 kcal/mol for hTYR and AbTYR, respectively) comparable to the one of Thiamidol on hTYR and to the one of Compound **6** in AbTYR.

Encouraged by these computational results, we decided to screen Compound **7** against hTYR and an outstanding result was obtained: it inhibited the enzyme at concentration of 5.4 μM, almost comparable to the one of Thiamidol. Kinetic studies were also carried out and competitive inhibition was also confirmed by Linewaver – Burk plots.

Molecular dynamic simulations of compounds 7, 6 and Thiamidol docking complexes

To give further evidence of our computational hypothesis we performed a 100 ns MD simulation on the docking complexes of the three compounds in hTYR homology model and AbTYR.

As result, all the compounds remain inside both isoforms along the simulation. However, comparing Thiamidol interaction diagram in hTYR with the one of the other two inhibitors there were some differences between their binding mode in hTYR.

Firstly, confronting the ligand RMSD values of Thiamidol and **6** along the simulation, it was noticed that while Thiamidol moved together with the protein, **6** showed an unstable behavior of the benzylpiperidine tail, displaying RMSD values exceeding 10Å. Secondly, apart from the lipophilic interactions with copper chelating histidines, no stable interaction were formed by the lipophilic tail of **6**, Thiamidol, as already seen in static complexes, contacted V377 and I368 with the thiazolyl and with the isopropyl moiety respectively. In addition, a very stable H-bond with S375, not seen in the static complexes, was formed by the carbonyl group of Thiamidol, further justifying its potency towards hTYR. For what concerns **7** in hTYR, intermediate ligand RMSD values were shown with respect to Thiamidol and **6**. Additionally, the lipophilic interactions at the binding site entrance already described are mantained, despite less frequent than Thiamidol. Finally, the relevant H-bond with S380 results more frequent in comparison with Thiamidol and 6, therefore supporting its median activity. (Figures 66-67)
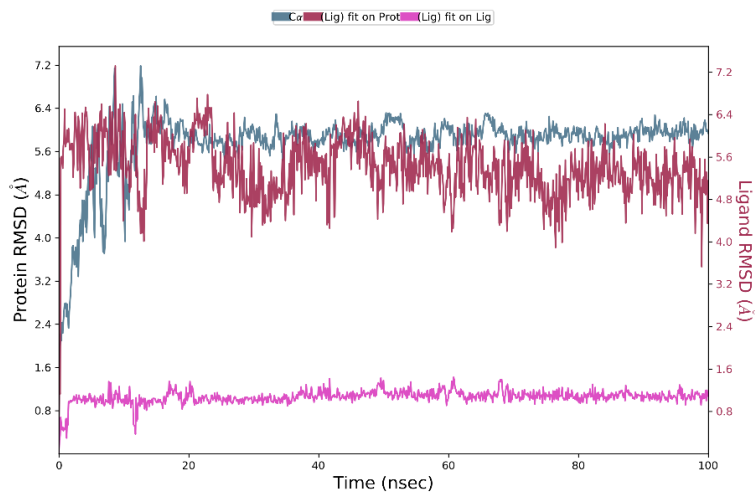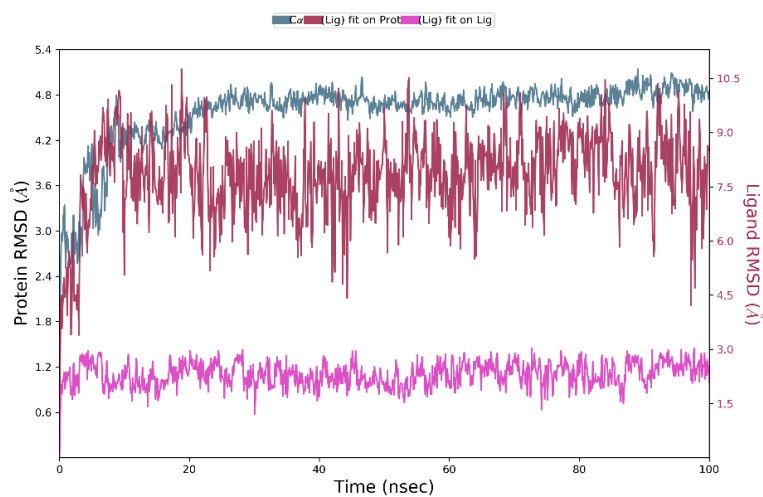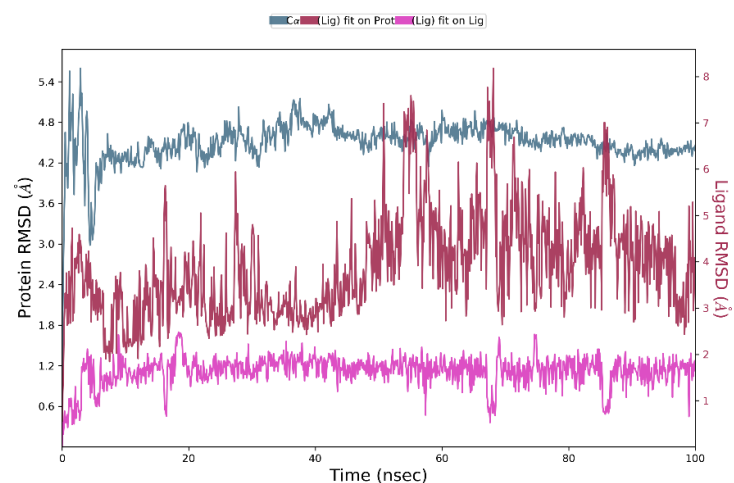
Figure 66. The RMSD plot of the hTYR in complex with compounds Thiamidol (A), 6 (B) and 7 (C). In the X-axis is reported the simulation time; in the left Y-axis is reported the protein RMSD evolution, while the right Y-axis indicates how stable are the compounds in the binding site during the simulation.

A
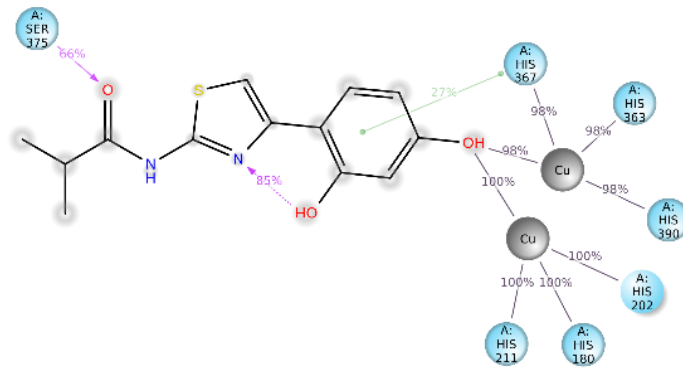
B
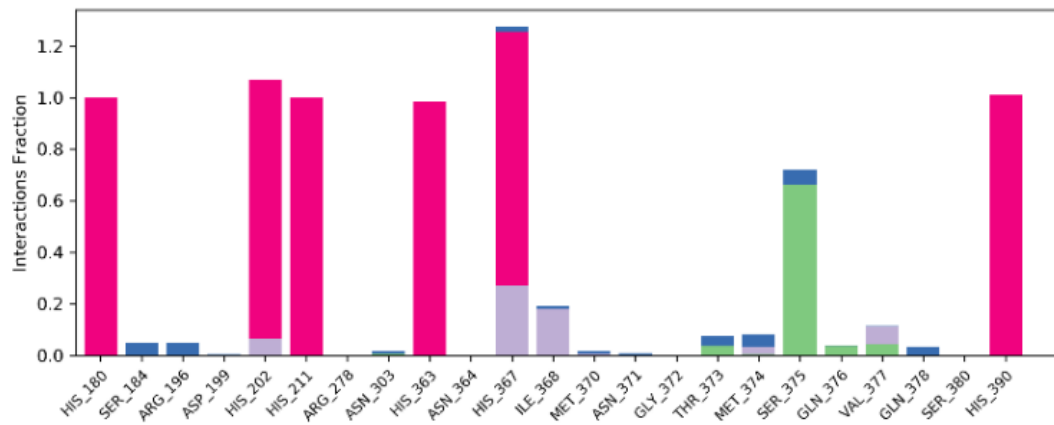
C

D

E

F

Figure 67. Interactions of compound Thiamidol (A), 6 (C) and 7 (E) hTYR occurring during the MD simulation considering the interactions that are manifested more than 30%. The tables in panel B, panel D and panel F show the protein-ligand interactions categorized into four types: Hydrogen Bonds (green bar), Hydrophobic (purple bar), Ionic (fuchsia bar) and Water bridges (blue bar).

Taking in exam the simulations conducted on AbTYR, all the three complexes result slightly more unstable than the ones on hTYR if we consider the ligand RMSD values. (Figure 66 and 68) Even so, also in this case, differences regarding the interaction occurrence of the inhibitors may justify their reversed activity. Firstly, while nice lipophilic interactions and H-bonds were stably formed by Thiamidol tail in hTYR, it poorly retained them in AbTYR. (Figure 67B and 69B) Furthermore, ligand RMSD values exceeding 10.5Å are shown, displaying ligand conformational changes around 10, 30, 50 and 80 ns. Compound 6, similarly as in hTYR, present as well in AbTYR an unstable behavior of its flexible benzylpiperidine fragment, reaching fluctuations of 13.0Å during the simulation. However, during most of the simulation the ligand RMSD values remains between 6 and 9Å. Besides, comparing the protein-ligand contacts of inhibitor **6** in hTYR and AbTYR, it was noticed that more frequent lipophilic interactions made by its lipophilic tail, mainly involving V283, F264 and V248, were present in AbTYR complexes as already seen in static poses. (Figure 69D) Finally, while in hTYR the p-OH group chelated CuA ion, but did not form any other stable contact (e.g. the one with S380), it strongly H-bonded E256 in AbTYR supporting its better activity towards this

isoform. Differently from Thiamidol and compound **6**, the dual inhibitor **7**, despite showing fluctuations that reach 9Å, keeps its lipophilic tail oriented toward the same side of the active site seen in the static poses, stably contacting V283 with the phenylpiperazine moiety and F264, V248 and M257 with the 2-methoxy-phenyl ring. Finally, an additional and stable H-bond between the carbonyl oxygen and N260 sidechain may explain the conformational change of the methoxy-benzoyl moiety seen at 45 ns and support the potency retained by compound **7** on AbTYR (Figure 68C and 69F)

A

B
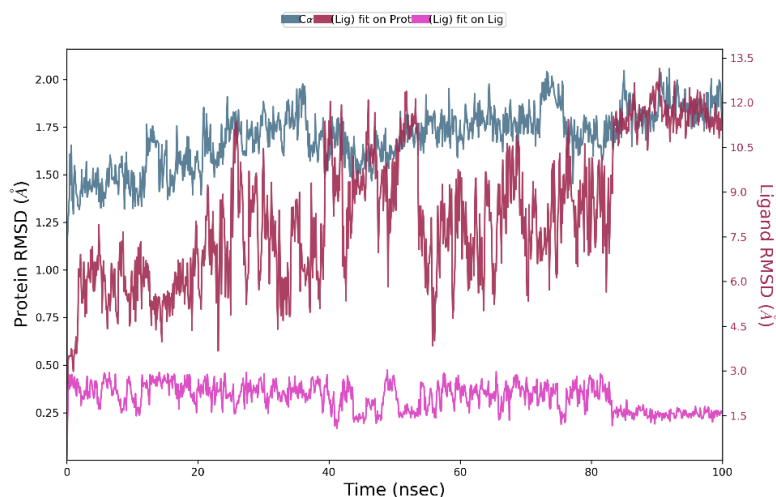
C
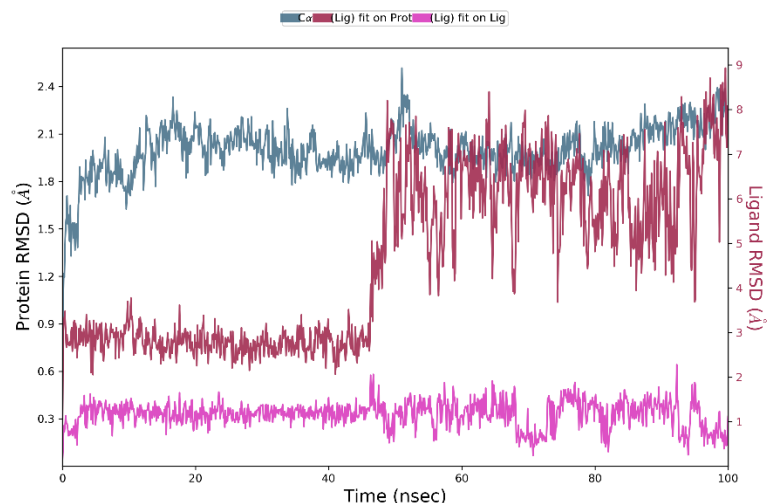
Figure 68. The RMSD plot of the AbTYR in complex with compounds Thiamidol (A), 6 (B) and 7 (C). In the X-axis is reported the simulation time; in the left Y-axis is reported the protein RMSD evolution, while the right Y-axis indicates how stable are the compounds in the binding site during the simulation
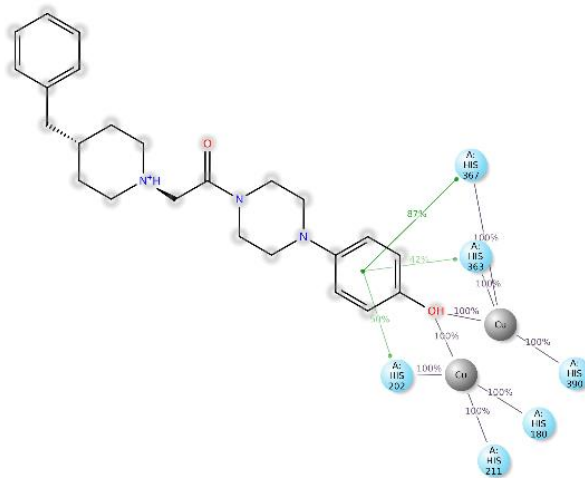
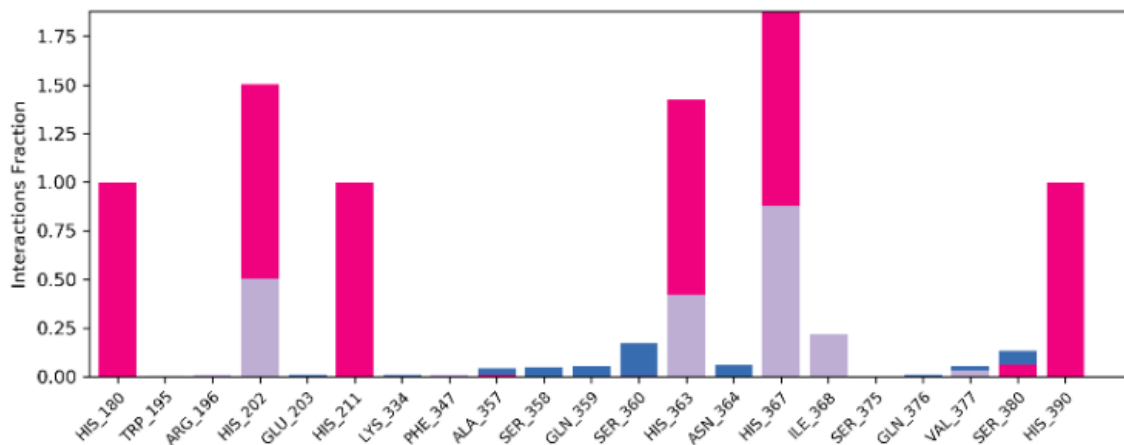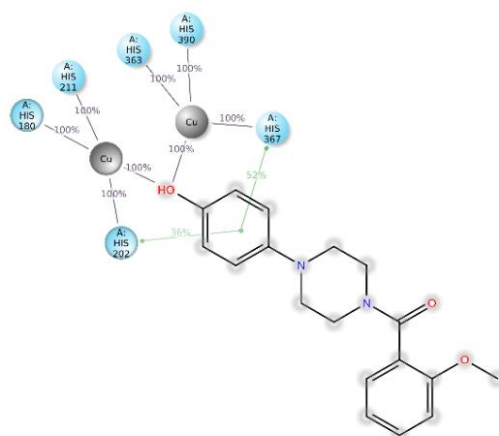**A**
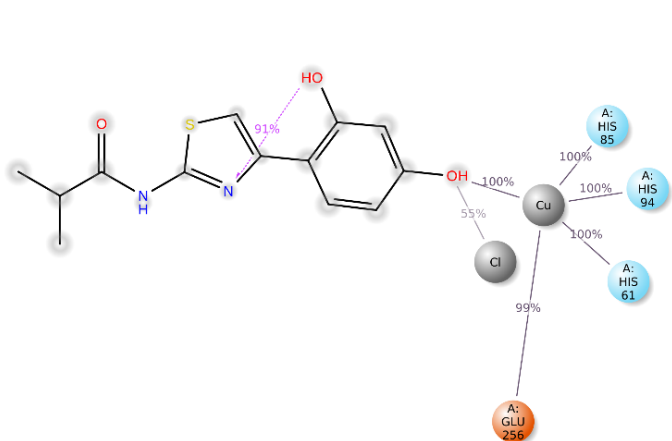
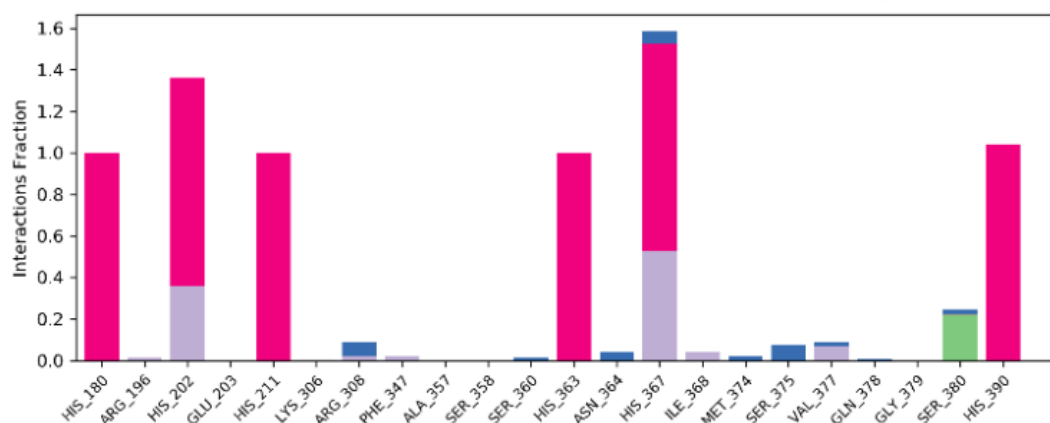

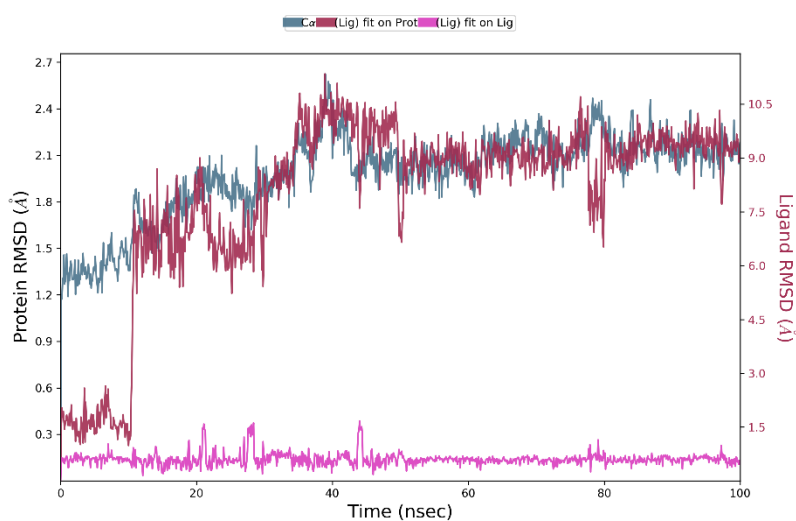**B**
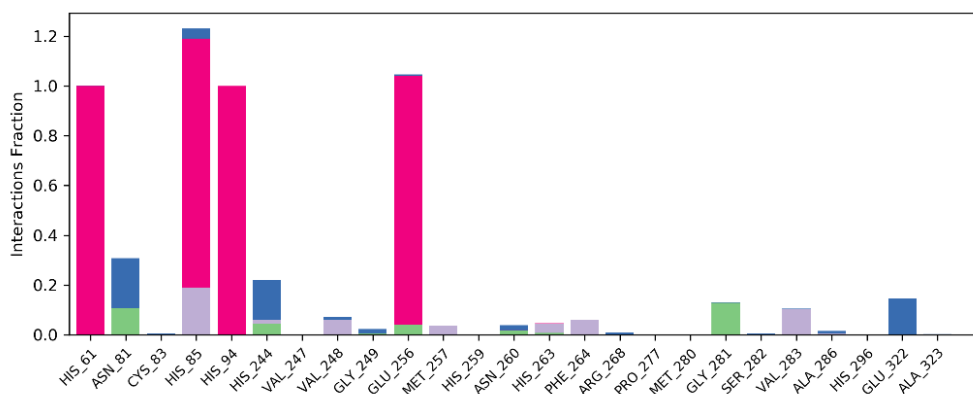
C
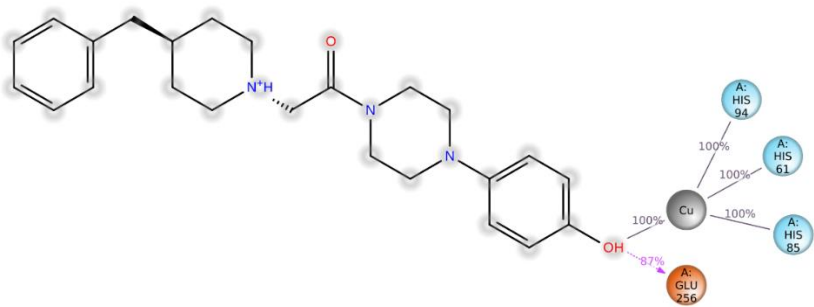
D
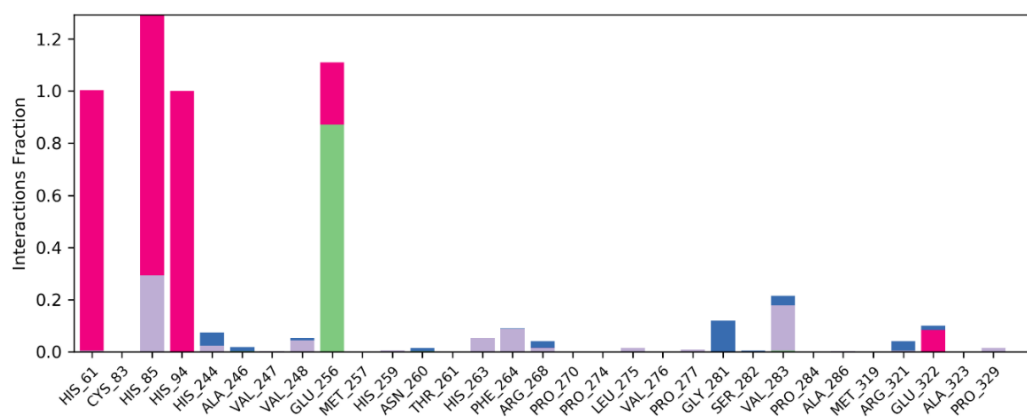
E
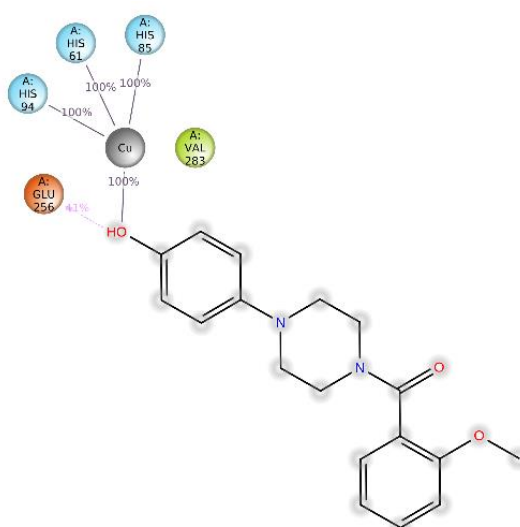
F
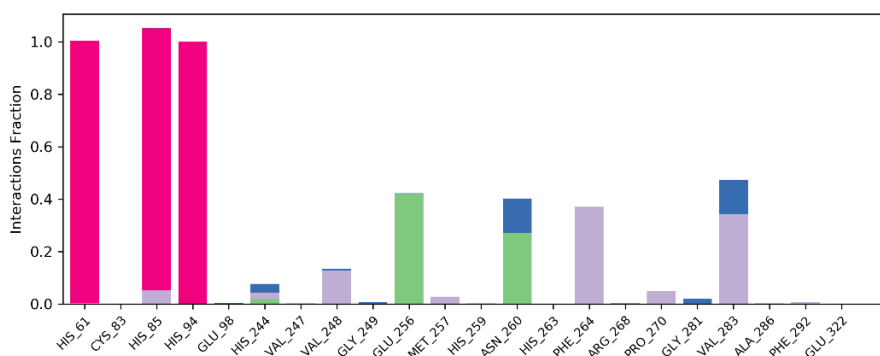
Figure 69. Interactions of compound Thiamidol (A), 6 (C) and 7 (E) hTYR occurring during the MD simulation considering the interactions that are manifested more than 30%. The tables in panel B, panel D and panel F show the protein-ligand interactions categorized into four types: Hydrogen Bonds (green bar), Hydrophobic (purple bar), Ionic (fuchsia bar) and Water bridges (blue bar).

Conclusions

The computational workflow reported in this study, that started with the obtainment of an homology model and a comparative docking procedure aimed to the identification of structural differences and analogies between hTYR and AbTYR exploitable for the design of new hTYR inhibitors that could be initially screened on the cheaper AbTYR, shed the light on potential key residues to consider for achieving potency in both isoforms (specifically S380/A286 – H367/263 - V377/V283 – I368/F264), additionally underscoring the importance of the length and lipophilic nature of the compound scaffolds. The computational insights presented found a final confirmation in the identification of the dual inhibitor **7**, thus providing hints for the future design of potent hTYR inhibitors.

6.1 Materials and methods

Homology modelling: protein preparation

The six initial models were generated giving as input the FASTA file P14679 downloaded from UniProt database. The output results of the four programs were then aligned and superimposed using the sequence and structural alignment method on MOE (Version 2020.09.1) using the Model1 from SwissModel (PDB template: 5M8L) [2] as reference. The models containing Zn ions in the active site taken from their respective pdb templates, were modified converting the Zinc ions into Cu ions, while in the two models obtained from Alphafold, not containing any metal ion in active site, the coordinates were sampled from the model used as reference for the alignment

(Model 1). Structure preparation was performed using MOE by adding missing side chain atoms, applying protonation states at physiological pH using Protonate3D [36], calculating charges using the OPLS-AA force field, capping C termini with NME and N termini by transferring them from complete models. Protonation of the copper-chelating histidines was further adjusted setting them as HID. Clashes and psi-phi outliers reported by the structure preparation wizard concerning residues out of the active-site or distant from the di-copper center were tried to be fixed through the protein builder minimization protocol (minimize residue or minimize side-chain when regarding clashes) using OPLS-AA forcefields. The ones regarding residues close to the copper-chelating histidines were accounted for seeing whether they were confirmed also by WHATCHECK [87]and PROCHECK [10.1107/S0021889892009944] and finally by visual inspection of the van der Waals radii. D-amino-acids as well as cis-amide bonds were accounted to see whether they were confirmed by WHATCHECK (D-amino-acids) and PROCHECK(cis-amide).

Ligand preparation

All the ligands were sketched using ChemDraw and saved as mol files. They were then processed on MOE Database Viewer (version 2020.09.1) using the following protocol: (i) Washing using Dominant protonation protocol setting a pH of 7.4, generating 3-D coordinates (ii) Processing with QuickPrep using default settings (iii) Calculation of charges using the OPLS-AA forcefield with default values, (iv) minimization using the OPLS-AA forcefield with default values and (v) saved in mol2 format.

Docking protocol for the co-crystalized ligands

The models retained from the first prefiltering (Model 4, Model3 and Model6) were submitted to rigid docking procedure on the program GOLD (2021) [37] using the ligands L-Tyrosine(substrate), L-DOPA (substrate) Hydroquinone(inhibitor) and Kojic-acid(inhibitor) earlier co-crystalized in BmTYR and TYRP1 [84,86]. The complex of L-Tyrosine-BmTYR (PDB: 4P6R, chain A) [84] was superimposed to each model and the coordinates of L-Tyrosine were sampled for defining the center of the binding-site with a radius of 10 Å. The ligands were submitted to 100 genetic algorithm runs using the default scoring function(CHEMPLP) and the solutions were clustered using a threshold of 0.75 Å. Scaffold constraints, considering the coordinates of the phenolic ring of L-Tyrosine pose in the X-Ray structure (PDB: 4P6R, chain A), were applied for the docking of L-Tyrosine and L-DOPA. Flip planar N and flip NRR and NHR function was set to true. All other parameters were left as default. The clusters (top ranked solution per cluster) obtained from docking were merged in each respective model analyzed and the X-ray structures of the ligands

used for validating the models were superimposed for choosing the poses from docking to submit to MD simulation. The poses with the highest superimposition with the X-ray conformers were selected for each of the three models.

MD simulation of the co-crystallized ligands on hTYR

Three replicas of 50 ns were performed for each docking complex selected using Desmond software (Version 2021, D.E. Shaw Research, 120 W. 45th St, NY, USA). Each docking complex was prepared prior the simulation as follows: (i) Removed N-terminus (signal peptide, residues: 1–18) and C-terminus (cytosolic domain, residues: 498–529). For Model 4, which lacked of the transmembrane domain (residues: 476–497), MOE (version 2020.09.01) has been used to align Model 3 on Model 4 and for sampling atom coordinates of the target region from the former, starting from the flanking region with highest superimposition in the two models, and (ii) Preprocessed the docking complexes on Maestro(Schrödinger, NY, USA) using the Structure Preparation Wizard, recapping both N and C-termini and leaving the other settings as default. Each system was created through the Desmond System builder tool using the following settings.

- Solvent model: TIP3P

- Forcefields: OPLs3e

- Box shape: orthorombic

- Box size: 30 x 40 x 40

- Membrane model: POPE

- Transmembrane residues: 476 to 497

- Buffer concentration (NaCl): 0.15 M

- Calculate the charges of each complexes and neutralize with counterion according to the system charge.

The simulation was performed at 310 K, using NPγT ensemble and the Noose-Hoover chain thermostat. The atom coordinates for trajectory analysis were recorded each 50ps (1000 frames). A random seed was generated for each of the three replicas simulated per docking complex.

Docking protocol for thiamidol, compounds 6 and 7 on hTYR

The same settings employed for the docking of the ligands used to validate the homology models of hTYR were applied for the docking Thiamidol and inhibitor 6. The top ranked pose of each ligand was selected for MM-GBSA binding energy calculation on Prime (Schrodinger) prior binding mode comparison.

Docking protocol for thiamidol, compounds 6 and 7 on AbTYR

The three compounds object of the study were docked in AbTYR (PDB code: 2Y9X)[96]. The protein structure was prepared using the Protein Preparation Wizard using the default setting. Again, 100 GA runs per compound were performed on GOLD software (2021), using the default settings and clustering docking solution using a threshold of 0.75 Å. A 10 Å radius from the following coordinates was set to define the binding-site: 10.021; - 28.823; - 43.596. A corrected version of ASP scoring function which has an additional metal coordination term, was employed for ranking the docking poses, since a better superposition during re-docking of the native co-crystallized ligand (Tropolone) was observed. The top ranked pose of each ligand was selected for MM-GBSA binding energy calculation on Prime (Schrodinger) prior binding mode comparison.

MM - GBSA calculation

The MM-GBSA calculation was performed using the Prime MM-GBSA [97] tool of the Schrödinger Suite [release 2020–3]. First, the Refine Protein-Ligand Complex function of Prime was used to optimize the complex from the docking calculation, considering the refinement of the residues within 5 Å of the ligands. VSGB and OPL3e were employed as the solvation model and force field, respectively. In addition, constraints were applied to the two copper ions and, in the case of hTYR, the

membrane was set up at the transmembrane residues 476–497 level. Then, for each complex the binding energy was predicted by means the MM-GBSA method. Again, VSGB was used as the solvation model, OPLS3e was set as the force field, and the implicit membrane model was employed only for the hTYR complexes. The other parameters were kept as default values.

Interaction analysis

The minimized complexes of Thiamidol, 6 and 7 with hTYR and AbTYR obtained from MM-GBSA calculation were analyzed on three different platforms, whose results were merged in order to develop our SAR hypothesis.

- Discovery Studio Ligand-receptor interaction tool to account lipophilic (described as Alkyl, phi – Alkyl, phi - sigma or phi – sulfur), phi-phi (stacked or T-shaped) and ionic interactions, as well as solvent exposure;

- LigPlus to account for metal coordination and van der Waals interactions

- Ligandscout (v.4.4.8): pharmacophores were employed to account hydrogen-bonds, lipophilic, phi-phi and ionic interactions involving specific chemical-physics properties of the ligand and their

environmental patterns. Receptor binding surfaces (data not shown) of each complex were used to rationalize vdW interactions reported by LigPlus according to the nature of the environment/binding-site surfaces (hydrophobic or hydrophilic);

The results obtained by the two software were merged to trace the SAR of the inhibitors for two the enzymes examined. All the settings were left as default.

MD simulations of Thiamidol, compounds 6 and 7 into hTYR homology model and AbTYR

The docking complexes obtained from GOLD software were firstly prepared using the Protein Preparation Wizard in Maestro (v.2020), removing the transmembrane domain of hTYR (residues 476 to 497), then capping N and C termini and leaving all the other settings as default for both hTYR and AbTYR complexes. The systems were prepared for both set of complexes (hTYR and AbTYR) using a 15 x 15 x 15 TIP3P box, using Na+ and Cl- as counterion and adding a salt buffer of 0.15 M. A 100 ns simulation, recording frames with an interval of 100 ps, has been performed using a NPT ensemble at 310 K and 1.01325 bar on Desmond software (v.2020)

Supplementary material

Supporting information: Experimental section 1.3

hCA VA homology modelling validation data
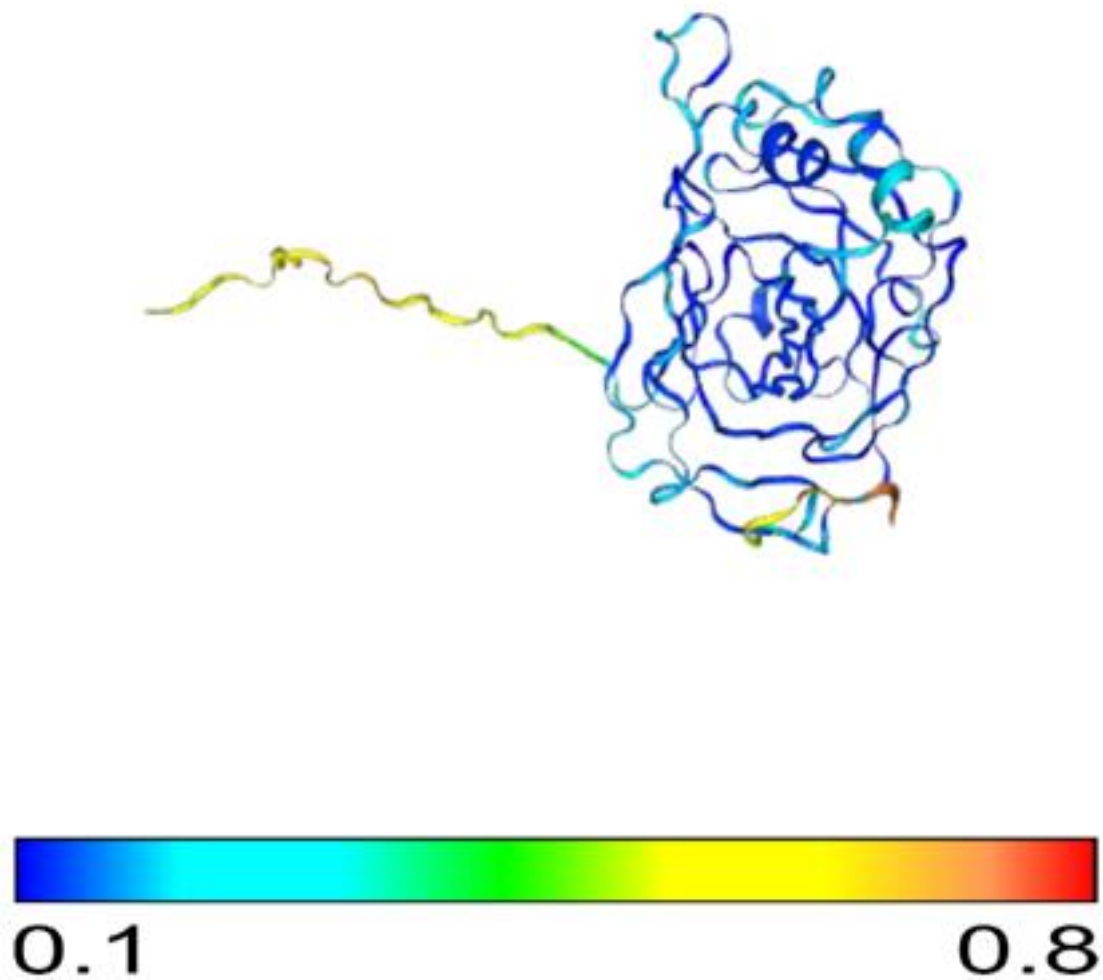
Figure S1. hCA VA homology model quality assessment by Topscore measurement. Blue regions correspond to low predicted errors (high quality). Red regions correspond to high predicted errors (low quality) (see color scale at the bottom).[98]
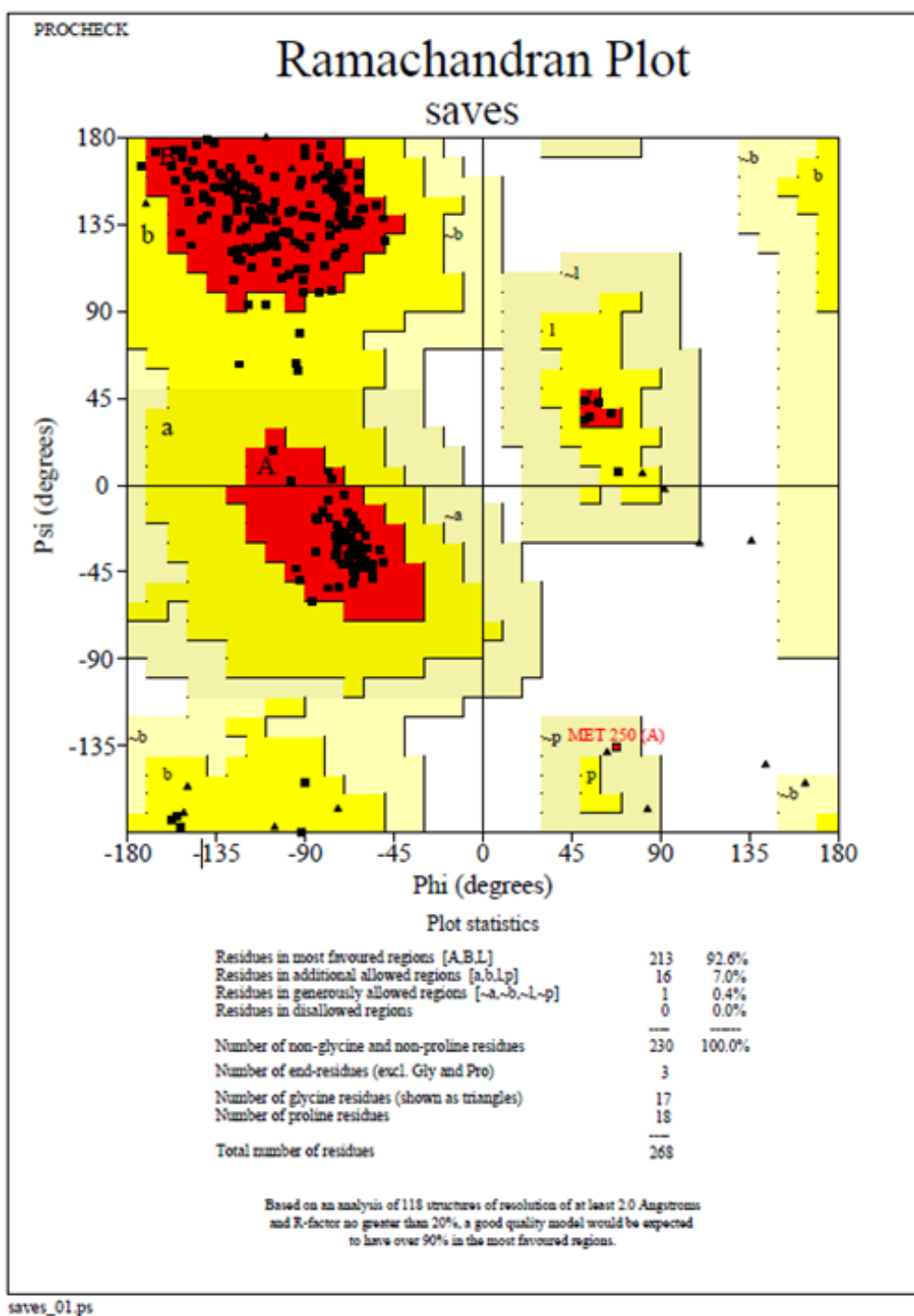
Figure S2. Ramachandran plot made with Procheck and SAVES for the homology model of hCA VA. Each black spot represents a residue (glycines as triangles, any other residues as a square). Red regions represent the most favoured values of Psi and Phi angles, yellow regions represent allowed or generously allowed (pale yellow) values of Psi and Phi angles; finally, white regions indicate not allowed values of Psi and Phi.[88]

127

hCA VA Virtual screening results

Table S1. Virtual Screening results on the 'Specs Compound Library' of 209,000 compounds (https://www.specs.net). The first round of LBVS provided 81 hit compounds. In the second round, the SBVS provided 38 hit compounds. Finally, by using modeled hCA VA the SBVS selected 30 hit compounds. Legend: ● compound retained; **X** compound filtered out.

| entry	1st round	2nd round	3rd round	smiles	IDNUMBER	VAME ID
1.	●	●	●	[H]N([H])S(=O)(=O)C1=C([H])C([H])=C(N=C1[H])N([H])C1=C([H])C([H])=C(=C1[H])C(F)(F)F	AJ-333/25006234	1
2.	●	●	●	[H]N([H])S(=O)(=O)C1=C([H])C([H])=C(N([H])C(=O)C2=C(ON=C2C2=C(Cl)C([H])=C([H])C([H])=C2Cl)C([H])([H])[H])C([H])=C1[H]	AK-968/12342186	2
3.	●	●	●	[H]N([H])S(=O)(=O)C1=C([H])C([H])=C(\\N=C(/C([H])([H])[H])[C@@]2([H])C(=O)OC(=C([H])C2=O)C([H])([H])[H])C([H])=C1[H]	AG-205/36732060	3
4.	●	●	●	[H]N([H])S(=O)(=O)C1=C([H])C([H])=C(N([H])C(=O)C([H])([H])N2C([H])=NC3=C(C(=C(S3)C([H])([H])[H])C([H])([H])[H])C2=O)C([H])=C1[H]	AO-476/43414289	4
5.	●	●	●	[H]N([H])S(=O)(=O)C1=C([H])C([H])=C(N([H])C(=S)N([H])C(=O)C2=C([H])C([H])=C(Cl)C([H])=C2Cl)C([H])=C1[H]	AN-329/41572627	5
6.	●	●	●	[H]N([H])S(=O)(=O)C1=C([H])C2=C(N=C(S2)N([H])C(=O)C2=C([H])C([H])=C([H])C([H])=C2Cl)C([H])=C1[H]	AG-219/09033021	6
7.	●	●	●	[H]N([H])S(=O)(=O)C1=C([H])C([H])=C(N([H])[C@]([H])(N([H])C(=O)C([H])(C([H])([H])[H])C([H])([H])[H])C(Cl)(Cl)Cl)C([H])=C1[H]	AE-848/07790029	7
8.	●	●	●	[H]N([H])S(=O)(=O)C1=C([H])C([H])=C(N([H])C(=O)C([H])([H])SC2=C([H])C(=NC3=NC([H])=NN23)C2=C([H])C([H])=C([H])C([H])=C2[H])C([H])=C1[H]	AO-476/43421025	8
9.	●	●	●	[H]N([H])S(=O)(=O)C1=C([H])C([H])=C(N([H])C(=O)C2=C(N=N=N2)C2=C([H])C([H])=C([H])C([H])=C2[H])C([H])([H])[H])C([H])=C1[H]	AP-501/43403608	9
10.	●	●	●	[H]N([H])S(=O)(=O)C1=C([H])C([H])=C(N([H])C([H])=C2C(=O)N(C(=S)N(C2=O)C([H])([H])C([H])([H])[H])C([H])([H])C([H])([H])[H])C([H])=C1[H]	AJ-030/12105722	10
11.	●	●	●	[H]N([H])S(=O)(=O)C1=C([H])C([H])=C(N([H])C(=O)C([H])([H])N2C(=O)C3=C([H])C([H])=C([H])C4=C3C(=C([H])C([H])=C4[H])C2=O)C([H])=C1[H]	AP-906/41642068	11
12.	●	●	●	[H]N([H])S(=O)(=O)C1=C([H])C([H])=C(N([H])C(=O)C2=C([H])C([H])=C(O2)C([H])([H])OC2=C([H])C([H])=C(F)C([H])=C2[H])C([H])=C1[H]	AK-968/40708444	12
13.	●	●	●	[H]N([H])S(=O)(=O)C1=C([H])C([H])=C(N([H])C(=O)C2=C([H])C([H])=C3C([H])=C([H])C([H])=C([H])C3=C2[H])C([H])=C1[H]	AG-690/40638148	13
14.	●	●	●	[H]N([H])S(=O)(=O)C1=C([H])C([H])=C(N([H])C(=O)C([H])([H])S(=O)(=O)C([H])([H])C2=C([H])C([H])=C([H])C([H])=C2[H])C([H])=C1[H]	AJ-292/42648647	14
15.	●	●	●	[H]N([H])S(=O)(=O)C1=C([H])C([H])=C(N([H])C([H])=C(C(=O)OC([H])([H])C([H])([H])[H])C(=O)OC([H])([H])C([H])([H])[H])C([H])=C1[H]	AG-389/33008010	15
16.	●	●	●	[H]N([H])S(=O)(=O)C1=C([H])C([H])=C(N([H])C(=S)N2C([H])([H])C3=C([H])C([H])=C([H])C([H])=C3C([H])([H])C2([H])[H])C([H])=C1[H]	AJ-292/41694495	16
17.	●	●	●	[H]N([H])S(=O)(=O)C1=C([H])C([H])=C(C([H])=C1[H])C([H])([H])C([H])([H])N([H])S(=O)(=O)C1=C(Cl)C([H])=C([H])C(Cl)=C1[H]	AJ-292/42062669	17
18.	●	●	●	[H]N([H])S(=O)(=O)C1=C([H])C([H])=C(N([H])C(=O)C([H])([H])C([H])([H])[C@]2([H])C(=O)OC(C([H])([H])[H])(C([H])([H])[H])C2([H])[H])C([H])=C1[H]	AL-281/42288999	18
19.	●	●	●	[H]N([H])S(=O)(=O)C1=C([H])C([H])=C(N([H])C(=O)C([H])([H])SC2=NC([H])=NC3=C2C(=C(S3)C([H])([H])[H])C([H])([H])[H])C([H])=C1[H]	AO-476/40923368	19
20.	●	●	●	[H]N([H])S(=O)(=O)C1=C([H])C([H])=C(N([H])C(=O)C([H])([H])N([H])S(=O)(=O)C2=C([H])C([H])=C(OC([H])([H])[H])C([H])=C2[H])C([H])=C1[H]	AH-487/42143056	20
21.	●	●	●	[H]N([H])S(=O)(=O)C1=C([H])C([H])=C(N([H])C(=O)C(\\[H])=C(/[H])C2=C(N(N=C2[H])C([H])([H])C([H])([H])[H])C([H])([H])[H])C([H])=C1[H]	AK-968/15605417	21
22.	●	●	●	[H]N([H])S(=O)(=O)C1=C([H])C([H])=C(N([H])C(=O)C([H])([H])N(C([H])([H])[H])[H])S(=O)(=O)C2=C(Cl)C([H])=C([H])C(Cl)=C2[H])C([H])=C1[H]	AH-487/41800142	22
23.	●	●	●	[H]N([H])S(=O)(=O)C1=C([H])C([H])=C(N([H])C(=O)C([H])([H])N2N=C(C(Cl)=C2C([H])([H])[H])[N+]([O-])=O)C([H])=C1[H]	AG-690/14006232	23
24.	●	●	●	[H]N([H])S(=O)(=O)C1=C([H])C([H])=C(N([H])C(=O)C2=C(N=N=C2[H])C([H])([H])C([H])([H])[H])C([H])([H])[H])C([H])=C1[H]	AK-968/40941043	24
25.	●	●	●	[H]N([H])S(=O)(=O)C1=C([H])C([H])=C(N([H])C(=O)C([H])([H])N2N=C(C([H])=C2C2([H])C([H])([H])C2([H])[H])C(F)(F)F)C([H])=C1[H]	AK-968/41171466	25
26.	●	●	●	[H]N([H])S(=O)(=O)C1=C([H])C([H])=C(N([H])C(=O)C2=C(N=C2[H])C2=C([H])C([H])=C([H])C([H])=N2)C([H])([H])[H])C([H])=C1[H]	AP-501/43403646	26

128

#				SMILES	ID	
27.	●	●	●	[H]N([H])S(=O)(=O)C1=C([H])C([H])=C(N([H])C(=O)C([H])([H])SC(=S)N(C([H])([H])C([H])([H])[H])C([H])([H])C([H])([H])[H])C([H])=C1[H]	AF-399/36980038	**27**
28.	●	●	●	[H]N([H])S(=O)(=O)C1=C([H])C([H])=C(N([H])C(=O)C([H])([H])N2C3=C(C([H])=C([H])C([H])=C3[H])C([H])([H])C([H])([H])C2([H])[H])C([H])=C1[H]	AO-476/43362648	**28**
29.	●	●	●	[H]N([H])S(=O)(=O)C1=C([H])C([H])=C(N([H])C(=O)C([H])([H])N2C3=C(C([H])=C([H])C([H])=C3[H])C([H])([H])C2([H])[H])C([H])=C1[H]	AO-476/43362651	**29**
30.	●	●	●	[H]N([H])S(=O)(=O)C1=C([H])C([H])=C(N([H])C(=O)C([H])([H])OC2=C(C([H])=C(Cl)C([H])=C2[H])C([H])([H])[H])C([H])=C1[H]	AK-968/12341015	**30**
31.	●	●	✕	[H]N([H])S(=O)(=O)C1=C([H])C([H])=C(N([H])C(=O)N([H])C2(OC3=C(O2)C([H])=C([H])C([H])=C3[H])C(F)(F)F)C([H])=C1[H]	AS-871/42709691	-
32.	●	●	✕	[H]N([H])S(=O)(=O)C1=C([H])C([H])=C(N([H])C(=O)C2=C([H])C(Br)=C(C([H])=C2[H])C(C([H])([H])[H])(C([H])([H])[H])C([H])([H])[H])C([H])=C1[H]	AN-329/41435149	-
33.	●	●	✕	[H]N([H])S(=O)(=O)C1=C([H])C([H])=C(N([H])C(=O)C2=C([H])C(Br)=C([H])C(=C2OC([H])([H])[H])C([H])([H])[H])C([H])=C1[H]	AN-465/42768143	-
34.	●	●	✕	[H]N([H])S(=O)(=O)C1=C([H])C([H])=C(N([H])C(=O)C2=C([H])C([H])=C(OC([H])([H])[H])C(I)=C2[H])C([H])=C1[H]	AN-329/14085098	-
35.	●	●	✕	[H]N([H])S(=O)(=O)C1=C([H])C([H])=C(N([H])C(=O)C2=C([H])C([H])=C([H])C([H])=C2OC([H])(C([H])([H])[H])C([H])([H])[H])C([H])=C1[H]	AN-329/43385553	-
36.	●	●	✕	[H]N([H])S(=O)(=O)C1=C([H])C([H])=C(N([H])C(=O)C2=C([H])C([H])=C([H])C([H])=C2OC([H])([H])C([H])(C([H])([H])[H])C([H])([H])[H])C([H])=C1[H]	AN-329/43385871	-
37.	●	●	✕	[H]N([H])S(=O)(=O)C1=C([H])C([H])=C(N([H])C(=O)C2=C([H])C([H])=C([H])C([H])=C2OC([H])([H])C([H])([H])C([H])([H])C([H])([H])[H])C([H])=C1[H]	AN-329/43386095	-
38.	●	●	✕	[H]N([H])S(=O)(=O)C1=C([H])C([H])=C(N([H])C([H])([H])C2=C([H])C([H])=C(OC([H])([H])[H])C(OC([H])([H])[H])=C2OC([H])([H])[H])C([H])=C1[H]	AN-465/42833758	-
39.	●	✕	✕	[H]N([H])S(=O)(=O)C1=C([H])C([H])=C(C([H])=C1[H])C([H])([H])N([H])C(=O)C1=C(OC([H])([H])[H])C([H])=C(OC([H])([H])[H])C([H])=C1[H]	AJ-292/14925196	-
40.	●	✕	✕	[H]N([H])S(=O)(=O)C1=C([H])C([H])=C2C([H])=C(OC([H])([H])C([H])([H])C([H])([H])[H])C([H])=C([H])C2=C1[H]	AP-263/43502804	-
41.	●	✕	✕	[H]N([H])S(=O)(=O)C1=C([H])C([H])=C(SC([H])([H])C2=C([H])C([H])=C([H])C([H])=C2[H])N=C1[H]	AJ-333/13050160	-
42.	●	✕	✕	[H]N([H])S(=O)(=O)C1=C([H])C([H])=C(N([H])C(=S)N([H])C(=O)C2=C([H])C3=C(OC([H])([H])O3)C([H])=C2[H])C([H])=C1[H]	AP-970/42769227	-
43.	●	✕	✕	[H]N([H])S(=O)(=O)C1=C([H])C([H])=C(N([H])C(=S)N([H])C(=O)C([H])(C([H])([H])[H])C([H])([H])[H])C([H])=C1[H]	AN-329/42613570	-
44.	●	✕	✕	[H]N([H])S(=O)(=O)C1=C([H])C([H])=C(N([H])C(=S)N([H])C(=O)C([H])([H])C([H])(C([H])([H])[H])C([H])([H])[H])C([H])=C1[H]	AN-329/41401096	-
45.	●	✕	✕	[H]N([H])S(=O)(=O)C1=C([H])C([H])=C(N([H])C(=S)N([H])C([H])([H])C([H])([H])C([H])([H])OC([H])([H])C([H])([H])[H])C([H])=C1[H]	AJ-292/41694749	-
46.	●	✕	✕	[H]N([H])S(=O)(=O)C1=C([H])C([H])=C(N([H])C(=O)C2=NN(C([H])=N2)C2=C([H])C([H])=C(Cl)C([H])=C2[H])C([H])=C1[H]	AP-501/43397807	-
47.	●	✕	✕	[H]N([H])S(=O)(=O)C1=C([H])C([H])=C(N([H])C(=O)C2=NN(C([H])=N2)C2=C([H])C([H])=C(C([H])=C2[H])C([H])([H])[H])C([H])=C1[H]	AP-501/43397727	-
48.	●	✕	✕	[H]N([H])S(=O)(=O)C1=C([H])C([H])=C(N([H])C(=O)C2=C(N(N=C2[H])C2=C([H])C([H])=C([H])C([H])=N2)C([H])([H])C([H])([H])[H])C([H])=C1[H]	AP-501/43403588	-
49.	●	✕	✕	[H]N([H])S(=O)(=O)C1=C([H])C([H])=C(N([H])C(=O)C2=C([H])C([H])=C(C([H])=C2[H])C([H])([H])C([H])([H])[H])C([H])=C1[H]	AP-970/43376291	-
50.	●	✕	✕	[H]N([H])S(=O)(=O)C1=C([H])C([H])=C(N([H])C(=O)C([H])([H])SC2=NN=C(N2C([H])([H])C([H])([H])[H])C([H])([H])N2N([H])C(=C([H])C([H])([H])C2=O)C([H])([H])[H])C([H])=C1[H]	AO-476/43415802	-
51.	●	✕	✕	[H]N([H])S(=O)(=O)C1=C([H])C([H])=C(N([H])C(=O)C([H])([H])SC2=NN=C(C3=C(N(N=C23)C2=C([H])C([H])=C([H])C([H])=C2[H])C([H])([H])[H])C([H])([H])[H])C([H])=C1[H]	AO-476/43421086	-
52.	●	✕	✕	[H]N([H])S(=O)(=O)C1=C([H])C([H])=C(N([H])C(=O)C([H])([H])SC2=C(C#N)C(=C([H])C(=N2)C([H])([H])[H])C([H])([H])[H])C([H])=C1[H]	AG-690/13770041	-
53.	●	✕	✕	[H]N([H])S(=O)(=O)C1=C([H])C([H])=C(N([H])C(=O)C([H])([H])OC2=C(Cl)C([H])=C(Br)C([H])=C2[H])C([H])=C1[H]	AN-329/41675142	-
54.	●	✕	✕	[H]N([H])S(=O)(=O)C1=C([H])C([H])=C(N([H])C(=O)C([H])([H])OC2=C(C([H])=C(Br)C([H])=C2[H])C([H])([H])[H])C([H])=C1[H]	AN-329/41328742	-
55.	●	✕	✕	[H]N([H])S(=O)(=O)C1=C([H])C([H])=C(N([H])C(=O)C([H])([H])OC2=C(C([H])=C([H])C([H])=C2C([H])([H])[H])C([H])([H])[H])C([H])=C1[H]	AN-329/42138558	-
56.	●	✕	✕	[H]N([H])S(=O)(=O)C1=C([H])C([H])=C(N([H])C(=O)C([H])([H])OC2=C(C([H])=C([H])C([H])=C2[H])C([H])([H])[H])C([H])=C1[H]	AN-329/15333057	-

129

No.				SMILES	ID	
57.	●	X	X	[H]N([H])S(=O)(=O)C1=C([H])C([H])=C(N([H])C(=O)C([H])([H])OC2=C(C([H])=C([H])C([H])=C2[H])[C@]([H])(C([H])([H])[H])C([H])([H])C([H])([H])[H])C([H])=C1[H]	AN-329/41868731	-
58.	●	X	X	[H]N([H])S(=O)(=O)C1=C([H])C([H])=C(N([H])C(=O)C([H])([H])OC2=C(Br)C([H])=C(Cl)C([H])=C2[H])C([H])=C1[H]	AN-329/41835947	-
59.	●	X	X	[H]N([H])S(=O)(=O)C1=C([H])C([H])=C(N([H])C(=O)C([H])([H])OC2=C(Br)C([H])=C(C([H])=C2[H])C([H])([H])C([H])([H])[H])C([H])=C1[H]	AN-329/41609874	-
60.	●	X	X	[H]N([H])S(=O)(=O)C1=C([H])C([H])=C(N([H])C(=O)C([H])([H])OC2=C(Br)C([H])=C(C([H])=C2[H])C([H])([H])[H])C([H])=C1[H]	AN-329/40863743	-
61.	●	X	X	[H]N([H])S(=O)(=O)C1=C([H])C([H])=C(N([H])C(=O)C([H])([H])OC2=C([H])C(=C([H])C([H])=C2C([H])(C([H])([H])[H])C([H])([H])[H])C([H])([H])[H])C([H])=C1[H]	AG-690/15437875	-
62.	●	X	X	[H]N([H])S(=O)(=O)C1=C([H])C([H])=C(N([H])C(=O)C([H])([H])OC2=C([H])C(=C([H])C([H])=C2[H])C([H])=C1[H]	AN-329/10165056	-
63.	●	X	X	[H]N([H])S(=O)(=O)C1=C([H])C([H])=C(N([H])C(=O)C([H])([H])OC2=C([H])C([H])=C(C([H])=C2[H])C([H])(C([H])([H])[H])C([H])([H])[H])C([H])=C1[H]	AN-329/42138523	-
64.	●	X	X	[H]N([H])S(=O)(=O)C1=C([H])C([H])=C(N([H])C(=O)C([H])([H])OC2=C([H])C([H])=C(Br)C(=C2[H])C([H])([H])[H])C([H])=C1[H]	AN-329/41044481	-
65.	●	X	X	[H]N([H])S(=O)(=O)C1=C([H])C([H])=C(N([H])C(=O)C([H])([H])OC2=C([H])C([H])=C([H])C([H])=C2OC([H])([H])[H])C([H])=C1[H]	AG-690/15441479	-
66.	●	X	X	[H]N([H])S(=O)(=O)C1=C([H])C([H])=C(N([H])C(=O)C([H])([H])OC2=C([H])C([H])=C([H])C([H])=C2Cl)C([H])=C1[H]	AN-329/12386227	-
67.	●	X	X	[H]N([H])S(=O)(=O)C1=C([H])C([H])=C(N([H])C(=O)C([H])([H])N(C([H])([H])[H])S(=O)(=O)C2=C(C([H])=C(C([H])=C2C([H])([H])[H])C([H])([H])[H])C([H])([H])[H])C([H])=C1[H]	AN-698/41932905	-
68.	●	X	X	[H]N([H])S(=O)(=O)C1=C([H])C([H])=C(N([H])C(=O)C([H])([H])C([H])([H])C(=O)OC2=C([H])C([H])=C(C([H])=C2[H])C([H])([H])[H])C([H])=C1[H]	AN-329/40805572	-
69.	●	X	X	[H]N([H])S(=O)(=O)C1=C([H])C([H])=C(N([H])C(=O)[C@@]([H])(OC2=C(C([H])=C([H])C(=C2[H])C([H])([H])[H])C([H])([H])[H])C([H])([H])[H])C(=C1[H]	AN-329/43341696	-
70.	●	X	X	[H]N([H])S(=O)(=O)C1=C([H])C([H])=C(N([H])C(=O)[C@@]([H])(OC2=C(C([H])=C([H])C([H])=C2[H])C([H])([H])[H])C([H])([H])C([H])([H])[H])C([H])=C1[H]	AN-329/43041618	-
71.	●	X	X	[H]N([H])S(=O)(=O)C1=C([H])C([H])=C(N([H])C(=O)[C@@]([H])(OC2=C([H])C(Cl)=C([H])C([H])=C2[H])C([H])([H])[H])C([H])=C1[H]	AK-968/12383420	-
72.	●	X	X	[H]N([H])S(=O)(=O)C1=C([H])C([H])=C(N([H])C(=O)[C@@]([H])(OC2=C([H])C(Cl)=C(Cl)C([H])=C2Cl)C([H])([H])[H])C([H])=C1[H]	AN-329/15538158	-
73.	●	X	X	[H]N([H])S(=O)(=O)C1=C([H])C([H])=C(N([H])C(=O)[C@@]([H])(OC2=C([H])C(C([H])=C2[H])C([H])([H])C([H])([H])[H])C([H])([H])[H])C([H])=C1[H]	AN-329/43385910	-
74.	●	X	X	[H]N([H])S(=O)(=O)C1=C([H])C([H])=C(N([H])C(=O)[C@@]([H])(OC2=C([H])C([H])=C([H])C([H])=C2[H])C([H])([H])C([H])([H])[H])C([H])=C1[H]	AK-968/12115057	-
75.	●	X	X	[H]N([H])S(=O)(=O)C1=C([H])C([H])=C(N([H])C(=O)[C@]([H])(OC2=C([H])C([H])=C(C([H])=C2[H])C([H])([H])[H])C([H])([H])C([H])([H])[H])C([H])=C1[H]	AN-329/43341771	-
76.	●	X	X	[H]N([H])S(=O)(=O)C1=C([H])C([H])=C(N([H])C([H])([H])C2=C([H])C([H])=C([H])C([H])=C2OC([H])([H])[H])C([H])=C1[H]	AN-465/42767434	-
77.	●	X	X	[H]N([H])S(=O)(=O)C1=C([H])C([H])=C(C([H])=C1[H])N1N=C(S\\C1=N/C#N)C(=O)OC([H])([H])C([H])([H])[H]	AI-067/31571048	-
78.	●	X	X	[H]N([H])S(=O)(=O)C1=C([H])C([H])=C(C([H])=C1[H])C([H])([H])N([H])C(=O)C1=C([H])C([H])=C(N([H])C(=O)C([H])(C([H])([H])[H])C([H])([H])[H])C([H])=C1[H]	AJ-292/42648429	-
79.	●	X	X	[H]N([H])S(=O)(=O)C1=C([H])C([H])=C(C([H])=C1[H])C([H])([H])C([H])([H])N([H])C(=O)C1=NOC(=C1C1=C(Cl)C([H])=C([H])C([H])=C1[H])C([H])([H])[H]	AJ-292/40762784	-
80.	●	X	X	[H]N([H])S(=O)(=O)C1=C([H])C([H])=C(C([H])=C1[H])C([H])([H])C([H])([H])N([H])C(=O)C1=C([H])C(=C(C([H])=C1[H])C([H])([H])[H])C([H])([H])[H]	AJ-292/42062787	-
81.	●	X	X	[H]N([H])N1C(SC([H])([H])C(=O)N([H])C2=C([H])C([H])=C(C([H])=C2[H])S(=O)(=O)N([H])[H])=NC2=C(C3=C(S2)C([H])([H])C([H])([H])C([H])([H])C3([H])[H])C1=O	AO-476/43417621	-

Table S2. Docking score values of inhibitors VAME 01-30

Compounds	CHEMPLP Docking Score
VAME-01	69.57
VAME-02	60.76
VAME-03	60.40
VAME-04	69.48
VAME-05	60.12
VAME-06	61.23
VAME-07	58.40
VAME-08	83.97
VAME-09	57.94
VAME-10	63.31
VAME-11	75.27
VAME-12	70.70
VAME-13	59.09
VAME-14	68.16
VAME-15	62.07
VAME-16	60.79
VAME-17	54.45
VAME-18	64.11
VAME-19	69.68
VAME-20	51.74
VAME-21	57.84
VAME-22	36.61
VAME-23	65.88
VAME-24	57.50
VAME-25	70.74
VAME-26	58.69
VAME-27	64.05
VAME-28	71.92
VAME-29	75.35
VAME-30	57.70

Supporting information: Chapter 5

hTYR homology model validation data
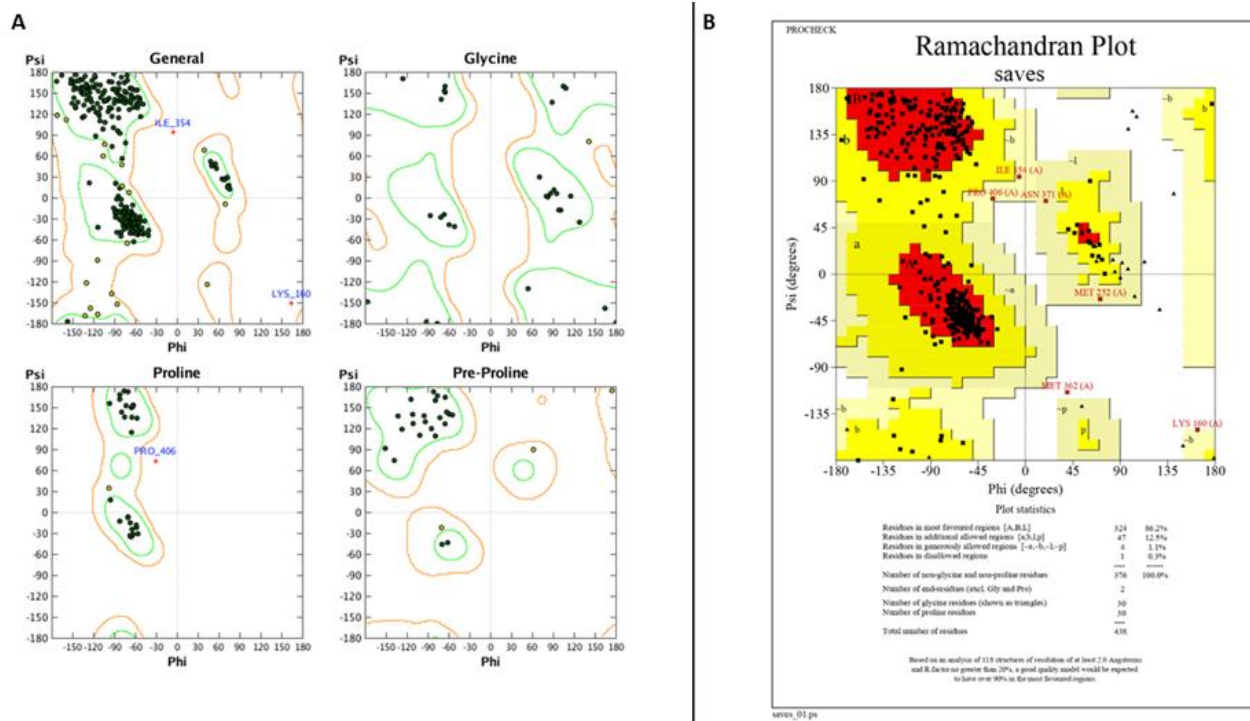
Figure S3. Ramachandran plots of Model 4 after refinement. (A) Plot generated by MOE software. Green and orange contour represent respectively the most favoured and the allowed regions, while Psi-Phi outliers are marked by red crosses and indicated by the text. (B) Plot created by PROCHECK software and statistics reports generated via SAVES server. Red areas describe the most favored combination of Psi and Phi values, yellow areas represent allowed ones, light – yellow regions mark generously allowed values of Psi and Phi and white areas disallowed ones. Therefore, violations are represented by the red squares in the white parts of the plot.
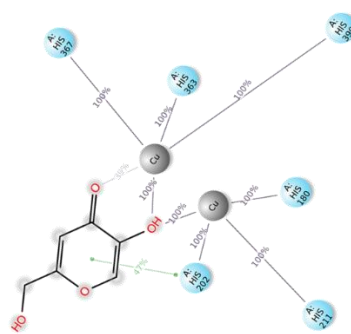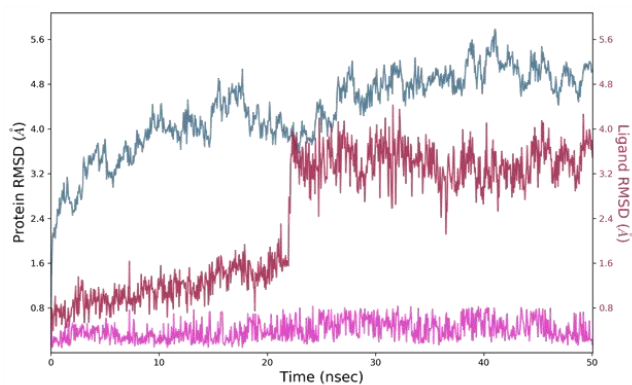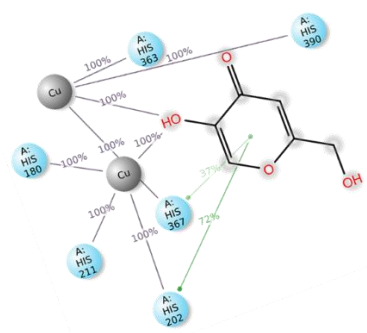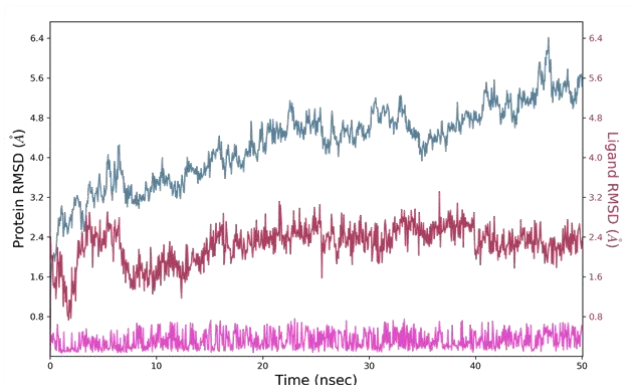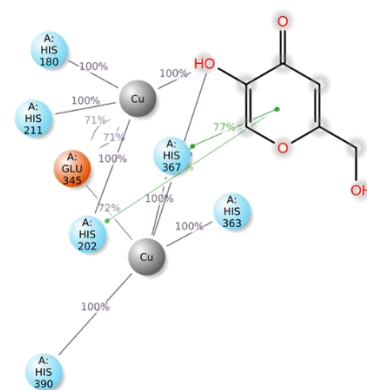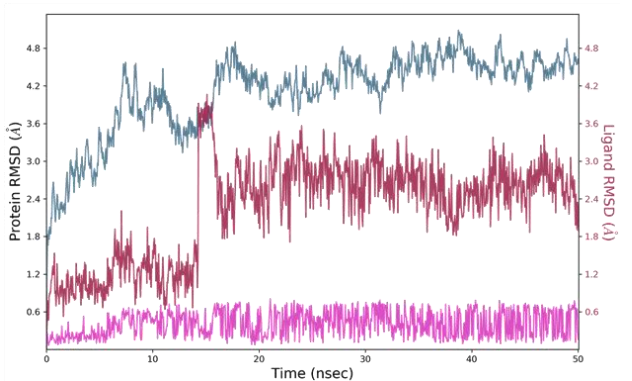
Figure S4. Simulation interaction diagram (SID) of 50 ns MD simulation of kojic acid docked on Model 4, generated via Desmond Software (v. 2020). The plots shown from the top to the bottom refer to each replicon of the simulation. (Left) RMSD values of the protein C-α during the simulation, aligning each frame of the simulation to the protein backbone atoms of the first frame (blue plot). RMSD values of the ligand atoms along the simulation, aligning each frame of the simulation to the protein backbone atoms in the first frame (red plot). RMSD values of the ligand atoms along the simulation, aligning each frame of the simulation to the ligand atoms in the first frame (magenta plot). (Right) Diagram of the interaction between kojic acid and hTYR Model 4 encountered with an occurrence greater than 30% during the simulation. Cu ions are represented by grey spheres while blue and red spheres represent respectively polar and negatively charged residue. Metal coordination is represented by grey lines while phi − phi interactions by green lines. Close to each interaction, its occurrence along the simulation (expressed in percentage of frames) is reported.

Acknowledgements

REFERENCES

1. Lothian A, Hare DJ, Grimm R, Ryan TM, Masters CL, Roberts BR: Metalloproteomics: principles, challenges and applications to neurodegeneration. *Frontiers in aging neuroscience* 2013, 5:35.
2. McCall KA, Huang C, Fierke CA: Function and mechanism of zinc metalloenzymes. *The Journal of nutrition* 2000, 130(5S Suppl):1437S-1446S.
3. Christianson DW: Structural chemistry and biology of manganese metalloenzymes. *Progress in biophysics and molecular biology* 1997, 67(2-3):217-252.
4. Nozadze E, Arutinova N, Tsakadze L, Shioshvili L, Leladze M, Dzneladze S, Chkadua G: Molecular mechanism of Mg-ATPase activity. *The Journal of membrane biology* 2015, 248(2):295-300.
5. Fischer K, Barbier GG, Hecht HJ, Mendel RR, Campbell WH, Schwarz G: Structural basis of eukaryotic nitrate reduction: crystal structures of the nitrate reductase active site. *The Plant cell* 2005, 17(4):1167-1179.
6. Alfano M, Cavazza C: Structure, function, and biosynthesis of nickel-dependent enzymes. *Protein science : a publication of the Protein Society* 2020, 29(5):1071-1089.
7. Chen AY, Adamek RN, Dick BL, Credille CV, Morrison CN, Cohen SM: Targeting Metalloenzymes for Therapeutic Intervention. *Chemical reviews* 2019, 119(2):1323-1455.
8. Supuran CT: Structure and function of carbonic anhydrases. *The Biochemical journal* 2016, 473(14):2023-2032.
9. Supuran CT: How many carbonic anhydrase inhibition mechanisms exist? *Journal of enzyme inhibition and medicinal chemistry* 2016, 31(3):345-360.
10. Mishra CB, Tiwari M, Supuran CT: Progress in the development of human carbonic anhydrase inhibitors and their pharmacological applications: Where are we today? *Medicinal research reviews* 2020, 40(6):2485-2565.
11. Lomelino CL, Andring JT, McKenna R: Crystallography and Its Impact on Carbonic Anhydrase Research. *International journal of medicinal chemistry* 2018, 2018:9419521.
12. Aggarwal M, Boone CD, Kondeti B, McKenna R: Structural annotation of human carbonic anhydrases. *Journal of enzyme inhibition and medicinal chemistry* 2013, 28(2):267-277.
13. Cercato C, Fonseca FA: Cardiovascular risk and obesity. *Diabetology & metabolic syndrome* 2019, 11:74.
14. Anandhakrishnan A, Korbonits M: Glucagon-like peptide 1 in the pathophysiology and pharmacotherapy of clinical obesity. *World journal of diabetes* 2016, 7(20):572-598.
15. Aprahamian TR, Sam F: Adiponectin in cardiovascular inflammation and obesity. *International journal of inflammation* 2011, 2011:376909.
16. Ruban A, Stoenchev K, Ashrafian H, Teare J: Current treatments for obesity. *Clin Med (Lond)* 2019, 19(3):205-212.
17. Tak YJ, Lee SY: Long-Term Efficacy and Safety of Anti-Obesity Treatment: Where Do We Stand? *Current obesity reports* 2021, 10(1):14-30.
18. Vullo D, Voipio J, Innocenti A, Rivera C, Ranki H, Scozzafava A, Kaila K, Supuran CT: Carbonic anhydrase inhibitors. Inhibition of the human cytosolic isozyme VII with aromatic and heterocyclic sulfonamides. *Bioorganic & medicinal chemistry letters* 2005, 15(4):971-976.
19. Di Fiore A, De Simone G, Alterio V, Riccio V, Winum JY, Carta F, Supuran CT: The anticonvulsant sulfamide JNJ-26990990 and its S,S-dioxide analog strongly inhibit carbonic anhydrases: solution and X-ray crystallographic studies. *Organic & biomolecular chemistry* 2016, 14(21):4853-4858.
20. Queen A, Khan P, Azam A, Hassan MI: Understanding the Role and Mechanism of Carbonic Anhydrase V in Obesity and its Therapeutic Implications. *Current protein & peptide science* 2018, 19(9):909-923.
21. Aspatwar A, Supuran CT, Waheed A, Sly WS, Parkkila S: Mitochondrial carbonic anhydrase VA and VB: properties and roles in health and disease. *The Journal of physiology* 2023, 601(2):257-274.
22. Boriack-Sjodin PA, Heck RW, Laipis PJ, Silverman DN, Christianson DW: Structure determination of murine mitochondrial carbonic anhydrase V at 2.45-A resolution: implications for catalytic proton

transfer and inhibitor design. *Proceedings of the National Academy of Sciences of the United States of America* 1995, 92(24):10949-10953.

23. Heck RW, Boriack-Sjodin PA, Qian M, Tu C, Christianson DW, Laipis PJ, Silverman DN: Structure-based design of an intramolecular proton transfer site in murine carbonic anhydrase V. *Biochemistry* 1996, 35(36):11605-11611.

24. Jude KM, Wright SK, Tu C, Silverman DN, Viola RE, Christianson DW: Crystal structure of F65A/Y131C-methylimidazole carbonic anhydrase V reveals architectural features of an engineered proton shuttle. *Biochemistry* 2002, 41(8):2485-2491.

25. Smaine FZ, Pacchiano F, Rami M, Barragan-Montero V, Vullo D, Scozzafava A, Winum JY, Supuran CT: Carbonic anhydrase inhibitors: 2-substituted-1,3,4-thiadiazole-5-sulfamides act as powerful and selective inhibitors of the mitochondrial isozymes VA and VB over the cytosolic and membrane-associated carbonic anhydrases I, II and IV. *Bioorganic & medicinal chemistry letters* 2008, 18(24):6332-6335.

26. Guzel O, Innocenti A, Scozzafava A, Salman A, Supuran CT: Carbonic anhydrase inhibitors. Phenacetyl-, pyridylacetyl- and thienylacetyl-substituted aromatic sulfonamides act as potent and selective isoform VII inhibitors. *Bioorganic & medicinal chemistry letters* 2009, 19(12):3170-3173.

27. Vullo D, Franchi M, Gallori E, Antel J, Scozzafava A, Supuran CT: Carbonic anhydrase inhibitors. Inhibition of mitochondrial isozyme V with aromatic and heterocyclic sulfonamides. *Journal of medicinal chemistry* 2004, 47(5):1272-1279.

28. Maresca A, Supuran CT: (R)-/(S)-10-camphorsulfonyl-substituted aromatic/heterocyclic sulfonamides selectively inhibit mitochondrial over cytosolic carbonic anhydrases. *Bioorganic & medicinal chemistry letters* 2011, 21(5):1334-1337.

29. Poulsen SA, Wilkinson BL, Innocenti A, Vullo D, Supuran CT: Inhibition of human mitochondrial carbonic anhydrases VA and VB with para-(4-phenyltriazole-1-yl)-benzenesulfonamide derivatives. *Bioorganic & medicinal chemistry letters* 2008, 18(16):4624-4627.

30. Cecchi A, Taylor SD, Liu Y, Hill B, Vullo D, Scozzafava A, Supuran CT: Carbonic anhydrase inhibitors: inhibition of the human isozymes I, II, VA, and IX with a library of substituted difluoromethanesulfonamides. *Bioorganic & medicinal chemistry letters* 2005, 15(23):5192-5196.

31. Winum JY, Thiry A, Cheikh KE, Dogne JM, Montero JL, Vullo D, Scozzafava A, Masereel B, Supuran CT: Carbonic anhydrase inhibitors. Inhibition of isoforms I, II, IV, VA, VII, IX, and XIV with sulfonamides incorporating fructopyranose-thioureido tails. *Bioorganic & medicinal chemistry letters* 2007, 17(10):2685-2691.

32. De Luca L, Angeli A, Ricci F, Supuran CT, Gitto R: Structure-guided identification of a selective sulfonamide-based inhibitor targeting the human carbonic anhydrase VA isoform. *Archiv der Pharmazie* 2023, 356(1):e2200383.

33. Wolber G, Langer T: LigandScout: 3-D pharmacophores derived from protein-bound ligands and their use as virtual screening filters. *Journal of chemical information and modeling* 2005, 45(1):160-169.

34. Mulnaes D, Porta N, Clemens R, Apanasenko I, Reiners J, Gremer L, Neudecker P, Smits SHJ, Gohlke H: TopModel: Template-Based Protein Structure Prediction at Low Sequence Identity Using Top-Down Consensus and Deep Neural Networks. *Journal of chemical theory and computation* 2020, 16(3):1953-1967.

35. Daina A, Michielin O, Zoete V: SwissADME: a free web tool to evaluate pharmacokinetics, drug-likeness and medicinal chemistry friendliness of small molecules. *Scientific reports* 2017, 7:42717.

36. Guzel O, Innocenti A, Scozzafava A, Salman A, Supuran CT: Carbonic anhydrase inhibitors. Aromatic/heterocyclic sulfonamides incorporating phenacetyl, pyridylacetyl and thienylacetyl tails act as potent inhibitors of human mitochondrial isoforms VA and VB. *Bioorganic & medicinal chemistry* 2009, 17(14):4894-4899.

37. Mancuso F, Di Fiore A, De Luca L, Angeli A, Monti SM, De Simone G, Supuran CT, Gitto R: Looking toward the Rim of the Active Site Cavity of Druggable Human Carbonic Anhydrase Isoforms. *ACS medicinal chemistry letters* 2020, 11(5):1000-1005.

38.   Pedretti A, Mazzolari A, Gervasoni S, Fumagalli L, Vistoli G: The VEGA suite of programs: an versatile platform for cheminformatics and drug design projects. *Bioinformatics* 2021, 37(8):1174-1175.

39.   Jones G, Willett P, Glen RC, Leach AR, Taylor R: Development and validation of a genetic algorithm for flexible docking. *Journal of molecular biology* 1997, 267(3):727-748.

40.   Supuran CT, Alterio V, Di Fiore A, K DA, Carta F, Monti SM, De Simone G: Inhibition of carbonic anhydrase IX targets primary tumors, metastases, and cancer stem cells: Three for the price of one. *Medicinal research reviews* 2018, 38(6):1799-1836.

41.   Hsieh MJ, Chen KS, Chiou HL, Hsieh YS: Carbonic anhydrase XII promotes invasion and migration ability of MDA-MB-231 breast cancer cells through the p38 MAPK signaling pathway. *European journal of cell biology* 2010, 89(8):598-606.

42.   Waheed A, Sly WS: Carbonic anhydrase XII functions in health and disease. *Gene* 2017, 623:33-40.

43.   Angeli A, Peat TS, Selleri S, Saleh Alfawaz Altamimi A, Supuran CT, Carta F: X-ray crystallography of Epacadostat in adduct with Carbonic Anhydrase IX. *Bioorganic chemistry* 2020, 97:103669.

44.   Kumar A, Siwach K, Supuran CT, Sharma PK: A decade of tail-approach based design of selective as well as potent tumor associated carbonic anhydrase inhibitors. *Bioorganic chemistry* 2022, 126:105920.

45.   Elsawi AE, Elbadawi MM, Nocentini A, Almahli H, Giovannuzzi S, Shaldam M, Salem R, Ibrahim TM, Abdel-Aziz HA, Supuran CT *et al*: 1,5-Diaryl-1,2,4-triazole Ureas as New SLC-0111 Analogues Endowed with Dual Carbonic Anhydrase and VEGFR-2 Inhibitory Activities. *Journal of medicinal chemistry* 2023, 66(15):10558-10578.

46.   Agamennone M, Fantacuzzi M, Carradori S, Petzer A, Petzer JP, Angeli A, Supuran CT, Luisi G: Coumarin-Based Dual Inhibitors of Human Carbonic Anhydrases and Monoamine Oxidases Featuring Amino Acyl and (Pseudo)-Dipeptidyl Appendages: In Vitro and Computational Studies. *Molecules* 2022, 27(22).

47.   Krasavin M, Zalubovskis R, Grandane A, Domraceva I, Zhmurov P, Supuran CT: Sulfocoumarins as dual inhibitors of human carbonic anhydrase isoforms IX/XII and of human thioredoxin reductase. *Journal of enzyme inhibition and medicinal chemistry* 2020, 35(1):506-510.

48.   Scozzafava A, Menabuoni L, Mincione F, Briganti F, Mincione G, Supuran CT: Carbonic anhydrase inhibitors. Synthesis of water-soluble, topically effective, intraocular pressure-lowering aromatic/heterocyclic sulfonamides containing cationic or anionic moieties: is the tail more important than the ring? *Journal of medicinal chemistry* 1999, 42(14):2641-2650.

49.   Ibrahim HS, Abou-Seri SM, Abdel-Aziz HA: 3-Hydrazinoindolin-2-one derivatives: Chemical classification and investigation of their targets as anticancer agents. *European journal of medicinal chemistry* 2016, 122:366-381.

50.   Karali N, Akdemir A, Goktas F, Eraslan Elma P, Angeli A, Kizilirmak M, Supuran CT: Novel sulfonamide-containing 2-indolinones that selectively inhibit tumor-associated alpha carbonic anhydrases. *Bioorganic & medicinal chemistry* 2017, 25(14):3714-3718.

51.   Sabet R, Mohammadpour M, Sadeghi A, Fassihi A: QSAR study of isatin analogues as in vitro anti-cancer agents. *European journal of medicinal chemistry* 2010, 45(3):1113-1118.

52.   Nocentini A, Trallori E, Singh S, Lomelino CL, Bartolucci G, Di Cesare Mannelli L, Ghelardini C, McKenna R, Gratteri P, Supuran CT: 4-Hydroxy-3-nitro-5-ureido-benzenesulfonamides Selectively Target the Tumor-Associated Carbonic Anhydrase Isoforms IX and XII Showing Hypoxia-Enhanced Antiproliferative Profiles. *Journal of medicinal chemistry* 2018, 61(23):10860-10874.

53.   Chahal V, Nirwan S, Kakkar R: A comparative study of the binding modes of SLC-0111 and its analogues in the hCA II and hCA IX active sites using QM/MM, molecular docking, MM-GBSA and MD approaches. *Biophysical chemistry* 2020, 265:106439.

54.   SitaRam, Ceruso M, Khloya P, Supuran CT, Sharma PK: 4-Functionalized 1,3-diarylpyrazoles bearing 6-aminosulfonylbenzothiazole moiety as potent inhibitors of carbonic anhydrase isoforms hCA I, II, IX and XII. *Bioorganic & medicinal chemistry* 2014, 22(24):6945-6952.

55.   Eldehna WM, Fares M, Ceruso M, Ghabbour HA, Abou-Seri SM, Abdel-Aziz HA, Abou El Ella DA, Supuran CT: Amido/ureidosubstituted benzenesulfonamides-isatin conjugates as low

nanomolar/subnanomolar inhibitors of the tumor-associated carbonic anhydrase isoform XII. *European journal of medicinal chemistry* 2016, 110:259-266.

56. Gitto R, Damiano FM, De Luca L, Ferro S, Vullo D, Supuran CT, Chimirri A: Synthesis and biological profile of new 1,2,3,4-tetrahydroisoquinolines as selective carbonic anhydrase inhibitors. *Bioorganic & medicinal chemistry* 2011, 19(23):7003-7007.

57. Gitto R, Agnello S, Ferro S, De Luca L, Vullo D, Brynda J, Mader P, Supuran CT, Chimirri A: Identification of 3,4-Dihydroisoquinoline-2(1H)-sulfonamides as potent carbonic anhydrase inhibitors: synthesis, biological evaluation, and enzyme--ligand X-ray studies. *Journal of medicinal chemistry* 2010, 53(6):2401-2408.

58. Tubiana T, Carvaillo JC, Boulard Y, Bressanelli S: TTClust: A Versatile Molecular Simulation Trajectory Clustering Program with Graphical Summaries. *Journal of chemical information and modeling* 2018, 58(11):2178-2182.

59. Sastry GM, Adzhigirey M, Day T, Annabhimoju R, Sherman W: Protein and ligand preparation: parameters, protocols, and influence on virtual screening enrichments. *Journal of computer-aided molecular design* 2013, 27(3):221-234.

60. Humphrey W, Dalke A, Schulten K: VMD: visual molecular dynamics. *Journal of molecular graphics* 1996, 14(1):33-38, 27-38.

61. Friesner RA, Murphy RB, Repasky MP, Frye LL, Greenwood JR, Halgren TA, Sanschagrin PC, Mainz DT: Extra precision glide: docking and scoring incorporating a model of hydrophobic enclosure for protein-ligand complexes. *Journal of medicinal chemistry* 2006, 49(21):6177-6196.

62. Roulier B, Peres B, Haudecoeur R: Advances in the Design of Genuine Human Tyrosinase Inhibitors for Targeting Melanogenesis and Related Pigmentations. *Journal of medicinal chemistry* 2020, 63(22):13428-13443.

63. Hida T, Kamiya T, Kawakami A, Ogino J, Sohma H, Uhara H, Jimbow K: Elucidation of Melanogenesis Cascade for Identifying Pathophysiology and Therapeutic Approach of Pigmentary Disorders and Melanoma. *International journal of molecular sciences* 2020, 21(17).

64. Logesh R, Prasad SR, Chipurupalli S, Robinson N, Mohankumar SK: Natural tyrosinase enzyme inhibitors: A path from melanin to melanoma and its reported pharmacological activities. *Biochimica et biophysica acta Reviews on cancer* 2023, 1878(6):188968.

65. Pereira JAL, Moraes LS, Sena CBC, Nascimento J, Rodrigues APD, Silva S, Silva EO: Inhibition of Melanization by Kojic Acid Promotes Cell Wall Disruption of the Human Pathogenic Fungus Fonsecaea sp. *Pathogens* 2022, 11(8).

66. Chang TS: An updated review of tyrosinase inhibitors. *International journal of molecular sciences* 2009, 10(6):2440-2475.

67. Qu Y, Zhan Q, Du S, Ding Y, Fang B, Du W, Wu Q, Yu H, Li L, Huang W: Catalysis-based specific detection and inhibition of tyrosinase and their application. *Journal of pharmaceutical analysis* 2020, 10(5):414-425.

68. Kanteev M, Goldfeder M, Fishman A: Structure-function correlations in tyrosinases. *Protein science : a publication of the Protein Society* 2015, 24(9):1360-1369.

69. Lai X, Wichers HJ, Soler-Lopez M, Dijkstra BW: Structure and Function of Human Tyrosinase and Tyrosinase-Related Proteins. *Chemistry* 2018, 24(1):47-55.

70. Li J, Feng L, Liu L, Wang F, Ouyang L, Zhang L, Hu X, Wang G: Recent advances in the design and discovery of synthetic tyrosinase inhibitors. *European journal of medicinal chemistry* 2021, 224:113744.

71. Lai X, Soler-Lopez M, Wichers HJ, Dijkstra BW: Large-Scale Recombinant Expression and Purification of Human Tyrosinase Suitable for Structural Studies. *PloS one* 2016, 11(8):e0161697.

72. Schweikardt T, Olivares C, Solano F, Jaenicke E, Garcia-Borron JC, Decker H: A three-dimensional model of mammalian tyrosinase active site accounting for loss of function mutations. *Pigment cell research* 2007, 20(5):394-401.

73. Haudecoeur R, Carotti M, Gouron A, Maresca M, Buitrago E, Hardre R, Bergantino E, Jamet H, Belle C, Reglier M *et al*: 2-Hydroxypyridine-N-oxide-Embedded Aurones as Potent Human Tyrosinase Inhibitors. *ACS medicinal chemistry letters* 2017, 8(1):55-60.

74. Vittorio S, Dank C, Ielo L: Heterocyclic Compounds as Synthetic Tyrosinase Inhibitors: Recent Advances. *International journal of molecular sciences* 2023, 24(10).

75. Pillaiyar T, Manickam M, Namasivayam V: Skin whitening agents: medicinal chemistry perspective of tyrosinase inhibitors. *Journal of enzyme inhibition and medicinal chemistry* 2017, 32(1):403-425.

76. Ielo L, Deri B, Germano MP, Vittorio S, Mirabile S, Gitto R, Rapisarda A, Ronsisvalle S, Floris S, Pazy Y *et al*: Exploiting the 1-(4-fluorobenzyl)piperazine fragment for the development of novel tyrosinase inhibitors as anti-melanogenic agents: Design, synthesis, structural insights and biological profile. *European journal of medicinal chemistry* 2019, 178:380-389.

77. Romagnoli R, Oliva P, Prencipe F, Manfredini S, Germano MP, De Luca L, Ricci F, Corallo D, Aveic S, Mariotto E *et al*: Cinnamic acid derivatives linked to arylpiperazines as novel potent inhibitors of tyrosinase activity and melanin synthesis. *European journal of medicinal chemistry* 2022, 231:114147.

78. Ferro S, De Luca L, Germano MP, Buemi MR, Ielo L, Certo G, Kanteev M, Fishman A, Rapisarda A, Gitto R: Chemical exploration of 4-(4-fluorobenzyl)piperidine fragment for the development of new tyrosinase inhibitors. *European journal of medicinal chemistry* 2017, 125:992-1001.

79. Mirabile S, Ielo L, Lombardo L, Ricci F, Gitto R, Germano MP, Pace V, De Luca L: Leveraging the 3-Chloro-4-fluorophenyl Motif to Identify Inhibitors of Tyrosinase from Agaricus bisporus. *International journal of molecular sciences* 2023, 24(9).

80. De Luca L, Germano MP, Fais A, Pintus F, Buemi MR, Vittorio S, Mirabile S, Rapisarda A, Gitto R: Discovery of a new potent inhibitor of mushroom tyrosinase (Agaricus bisporus) containing 4-(4-hydroxyphenyl)piperazin-1-yl moiety. *Bioorganic & medicinal chemistry* 2020, 28(11):115497.

81. Mann T, Gerwat W, Batzer J, Eggers K, Scherner C, Wenck H, Stab F, Hearing VJ, Rohm KH, Kolbe L: Inhibition of Human Tyrosinase Requires Molecular Motifs Distinctively Different from Mushroom Tyrosinase. *The Journal of investigative dermatology* 2018, 138(7):1601-1608.

82. Jumper J, Evans R, Pritzel A, Green T, Figurnov M, Ronneberger O, Tunyasuvunakool K, Bates R, Zidek A, Potapenko A *et al*: Highly accurate protein structure prediction with AlphaFold. *Nature* 2021, 596(7873):583-589.

83. Waterhouse A, Bertoni M, Bienert S, Studer G, Tauriello G, Gumienny R, Heer FT, de Beer TAP, Rempfer C, Bordoli L *et al*: SWISS-MODEL: homology modelling of protein structures and complexes. *Nucleic acids research* 2018, 46(W1):W296-W303.

84. Sali A, Blundell TL: Comparative protein modelling by satisfaction of spatial restraints. *Journal of molecular biology* 1993, 234(3):779-815.

85. Lai X, Wichers HJ, Soler-Lopez M, Dijkstra BW: Phenylthiourea Binding to Human Tyrosinase-Related Protein 1. *International journal of molecular sciences* 2020, 21(3).

86. Mulnaes D, Koenig F, Gohlke H: TopSuite Web Server: A Meta-Suite for Deep-Learning-Based Protein Structure and Quality Prediction. *Journal of chemical information and modeling* 2021, 61(2):548-553.

87. Hooft RW, Vriend G, Sander C, Abola EE: Errors in protein structures. *Nature* 1996, 381(6580):272.

88. Laskowski RA, Rullmannn JA, MacArthur MW, Kaptein R, Thornton JM: AQUA and PROCHECK-NMR: programs for checking the quality of protein structures solved by NMR. *Journal of biomolecular NMR* 1996, 8(4):477-486.

89. Colovos C, Yeates TO: Verification of protein structures: patterns of nonbonded atomic interactions. *Protein science : a publication of the Protein Society* 1993, 2(9):1511-1519.

90. Luthy R, Bowie JU, Eisenberg D: Assessment of protein models with three-dimensional profiles. *Nature* 1992, 356(6364):83-85.

91. Pontius J, Richelle J, Wodak SJ: Deviations from standard atomic volumes as a quality measure for protein crystal structures. *Journal of molecular biology* 1996, 264(1):121-136.

92. Goldfeder M, Kanteev M, Isaschar-Ovdat S, Adir N, Fishman A: Determination of tyrosinase substrate-binding modes reveals mechanistic differences between type-3 copper proteins. *Nature communications* 2014, 5:4505.

93. Deri B, Kanteev M, Goldfeder M, Lecina D, Guallar V, Adir N, Fishman A: The unravelling of the complex pattern of tyrosinase inhibition. *Scientific reports* 2016, 6:34993.

94.   Lai X, Wichers HJ, Soler-Lopez M, Dijkstra BW: Structure of Human Tyrosinase Related Protein 1 Reveals a Binuclear Zinc Active Site Important for Melanogenesis. *Angew Chem Int Ed Engl* 2017, 56(33):9812-9815.

95.   Mirabile S, Germano MP, Fais A, Lombardo L, Ricci F, Floris S, Cacciola A, Rapisarda A, Gitto R, De Luca L: Design, Synthesis, and in Vitro Evaluation of 4-(4-Hydroxyphenyl)piperazine-Based Compounds Targeting Tyrosinase. *ChemMedChem* 2022, 17(21):e202200305.

96.   Ismaya WT, Rozeboom HJ, Weijn A, Mes JJ, Fusetti F, Wichers HJ, Dijkstra BW: Crystal structure of Agaricus bisporus mushroom tyrosinase: identity of the tetramer subunits and interaction with tropolone. *Biochemistry* 2011, 50(24):5477-5486.

97.   Jacobson MP, Pincus DL, Rapp CS, Day TJ, Honig B, Shaw DE, Friesner RA: A hierarchical approach to all-atom protein loop prediction. *Proteins* 2004, 55(2):351-367.

98.   Mulnaes D, Gohlke H: TopScore: Using Deep Neural Networks and Large Diverse Data Sets for Accurate Protein Model Quality Assessment. *Journal of chemical theory and computation* 2018, 14(11):6117-6126.

List of publications

TITLE

Computational methods to analyze and predict the binding mode of inhibitors targeting both human and mushroom tyrosinase

AUTHORS

Federico Ricci, Kristina Schira, Lyna Khettabi, Lisa Lombardo, Salvatore Mirabile, Rosaria Gitto, Montserrat Soler-Lopez, Jörg Scheuermann, Gerhard Wolber, Laura De Luca

ABSTRACT

Tyrosinase, a copper-containing enzyme critical in melanin biosynthesis, is a key drug target for hyperpigmentation and melanoma in humans. Testing the inhibitory effects of compounds using tyrosinase from Agaricus bisporus (AbTYR) has been a common practice to identify potential therapeutics from synthetic and natural sources. However, structural diversity among human tyrosinase (hTYR) and AbTYR presents a challenge in developing drugs that are therapeutically effective. In this study, we combined retrospective and computational analyses with experimental data to provide insights into the development of new inhibitors targeting both hTYR and AbTYR. We observed contrasting effects of Thiamidol™ and our 4-(4-hydroxyphenyl)piperazin-1-yl-derivative (6) on both enzymes; based on this finding, we aimed to investigate their binding modes in hTYR and AbTYR to identify residues that significantly improve affinity. All the information led to the discovery of compound [4-(4-hydroxyphenyl)piperazin-1-yl](2-methoxyphenyl)methanone (MehT-3, 7), which showed comparable activity on AbTYR (IC50 = 3.52 μM) and hTYR (IC50 = 5.4 μM). Based on these achievements we propose the exploitation of our computational results to provide relevant structural information for the development of newer dual-targeting molecules, which could be preliminarily tested on AbTYR as a rapid and inexpensive screening procedure before being tested on hTYR.

TITLE

Screening Campaign and Docking Investigations in Identifying New Hit Compounds as Inhibitors of Human Carbonic Anhydrases Expressed In Tumour Cells

AUTHORS

Federico Ricci, Andrea Angeli, Francesca Mancuso, Laura De Luca, Claudiu T. Supuran, Rosaria Gitto

ABSTRACT

The tumor-expressed human carbonic anhydrase (hCA) isoforms hCA IX and hCA XII have been extensively studied to develop anticancer agents targeting solid tumors in combined therapy. These CA isoforms are considered key factors in controlling tumor microenvironment (TME) of cancer lines that develop high metastatic activity. Herein, we report the discovery of potent hCA IX/hCA XII inhibitors that were disclosed through a screening campaign on an in-house collection of arylsulfonamides preliminary tested toward other hCAs. Among them, the N-(4-sulfamoylphenyl)naphthalene-2-carboxamide (12) and N-(4-sulfamoylphenyl)-3,4-dihydroisoquinoline-2(1H)-carbothioamide (15) proved to be the most intriguing hCA IX/hCA XII inhibitors displaying favourable selectivity ratios over widespread hCA I and hCA II isoforms. To explore their binding mode, we conducted docking studies that described the poses of the best inhibitors in the catalytic site of hCA IX and hCA XII, thus suggesting the privileged pattern of interactions. These structural findings might further improve the knowledge for a successful identification of new sulfonamides as adjuvant agents in cancer management.

TITLE

Leveraging the 3-Chloro-4-fluorophenyl Motif to Identify Inhibitors of Tyrosinase from Agaricus bisporus

AUTHORS

Salvatore Mirabile, Laura Ielo, Lisa Lombardo, **Federico Ricci**, Rosaria Gitto, Maria Paola Germanò, Vittorio Pace, Laura De Luca

ABSTRACT

Tyrosinase (EC 1.14.18.1) is implicated in melanin production in various organisms. There is a growing body of evidence suggesting that the overproduction of melanin might be related to several skin pigmentation disorders as well as neurodegenerative processes in Parkinson's disease. Based on this consideration, the development of tyrosinase inhibitors represents a new challenge to identify new agents in pharmaceutical and cosmetic applications. With the goal of identifying tyrosinase inhibitors from a synthetic source, we employed a cheap and facile preliminary assay using tyrosinase from Agaricus bisporus (AbTYR). We have previously demonstrated that the 4-fluorobenzyl moiety might be effective in interactions with the catalytic site of AbTYR; moreover, the additional chlorine atom exerted beneficial effects in enhancing inhibitory activity. Therefore, we planned the synthesis of new small compounds in which we incorporated the 3-chloro-4-fluorophenyl fragment into distinct chemotypes that revealed the ability to establish profitable contact with the AbTYR catalytic site. Our results confirmed that the presence of this fragment is an important structural feature to improve the AbTYR inhibition in these new chemotypes as well. Furthermore, docking analysis supported the best activity of the selected studied compounds, possessing higher potency when compared with reference compounds.

TITLE

Structure-guided identification of a selective sulfonamide-based inhibitor targeting the human carbonic anhydrase VA isoform

AUTHORS

Laura De Luca, Andrea Angeli, **Federico Ricci**, Claudiu T. Supuran, Rosaria Gitto

ABSTRACT

In recent years, multistep hybrid computational protocols have attracted attention for their application in the drug discovery of enzyme inhibitors. So far, there are large collections of human carbonic anhydrase (hCA) inhibitors, but only a few of them selectively inhibit the mitochondrial isoforms hCA VA and VB as potential therapeutics in obesity treatment. Most sulfonamide-based inhibitors show poor selectivity for inhibiting isoforms of therapeutic interest over ubiquitous hCA I and hCA II. Herein, we propose a combination of ligand- and structure-based approaches to generate pharmacophore models for hCA VA inhibitors. Then, we performed a virtual screening (VS) campaign on a database of commercially available sulfonamides. Finally, the in silico screening followed by docking studies suggested several "hit compounds" that demonstrated to inhibit hCA VA at a low nanomolar concentration in a stopped-flow CO_2 hydrase assay. Notably, the best candidate, 2-(3,4-dihydro-2H-quinolin-1-yl)-N-(4-sulfamoylphenyl)acetamide (code name VAME-28) proved to be a potent hCA VA inhibitor (Ki value of 54.8 nM) and a more selective agent over hCA II when compared to the reference compound topiramate.

TITLE

Design, Synthesis, and in Vitro Evaluation of 4-(4-Hydroxyphenyl)piperazine-Based Compounds Targeting Tyrosinase

AUTHORS

Salvatore Mirabile, Maria Paola Germanò, Antonella Fais, Lisa Lombardo, **Federico Ricci**, Sonia Floris, Anna Cacciola, Antonio Rapisarda, Rosaria Gitto, Laura De Luca

ABSTRACT

Melanin biosynthesis is enzymatically regulated by tyrosinase (TYR, EC 1.14.18.1), which is efficiently inhibited by natural and synthetic phenols, demonstrating potential therapeutic application for the treatment of several human diseases. Herein we report the inhibitory effects of a series of (4-(4-hydroxyphenyl)piperazin-1-yl)arylmethanone derivatives, that were designed, synthesised and assayed against TYR from Agaricus bisporus (AbTYR). The best inhibitory activity was predominantly found for compounds bearing selected hydrophobic ortho-substituents on the aroyl moiety (IC50 values in the range of 1.5–4.6 μM). They proved to be more potent than the reference compound kojic acid (IC50=17.8 μM) and displayed competitive mechanism of inhibition of diphenolase activity of AbTYR. Docking simulation predicted their binding mode into the catalytic cavities of AbTYR and the modelled human TYR. In addition, these compounds displayed antioxidant activity combined with no cytotoxicity in MTT tests. Notably, the best inhibitor affected tyrosinase activity in α-MSH-stimulated B16F10 cells, thus demonstrating anti-melanogenic activity.

TITLE

In Silico Insights towards the Identification of SARS-CoV-2 NSP13 Helicase Druggable Pockets

AUTHORS

Federico Ricci, Rosaria Gitto, Giovanna Pitasi, Laura De Luca

ABSTRACT

The merging of distinct computational approaches has become a powerful strategy for discovering new biologically active compounds. By using molecular modeling, significant efforts have recently resulted in the development of new molecules, demonstrating high efficiency in reducing the replication of severe acute respiratory coronavirus 2 (SARS-CoV-2), the agent responsible for the COVID-19 pandemic. We have focused our interest on non-structural protein Nsp13 (NTPase/helicase), as a crucial protein, embedded in the replication–transcription complex (RTC), that controls the virus life cycle. To assist in the identification of the most druggable surfaces of Nsps13, we applied a combination of four computational tools: FTMap, SiteMap, Fpocket and LigandScout. These software packages explored the binding sites for different three-dimensional structures of RTC complexes (PDB codes: 6XEZ, 7CXM, 7CXN), thus, detecting several hot spots, that were clustered to obtain ensemble consensus sites, through a combination of four different approaches. The comparison of data provided new insights about putative druggable sites that might be employed for further docking simulations on druggable surfaces of Nsps13, in a scenario of repurposing drugs.

TITLE

Cinnamic acid derivatives linked to arylpiperazines as novel potent inhibitors of tyrosinase activity and melanin synthesis

AUTHORS

Romeo Romagnoli, Paola Oliva, Filippo Prencipe, Stefano Manfredini, Maria Paola Germanò, Laura De Luca, **Federico Ricci**, Diana Corallo, Sanja Aveic, Elena Mariotto, Giampietro Viola, Roberta Bortolozzi

ABSTRACT

A novel series of twenty-seven cinnamides constituted by cinnamic acid derivatives liked to 1-aryl piperazines were synthesized and evaluated for their potential inhibitory diphenolase activity of mushroom tyrosinase. Among them, the presence of a 3-chloro-4-fluorophenyl moiety at the N-1 position of piperazine ring was essential for a potent tyrosinase inhibitory effect, with the 3-nitrocinnamoyl (19p) and 2-chloro-3-methoxycinnamoyl (19t) derivatives as the most potent compounds of the series, with IC50 of 0.16 and 0.12 µM, respectively, resulting much active than kojic acid, whose IC50 value was 17.76 µM. In general, all compounds characterized by the presence of a 1-(3-chloro-4-fluorophenyl)piperazine moiety showed an excellent potency, and the nature, position and number of the substituents on the aryl of the cinnamic acid did not affect significantly the anti-tyrosinase activity. The molecular docking to the active site of the enzyme has been also performed to investigate the nature of enzyme-inhibitor interactions. Furthermore, for selected highly active compounds, their ability to inhibit melanogenesis in the A375 human melanoma cells and in vivo zebrafish model was also evaluated. One of the most potent compounds of series (19t) significantly reduced the pigmentation of zebrafish at 50 µM, unfortunately showing 100% mortality in the Fish Embryo Acute Toxicity (FET) test at the same concentration, Moreover, the zebrafish assay reveals that also compound 19r (IC50:0.51 µM against mushroom tyrosinase) effectively reduces melanogenesis with no acute toxicity effects and it could be proposed as potential candidate to treat tyrosinase-mediated hyperpigmentation.

TITLE

Synthesis and biochemical evaluation of 5-(pyridin-4-yl)-3-(alkylsulfanyl)-4H- 1,2,4-triazol-4-amine-based inhibitors of tyrosinase from Agaricus bisporus

AUTHORS

Laura De Luca, Salvatore Mirabile, **Federico Ricci**, Ilenia Adornato, Anna Cacciola, Maria Paola Germanò, Rosaria Gitto

ABSTRACT

Several studies demonstrated that hyperpigmentation pathologies might be treated by using agents targeting the enzymatic metallo-protein tyrosinase. Therefore, we predicted the development of a series of small molecules able to inhibit diphenolase activity of tyrosinase from Agaricus bisporus. The designed compounds were readily synthesized by S-alkylation and the synthesized compounds were tested through biochemical screening, thus providing structure-affinity relationships for this class of 5-(pyridin-4-yl)-3-(alkylsulfanyl)-4H- 1,2,4-triazol-4-amine derivatives. In addition, docking simulations suggested the binding mode within the catalytic site of the targeted enzyme.

List of communications

- **Oral communication - Learning on human Tyrosinase: from homology modelling to new inhibitors selection.**
  F. Ricci, K. Schira, L. Khettabi, L. Lombardo, S. Mirabile, R. Gitto, M. Soler-Lopez, J. Scheuermann, G. Wolber and L. De Luca L.; presented at *XXVIII NMMC 2023;* 17 – 20 September 2023, Chieti, Italy

- **Poster communication - A fast ensemble docking method for ligand recognition in hCA IX/hCA XII isoforms.**
  F. Ricci, L. De Luca, A. Angeli, CT. Supuran and R. Gitto; presented at *XII Paul Ehrlich PhD NetWork in Medicinal Chemistry;* 16 – 18 July 2023, Thessaloniki, Greece

- **Poster communication - From Retrospective to Perspective studies on 1-2-3-4-Tethrahydroisoquinolin-2-ylsulfonamides as hCA IX/XII inhibitors.**
  F. Ricci, A. Di Fiore, A. Angeli, R. Gitto, G. De Simone, C.T. Supuran and L. De Luca; presented at *12th International conference on Carbonic Anydrases*; 5-7 July 2023, Naples, Italy

- **Poster communication - Structural prediction and comparative docking studies of human and Agaricus bisporus Tyrosinases.**
  F. Ricci, L. Lombardo, S. Mirabile, R. Gitto, G. Wolber and L. De Luca; presented at *23rd EuroQSAR*; 26 – 30 September 2022; Heidelberg, Germany

- **Poster communication - Ensemble-Consensus binding-site detection of SARS - CoV-2 non - structural protein 13(NSP13).**
  F. Ricci, L. De Luca and Rosaria Gitto; presented at *Convegno SCI Sicilia 2021*; 2 December 2021; Catania (Online Meeting), Italy

- **Poster communication - Crossing Ligand and Structure – based techniques for In Silico retrieving of hCA VA inhibitors.**
  F. Ricci, E. D'Agostino, L. De Luca and R. Gitto; presented at *NPCF13*; 26 – 29 April 2021; Online Meeting, Italy

Abbreviation list

hCA	Human Carbonic Anhydrase
hTYR	Human Tyrosinase
AbTYR	Agaricus Bisporus Tyrosinase
VS	Virtual Screening
MD	Molecular Dynamics
ROS	Oxygen reactive species
SOD	Superoxide dismutase
CCK	Cholecystokinin
GLP − 1	Glucagon-like peptide-1
PYY	Peptide YY
WAT	White adipose tissue
BAT	Brown adipose tissue
TNF − α	Tumor Necrosis factor α
IL − 6	Interleukin 6
LPS	Lipopolysaccharide
TLR4	Toll − like receptor 4
RNS	Reactive nitrogen species
LAGB	Adjustable gastric banding
RYGB	Roux − en − Y gastric bypass
SG	Sleeve gastrectomy
BPD-DS	Bilio-pancreatic diversion with duodenal switch
IGB	Intragastric balloon
POMC	Proopiomelanocortin
5-HT2b	5-hydroxytryptamine 2B

VTA	Ventral tegmental area
ARC	Arcuate nucleus
AGRP	Agouti-related peptide
CART	Cocaine and amphetamine-regulated transcript
D1R	Dopamine 1-class receptor
D2R	Dopamine 2-class receptor
GABA	γ-aminobutyric acid
GABAAR	γ-aminobutyric acid type A receptor
GLP – 1R	Glucagon-like peptide-1 receptor
MC3R	Melanocortin-3 receptor
MC4R	Melanocortin-4 receptor
MOPR	μ-opioid receptor
NAc	Nucleus accumbens
NPY	Neuropeptide Y
Y1R	Neuropeptide Y type 1 receptor
AMPA	α-Ammino-3-idrossi-5-Metil-4-isossazol-Propionic Acid
FDA	Food and Drug Administration
EMA	European Medicines Agency
GCGR	Glucagon receptor
PC	Pyruvate carboxylase
MCC	Methylcrotonyl – CoA carboxylase
OAA	Oxalacetate
ETZ	6-Ethoxyzolamide
ACC	Acetyl-CoA carboxylase
ACL	ATP citrate lyase
αKG	α-ketoglutarate

CS	Citrate synthase
FAS	Fatty acid synthase
PDH	Pyruvate dehydrogenase
AZM	Acetazolamide
mCA	Murine Carbonic Anhydrase
SAR	Structure - activity relationship
LB	Ligand – based
SB	Structure – based
ROC	Receiver operating characteristic
EF	Enrichment Factor
AUC	Area under the curve
TPM	Topiramate
ZNS	Zonisamide
HIF – 1α	Hypoxia inducible factor 1α
FIH – 1	Factor inhibiting HIF-1
PHDs	Prolyl hydroxylase domain proteins
pVHL	Von Hippel Lindau tumor suppressor protein
HIF – 1β	Hypoxia inducible factor 1β
RCC	Renal clear cell carcinoma
CBP	CREB binding protein
HRE	Hypoxia Response Element
NBC	Na^+/HCO_3^- cotransporter
AE	Anion exchanger
MCT	Monocarboxylate transporter
V-ATPase	V-type H^+ ATPase
MMP – 14	Matrix metalloproteinase 14

MMP – 2	Matrix metalloproteinase 2
MMP – 9	Matrix metalloproteinase 9
U – PA	Urokinase-type Plasminogen Activator
MAPK	Mitogen - activated protein kinases
TIMP	Tissue inhibitors of metalloproteinases
PAI	Plasminogen Activator Inhibitor
PG	Proteoglycan - like domain
SP	Signal peptide
TM	Transmembrane domain
IC	Intracellular domain
VEGFR	Vascular Endothelial Growth Factor receptor
MAO	Monoamine oxidases
ZBG	Zinc – binder group
IDO – 1	Indoleamine 2,3-dioxygenase 1
SAC	Saccharin
Ace K	Acesulfame K
RMSD	Root – means square deviation
SID	Simulation Interaction Diagram
MCS	Maximum common substructure
v. atoms	Visible atoms
MM – GBSA	Molecular Mechanics Generalized Born Surface Area
CCD	Chemical component dictionary
VSGB	Variable dielectric Generalized Born Surface
OPLS	Optimized Potentials for Liquid Simulations
TIP4PEW	Transferable intermolecular potential 4 points Ewald
UVR	UV radiation

α – MSH	α - Melanocyte Stimulating Hormone
MIFT	Microphtalmia – associated transcription factor
CREB	cAMP response element binding protein
CRTC	CREB-regulated transcription coactivator
SIK	Salt inducible kinase
PKA	Protein kinase A
DCT	Dopachrome tautomerase
PMEL	Promelanosome protein
TYRP1	Tyrosinase - related protein 1
AP	Adaptor protein
BLOC	Biogenesis of lysosome-related organelles complex
GGA	Golgi-localized γ-ear-containing ADP-ribosylation factor-binding protein
CNS	Central nervous system
PD	Parkinson's disease
HGA	Homogentisic acid
HGD	Homogentisic acid dehydrogenase
PPO3	Polyphenol Oxidase 3
BmTYR	Bacillus Megaterium Tyrosinase
PROTACs	Proteolysis-targeting chimeras
TIP3P	Transferable intermolecular potential 3 points